The Stability and Behaviour of Flows in Stenotic Geometries

by

Martin D. Griffith BA/BEng(Hons)

A thesis submitted in fulfillment of the requirements for the degree of Doctor of Philosopy (Cotutelle)

Department of Mechanical Engineering, Monash University

and

Institut de Recherche sur les Phénomènes Hors Equilibre (IRPHE), Université de Provence Aix-Marseille I

September 2007

Contents

1 Introduction **1**

1.1 Project aims 1

1.2 Overview of the study 2

1.3 Structure of the thesis 3

2 Literature Review **5**

2.1 Fluid mechanics in blood flow 5

2.1.1 Modelling blood flow 5

2.1.1.1 Analytical solution to pulsatile flow 6

2.1.1.2 Lumped parameter models 9

2.1.1.3 One-dimensional models 9

2.1.1.4 Localised cardiovascular phenomena 10

2.1.2 Biological response to fluid mechanical characteristics 11

2.2 Steady flow in occluded paths 14

2.2.1 The backward-facing step 15

2.2.1.1 Paths to instability 16

2.2.1.2 Expansion ratio effects in backward-facing step type flows 20

2.2.1.3 Present work (chapter 4) 22

2.2.2 Stenotic geometries – steady flow 22

2.2.2.1 Present work (chapter 5) 27

2.3 Pulsatile flows 28

2.3.1 Two-dimensional geometries 28

2.3.2 Stenotic geometries – pulsatile flows 29

2.3.2.1 Direct stenotic flow modelling 30

2.3.2.2 Idealised stenosis modelling 31

2.3.2.3 Present work (chapter 6) 40

2.4 Chapter summary 40

3 Methodology **43**

3.1 Numerical method: simulating the flow field 43

3.1.1 The spectral-element method . . . 44
3.1.1.1 Temporal discretisation . . . 44
3.1.1.2 Coordinate systems . . . 45
3.1.2 Floquet stability analysis . . . 45
3.2 Creating the flow models . . . 49
3.2.1 The two-dimensional channel . . . 49
3.2.1.1 Boundary conditions . . . 51
3.2.1.2 Mesh layout and resolution . . . 51
3.2.2 Axisymmetric problem definition: steady inlet flow . . . 54
3.2.2.1 Boundary conditions . . . 55
3.2.2.2 Mesh layout and resolution . . . 56
3.2.3 Numerical pulsatile flow . . . 57
3.2.3.1 Pulsatile boundary condition: Womersley's solution . . . 58
3.2.4 Mesh layout and validation: pulsatile flow . . . 60
3.3 Experimental method . . . 62
3.3.1 Description of the apparatus . . . 62
3.3.2 Diagnostic techniques . . . 68
3.3.2.1 Coloured dye visualisation . . . 68
3.3.2.2 Particle image velocimetry (PIV) . . . 70
3.3.3 Optimisation of the apparatus . . . 73
3.4 Chapter summary . . . 74

4 Wake Behaviour Through a Constricted Channel 77
4.1 Introduction . . . 77
4.2 Flow recirculation length . . . 79
4.3 Wake behaviour . . . 82
4.4 Three-dimensional behaviour . . . 86
4.4.1 Instability growth rates . . . 86
4.4.2 Structure of the instability . . . 89
4.4.3 Instability mechanism - centrifugal . . . 91
4.4.4 Instability mechanism - elliptic . . . 95
4.5 Chapter summary and discussion . . . 98

5 Steady Flow Through an Axisymmetric Stenotic Geometry 101
5.1 Introduction . . . 101
5.2 Flow characteristics . . . 102
5.2.1 Recirculation zone lengths . . . 104
5.2.2 Similarity . . . 109
5.3 Instability . . . 112

5.3.1 Linear stability analysis . . . 112
5.3.1.1 Mode structures . . . 112
5.3.2 Instability: experimental . . . 115
5.3.2.1 Shear-layer oscillations . . . 119
5.3.2.2 Periodically-forced flows: experimental . . . 123
5.3.2.3 Periodically-forced flows: numerical . . . 125
5.4 Chapter summary and discussion . . . 133

6 Pulsatile Flow in Axisymmetric Stenotic Geometries 137
6.1 Introduction . . . 137
6.2 Flow characteristics . . . 138
6.2.1 Vortex ring behaviour . . . 141
6.2.2 Wall shear stresses . . . 147
6.3 Floquet stability analysis: blockage ratio effect . . . 152
6.3.1 Stability analysis: $T = 2.5$ . . . 152
6.3.2 Stability analysis: $T = 5.0$ . . . 156
6.3.3 Stability analysis: $T = 1.0$ . . . 159
6.3.4 Stability analysis summary: $A = 0.75$ . . . 165
6.3.5 Effect of amplitude on absolute stability . . . 166
6.4 Experimental results . . . 173
6.4.1 Experimental validation . . . 173
6.4.2 Stability of the experimental flow . . . 176
6.4.2.1 Instability: $b = 0.50$ . . . 180
6.4.2.2 Instability: $b = 0.75$ . . . 182
6.4.2.3 Instability: $b = 0.90$ . . . 189
6.5 Chapter summary and discussion . . . 193

7 Conclusions 199
7.1 Summary of conclusions . . . 199
7.2 Possible future work . . . 204

Abstract

Steady and pulsatile flows in two blockage geometries are investigated. The geometries serve as idealised models of arterial stenosis, a common condition whereby a localised constriction grows within an artery, reducing the blood flow and pressure downstream and potentially causing stroke. The geometries are simplified models of the physiological reality of diseased arteries; the aim is to isolate and describe the fundamental fluid mechanical characteristics of stenotic flows. An emphasis is placed on the effect on the flow and its stability of changes in blockage ratio, or stenosis severity.

The first part of the thesis presents a numerical investigation of the steady inlet flow through a two-dimensional channel with a semi-circular blockage on one side of the channel, for blockage ratios of 0.05 to 0.9 and Reynolds numbers up to 3000. Variations in the wake behaviour and stability with Reynolds number and blockage are reported. The leading instability mode of the flow is described and its underlying mechanism determined to be elliptical.

A geometry consisting of a straight tube with an axisymmetric blockage is the focus of the second part of the thesis. Flows of both steady and pulsatile inlet velocity are modelled numerically and experimentally, for blockage ratios of 0.20 to 0.95 and Reynolds numbers up to 2400 for steady flow and 700 for pulsatile flow. The changes in wake behaviour with the various flow parameters are described. Numerically, different linear modes of instability are identified for different blockage ratios. Experimentally, the action of convective shear layer instability is found to be important. For steady flow, comparisons are made between the periodic behaviour of the convective instability and the response of stable flows to periodic forcing. For pulsatile flow, some evidence is found of the action of linear instability modes experimentally, although convective shear layer instability dominates. The variation of both forms of instability with Reynolds number and blockage ratio is characterised.

Les écoulements stationnaires et pulsés sont examinés dans deux géométries bloqués. Les géométries utilisées sont des modèles d'artères sténotiques, une condition commune ou une constriction localisée grandit dans une artère, réduisant ainsi l'écoulement du sang et la pression en aval et pouvant conduire à la formation d'un caillot. Les géométries sont des modèles simplifiés de la réalité physiologique d'une vrai sténose, l'intention de l'étude étant avant tout d'isoler et de décrire les caractéristiques fondamentales des écoulements sténotiques. L'étude se concentre sur l'effet sur l'écoulement et la stabilité de la variation du taux constriction, autrement dit la sévérité du sténose.

La première partie de la thèse présente une investigation de l'écoulement stationnaire à travers une conduite bidimensionelle, avec une constriction asymmétrique semi-circulaire, pour des taux de constriction de 0.05 à 0.9 et des nombres de Reynolds jusqu'à 3000. Les changements de la stabilité et du comportement du sillage avec le nombre de Reynolds et le taux de constriction sont réportés. Le mode primaire de l'instabilité est décrit et son mécanisme déterminé analytiquement comme étant élliptique.

La deuxième partie concerne une géométrie cylindrique avec une constriction axisymmétrique. Les écoulements stationnaires et pulsés sont examinés numériquement et expérimentalement, pour des taux de constriction de 0.20 à 0.95 et des nombres de Reynolds jusqu'à 2400 pour l'écoulement stationnaire et 700 pour l'écoulement pulsé. Numériquement, différents modes linéaires d'instabilité sont identifiés aux taux de constriction. Expérimentalement, l'influence importante d'une instabilité convective est observée. Pour l'écoulement stationnaire, des comparaisons entre le comportement périodique de l'instabilité convective et la réponse d'un forcage sur l'écoulement stable sont éffectuées. Pour l'écoulement pulsé, l'instabilité convective domine pour la plûpart des cas considérés. La variation des deux formes d'instabilité est caractérisée avec le nombre de Reynolds et le taux de constriction.

Declaration of Originality

I, Martin D. Griffith, declare that this thesis is my own work and contains no material that has been accepted for the award of a degree or diploma in this or any other university. To the best of my knowledge, information derived from the published and unpublished work of others has been acknowledged in the text of the thesis and a list of references is provided in the bibliography.

September 5, 2007

Acknowledgments

I thank my three supervisors, Professor Kerry Hourigan, Professor Mark Thompson and Dr. Thomas Leweke. Their collective guidance throughout the thesis has been crucial to its completion and their professionalism a fine role-model for a young researcher. I am also enormously grateful for the wonderful opportunity they granted me of doing my PhD by cotutelle; undertaking my work at two institutions in two countries has been an enriching and indelible experience.

I also thank Thomas Leweke for the warm welcome and hospitality he extended to me during my time in Marseille; his patience with my efforts to learn the French language and his interest in making sure I was happy, comfortable and productive while at IRPHE are greatly appreciated.

Financially, I was supported throughout my candidature by the Mechanical Engineering Department at Monash University, for which I am very grateful. I acknowledge assistance from the French Embassy of Australia in the form of a travel grant.

I thank all of the students, post-docs and academics with whom I shared an office, laboratory or corridor, who all contributed to the thesis in their own particular way. I especially thank Jérôme Hœpffner at IRPHE, whose fresh perspective on the project gave a much-needed impetus.

Finally, I extend my gratitude to my family, not for their direct contribution (only limited mention of bubbles is made in the thesis), but for their support throughout; particularly my parents, for letting me come and go as I please, and my brother Ian, for lending me his laptop computer.

Publications

Griffith, M., Hourigan, K. & Thompson, M.C. 2004 The effect of semi-circular blockages on the laminar two-dimensional flow between two flat plates. *In proceedings of the 12th Computational Techniques and Applications Conference*, The University of Melbourne, Melbourne, Australia, September 2004.

Griffith, M., Hourigan, K. & Thompson, M.C. 2004 Numerical investigation of the effect of semi-circular blockages on the laminar two-dimensional flow between two flat plates. *In proceedings of the 15th Australasian Fluid Mechanics Conference*, The University of Sydney, Sydney, Australia, December 2004.

Griffith, M.D., Hourigan, K. & Thompson, M.C. 2005 Modelling blockage effects using a spectral element method. *J. ANZIAM Soc.* **46**, C167–C180.

Griffith, M.D., Leweke, T., Hourigan, K. & Thompson, M.C. 2006 Steady and pulsatile flow through a locally constricted tube. *In the 6th Euromech Fluid Mechanics Conference – Book of Abstracts*, KTH Mechanics, Stockholm, Sweden, June 2006.

Griffith, M.D., Leweke, T., Hourigan, K., Thompson, M.C. & Anderson, W.P. 2006 Flow behaviour and blockage effects in stenosed arteries. *In proceedings of the 5th World Congress of Biomechanics*, Technical University of Munich, Munich, Germany, July 2006.

Griffith, M.D., Leweke, T., Thompson, M.C. & Hourigan, K. 2006 Blockage effects on steady and pulsatile flows in stenotic geometries. *Bull. Am. Phys. Soc.*, 51(10):134, 59th Annual Meeting of the Division of Fluid Mechanics, American Physical Society, Tampa Bay, USA, November 2006.

Griffith, M.D., Thompson, M.C., Leweke, T., Hourigan, K. & Anderson, W.P. 2007 Wake behaviour and instability of flow through a partially blocked channel. *J. Fluid Mech.* **582**, 319–340.

Nomenclature

Symbol	Description
α	Womersley number
β	streamline eccentricity
$\triangle P$	pressure gradient
$\triangle t$	time step
ε	strain rate
Γ	circulation
λ	wavelength
λ_c	critical wavelength
μ	fluid dynamic viscosity, Floquet multiplier
ν	fluid kinematic viscosity
ϕ	phase correction
$\hat{\phi}_s$	two-dimensional perturbation field eigenfunction
ρ	fluid density
σ	non-dimensional growth rate
σ_f	real Floquet exponent of the growth of instability on closed streamlines
σ_i	inviscid growth rate
θ	azimuthal cylindrical polar coordinate, angle between perturbation wave vector and recirculation zone axis of rotation
θ_0	phase of a complex Bessel function of order zero
θ_s	angular displacement of crank gear
τ	non-dimensionalised wall shear stress

Symbol	Description
τ_{wall}	dimensional wall shear stress
ψ	streamfunction
ψ_0	critical streamfunction for centrifugal instability
ω	angular frequency, vorticity
A	pulsation amplitude
A_c	critical pulsation amplitude for instability
b	blockage ratio by area
d	stenosis throat diameter
C	intermediate term for the prediction of centrifugal instability
D	channel width, tube diameter
f	frequency
h	backward-facing step height
J_0	Bessel function of order zero
L	characteristic length scale of the base flow
L_i	inlet length upstream of blockage
L_o	outlet length downstream of blockage
L_R	recirculation zone length
L^*	re-scaled recirculation length
m	azimuthal wavenumber
M	real part of the complex pressure gradient
M_0	modulus of a complex Bessel function of order zero
n_y	outward direction from a wall, normal to the fluid
p	perturbed pressure vector
p'	pressure perturbation vector
$\overline{p}$	pressure vector
q	flow rate over channel width

Symbol	Description
Q	flow rate in tubular geometry
r	radial cylindrical polar coordinate, radius of the blockage in the two-dimensional channel
r_b	radius of the blockage in the axisymmetric stenotic geometry
r_c	radial position of the crank pin
R	tube radius
Re	Reynolds number
Re_c	critical Reynolds number for instability
Re_{cyl}	Reynolds number for the flow around a cylinder in a freestream
Re_p	instantaneous time-dependent Reynolds number, calculated using $\overline{u}(t)$
$\hat{Re}_p$	maximum value of Re_p obtained during one pulsation period
s	total growth rate for centrifugal instability
S_P	piston stroke length
t	time
t^*	vortex ring formation number
t_i	indeterminate or reference time
T	non-dimensionalised period
T_p	peak forcing frequency
T_s	vortex ring formation time for pulsatile flow, equal to one half of T
T_D	pulsation period, in dimensional form
u	streamwise velocity component in the Cartesian x-direction, axial velocity component in the cylindrical polar z-direction
u_{max}	centreline velocity of the two-dimensional channel flow, peak velocity during a single pulsatile flow period
u', v', w'	perturbation velocity components
$\overline{u}(t)$	time-dependent cross-sectional area average of the fluid velocity
$\mathbf{u}^*$	intermediate velocity field
$\mathbf{u}^{**}$	second intermediate velocity field

Symbol	Description
$\mathbf{u}$	perturbed two-dimensional velocity vector
$\mathbf{u}'$	two-dimensional perturbation velocity vector
$\overline{\mathbf{u}}$	two-dimensional velocity vector
$\overline{\mathbf{u}}_{base}$	non-perturbed two-dimensional velocity vector
U_f	freestream velocity
U_{red}	reduced velocity
$\overline{U}$	mean value of velocity, temporally and cross-sectionally averaged
$\overline{U}_p$	mean piston velocity
v	transverse velocity component in the Cartesian y-direction, radial velocity component in the cylindrical polar r-direction
v_p	velocity of a particle in a PIV interrogation window
V_v	vortex ring axial velocity, normalised by the velocity ratio of the blockage
w	spanwise velocity component in the Cartesian z-direction, azimuthal velocity component in the cylindrical polar θ-direction
W	summation over the domain of the velocity of a perturbed flow minus an unperturbed flow
W_z	summation for a single axial location of the velocity of a perturbed flow minus an unperturbed flow
x	streamwise Cartesian coordinate
y	transverse Cartesian coordinate
z	spanwise Cartesian coordinate, axial cylindrical polar coordinate
z'_{max}	axial location of the maximum value of W_z
z_i	reference axial location

Chapter 1

Introduction

1.1 Project aims

An arterial stenosis is a lesion that forms on the inside wall of an artery; its principal effect is to constrict the flow of blood through it. As well as putting a greater strain on the heart in order to maintain a normal blood flow rate, arterial stenosis can result in various pathological conditions, such as strokes and aneurysms. Figure 1.1 shows an angiogram of a diseased carotid artery. The stenosis is highly-localised, creating a sharp reduction in artery diameter. Being located on the artery leading to the brain, this particular stenosis is in a critical location, causing reductions in blood flow and pressure. Stenoses, such as that shown in figure 1.1, constitute one of the most common modes of death in the Western world, making the genesis, growth and pathology of arterial stenosis a major focus of medical research.

The motivation to study the role of fluid mechanics in arterial stenosis has come

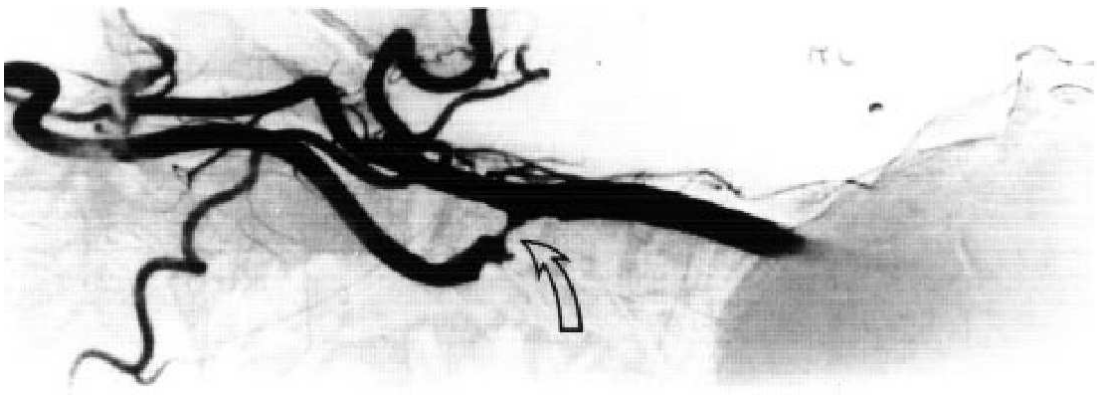

FIGURE 1.1: Angiogram of a stenotic carotid artery bifurcation, with the arrow indicating the location of the stenosis; from Ku (1997).

from the establishment of the importance of parameters such as wall shear stress and pressure to the normal and pathological function of arteries. This link – discussed in more detail in the following chapter – has motivated researchers to explore the fluid mechanics of normal and diseased arterial flows, and how they relate to the various biological phenomena of the cardiovascular system. Previous studies have investigated the variation of wall shear stress and the transition to turbulence in stenotic flows. With much the same motivation, the current study aims to describe the fundamental characteristics of the flow through stenotic arteries.

From a fluid mechanics perspective, the pulsatile flow through an actual stenotic artery is complex. The flow features an oscillating waveform of many harmonics and the geometry is irregular and highly variable both within the cardiovascular system and from one patient to another. Being a fluid mechanics study, the approach of the current research is to investigate the flow in idealised stenotic geometries. Doing so yields a more tractable problem, but also makes the results and conclusions more general. By simplifying the problem and reducing the number of parameters, it allows us to isolate any observed effects and make stronger conclusions regarding their nature or cause. In this way, the aim is to provide conclusions on the fundamental characteristics of stenotic flows, providing base case information which may then be referenced in the study of flows closer to the physiological reality.

1.2 Overview of the study

The study investigates idealised stenotic flows, using numerical and experimental methods. The first problem investigated is a highly idealised geometry, consisting of the blocked flow in a two-dimensional channel. The other geometry investigated is a tube with an axisymmetric blockage. For both geometries, an emphasis is placed on the effects of the severity of the blockage on the flow, as well as the variation of the flow stability. In this way, we hope to characterise the changes in stenotic flows through the growth of a stenosis

The other primary control parameter in the study is the Reynolds number, a dimensionless term which gives a ratio of the inertial forces to the viscous forces acting on a fluid. The variation with Reynolds number and blockage ratio of the stability

of the mostly laminar flows under investigation is a major focus of the study. Linear stability analysis is used extensively in the numerical work; many comparisons are made between numerical and experimental results, particularly on the relation of linear stability analysis results to experimental flows.

The work undertaken for this thesis was conducted over three and a half years, over two universities. Most of the numerical results presented were obtained during the first eighteen months of the candidature at Monash University in Melbourne. The following sixteen months were spent at the Université de Provence in Marseille. This time was spent constructing and running the experimental apparatus used in this research. The final six months were spent at Monash University.

1.3 Structure of the thesis

The thesis is separated into seven chapters; following the present introduction, chapter 2 is a review of previous work in the literature on subjects relevant to the work undertaken in this thesis. Chapter 3 provides a description of the methodology used in the current research. Results are presented in chapters 4 to 6, the first dealing with a numerical investigation of the two-dimensional flow in a partially-blocked channel. Chapter 5 details the investigation of the steady inlet flow through an idealised axisymmetric stenotic geometry. Chapter 6 presents the results obtained on the geometry investigated in chapter 5, but with a pulsatile inlet flow. A summary of the conclusions is given in chapter 7.

Chapter 2

Literature Review

The chapter begins with an overview of the broad role that fluid mechanics has played in research on blood flow. One of the aims of this first section is to present to the reader some of the motivations that fluid mechanics researchers have for researching blood flow. Reviews of some of the fluid mechanical studies pertinent to the stenotic flows investigated in this thesis are examined, beginning with a review of steady inlet flows in blocked geometries. This includes discussion of a number of different geometry types, including the backward-facing step and tubular stenotic geometries. The final section deals with pulsatile flows in a wide sample of different geometries.

2.1 Fluid mechanics in blood flow

On first inspection, blood flow can be described as a laminar flow in a circular pipe, upon which there is a thorough body of scientific theory and research. The standard Poiseuille solution is well-known, with the important dimensionless parameter being the Reynolds number. The first major complication one encounters moving from this solution for laminar pipe flow to blood flow in arteries involves the presence of unsteady or pulsatile flow. The first significant progress began to be made in adequately describing this flow during the 1950s.

2.1.1 Modelling blood flow

Many different methods have been used to model blood flow over the years, mathematically, numerically and experimentally (Taylor & Draney 2004). This section deals first with a description of the analytical solution to pulsatile flow and is followed by a review of some of the literature on modelling blood flow.

2.1.1.1 Analytical solution to pulsatile flow

One of the earlier forays of fluid mechanics into blood flow took the form of a collaboration between a mathematician and a physiologist. The experimental work of McDonald (1952), Helps & McDonald (1953) and McDonald (1955) had identified localised flow reversals in rabbit and dog arteries. In Helps & McDonald (1953), measurements of the pressure gradient showed a phase lag between the pulsatile pressure gradient and the flow velocity. The authors theorised that the observed flow reversals resulted from the elastic nature of the artery walls and attempted to draw an analogy with the phase lag between voltage and current in a conductor carrying alternating current.

In an effort to explain these observations, Womersley (1955) analytically described, for flow in a circular pipe, the observed phase lag between the motion of the fluid and the periodic pressure gradient that drove it. The analysis of Womersley (1955) begins with the equation of motion for flow in a tube generated by a constant pressure gradient, given as

$$\frac{d^2u}{dr^2} + \frac{1}{r}\frac{du}{dr} + \frac{\triangle P}{\mu} = 0, \tag{2.1}$$

where r is the radial coordinate, μ is the viscosity, $\triangle P$ is the pressure gradient and u is the longitudinal or axial velocity of the fluid. The solution to this equation is known as the Poiseuille solution, given by

$$u = \frac{\triangle P}{4\mu}(R^2 - r^2), \tag{2.2}$$

where R is the radius of the tube. To generate a pulsatile solution, we assume that the pressure gradient acting on the fluid is not constant, but varies with time, such that

$$\triangle P = A\mathrm{e}^{i\omega t}, \tag{2.3}$$

which is periodic in time with a frequency $f = \omega/2\pi$. With a varying pressure gradient, a new term is introduced into the equation of motion, now given as

$$\frac{\partial^2 u}{\partial r^2} + \frac{1}{r}\frac{\partial u}{\partial r} - \frac{1}{\nu}\frac{\partial u}{\partial t} = -\frac{A}{\mu}\mathrm{e}^{i\omega t}. \tag{2.4}$$

The solution to this equation is given as

$$u = -\frac{Ai}{\rho\omega}(1 - \frac{J_0(r\sqrt{\frac{\omega}{\nu}}i^{\frac{3}{2}})}{J_0(R\sqrt{\frac{\omega}{\nu}}i^{\frac{3}{2}})})\mathrm{e}^{i\omega t}, \tag{2.5}$$

where $J_0(xi^{\frac{3}{2}})$ is a Bessel function of order zero and complex argument. The corresponding flow can be found by taking the real part of equation 2.5 (a procedure for doing this is outlined in chapter 3). A solution can be calculated for any chosen harmonic; theoretically, any periodic waveform can be constructed from equation 2.5. Any function which is periodic in time can be expressed by a linear combination of a series of solutions to equation 2.5. A solution for a pulsatile flow with a net positive mean flow rate can be generated by adding the calculated harmonic solution to a steady Poiseuille solution.

The behaviour of the solution generated from equation 2.5 depends on the arguments of the Bessel functions, which are themselves determined by the term

$$\alpha = R\sqrt{\frac{\omega}{\nu}}. \tag{2.6}$$

This important non-dimensional term is known as the Womersley number, and can be thought of as a ratio between the unsteady and the viscous forces on the flow. Womersley (1955) found that in the femoral arteries of humans, rabbits, cats and dogs, α was of approximately the same magnitude. If one calculates the Womersley number for different points in the cardiovascular system, one finds that it varies throughout, starting out at the high end of the scale, $15 \lesssim \alpha \lesssim 25$ in the larger arteries near the heart, and then reducing to $\alpha < 5$ for the smaller capillaries located further downstream.

The nature of the velocity profiles generated by the solution depend strongly on α. Loudon & Tordesillas (1998) gives a detailed description of the Womersley number and its usefulness in classifying pulsatile flows; from the same article, figure 2.1 presents velocity profiles typical of oscillating flows of different Womersley numbers. From this figure, we can see how the Womersley number represents the development time of the boundary layer – determined by the fluid viscosity – in relation to the length of the pulse period. In this way, flows of different Womersley number exhibit different near wall behaviours. As the Womersley number approaches zero, the viscous forces dominate and the velocity profiles approach the Poiseuille solution. In this flow regime, the centreline velocity of the flow oscillates in phase with the pressure gradient. This synchronised oscillation becomes increasingly out of phase as the Womersley number increases to 10, as is found in the larger arteries. Beyond 10, the unsteady forces dominate the flow and we see that the development of the boundary layer during one

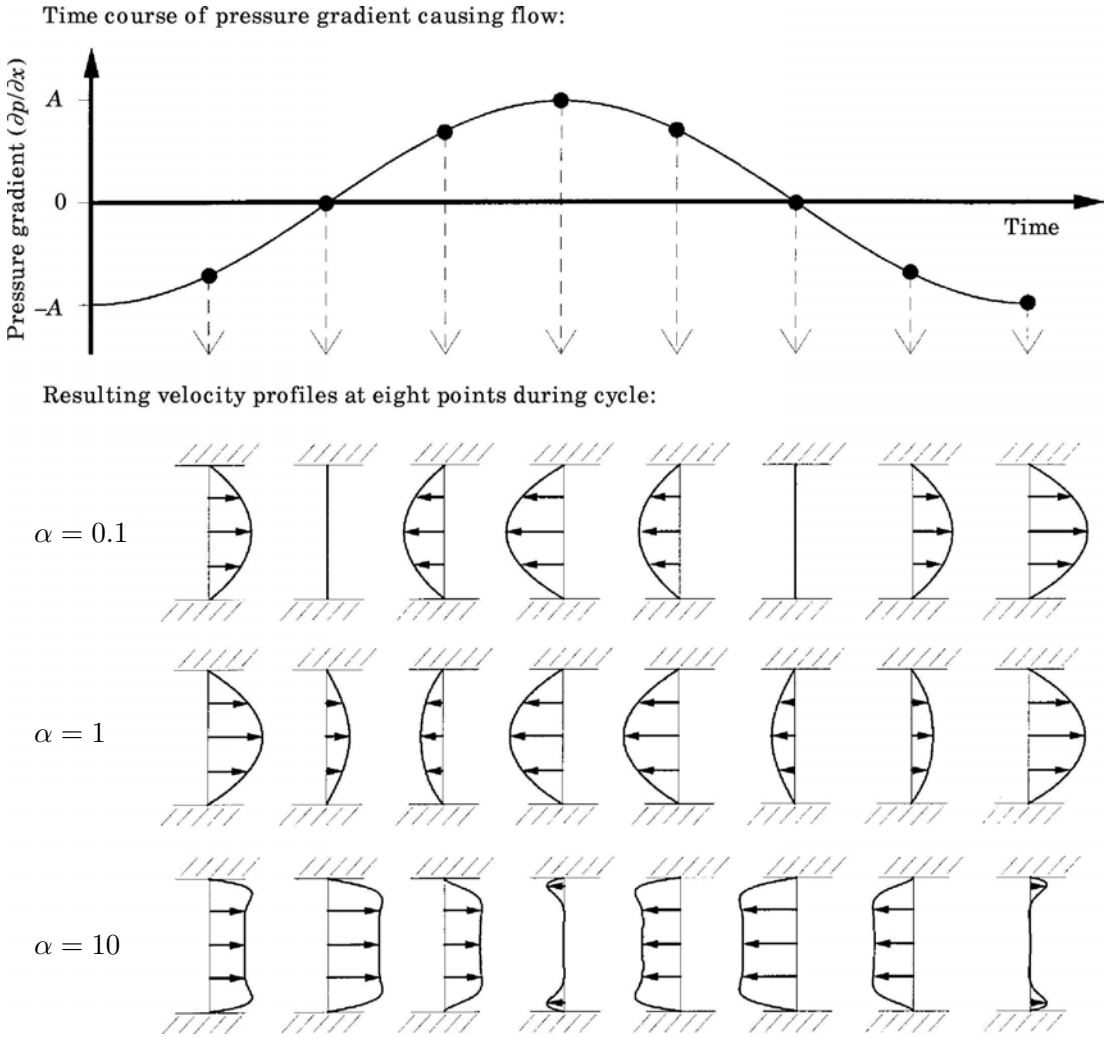

FIGURE 2.1: From Loudon & Tordesillas (1998), velocity profiles calculated for a single harmonic from Womersley's solution from three different Womersley numbers and several phases.

pulse cycle only extends a short distance from the tube wall. In this regime, the velocity profiles become flatter, particularly on the tube centreline.

Although the application of the Womersley solution is limited by the fact that only very short distances of one-dimensional tube geometries exist in the cardiovascular system, the Womersley number presents a useful method of characterising arterial flows. We know that when considering flows in the larger arteries, we deal in Womersley numbers of $10 \lesssim \alpha \lesssim 25$, and that when considering flows further downstream in the smaller arteries, arterioles and capillaries we have $\alpha \lesssim 10$.

Armed with this important tool, we now review some of the methods used for

modelling blood flow.

2.1.1.2 Lumped parameter models

Lumped parameter models are derived from an analogy between the fluid flow in the cardiovascular system and electric circuits. They are useful when considering the cardiovascular system as a closed circulatory loop, as they can be used to estimate the "load" that a heart must carry in driving the circulation (Westerhof, Elzinga & Sipkema 1971). The analogy was mentioned in Womersley (1955); indeed, the type of Bessel function used in the Womersley solution also arises in the analysis of current distribution in conductors. According to the analogy, pressure and flow rate replace voltage and current, the compliant aorta acts as a capacitor and the myriad of small downstream arterioles behaves as the resistor (Patel & van den Berg 1969). During the systole, or the peak of the pulse waveform, the aorta expands to store blood, whilst during diastole, or the trough of the pulse waveform, the elasticity and contraction of the aorta pushes the blood through the downstream resistance.

However, lumped parameter models have several limitations; they stem from the fact that no geometry is defined in such a model, that the model is considered as an entire closed system. Therefore, wave propagation effects as well as any localised changes or variations in the system cannot be adequately modelled.

2.1.1.3 One-dimensional models

The cardiovascular system consists of a vast network carrying an unsteady, pulsatile flow, varying from large arteries, close to the heart, to far smaller arterioles, further downstream. Across this range of blood flow, Reynolds number can vary from 1 to 4000 (Ku 1997), from high flow rates with low resistance, to viscous-dominated creeping flows. The velocity pulse waveform near the heart features a large and rapid peak followed by a long trough, smoothing out as we move away from the heart and reaching an almost constant flow rate in the extreme arterioles (Caro 1978). It is possible to simplify this large variance into a one-dimensional model.

Such a model is based on the assumption that the axial components of the blood velocity are much greater than the radial and azimuthal components. One-dimensional models are useful in predicting and explaining the streamwise variation of the pressure

and flow waveforms throughout the cardiovascular network (McDonald 1974). However, their weakness lies in the degree of simplification involved. The assumption of a predominantly axial flow is valid the further downstream the flow under consideration is in the cardiovascular system. However, as is shown in the following sections, cell and arterial responses often rely on characteristics of the fluid flow which cannot be adequately described one-dimensionally.

2.1.1.4 Localised cardiovascular phenomena

From a fluid mechanics perspective, the arterial system consists of a highly complex geometry, with few instances of long, uninterrupted pipes, while junctions and branchings are frequent and varied. Given these geometric considerations, the presence of separated and three-dimensional flows is to be expected. Recently, there has been a drive to gain data and insight into more local hemodynamic flow conditions, such as through heart valves or certain branchings, particularly those where arterial disease is common (Perktold & Rappitsch 1995; Taylor, Hughes & Zarins 1998). The focus on more localised phenomena stems from the interest in the biological response of arteries to fluid mechanical properties. Caro, Fitzgerald & Schroter (1971) were among the first to suggest the possibility of a shear stress related mechanism for mass transfer from blood to arterial wall. This, they argued, also played a role in the genesis of arterial disease, that atherosclerosis was caused by excessive mass deposit via this shear related mechanism. Later researchers would build on this establishment of shear stress, and particularly wall shear stress, as a crucial property in understanding the link between biology and fluid mechanics.

Work on local arterial phenomena has dealt with a large number of regions of the cardiovascular system. Modelling of the flow in the carotid bifurcation has attracted much attention (Ku & Giddens 1987; Anayiotos, Jones, Giddens, Glagov & Zarins 1994), as well as the abdominal aorta (Moore, Xu, Glagov, Zarins & Giddens 1994) and arterial bifurcations more generally (He & Ku 1996). The following section describes some of the biological responses that have motivated much of this fluid mechanics research into cardiovascular flows.

2.1.2 Biological response to fluid mechanical characteristics

The fluid mechanical characteristic that seems to be the most important in relation to arterial flows is the wall shear stress. Cells located on the arterial wall, such as endothelial cells, respond to the wall shear stress because in contrast to, for example the fluid pressure, it is directly felt as a force on the cell. Several studies have been devoted to its accurate calculation, measurement or prediction (Deplano & Siouffi 1999; Reese & Thompson 1998) and it is often the main focus of studies of biological flows (Sucosky, Osorio, Brown & Neitzel 2004; Strony, Beaudoin, Brands & Adelman 1993; Caro, Fitzgerald & Schroter 1971; Hodgson & Tarbell 2002).

There are many and varied links between cell responses in the arterial wall (the endothelium) and fluid shear stress. Early work on establishing these links was performed by Dewey, Bussolari, Gimbrone & Davies (1981), who found the shape and orientation of endothelial cells changed when exposed to different fluid stress levels. This investigation of the direct effects on endothelial cells explained earlier observations of changes in the endothelium caused by increased blood flow rates (Fry 1968; Caro, Fitzgerald & Schroter 1971; Stoker 1973). The work of Davies, Remuzzi, Gordon, Dewey & Gimbrone (1986) established that endothelial cells respond differently depending on whether they are exposed to laminar or turbulent flow, aligning themselves differently in each case.

The behaviour and response of endothelial cells in relation to the pulsatile nature of blood flow has also interested many researchers. Frangos, Eskin, McIntire & Ives (1985) observed that endothelial cells subjected to a steady shear stress produced more platelet aggregation inhibitors than cells in a stationary fluid. The rate of platelet aggregation inhibitors was increased further by exposing the cells to pulsatile shear stresses, as they would be under normal physiological conditions. This study was important in further establishing the link between biological response and fluid mechanical characteristics. Similar results, showing a dependence of endothelial cell response on flow, were made by Levesque, Nerem & Sprague (1989). Other studies have explored the links between biological response and shear stress: Hillsley & Tarbell (2002) and Sills, Chang, Artman, Frangos, Hollis & Tarbell (1995) investigated how shear stress affected the hydraulic conductivity of the endothelium, Helmlinger, Geiger, Schreck & Nerem (1991) focused on the morphology of cells as they varied with shear stress and Jo, Dull, Hollisand &

Tarbell (1991) described the dependence of endothelial albumin permeability on fluid shear. White, Haidekker, Bao & Frangos (2001) investigated the effect of different velocity profiles on the endothelial cell response and found a stronger dependence of cell proliferation on temporal rather than spatial gradients of shear stress. Further information on the effects of fluid stresses on endothelial cells and arterial walls can be found in review articles by Wootton & Ku (1999) and Tarbell (2003).

The large body of work on the association between endothelial cell response and shear stress serves to illustrate the potential contribution fluid mechanics research can make to the understanding of the cardiovascular system. Furthermore, apart from cell response, other phenomena in arteries have been found to be dependent on fluid mechanical considerations. Chesler & Enyinna (2003) measured particle deposition on the walls of a carotid artery *ex vivo* as it varied with pressure and flow waveform. The motivation for such a study comes from the role of plasma protein accumulation in the formation of arterial lesions and stenoses, or atherogenesis. Stary, Chandler, Glagov, Guyton, Insull, Rosenfeld, Schaffer, Schwartz, Wagner & Wissler (1994) found that the rate of particle deposition along the artery intima was largely pressure dependent, but that it did vary with the flow waveform. They found the lowest deposition rate was with no flow, followed by steady flow; it was found that oscillatory flow led to the largest accumulation of particles. Details were not given as to why this would be the case, but it would appear to be related to the wall shear stress. In terms of the near-wall vicinity of the fluid, the most obvious change in condition between the steady case and the oscillatory would have been the change in wall shear stress behaviour.

The importance of wall shear stress was further demonstrated by Giddens, Zarins & Glagov (1990), Giddens, Zarins & Glagov (1993) and Glagov, Zarins, Giddens & Ku (1988) in their descriptions of more pathological arterial responses. Whereas the previous section dealt with the reaction of cells on the arterial wall to the fluid flow, we now move onto the effects of the flow on intimal wall thickness and the creation and exacerbation of pathological conditions such as thrombi (blood clots occurring within the arterial system) and atherosclerosis (the most common form of heart disease, consisting of a lesion on the arterial wall which grows to occlude the artery). It has been known for some time that arteries can quickly expand to accommodate short-term demands for increased blood flows and also contract for decreased blood flows. What has not

been as clearly understood are the causes of the long-term changes in arterial size and thickness. Investigating these causes was the principal focus of the work of Glagov *et al.* (1988) and Giddens *et al.* (1990), who conducted experiments with physiologically realistic geometries and conditions, and combined these with mappings of thickness and shape in human arteries. As well as establishing further that atherosclerotic plaques formed predominantly at sites of low and oscillating wall shear stress, they found that arteries adapted their diameters, long-term, in order to maintain a particular average wall shear stress. This value was found to be common to humans and animals. The interesting hypothesis to arise from this work was that the correction by an artery of an area of low average wall shear stress took the form of a local thickening of the artery intima. This hypothesis then led to the proposal that intimal thickening was a key ingredient in the genesis of atherosclerosis, providing an early plaque from which the disease could spring. The correlation between low wall shear stress and intimal thickening was further strengthened by studies also concentrating on wall shear stress as the salient fluid dynamical characteristic (Friedman, Hutchins, Bargeron, Deters & Mark 1981). The work of Ku, Giddens, Zarins & Glagov (1985), Cavalcanti (1995), Salam, Lumsden, Suggs & Ku (1996) and Delfino, Moore, Stergiopulos, Vaclavik, Genton & Meister (1998) also investigated the link between wall shear stress and the genesis and progression of atherosclerosis.

With the strong association between wall shear stress and arterial response established, researchers began to investigate the fluid dynamics of flows modelled on the real physiological conditions which give rise to atherosclerosis. Because of the link between arterial wall response and wall shear stress, many studies, taking a more classical fluid mechanics approach, have sought to describe the behaviour of the flow and the variation of the wall shear stress in model stenoses. It is this motivation which has driven the investigation of steady and pulsatile flows through stenotic geometries and, indeed, the research presented in this thesis.

The impetus for this focus on stenoses lies in their obvious significance to the pathological nature of arterial disease. Stenoses lead to blocked, or partially occluded arteries, which can result in reduced flow to crucial organs (Wootton & Ku 1999). The high fluid shear stress in blood moving past the stenosis can lead to the aggregation of red blood cells, or clotting. These blood clots, or thrombi, can grow to completely occlude the

artery, or break off and block smaller diameter arteries downstream. The break-off of a thrombus near the heart and its lodging further downstream near the brain is the most common mode of stroke. Of interest to physicians is an understanding of at what stage a stenosis becomes critical. Typically, a stenosis of 65–80 percent severity is considered critical (Wootton & Ku 1999); however, a more complete understanding would include an appreciation of the effects of a stenosis on the immediate downstream artery, as well as of more global effects, such as a renal stenosis might have on kidney function. Furthermore, the appearance of turbulence in the flow immediately downstream of some stenoses needs to be considered. Transition to turbulence has being observed in several studies, experimentally and computationally, under physiologically realistic conditions; the presence of turbulence or transition to turbulence in stenotic flows potentially has a role to play in the detection of severe stenoses (Mittal, Simmons & Najjar 2003).

The following sections deal with the literature on steady and pulsatile flows through occluded paths and stenotic geometries, which forms the more direct background to the research presented in chapters 4, 5 and 6 of the thesis.

2.2 Steady flow in occluded paths

Based on the hemodynamic considerations presented in the previous section, we next review some of the work that has been performed on occluded flows. The first problem investigated in this thesis is that of the flow through a partially-blocked two-dimensional channel. While not being a tubular geometry, like an artery, it nonetheless provides a low-dimensional starting point for investigating occluded flows.

In a more classical fluid mechanical sense, the geometry and resultant flow of chapter 4 have much in common with the flow over a backward-facing step. The investigation presented in chapter 4 leads to comparison with the backward-facing step and indeed extends on some of the questions still open regarding that geometry. Therefore, the next section is devoted to a review of the literature on the backward-facing step, in order to give the reader background on the questions that the research of chapter 4 addresses. A review of steady flow in tubular stenotic geometries follows the review of the backward-facing step.

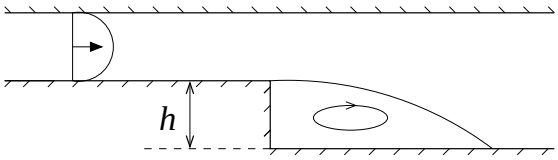

FIGURE 2.2: Schematic of a backward-facing step.

2.2.1 The backward-facing step

The flow past a backward-facing step presents a simple and well-defined occurrence of separated flow; however, it is not strictly a constricted path. The standard test section geometry is well known, consisting of a two-dimensional channel followed by a right-angled step on one side, as shown in the schematic of figure 2.2. The expansion creates a separating shear layer emanating from the step edge, forming a recirculation zone immediately downstream of the step. The flow has a wide number of engineering applications, its simplicity making it useful for examining phenomena such as flow separation (Armaly, Durst, Pereira & Schoenung 1983; Adams & Johnston 1988). It is also considered an important benchmark problem for computational fluid dynamics (Ghia, Osswald & Ghia 1989; Gartling 1990).

The work of Armaly *et al.* (1983) offers a detailed review of the subject, including an experimental investigation with a fixed expansion ratio of 0.516, and Reynolds numbers ranging through the laminar, turbulent and transitional regimes. The aspect ratio of the experimental test section was 1:36, in order to yield a nominally two-dimensional flow, although little was put forward as to why this would be sufficient. The relationship between Reynolds number and the length of the first recirculation zone was explored and is reproduced in figure 2.3. With increasing Reynolds number in the laminar regime, the length of the first recirculation zone increases, accompanied by the appearance downstream of more recirculation zones on alternating sides of the channel. The transition to turbulence was observed to begin at a Reynolds numbers of 1200, (defined as $Re = \frac{VD}{\nu}$, where V is two-thirds of the maximum inlet velocity (corresponding with the average velocity in the laminar regime) and D is the hydraulic diameter of the smaller, inlet channel). The flow was observed to become three-dimensional above $Re = 400$. The authors argued the flow to be inherently three-dimensional at this point, believing there to be an instability mechanism associated with the appearance

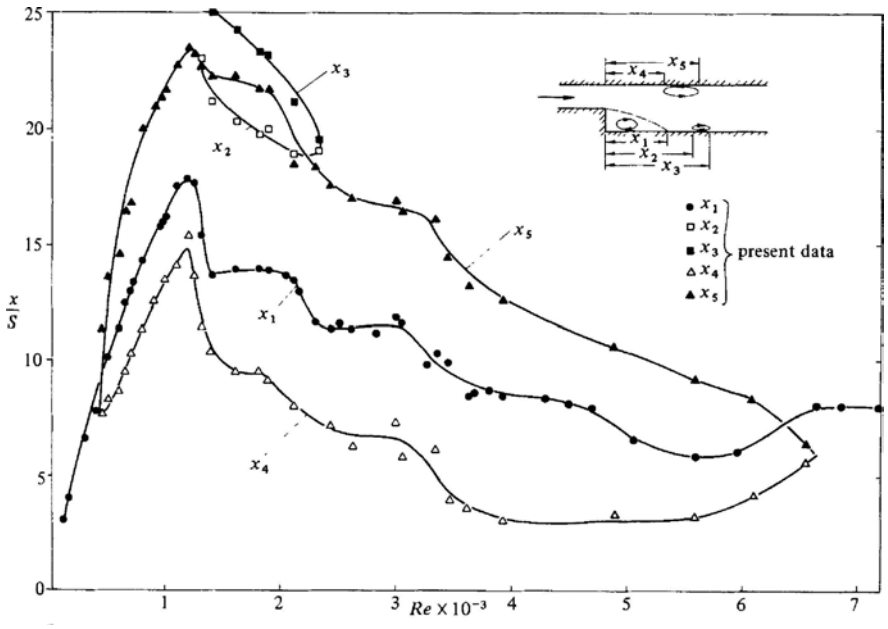

FIGURE 2.3: Recirculation lengths for the backward-facing step, from Armaly *et al.* (1983).

of the secondary recirculation zone. The divergence at this Reynolds number in the initial recirculation length between their own two-dimensional numerical simulations and their experiments supported the argument. Since then, this hypothesis has been tested using computational methods.

2.2.1.1 Paths to instability

Numerical studies of the problem began to give more insight to the nature of the instability. In an effort to explain the three-dimensionality in the flow above $Re = 400$, Ghia *et al.* (1989) suggested that the instability was linked to the appearance of the secondary recirculation zone on the upper wall. They postulated that the secondary circulation subjected the mainstream flow to a concave curvature, which activated a centrifugal Taylor-Görtler instability.

Kaiktsis, Karniadakis & Orszag (1991, 1996) investigated the flow further, finding it to be convectively unstable for Reynolds numbers in the range $700 \leq Re \leq 2500$. Hence, they found a higher Reynolds number for the appearance of three-dimensionality in the flow than did Armaly *et al.* (1983) in their experimental investigation. One possible reason for this discrepancy was the wall-effects in the Armaly experimental rig, which would form the motivation for several later backward-facing step studies.

In Kaiktsis *et al.* (1996), the problems with convective instability in internal separated flows are investigated. Testing their flow subject to single-frequency forcing, as well as to random noise, they concluded that the path to instability is via noise-induced convective instability, suggesting caution in interpreting numerical stability results.

Further numerical simulations of backward-facing step flow by Williams & Baker (1997) shed light on the significance of end-wall effects. Comparing their three-dimensional simulations with two-dimensional experiments and numerical solutions, they showed that the cause of this instability was not the appearance of the secondary recirculation zone, but rather a result of low aspect ratio of the test section. They identified an interaction between the main fluid flow and a wall jet, formed at the junction of the step and end-wall. Figure 2.4*a* shows a Lagrangian particle track from the wall of the three-dimensional simulated flow. This penetration of three-dimensionality into the main two-dimensional flow increased with Reynolds number, showing that what was thought to be an instability inherent to the two-dimensional flow was rather an extrinsic idiosyncrasy of the test section. A further investigation of this phenomenon was that of Tylli, Kaiktsis & Ineichen (2002), who also showed the penetration of an end-wall separation zone into the mainstream flow at Reynolds numbers greater that 400. A second Lagrangian particle tracking, this time from Tylli *et al.* (2002), is shown in figure 2.4(*b*). These works serve to highlight the issues faced, and qualifications necessary, when investigating a nominally two-dimensional flow. As a result, more recent work has concentrated on identifying the intrinsic stability of the flow.

In light of this demonstration of the significance of end effects, Barkley, Gomes & Henderson (2002) sought to characterise the stability of backward-facing step flow free from any extrinsic effects associated with the test geometry. Performing linear stability analysis on two-dimensional numerical simulations of the flow, they found that the primary instability was a three-dimensional, steady bifurcation, occurring at a critical Reynolds number of 997 (calculated using the same definition of Reynolds number used in Armaly *et al.* (1983)). Figure 2.5 depicts the structure of the instability mode. This instability was located primarily in the initial recirculation zone, possessing a "flat roll structure", with a spanwise wavelength of 6.9 step heights. It was also shown that this instability became critical at a lower Reynolds number than any two-dimensional bifurcation of the flow.

(*a*)

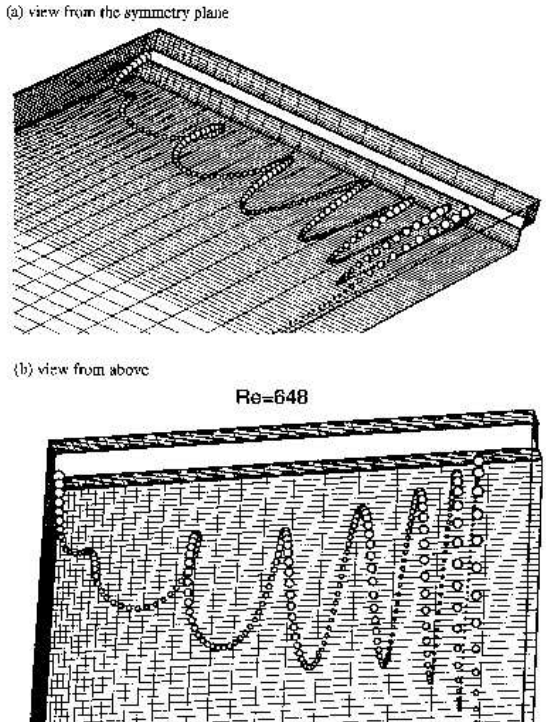

(*b*)

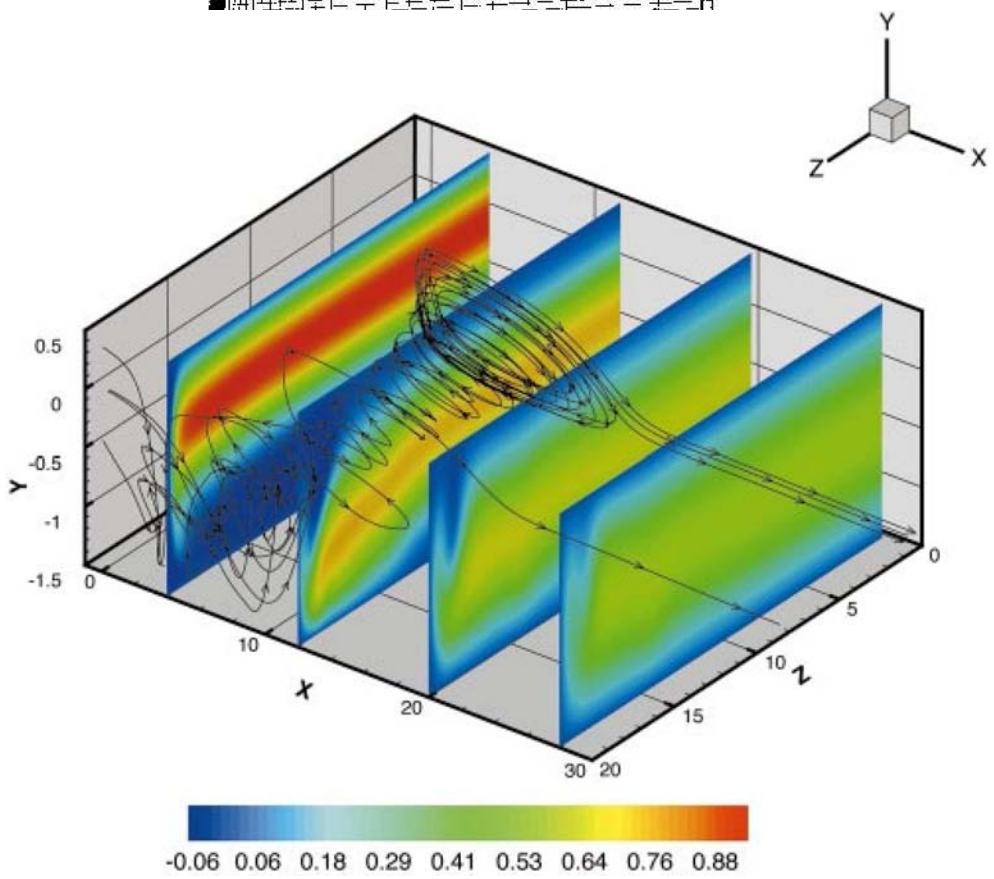

FIGURE 2.4: Lagrangian particle tracks, both at $Re = 648$, from (*a*) Williams & Baker (1997) and (*b*) Tylli *et al.* (2002), along with contours of the downstream velocity.

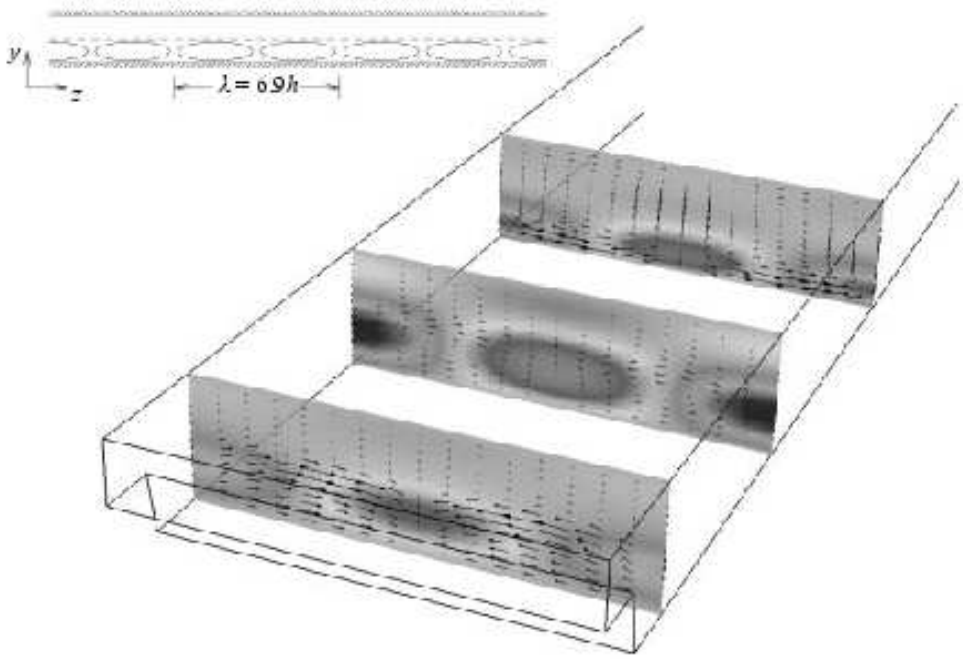

FIGURE 2.5: Three-dimensional flow structure of the leading instability mode at, at $Re = 1000$ and wavelength $\lambda = 6.9$. Contours indicate the strength of the streamwise velocity component and vectors the flow pattern in each cross-section, located at 1.2, 6.2 and 12.2 step heights from the step; from Barkley *et al.* (2002).

Like Ghia *et al.* (1989), Barkley *et al.* (2002) suggested the instability mechanism to be centrifugal in nature; however, in locating the instability within the first recirculation zone, they argued that the principal mechanism could not be an interaction with the second recirculation zone. They proposed that the instability was caused by the increasing curvature of the closed streamlines within the initial recirculation zone.

The theory on centrifugal instability is given in Drazin & Reid (1981). The extension of this theory by Bayly (1988) states that the sufficient conditions for centrifugal instability are that the streamlines be convex and closed in some region of the flow, with an outward decrease in the magnitude of the circulation. Testing this condition for backward-facing step flow, Barkley *et al.* (2002) calculated the circulation within the initial recirculation zone at a Reynolds number just above the critical Reynolds number for absolute instability. The results of this are re-shown in figure 2.6(a). Here, two regions of black, at the extreme left and right ends of the zone, show where the circulation is decreasing as we move outwards from the centre. In figure 2.6(b), contours of the spanwise velocity component of the instability mode are plotted, showing

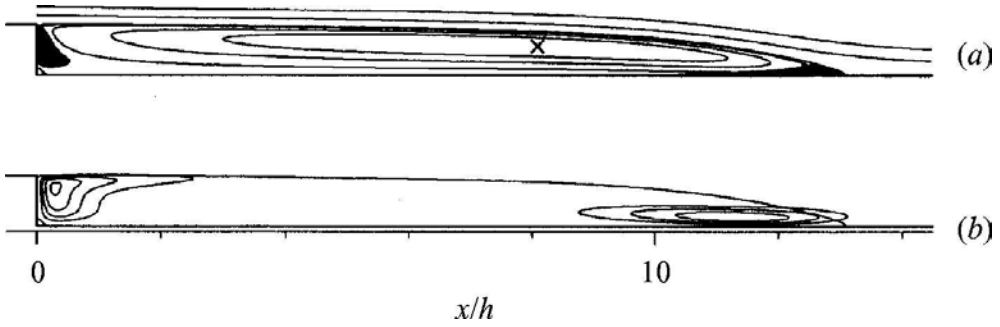

FIGURE 2.6: From Barkley *et al.* (2002), at $Re = 750$, (a) regions (black) where the magnitude of the angular momentum decreases away from the centre (marked with a cross) of the recirculation zone. Representative streamlines are also shown. (b) Contours of the magnitude of the spanwise velocity component w or the critical instability eigenmode; the separating streamline of the base flow is also shown.

that the maximum velocities of the mode occur in roughly the same regions where an outward decrease in circulation is measured.

This match-up of the condition for centrifugal instability with the structure of the instability mode, argued the authors, suggested the instability to be centrifugal in nature. However, there are some problems with this argument. Firstly, the calculations of circulation were performed using the centre of the recirculation zone as the centre of curvature, rather than calculating a centre dependent on the local curvature of the streamline. Secondly, the theory as proposed by Bayly (1988) predicts short-wave instability modes of a wavelength of a magnitude similar to the distance over which the circulation is decreasing outwardly. If we consider the magnitude of this distance in backward-facing step flow, as suggested by the black regions in figure 2.6(a), we would expect an instability mode of a wavelength considerably shorter than the 6.9 step heights predicted by their linear stability analysis.

Nonetheless, an outward decrease in circulation is still present; therefore, the argument requires further testing and the exact nature of the primary instability of two-dimensional backward-facing step flow remains an open question.

2.2.1.2 Expansion ratio effects in backward-facing step type flows

Relatively few studies exist which explore the effects of step height in backward-facing step flow. Although only appearing as a brief communication, the study of Thangam & Knight (1989) seems to be the only work available that investigates the effect of a wide number of expansion ratios on backward-facing step flow. They found a strong

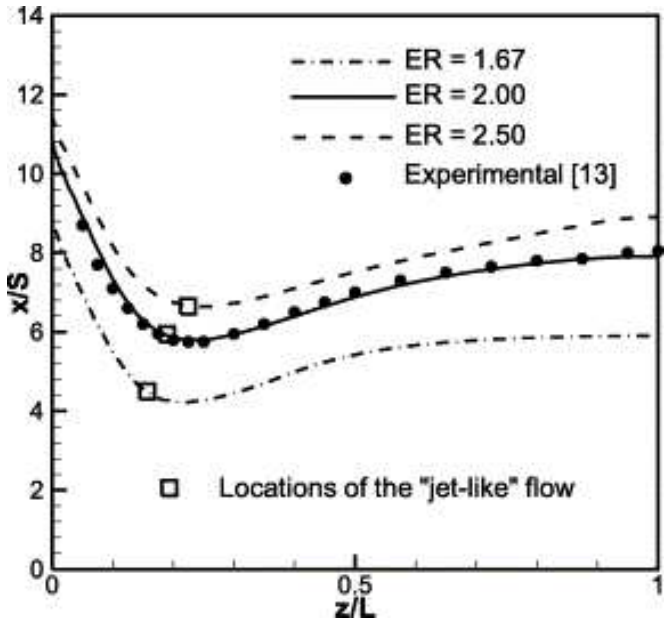

FIGURE 2.7: Reattachment lines for different expansion ratios (ER), Reynolds number unknown, from Nie & Armaly (2002).

dependence of recirculation length on step height, with a Reynolds number based on the width of, and maximum velocity in, the small inlet before the expansion. The work of Nie & Armaly (2002) looked at the effect of step height on three-dimensional backward-facing step flow, but focused only on a narrow range of expansion ratios (1.67–2.50). They found an increase in step height caused an increase in reattachment length and in the general three-dimensional features of the flow. Figure 2.7 plots the line of reattachment, or the end of the initial recirculation zone, as it varies with step height and with distance from the end wall. From the figure, we see that at greater step heights, the penetration of three-dimensional effects caused by the end wall increases.

However, to maintain a constant Reynolds number across different step heights, the inlet velocity profile was varied. This kept the Reynolds number constant, but not the mass flow rate over the step. This is an issue in both the studies mentioned here, in that the inlet conditions of the experiments and simulations are not constant over different expansion ratios. These studies, although investigating the effects of step height, do not explore with any great depth a full range of blockage effects.

Considering the study of blockage effects more generally, most work has tended to be aimed at determining correction factors and design parameters for wind tunnels. Hence, the focus has been more on internal flows with relatively small blockage ratios.

One of the few papers focusing on higher blockage ratio effects was carried out by Sahin & Owens (2004), with a geometry consisting of a freely suspended cylinder between two plates. However, the research was directed more at questions relating to the unbounded flow past cylinders. Although the geometry bears only a limited similarity to backward facing step flow, (it is symmetrical and creates a wake consisting of twin vortices), the work showed that the proximity of the walls had a suppressive effect, delaying bifurcation to three-dimensional states and increasing the critical Reynolds number at which shedding would occur. Beyond this work, there seems to have been little attempt in the scientific literature to characterise the direct effect of blockage size on an internal flow.

2.2.1.3 Present work (chapter 4)

There are several gaps in the research here which the work presented in chapter 4 of this thesis seeks to address. The geometry chosen (discussed further in the following chapter) bears much similarity to the backward-facing step; however, it eliminates the problems to do with the variable volume flow rate present in the previous studies of expansion ratio effects on backward-facing step flow (Thangam & Knight 1989; Nie & Armaly 2002). The geometry consists of a contraction upstream of the expansion; this means that the Reynolds number is calculated on the unblocked flow condition and is unaffected by any change in blockage ratio. The aim of the study is to provide a comprehensive analysis on a full range of blockage or expansion ratio effects on two-dimensional channel flows.

The other open question on backward-facing step flow relates to the nature of the primary three-dimensional instability of the flow. The analytical method of Bayly (1988) has been referenced to support an argument for centrifugal instability; however, the theory is yet to be applied in its entirety to the flow under question. In this thesis, we aim to address this shortcoming.

2.2.2 Stenotic geometries – steady flow

In this section, the literature on steady flows in stenotic geometries is discussed. One of the earliest studies on the fluid mechanics of steady flow in idealised stenotic geometries was by Clark (1976a), which measured the pressure drop across several nozzle designs

representing different stenosis shapes; the proposed theory relating pressure drop to the stenosis was later extended to pulsatile flow (Clark 1976b). However, beyond measuring the pressure on the centreline of the tube, they did not attempt to describe in detail the stenotic flow.

Of the published work on steady stenotic flows, much of it appears to have been aimed at finding methods to detect atherosclerotic plaques, the idea being that stenoses would create instabilities or disturbances exhibiting particular frequencies which could then be detected. Tobin & Chang (1976) examined wall pressure spectra in stenotic flows of occlusion severities of 75% and greater, in an attempt to identify frequencies in the flow that might help characterise stenotic flows. They argued the flow to consist of a turbulent shear layer in the immediate flow downstream of the stenosis; however, they did not identify critical Reynolds numbers, nor describe the transition in any detail. Another example of such work is presented in Cassanova & Giddens (1978), which investigates a smooth stenosis of 75% occlusion. Although critical Reynolds numbers are not determined, Cassanova & Giddens (1978) gives a description of the form the instability takes. In the figure, we see the unsteadiness and instability in the flow at approximately 4 or 5 diameters downstream of the blockage. The instability in the dye visualisation appears to be a Kelvin-Helmholtz-type shear-layer oscillation. This unsteadiness in the flow downstream of the stenosis is a recurring characteristic throughout the literature on steady stenotic flows, and indeed through much of the literature on pulsatile flows.

Cassanova & Giddens (1978) conclude that a degree of occlusion of approximately 50% is required to create observable disturbances in the poststenotic flow. They state this as applying generally to the Reynolds number range tested, which is 318–2540. This seems problematic, as one would expect different critical degrees of occlusion at different Reynolds numbers; one would expect any critical boundary for stability to be a function of both the occlusion severity and the Reynolds numbers. With regards to stability, the key findings to be drawn from the work relate to the nature of the instability, rather than the conditions of its appearance. A description of the instability was given, but no explanations put forward as to its origins.

The work presented in Cassanova & Giddens (1978) continues in Ahmed & Giddens (1983a) and Ahmed & Giddens (1983b). A steady stenotic flow was created experimen-

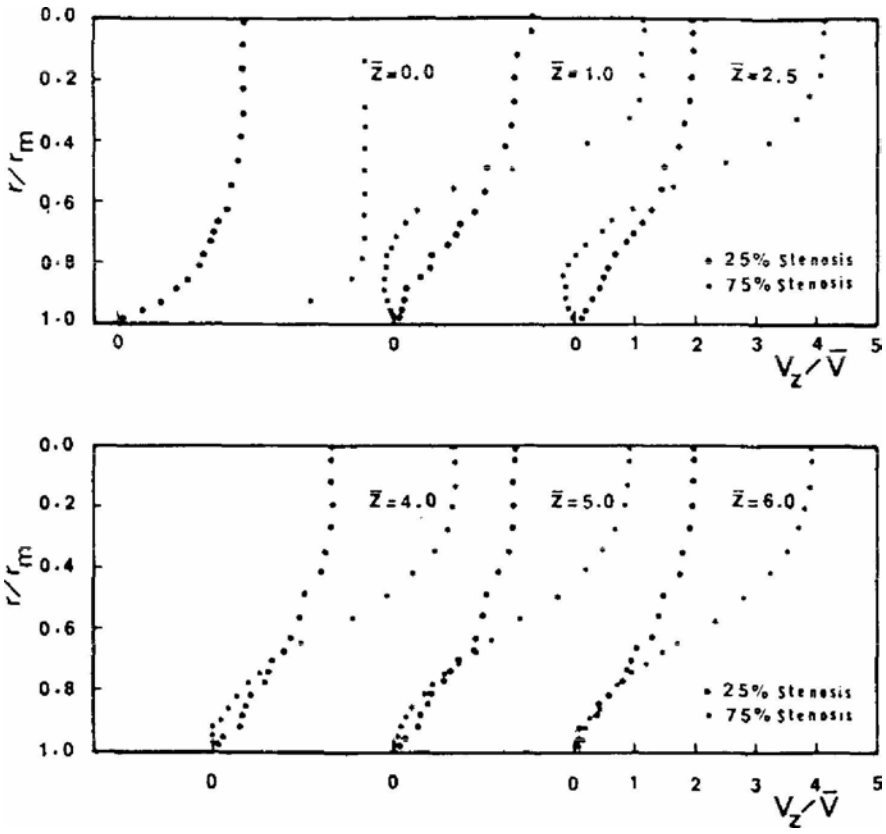

FIGURE 2.8: Velocity profiles from Ahmed & Giddens (1983b), at Reynolds number $Re = 500$, occlusion severity at 25 and 75%, at different axial locations.

tally. Using laser Doppler anemometry, velocity profiles were measured and presented for a smooth-stenosis with severities of 25, 50 and 75%. Reynolds numbers of 500, 1000 and 2000 were tested. Figure 2.8 presents an example of the velocity profiles in Ahmed & Giddens (1983b). This work, in particular this figure, describes a recirculation zone which forms downstream of the occlusion. From the velocity profiles, the variation in the downstream extent of the recirculation zone can be seen as well as the greater velocity of the fluid at higher occlusion severity. For steady flow in axisymmetric stenotic geometries, these findings on the effects of blockage severity appear to be the most comprehensive available in the literature.

In regards to instability, in Cassanova & Giddens (1978) and Ahmed & Giddens (1983b), much data are presented on disturbance intensities and flow energy spectra. Ahmed & Giddens (1983b) observed discrete frequency oscillations at $Re = 500$, while at $Re = 1000$ and 2000, they observed similar oscillations, this time with turbulence in the region further than 4 diameters downstream of the blockage. No critical Reynolds

numbers for instability are presented, only observations of unsteadiness and turbulence at the Reynolds numbers tested.

Since the papers referred to in the preceding paragraphs were published, there has not been a great deal of research into steady stenotic flows. Comparatively, there has been much more research performed on pulsatile stenotic flows; the usefulness of the steady flow as a limiting case of the pulsatile flow has not been reflected in more research being carried out on it.

The open questions remaining from the relatively few works which were published in the early eighties on the subject relate to the appearance and nature of the observed instability. Only recently, this flow has been again investigated, this time numerically, by Sherwin & Blackburn (2005). Dealing with a smooth stenosis of length $2D$, they determined a critical Reynolds number of 722 from a linear stability analysis of the flow. The leading perturbation mode (azimuthal wavenumber $m = 1$) consisted of a loss of symmetry of the jet. This deflection of the centreline of the jet was described as promoting a "mild Coanda-type attachment".

Direct numerical simulation of the three-dimensional flow at $Re = 750$ revealed the instability to be subcritical; hysteresis was confirmed with the instability being observed down to $Re = 688$. The asymptotic flow simulated at $Re = 750$ is shown in figure 2.9. A long-period oscillation was observed; the vorticity plots of figure 2.9 are distributed over one such period. The beginning of the turbulent region of the flow oscillates between axial locations 4 and 10 diameters downstream of the blockage.

Sherwin & Blackburn (2005) asserted that the instability in the direct numerical simulation at $Re = 750$ – along with the hysteresis – was consistent with the instabilities seen in the experimental works of Cassanova & Giddens (1978) and Ahmed & Giddens (1983b). Critical Reynolds numbers were not reported in the experimental works; instability was reported as beginning between $Re = 500$ and $Re = 1000$, however, it was described as discrete frequency oscillations. It would appear that even though the critical Reynolds number reported in Sherwin & Blackburn (2005) (and its lower subcritical value) is consistent with the Reynolds numbers for instability in the experimental work of Cassanova & Giddens (1978) and Ahmed & Giddens (1983b), the causes of the instabilities are perhaps different. In the earlier experimental work, the observed instabilities seemed to be convective and dependent on the experimental noise;

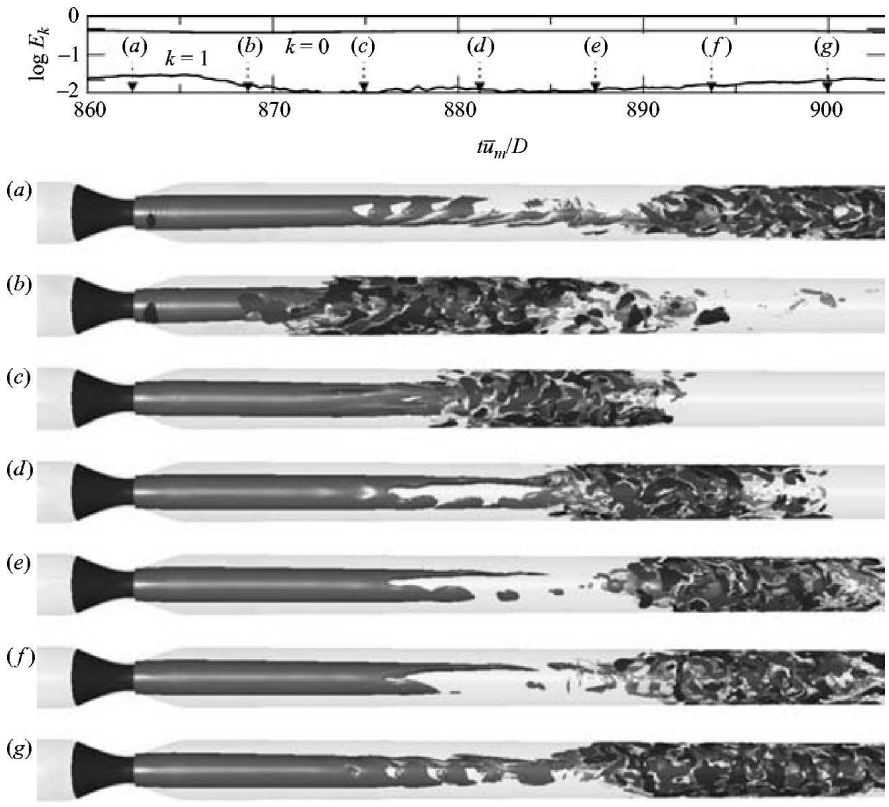

FIGURE 2.9: From Sherwin & Blackburn (2005), at top, a time series of energies for the steady inlet flow at $Re = 750$ showing a long-period oscillation. At bottom, isosurfaces of azimuthal and streamwise vorticity of the direct numerical simulation at seven points in the cycle are shown.

for the numerical simulations of Sherwin & Blackburn (2005), the initial bifurcation to instability was absolute.

Convective instability seems to play an important role in stenotic flows of steady inlet; therefore, in an extension of their earlier work, Blackburn & Sherwin (2007) investigated the response of their steady flow simulations to periodic forcing. Figure 2.10 plots the vorticity for a simulation for $Re = 700$, subject to a periodic forcing on the velocity inlet, for a period of $t\overline{U}/D = 0.3$, where $\overline{U}$ represents the sectionally-averaged velocity in the tube. The quantity $t\overline{U}/D$ was labelled the reduced velocity, U_{red}; this term has more meaning in the context of pulsatile flow, but for the present discussion of steady flow can be thought of as a non-dimensionalised period. The response of the flow to the forcing can be seen in the roll-up of the shear layer into discrete vortices. This form of instability is more consistent with the type of disturbance seen in Cassanova & Giddens (1978) and Ahmed & Giddens (1983b). Blackburn & Sherwin (2007) also

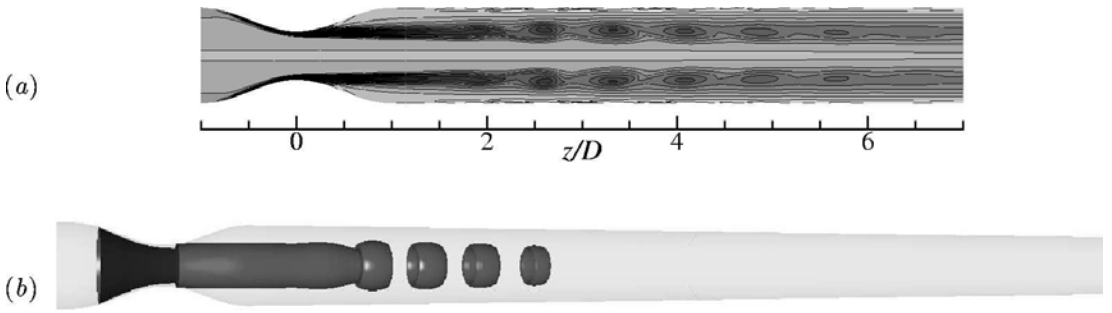

FIGURE 2.10: From Blackburn & Sherwin (2007), (a) contours and (b) isosurface of azimuthal vorticity for the steady flow at $Re = 700$, subject to a periodic forcing at $t\overline{U}/D = 0.3$. The shear layer roll-up caused by the forcing can be clearly seen.

quantified the response of the flow at different forcing periods, by calculating the extra kinetic energy generated by the forcing. For $200 < Re < 700$, they found a maximum response to forcing at a reduced velocity $U_{red} \approx 0.3$.

In a very recent study, Varghese, Frankel & Fischer (2007a) conducted direct numerical simulations of the steady inlet flow for Reynolds numbers of 500 and 1000, through a smooth axisymmetric stenosis, such as that used in previous experiments by Ahmed & Giddens (1983b). In contrast to the experiments, they found that the jet emanating from the stenosis remained laminar for both the Reynolds numbers tested. However, the introduction of a 5% eccentricity to the stenosis geometry created a perturbation which resulted in a poststenotic flow that matched closer the experiments of Ahmed & Giddens (1983b). The absence of experimental noise in the simulations would appear to account for the wholly linear behaviour of the flow through the axisymmetric stenosis. The closeness of the results in the eccentric case is a result of the geometric eccentricity in the simulations acting as a substitute for the noise undoubtedly present in the experiments.

The need for a geometric perturbation in the work of Varghese *et al.* (2007a) to produce results comparable to experiments and the study of shear layer response to periodic forcing in Blackburn & Sherwin (2007) hint at the role of convective instability in steady stenotic flow, providing an avenue of inquiry still to be explored.

2.2.2.1 Present work (chapter 5)

In relation to the research on steady stenotic flows presented in the previous section, there are several open questions, to which chapter 5 of this thesis is devoted. Firstly, a

complete characterisation of the flow as it varies with changes in the blockage ratio of a stenotic geometry has not been performed.

A further open question for stenotic flows is the variation of the stability of the flow with changes in blockage and Reynolds number. Although Sherwin & Blackburn (2005) have described the stability of numerical flows through their stenosis geometry of 75% area reduction, it is not clear exactly how this would apply to a real flow subject to experimental noise. The possible role of any linear instability modes in the transition of experimental stenotic flows has yet to be fully explored.

Furthermore, no experiments appear to have been conducted at low Reynolds numbers, where the flow would be wholly steady and laminar in the poststenotic region. Because of this, for all of the numerical work conducted on the subject, comparisons have only been possible with experimental flows exhibiting noise-dependent unsteadiness. Comparisons are still possible with the unsteady flows observed up to now; however, they are weakened by the differences in the perturbation applied to the direct numerical simulations, be they the addition of a small perturbation flow or of a geometric perturbation. The comparison of steady experimental flows to numerical simulations is also undertaken in this thesis.

2.3 Pulsatile flows

Pulsatile flows consist of a mean flow downstream and an harmonic oscillation. Pulsatile flows of many different waveforms can be constructed, although for the majority of work reviewed here, waveforms of a single harmonic have been applied. The reasons for this simplification of the flow are firstly to make the problem more tractable, but also the results more generally applicable.

The section will begin with a review of the work performed on pulsatile flows in two-dimensional geometries, followed by a review of the mostly biomedical studies which have modelled stenotic flows to varying levels of physiological realism, followed by a review of fluid mechanical studies on flows in idealised stenotic geometries.

2.3.1 Two-dimensional geometries

Few studies have dealt with pulsatile flows in purely two-dimensional geometries. Most researchers wanting to investigate the problem have skipped directly to tubular ge-

ometries; for the numerical fluid dynamicist the leap to a tubular geometry and flow is technically not a difficult one. Also, experimentally, the bounded flow through a stenotic tube is much easier to model than the flow in a channel. The experimental modelling of a flow with one nominally infinite dimension (see the discussion in section 2.2.1.1 on the backward-facing step) can be difficult, with the isolation of end effects being potentially problematic.

Sobey (1985) investigated experimentally a channel flow with a variety of symmetric and asymmetric expansion geometries, concentrating on the presence of vortex waves in the oscillatory flow in asymmetric geometries. Later work, in Sobey & Drazin (1986), focused on the steady flow bifurcations in the symmetric channel expansion; the most common example was the Coanda wall attachment, where the jet created downstream of the expansion deflected to one side of the channel. Pitt, Sherwin & Theofilis (2005) also investigated the stability of steady inlet stenotic channel flows for a 60% occlusion severity. Again on pulsatile flow, Tutty (1992) investigated the flow through a channel with an asymmetric semi-circular blockage of 50% occlusion, observing that the maximum wall shear stresses in the channel were much greater for pulsatile than for steady flow. Rosenfeld & Einav (1995) investigated constriction effects on stenotic channel flow. The strength and survival time of vortices created every pulse period increased with the severity of the stenosis.

Mittal *et al.* (2003) investigated the same geometry as Tutty (1992), performing large-eddy simulations (LES), but also allowing for spanwise variations in the flow. They found two separating shear layers, one emanating from the blockage, the other from the wall opposite the blockage. Going on previous assertions made in the literature (Tobin & Chang 1976), the authors suggested that the areas downstream of the blockage where the separating shear layers impacted on the wall may explain the phenomenon of arterial murmurs in stenotic arteries.

The following section will now detail some of the literature on the modelling of flows through tubular stenotic geometries.

2.3.2 Stenotic geometries – pulsatile flows

When considering all of the various parameters of pulsatile stenotic flows (Reynolds number, pulse waveform, pulse amplitude and period, blockage severity and any num-

ber of blockage shapes) the highly varied range of studies available on stenotic flow modelling in the literature is not surprising. For the review of this section, only a selection of the studies available on stenotic flow modelling is presented, with an emphasis placed on those ones bearing similarity to the research undertaken and presented in chapter 6 of the thesis.

2.3.2.1 Direct stenotic flow modelling

In this section, some of the studies in the literature undertaken on stenosis models derived directly from real stenotic geometries are summarised. One of the most common regions in the cardiovascular system for the development of stenosis, the carotid bifurcation has attracted much interest (Nazemi, Kleinstreuer & Archie 1990; Cheng, Deville, Dheur & Vanderschuren 1992). Much of this research is undertaken with the aim of improving modelling techniques for patient-specific flow modelling. The work of Stroud *et al.* (2002) focuses on numerical simulations performed on a mesh constructed from a magnetic resonance image of an actual stenotic carotid artery. Figure 2.11 shows streamlines and pressure contours from one of the numerical simulations of Stroud *et al.* (2002). This figure serves firstly to illustrate the complicated geometry presented by an actual stenotic artery. Secondly, the figure, and the article, show that the flow is a highly complicated one, with numerous recirculations appearing throughout the flow domain. However, from a fluid mechanics perspective, the conclusions to be drawn from the study are limited to general ones, stating that the stenotic flow is different to the flow in an un-diseased artery, with higher wall shear stresses and cyclic loadings on the stenosis. The authors go on to state that such cyclic loading could indicate fatigue as a cause of ruptures in the stenotic plaque.

In order to draw more definite conclusions about the fluid mechanics of stenotic flows, researchers have chosen to investigate idealised stenotic flows. By simplifying the geometry and velocity waveform, the more fundamental features of the flow can be elucidated. The following section provides a review of this work on idealised stenotic flows.

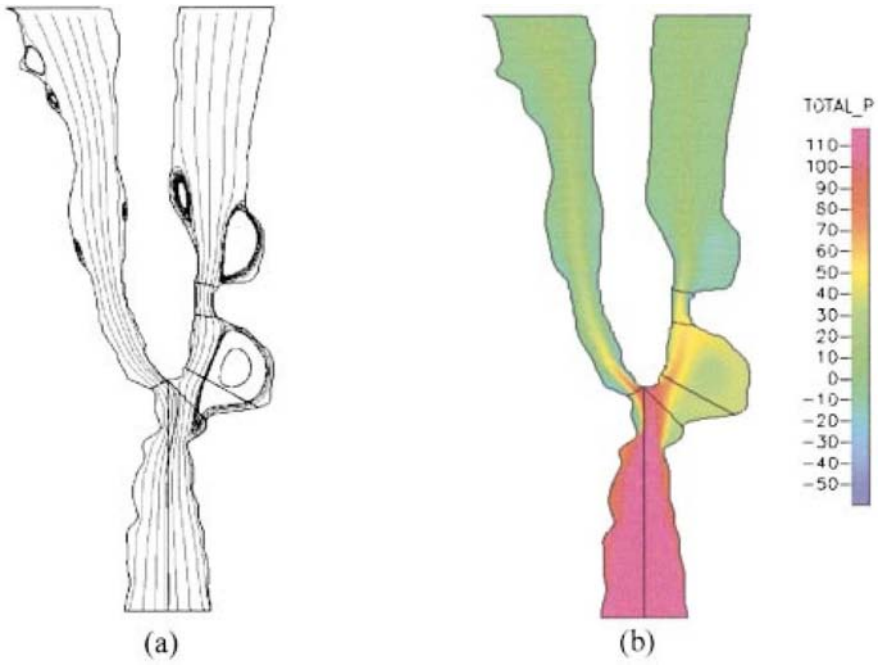

FIGURE 2.11: From Stroud *et al.* (2002), during diastole (a) instantaneous streamlines and (b) pressure contours of the flow at $Re = 330$ and Womersley number $\alpha = 5$ in a model of a stenotic carotid artery bifurcation.

2.3.2.2 Idealised stenosis modelling

Some of the earliest experimental work on pulsatile stenotic flows in an idealised geometry is presented in Cassanova & Giddens (1978). They provided energy spectra of pulsatile flow through a smooth axisymmetric stenosis in a straight pipe, aiming to identify flow disturbances which might provide indications of the presence of a stenosis. It was hoped such data could be used to develop new diagnostic methods to detect the presence of atherosclerosis using non-invasive techniques, such as Doppler ultrasound. They found that the presence of mild stenosis could be established from flow energy spectra, but not the severity of the stenosis. With the same motivation, the work of Khalifa & Giddens (1978) and Khalifa & Giddens (1981) sought to characterise the change in flow energy spectra with the severity of the blockage.

In the work of Ahmed & Giddens (1984), the focus moves away from the possible identification of stenosis from turbulent flow energy spectra of Doppler ultrasound images, to the identification of stenosis by the structure of the poststenotic flow. To this end, Ahmed & Giddens (1984) sought to describe the poststenotic flow using flow visualisation techniques and laser Doppler velocimetry to extract velocity profiles. They

modelled the stenosis axisymmetrically, using a cosine curve, with area reductions of 25, 50 and 75%; the velocity waveform consisted of a median Reynolds number of 600 and a Womersley number of 7.5. From hydrogen bubble visualisations they identified increased flow disturbances with increasing area reduction. For the 75% reduction, they observed discrete oscillations in the near field flow and then turbulence at approximately 6 diameters downstream of the blockage, during the deceleration phase of the cycle. They concluded that the identification of flow disturbances such as those observed in their study were better indicators of stenosis severity than turbulent energy spectra derived from Doppler ultrasound techniques. However, no critical boundaries for the instabilities they observed in their experiment were included. If such a diagnostic tool as suggested in the paper were to be developed, the boundaries for the appearance of these flow disturbances would need to be known.

Ohja, Cobbold, Johnston & Hummel (1989) investigated poststenotic pulsatile flow through a number of stenosis geometries, this time using a photochromatic tracer method, which involves the irradiation at a given axial location of an indicator in the fluid. A photochemical reaction of the indicator acts as a tracer, providing visualisations of velocity profiles and also allows relatively accurate measurements of wall shear stress. A single pulsatile waveform was used and both their stenosis geometries had sharp edges. The photochromatic tracer method was effective in delineating velocity profiles and also in indicating the breakdown of the flow in the poststenotic region. Figures 2.12(a) and 2.12(b) give examples of the method from Ohja *et al.* (1989). For Reynolds number 575, Womersley number 7.5 and for the area reduction 45%, a slight breakdown of the flow can be observed in the third tracer profile, 4 diameters downstream of the blockage. For the 75% area reduction, the breakdown of the poststenotic flow is more pronounced, with a strong diffusion of the second velocity profile. They identified a turbulent phase, during deceleration, where the flow became turbulent around 5 diameters downstream of the blockage, and a relaminarisation phase, during acceleration, where the turbulence was convected downstream and the jet emanating from the blockage was stable and laminar. This observation of turbulence occurring only during a portion of the velocity waveform is one common to other studies on pulsatile stenotic flow (Ahmed & Giddens 1984; Lieber & Giddens 1990; Ahmed 1998). For the turbulent phase of the 75% area reduction, Ohja *et al.* (1989) divided the post-

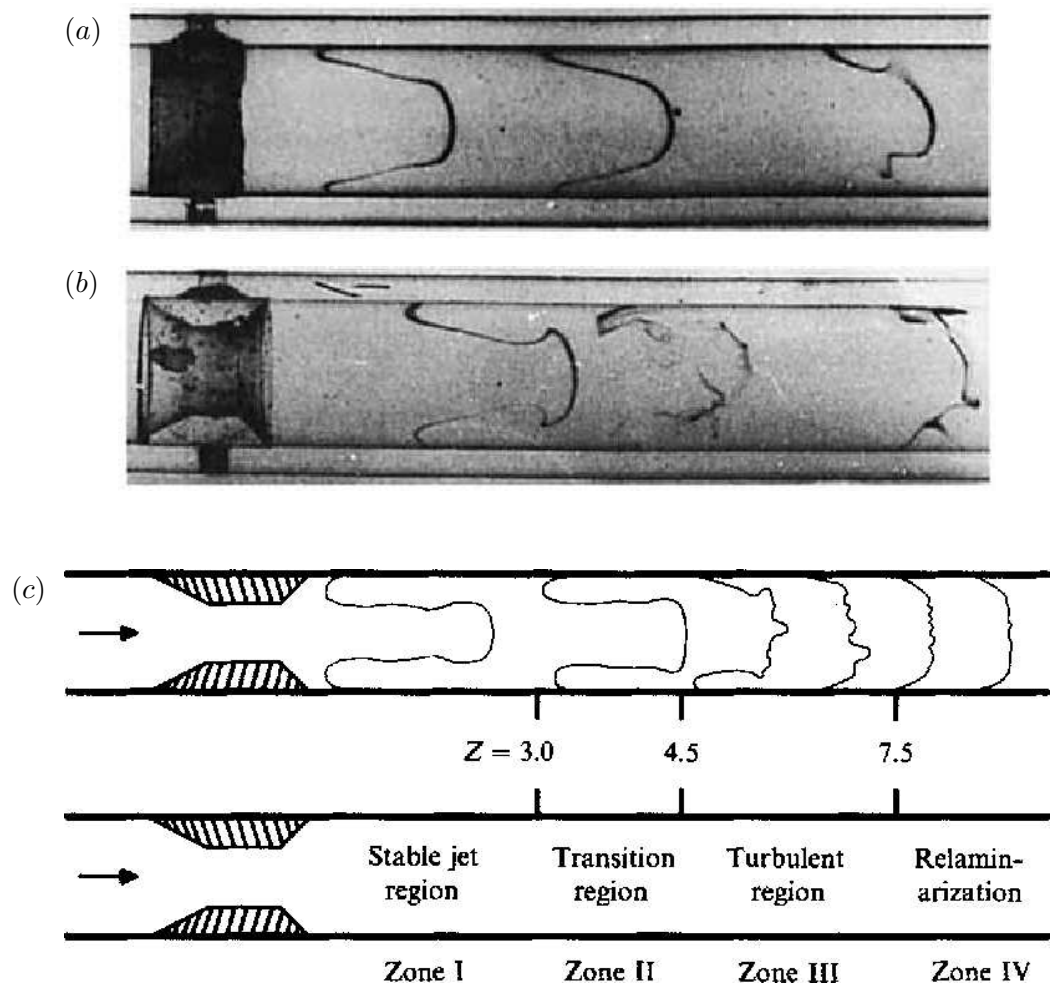

FIGURE 2.12: Examples of the photochromatic tracer method used in Ohja *et al.* (1989), for the flow at a single phase for Reynolds number of 575, Womersley number of 7.5 and area reductions of (*a*) 45% and (*b*) 75%. The axisymmetric stenosis can be seen at the left of each image. (*c*) Classification of the zones of the poststenotic flow for the axisymmetric stenosis of area reduction 75%.

stenotic flow into regions, classifying each zone. The classifications are re-shown in figure 2.12(*c*).

Four zones are identified. In the stable jet region, three Kelvin-Helmholtz-type vortex roll-ups were observed. In the transition region, these roll-ups lost their symmetry, leading to their breakdown in the turbulent region. This turbulent region extended over the entire diameter of the tube and three diameters axially. The relaminarisation of the flow occurred anywhere beyond 7.5 diameters downstream of the blockage. The zone classifications give a good general characterisation of an experimental pulsatile stenotic flow and are consistent with the observations regarding flow instability of Ahmed &

Giddens (1984).

More recently, many researchers have used computational fluid dynamics (CFD) to investigate pulsatile flows in idealised stenotic geometries (Tu, Deville, Dheur & Vanderschuren 1992; Deplano & Siouffi 1999; Liu & Yamaguchi 2001; Varghese & Frankel 2003). Experiments into hemodynamics are hampered by the fact that arteries, given their position and critical function within the body, are relatively difficult to extract data from. Experimental modelling of arterial flows is more common; however, most recent studies have focused on computational methods to investigate stenotic flows. This is perhaps due to difficulties in measuring wall shear stress, the importance of which has been discussed earlier.

The work of Deplano & Siouffi (1999) combined a laboratory model of a stenosis with a computational (finite element) investigation. The experimental model used a polymer 75% severity stenosis. This was fitted with a hydrodynamic generator capable of creating any shape of pulsatile waveform. On both models, simple pulsatile and physiologically realistic waveforms were tested. As expected, high average wall shear stresses were found at the throat of the stenosis, and low values downstream. The key finding of the paper stems from the locating of areas of negative average wall shear stress, that the presence of a stenosis causes the artery to work in a direction opposite to that of a healthy artery. This could lead to the compounding of the disease, with conditions present having the potential for the development of further disease or intimal thickening.

Using a three-dimensional finite volume fluid flow solver, Stroud, Berger & Saloner (2000) studied the influence of morphology on stenotic flows; their work also featured heavily in the review paper of Berger & Jou (2000). The key drive of the study seems to be to demonstrate the inadequacy of "percent stenosis" as a diagnostic measure for arterial disease. This was done by investigating, independently of stenosis severity, the importance of such factors as surface irregularity and aspect ratio on flow behaviour. Figure 2.13 shows some of the effects of an irregular stenosis. Many differences are found; however, the irregularities selected for the simulations seem fairly arbitrary. The work identifies the significance of stenosis morphology, but falls short of assessing or quantifying that significance. It is suggested that such a quantification may "usefully supplement" a standard diagnostic parameter for stenosis severity, but no method for

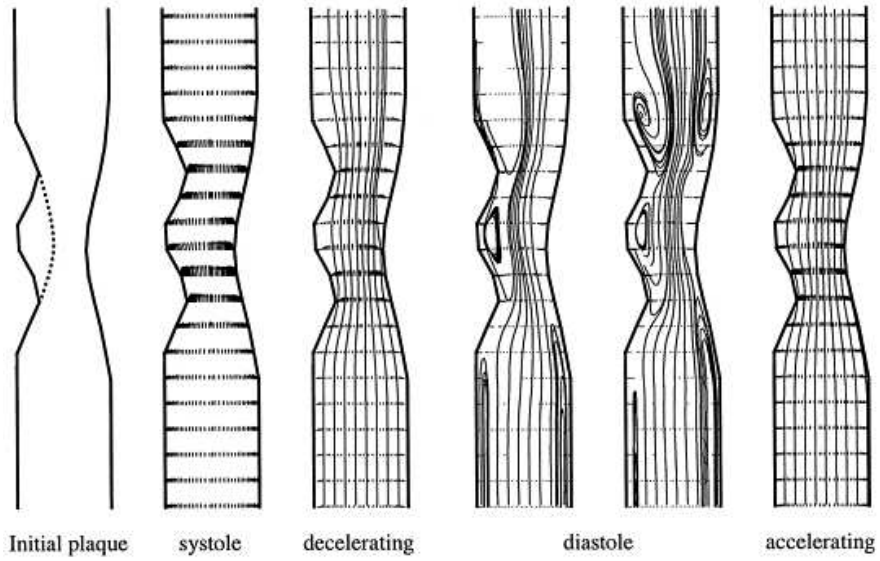

FIGURE 2.13: Instantaneous streamlines and velocity profiles for vessels with cratered valley affecting one half of the cross section; from Stroud *et al.* (2000). The streamlines show some of the effects of irregular stenosis shape.

doing so is suggested. This study is typical of many investigations of stenotic flow, in that it identifies a phenomenon, but does not make an attempt at characterising it. The further work by Stroud, Berger & Saloner (2002), discussed in the previous section, followed in a similar strain. The simulations focused on matching and reproducing as closely as possible the physiological conditions, without investigating any underlying physical relationships.

The work of Long, Xu, Ramnarine & Hoskins (2001) made more of an attempt at characterising the direct effects of different stenosis shapes and sizes. Using a three-dimensional finite volume solver, they investigated the flow through symmetric and asymmetric smooth stenoses of three different severities. All the stenoses shared the same aspect ratio. The study found that the axisymmetric 75% stenosis had an influence on the flow up to $20D$ downstream compared to $15D$ downstream for the asymmetric stenosis. Only general statements were made regarding the particular influence of the stenosis geometry.

More recently, the transition to turbulence observed in many stenotic flow experiments (Ahmed & Giddens 1984; Ohja *et al.* 1989) has been examined computationally. Simulating the pulsatile flow through an axisymmetric 75% severity stenosis, Mallinger & Drikakis (2002) were able to recreate the downstream transition observed in previ-

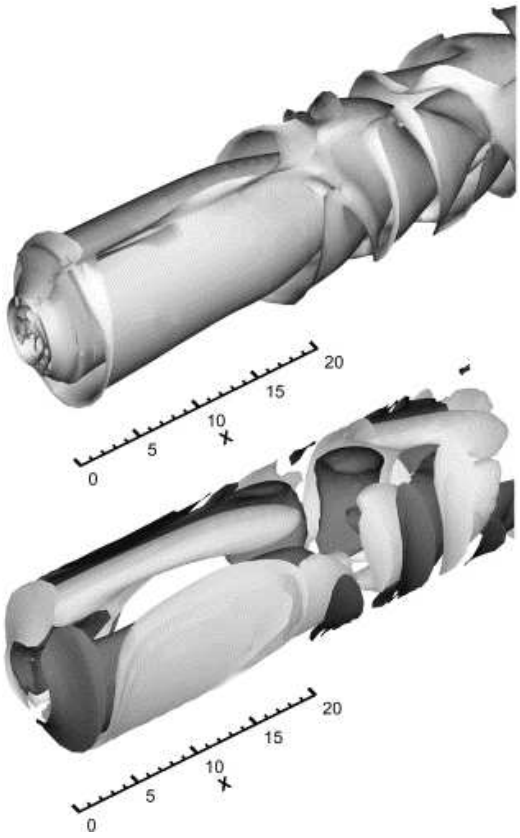

FIGURE 2.14: Zero isosurface of streamwise vorticity (top), and volumes of positive and negative streamwise vorticity, from Mallinger & Drikakis (2002).

ous experiments. The plots of vorticity in figure 2.14 show the flow becoming highly three-dimensional downstream of the blockage. Initially, the flow would remain laminar; the instability would then progress upstream and "sit" at the point shown in figure 2.14. The physical cause of this instability was not examined in any depth, however the authors linked it to increases in the circumferential stress on the artery and to larger-than-normal fluctuations of the wall shear stress. A qualitatively similar instability was also recreated and analysed in Sherwin & Blackburn (2005) in their simulations, using a similar geometry to that of figure 2.14.

The determination of even approximate critical Reynolds numbers or area reductions for instability is lacking from much of the work on stenotic flows; recently, this has begun to be addressed, the work of Sherwin & Blackburn (2005) and Blackburn & Sherwin (2007) featuring more in-depth stability analysis. Using Floquet stability analysis, Sherwin & Blackburn (2005) determined critical Reynolds numbers of pulsatile flow through a smooth cosine stenosis, similar to that used in Ahmed & Giddens

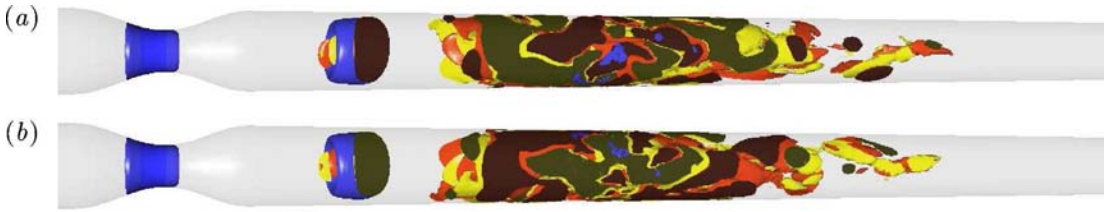

FIGURE 2.15: Two visualisations of the asymptotic turbulent state at $Re = 400$ and pulse period 2.5, at a time interval of one period, from Blackburn & Sherwin (2007). Instantaneous isosurfaces of velocity gradient tensor are shown; the period-doubling of the instability can be seen in the mirror image that each image forms of the other.

(1984). For the greater part of the pulse period range relevant to physiological flows in large arteries, they identified the primary linear instability in the flow as a period-doubling vortex-tilting (azimuthal wavenumber $m = 1$). The instability acted on the vortex ring generated each pulse period, tilting each successive ring in opposite directions. Direct numerical simulation of the flow with a small flow perturbation added, revealed the breakdown of the vortex rings far downstream, with an eventual relocation of this breakdown upstream, to within $4D$ downstream of the stenosis. Figure 2.15 plots visualisations of the asymptotic flow, illustrating the period-doubling nature of the instability. This asymptotic behaviour compares well with the instabilities described in the previous experimental work of Ohja *et al.* (1989) and Ahmed & Giddens (1984). However, the exact role of linear instability modes in the stability of experimental flows is not determined, there being no experimental noise present in the numerical simulations.

Blackburn & Sherwin (2007) presents an investigation of flows of a wider range of pulse periods than in Sherwin & Blackburn (2005). Different leading linear instability modes were identified for flows of shorter pulse period, at the higher end of the range of Womersley numbers relevant to real physiological flows. Modes of azimuthal wavenumber $m = 3$ and 4 dominated at higher Womersley numbers, the authors arguing them to be Widnall instability modes (Widnall, Bliss & Tsai 1974), manifesting as azimuthal waves growing on each vortex ring. The asymptotic flow of an unstable Reynolds number, generated from perturbed direct numerical simulations, found the breakdown of the flow progressed upstream to settle just a few diameters downstream of the stenosis throat.

Blackburn & Sherwin (2007) also investigated further the possibility of convective

shear layer instability in pulsatile stenotic flow. To do this they simulated pulsatile flows with a high-frequency, low-amplitude oscillation added to the inlet velocity. Performing Floquet stability analysis on these periodically-forced pulsatile flows, they found the flows to be significantly less stable to linear instability modes when perturbed in such a manner, particularly for flows of longer pulse period. They suggested a possible interaction between the convective shear layer instability and the linear Floquet instability. This took the study a step closer to the noise-driven instabilities seen in the experimental flows of Ahmed & Giddens (1984) and Ohja *et al.* (1989); however, the question of the exact role these linear instability modes might play in the experimental flows is still an open one.

A further observation was made in Blackburn & Sherwin (2007) regarding the periodic formation of vortex rings in pulsatile stenotic flow, which is worthy of mention here. They related the vortex ring formation to the work of Gharib, Rambod & Shariff (1998), who investigated the generation by piston of laminar vortex rings entering an unbounded domain. Gharib *et al.* (1998) developed the theory that a vortex ring is limited to a certain amount of circulation; if this limit is exceeded during vortex generation, the vortex ring "pinches off", leaving any excess circulation as a vorticity trail in its wake. Figure 2.16 shows dye visualisations of three vortex rings, each generated with a different amount of input circulation (generated by the piston motion). Gharib *et al.* (1998) characterised the input circulation as a formation time ($\overline{U}_p t/D$, where $\overline{U}_p$ is the mean of the piston velocity, t is the discharge time and D is the diameter of the piston). They argued the existence of a universal formation number, $\overline{U}_p t/D \approx 4$, which described the formation time beyond which a forming vortex ring could take up no further circulation, and would pinch off. Figure 2.16(a) shows a vortex generated with a formation time less than 4; there is no trailing wake of vorticity and the vortex ring is smaller than in figure 2.16(b), which shows a vortex generated with a formation time of approximately 4. Figure 2.16(c) shows a vortex generated with a formation time much greater than 4; the leading vortex ring is the same size as the vortex ring in figure 2.16(b), with the excess circulation being deposited in the wake of the vortex. This indicates a limiting value to the amount of circulation able to be deposited in a vortex ring.

Blackburn & Sherwin (2007) argued a similar phenomenon to be at play in the

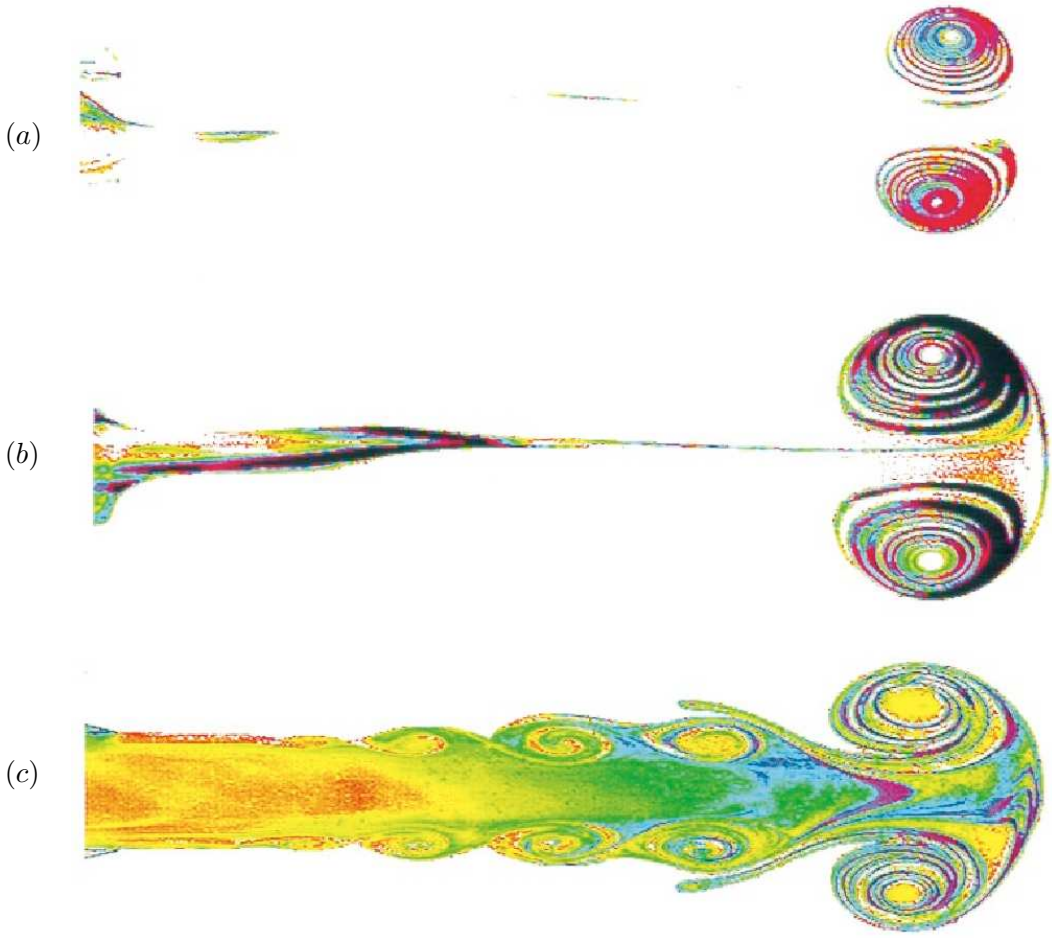

FIGURE 2.16: From Gharib *et al.* (1998), visualisation of vortex rings in an unbounded domain, generated with different input circulations. The visualisation of (a) is generated with a circulation corresponding to a formation time, $\overline{U}_p t/D$, of 2, (b) to a formation time of 3.8 and (c) to a formation time of 14.5.

pulsatile stenotic flow, even though the generation of the vortex ring takes place in a constrained domain. However, they did not attempt to strengthen the analogy beyond identifying a qualitative similarity in plots of vorticity field.

In very recent work, Varghese, Frankel & Fischer (2007b) have presented a detailed study of wall shear stress and velocity profiles for direct numerical simulations of pulsatile flow in an axisymmetric stenotic geometry of 75% area reduction, using the same flow parameters and geometry used in Ahmed & Giddens (1984) (Reynolds number 600, pulse amplitude 0.667 and Womersley number 7.5). They also performed simulations using the same stenosis model, but with a geometric perturbation in the form of a 5% eccentricity of the stenosis geometry. A comparison of velocity profiles between their

simulations and the experimental measurements of Ahmed & Giddens (1984) showed a good agreement, with small differences in reattachment length appearing between 4 and 6 diameters downstream of the stenosis; these differences were likely due to turbulence in the experimental flow of Ahmed & Giddens (1984). They only observed a breakdown of the poststenotic flow in simulations performed with the stenosis of 5% eccentricity, with periodic localised transitions (4 to 6 diameters downstream of the blockage) to turbulence occurring during the deceleration phase of the waveform. In this way, the geometric eccentricity acted as a tripping mechanism for instability and turbulence, rather than an added flow perturbation (Sherwin & Blackburn 2005) or experimental noise (Ahmed & Giddens 1984; Ohja *et al.* 1989).

2.3.2.3 Present work (chapter 6)

Chapter 6 of the thesis is devoted to pulsatile stenotic flows. An emphasis is placed on changes in the flow with blockage ratio. Similar to the steady flow, there are few studies in the literature dealing with blockage effects on pulsatile stenotic flows for a broad range of area reductions. Characterisations of stability and wall shear stress distribution with blockage ratio constitute two areas of interest.

The possibility of formulating a formation time for the vortex rings of pulsatile stenotic flow is also of interest, the intention being to analyse the analogy with the theory of a universal formation number for isolated vortex rings generated by the motion of a piston. The investigation of the analogy would also tie into an analysis of the vortex ring behaviour and propagation downstream of the stenosis.

Experimentally, there is no recent work on pulsatile flow through idealised stenoses; furthermore, the experimental work performed has tended to focus on only one or two configurations of flows parameters. Visualisations of stenotic flow for a wider range of flow parameters than tested thus far would be helpful in validating numerical simulations.

2.4 Chapter summary

The intention of this chapter has been to present a background to the role of fluid mechanics in the research of stenotic flows, as well as a review of particular studies relevant to the work presented in this thesis. The first section gave an overview of the

contribution fluid mechanics can and has made to research on the subject, including a description of the importance of various fluid mechanical characteristics to the biological responses and functions of arteries and particular cells.

The second section has reviewed work on steady flows in a range of geometries, including stenotic geometries and the backward-facing step. Although consisting of only an expanding channel, the wide body of literature available on backward-facing step flow provides a useful background to some of the research presented in this thesis. The final section of the chapter deals with the literature available on pulsatile flows in stenotic geometries, ranging from realistic re-creations of actual diseased arteries to idealised stenoses.

The following chapter presents a description of the various numerical and experimental techniques used to model and analyse the flows investigated in this thesis.

Chapter 3

Methodology

The thesis examines steady and pulsatile flows through a number of geometries, with methods both numerical and experimental. Section 3.1 of this chapter discusses the techniques used to solve the governing equations for the numerical simulations, followed by details of the method used for linear stability analysis. Section 3.2 describes the geometries and boundary conditions of each of the problems under investigation in this thesis. A description of the experimental apparatus and analysis techniques is given in section 3.3.

3.1 Numerical method: simulating the flow field

Numerical simulations are conducted by discretising the domain under consideration and then solving the governing equations. For fluid flow, the governing equations are the incompressible Navier-Stokes equations, given here:

$$\frac{\partial \overline{\mathbf{u}}}{\partial t} + \overline{\mathbf{u}} \cdot \nabla \overline{\mathbf{u}} = -\nabla \overline{p} + \nu \nabla^2 \overline{\mathbf{u}}, \tag{3.1}$$

$$\nabla \cdot \overline{\mathbf{u}} = 0, \tag{3.2}$$

where $\overline{\mathbf{u}} = (u(t,x,y), v(t,x,y))$ is the two-dimensional velocity vector and $\overline{p}$ and ν are the kinematic pressure and viscosity. Equation 3.1 is the momentum equation, including an advection term ($\overline{\mathbf{u}} \cdot \nabla \overline{\mathbf{u}}$), a pressure term ($-\nabla \overline{p}$) and a diffusion term ($\nu \nabla^2 \overline{\mathbf{u}}$). Equation 3.2 is the continuity equation and is a constraint which follows from the incompressibility of the fluid.

3.1.1 The spectral-element method

The spectral-element method is employed to discretise the Navier-Stokes equations and solve for the flow field. The current implementation of the method has been developed at Monash University by Mark C. Thompson and has been used and validated in the prediction of wake flows past rings (Sheard *et al.* 2003), spheres (Thompson *et al.* 2001a) and circular cylinders (Thompson *et al.* 1996). The method uses a Galerkin finite-element method in two dimensions, with high-order Lagrangian interpolants used within each element. These elements spatially-discretise the domain under consideration and are divided further into $n \times n$ internal nodes. The nodes are distributed according to Gauss-Legendre-Lobatto quadrature integration points.

3.1.1.1 Temporal discretisation

The three-step time-splitting algorithm employed to temporally discretise the Navier-Stokes equations was developed by Karniadakis, Israeli & Orszag (1991). The method uses a pressure boundary condition which reduces the domain boundary divergence errors typically associated with time-splitting techniques (Karniadakis *et al.* 1991). The implementation of the method has been verified to give second-order accuracy in time.

The three sub-steps of the method treat in turn the advection, pressure and diffusion terms of the Navier-Stokes equations. The sub-steps employ a variety of solving techniques.

Using the nonlinear convective term, the first sub-step computes an intermediate velocity field $\mathbf{u}^*$, according to

$$\frac{\mathbf{u}^* - \mathbf{u}^{(n)}}{\triangle t} = \overline{\mathbf{u}} \cdot \nabla \overline{\mathbf{u}}. \tag{3.3}$$

The equation is solved using the explicit third-order Adams-Bashforth technique.

The second sub-step computes another intermediate velocity field $\mathbf{u}^{**}$, from the pressure term of equation 3.1, according to

$$\frac{\mathbf{u}^{**} - \mathbf{u}^*}{\triangle t} = -\nabla \overline{p}^{n+1}. \tag{3.4}$$

By taking the divergence of this equation and utilising the incompressibility constraint

of equation 3.2, we obtain a Poisson equation for the pressure,

$$\nabla^2 \overline{p}^{n+1} = \frac{1}{\triangle t} \nabla \cdot \mathbf{u}^*, \tag{3.5}$$

from which the second intermediate velocity can be solved.

The velocity field, $\mathbf{u}^{n+1}$, is obtained in the third sub-step, which is described as

$$\frac{\mathbf{u}^{n+1} - \mathbf{u}^{**}}{\triangle t} = \nu \nabla^2 \overline{\mathbf{u}}. \tag{3.6}$$

The velocity field is solved implicitly using a second-order Crank-Nicholson scheme, with the theta modification. This technique maintains second-order accuracy in space and time (Canuto, Hussaini, Quarteroni & Zang 1990). Provided first order pressure boundary conditions are used, the entire three-step splitting scheme achieves second-order accuracy in time for the velocity field (Karniadakis *et al.* 1991).

3.1.1.2 Coordinate systems

The first problem dealt with in this thesis involves purely two-dimensional flow between flat plates. In this case, the x-coordinate describes the direction parallel to the plates and the y-coordinate describes the perpendicular direction. Although the simulations are purely two-dimensional, linear stability analysis (described in section 3.1.2) is conducted, involving a z-coordinate, which can be thought of as a depth, or as 'into the page'.

The second problem studied – which involves flow in a tube – is simulated using axisymmetric computations. In this coordinate system, the z-coordinate describes the axial direction, the r-coordinate the radial and the θ-coordinate the azimuthal. The velocity fields of these simulations are assumed to vary with z and r, but are independent of θ. The linear stability analysis technique described in the next section is used to predict the development of the θ-dependence of the fields.

3.1.2 Floquet stability analysis

Floquet stability analysis is usually employed to analyse the growth of three-dimensional perturbations on a two-dimensional periodic base flow. Floquet multipliers, μ, are returned which represent the stability of the base flow to a specific wavelength perturbation. A Floquet multiplier $|\mu| > 1$ indicates an unstable flow, while $|\mu| < 1$ indicates

a stable one. A Floquet multiplier $|\mu| = 1$ represents neutral stability; in such a case the flow is at a critical Reynolds number Re_c, above which it is stable, below which it is unstable.

Floquet analysis is associated with periodic base flow. Throughout much of the thesis however, the stability of steady, time-independent flows is also investigated. For steady flows, the multiplier used to describe the amplification of the mode is replaced by a description in terms of a non-dimensional growth rate, σ. The two descriptions are interchangeable, according to the relation

$$\mu \equiv \mathrm{e}^{\sigma T}. \tag{3.7}$$

For periodic flow, T is equal to the period of the base flow; for steady flow, there is no base flow period, therefore, T is assumed to be equal to one non-dimensional time unit.

The stability of the two-dimensional base flow is determined by solving the linearised Navier-Stokes equations. The main aim is to determine the stability as a function of Reynolds number and spanwise wavelength, λ, or equivalently the wavenumber, $m = 2\pi/\lambda$, allowing for the possibility of both steady and time-dependent bifurcations. For the purely two-dimensional problem studied in this thesis, perturbations are expressed in terms of their wavelength λ, while for the axisymmetric simulations they are expressed in terms of their wavenumber m. In the two-dimensional case, perturbations can theoretically take any wavelength; however, in the axisymmetric case, perturbations are restricted to being periodic with the azimuthal direction, namely of wavelengths of 2π, π, $2\pi/3$, $\pi/2$ ... As a result it is more convenient to express the perturbations according to their corresponding wavenumbers, $m = 1, 2, 3, 4$ ... The outline of the analysis method given below is described in terms of the coordinates for the two-dimensional case; the method is essentially the same for the axisymmetric simulations, only with different coordinates. The same or similar techniques have been used successfully in many previous studies, for example Barkley & Henderson (1996) and Thompson *et al.* (2001b).

Starting with the two-dimensional base flow, with the w-velocity in the spanwise (or azimuthal) direction, the velocity components and the kinematic pressure can be

written as the base flow plus a perturbation

$$\mathbf{u}(x,y,z,t) = \overline{\mathbf{u}}(x,y,t) + \mathbf{u}'(x,y,z,t), \tag{3.8}$$

$$p(x,y,z,t) = \overline{p}(x,y,t) + p'(x,y,z,t), \tag{3.9}$$

where $\overline{\mathbf{u}} = (u, v)$ and $\overline{p}$ describe the two-dimensional base flow and $\mathbf{u}' = (u', v', w')$ and p' are perturbations. Substituting these definitions into the Navier-Stokes equations, subtracting the base flow and removing non-linear terms yields the following equations which describe the evolution of small disturbances

$$\frac{\partial \mathbf{u}'}{\partial t} + \overline{\mathbf{u}} \cdot \nabla \mathbf{u}' + \mathbf{u}' \cdot \nabla \overline{\mathbf{u}} = -\nabla p' + \nu \nabla^2 \mathbf{u}', \tag{3.10}$$

$$\nabla \cdot \mathbf{u}' = 0. \tag{3.11}$$

Because these equations are linear and the coefficients are not a function of z, the variation in z can be constructed as a sum of complex exponentials. The coupling is such that representative modes from the series expansion, characterised by their spanwise wavelength λ, can be written in the form

$$u'(x,y,z,t) = \hat{u}(x,y,t)\sin(2\pi z/\lambda), \tag{3.12}$$

$$v'(x,y,z,t) = \hat{v}(x,y,t)\sin(2\pi z/\lambda), \tag{3.13}$$

$$w'(x,y,z,t) = \hat{w}(x,y,t)\cos(2\pi z/\lambda), \tag{3.14}$$

$$p'(x,y,z,t) = \hat{p}(x,y,t)\sin(2\pi z/\lambda). \tag{3.15}$$

Alternatively, sine and cosine terms can be interchanged to give an equivalent solution set (see for example Barkley & Henderson (1996)).

These variables can then be substituted into the perturbation equations. The resultant equations describing $\hat{u}, \hat{v}, \hat{w}$ and $\hat{p}$ can be solved with the same numerical method used to solve for the base flow. Regarding the boundary conditions, the velocity and pressure perturbations are set to zero on all boundaries of the computational domain, except the outflow section, where the normal derivatives of the velocity perturbations vanish.

In this way, the evolution of spanwise perturbations to the two-dimensional flow at a given wavelength λ can be determined. In general, the perturbations will either grow or decay exponentially. In fact, the time-dependence of each component of the

perturbation field can be expressed as

$$\hat{\phi}_s(x, y, t) = \mathrm{e}^{\sigma_s t}\hat{\phi}_s(x, y, 0), \tag{3.16}$$

where σ_s is the growth rate, and $\hat{\phi}_s$ denotes one of the eigenfunctions in the transverse x–y plane that can be used to reconstruct the two-dimensional perturbation field. The perturbation mode will either grow or decay depending on whether its growth rate, σ_s, is positive or negative.

The growth rate is a function of the eigenmode, the spanwise wavelength and the Reynolds number. For each Reynolds number, the aim is to determine the fastest-growing or slowest-decaying mode for each wavelength. At the critical Reynolds number marking the transition to three-dimensional flow, the growth rate passes from negative to positive for a particular wavelength (or from < 1 to > 1 for a Floquet multiplier). In practice, the maximum growth rate for each wavelength and Reynolds number pair is determined by the power method. Initially, the perturbation field is given a white-noise randomisation; the perturbation equations are then integrated in time, with the base flow, using the same numerical technique as described in section 3.1.1.1. The perturbation fields are normalised again each period, T; after many cycles only the fastest-growing Floquet mode remains. The ratio of the mode amplitude to the amplitude one period later gives the Floquet multiplier for the dominant mode.

For periodic base flows, several different mode classifications are possible. A real bifurcation ($\mu = 1$) has the same period as the base flow; well-known examples are the Mode A and B bifurcations in the wake of a circular cylinder in a freestream velocity (Barkley & Henderson 1996). A subharmonic bifurcation is indicated by a negative Floquet multiplier ($\mu = -1$); here the perturbation is period-doubling, operating at a period twice that of the base flow. A subharmonic mode can be detected by investigation of the perturbation field; the sign of a period-doubling bifurcation will alternate from one base flow period to the next. Both real and subharmonic bifurcations are encountered in this study. Several period-doubling bifurcations occur in pulsatile flow in tubes, and can be seen in later chapters of this thesis and in Sherwin & Blackburn (2005). A third type, complex-conjugate bifurcations, consist of standing- or travelling-wave solutions. These modes generate Floquet multipliers which oscillate around a mean value. Such modes are not encountered in this thesis, or at least not as

the dominant mode.

The relation of these numerically-predicted linear absolute instabilities to the fully-developed full-dimensional flows is not always clear. In Reynolds number flows above critical, a perturbation will grow; however, its further evolution will be non-linear. There are several ways that the non-linear growth can begin: the first arises when the base flow is changed as the perturbation grows, meaning that the various growth rates of the perturbation modes – which are calculated on the unperturbed base flow – may alter. Alternatively, as perturbation amplitudes become large, the non-linear terms removed in equation 3.10 become non-negligible. These control the saturation of the mode, but may also alter the structure of the mode. Finally, of modes are non-normal, then it is possible to have substantial transient growth. This is believed to be responsible for the transition of straight pipe flows, which generally become turbulent at $Re \approx 2000$, even though the flow is linearly stable.

Therefore, with this non-linear evolution, the action of the initial linear perturbation mode is not always evident in the asymptotic flow. This can make the detection of perturbation modes in, for example, unstable experimental flows, problematic. Such difficulties are discussed in detail in later chapters.

3.2 Creating the flow models

Several flows are investigated in the thesis, the first being that of the flow through a two-dimensional partially blocked channel.

3.2.1 The two-dimensional channel

A schematic of the geometry under question in chapter 4 is presented in figure 3.1. It is a geometry which shares much in common with the backward-facing step. It has the advantage of reducing the description of the blockage to a single parameter, and also isolating it from the calculation of the Reynolds number. The two non-dimensional parameters governing the flow behaviour are the Reynolds number Re, and the blockage ratio, defined as $b = r/D$, where r is the radius of the blockage and D the distance between the unblocked walls. The blockage ratios considered for this study lie in the

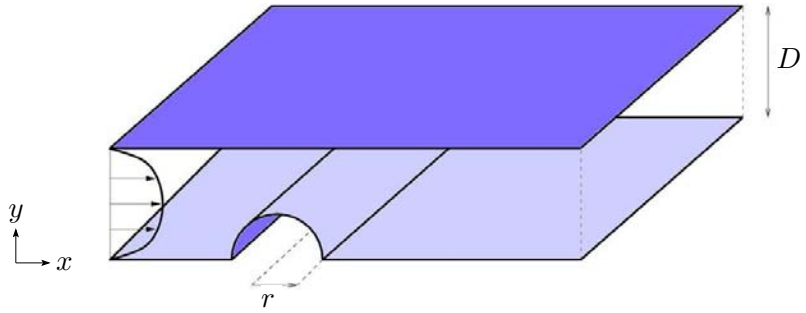

FIGURE 3.1: Schematic of the partially blocked two-dimensional geometry.

range 0.05 to 0.9. The Reynolds number Re is defined as,

$$Re = \frac{2D\overline{U}}{\nu}, \tag{3.17}$$

where ν is the kinematic viscosity and the quantity $2D$ corresponds to the hydraulic diameter of the channel. $\overline{U}$ is the mean flow speed in the channel. The Reynolds number used here differs from that used in many studies of the backward-facing step, which usually take the inlet channel width or the step height as the length scale. The velocity scale used in the present work is the mean velocity in the unblocked part of the channel, which would correspond to the region downstream of a backward-facing step. (Results from other studies are expressed using the Reynolds number definition in equation 3.17). All distances and times expressed in the study are non-dimensionalised by D and $D/\overline{U}$, respectively. The study examines laminar flows for Reynolds numbers ranging from 25 up to 3000, wherever possible. The highest Reynolds number for each blockage ratio was limited by the greater mesh resolution and computational time required to resolve the increased fluid velocity through the constriction. Hence, as the blockage ratio approached 0.9, the highest achievable Reynolds number fell accordingly. Furthermore, it is generally considered that the unblocked flow between two flat plates (plane Poiseuille flow) becomes turbulent at $Re \approx 2000$. Also germane to the issue of transition to turbulence is the potential for the blockage to act as a tripping mechanism, lowering the critical upstream Reynolds number for the appearance of turbulence. These issues of transition and three-dimensionality will be important in our considerations of instabilities in the two-dimensional base flow.

3.2.1.1 Boundary conditions

On the blockage surface and the channel walls, no-slip conditions were imposed. At the inlet boundary, an equilibrium Poiseuille parabolic profile was prescribed. Although the walls of the channel have been described at $y = 0$ and 1, purely for the purpose of defining the inlet velocity boundary condition, we place the walls at $y_w = \pm 0.5/D$, with $y = 0$ the centreline; the solution to the flow velocity in a channel is then given by

$$u(y) = -\frac{dp}{dx}\frac{y_w^2}{2\mu}(1 - \frac{y^2}{y_w^2}), \tag{3.18}$$

where $\frac{dp}{dx}$ is the pressure gradient and μ is the dynamic viscosity (White 1999). The maximum velocity occurs at the centre, where $y = 0$, giving

$$u_{max} = -\frac{dp}{dx}\frac{y_w^2}{2\mu}. \tag{3.19}$$

However, our Reynolds number is defined using $\overline{U}$, the average value of $u(y)$. Given that for numerical simulations, we set our reference velocity term as $\overline{U}$, we need a relation between equation 3.18 and $\overline{U}$. The average velocity is given as $\overline{U} = q/D$, where q is the flow rate over the width of the channel, $q = \int u(y)dy$. Therefore,

$$\overline{U} = \frac{1}{D}\int u(y)dy = \frac{1}{D}\int_{-y_w}^{+y_w} u_{max}(1 - \frac{y^2}{y_w^2})dy = \frac{2}{3}u_{max}. \tag{3.20}$$

Therefore, the Poiseuille profile implemented in the simulations is given by

$$u(y) = \frac{3\overline{U}}{2}(1 - \frac{4y^2}{D^2}). \tag{3.21}$$

At the outflow boundary, the standard zero normal velocity gradient condition is imposed.

3.2.1.2 Mesh layout and resolution

Ten meshes were constructed, with blockage ratios varying between 0.05 and 0.9. The same macro-element resolution was maintained across the blockage range, as far as possible. Figure 3.2 depicts the macro-element distribution close to the blockage sections of the grids corresponding to $b = 0.5$, 0.6 and 0.7.

Each grid was constructed using the same basic layout, but adjusted for the chosen blockage ratio. In order to sufficiently resolve higher velocity gradients, the macro-element distribution was more highly concentrated near the walls of the channel and

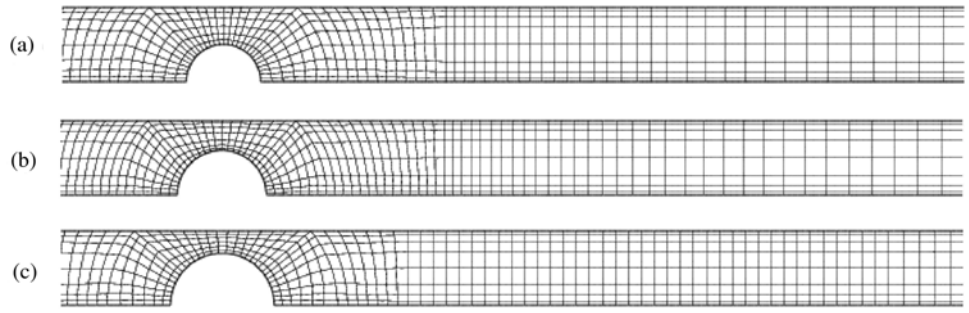

FIGURE 3.2: Sections of the computational meshes, from $2D$ upstream to $10D$ downstream of the blockage, showing macro-elements, used for blockage ratios (a) 0.5, (b) 0.6, (c) 0.7. The complete mesh extends from $6D$ upstream to $50D$ downstream in most simulations.

	Re=2400, b=0.3		Re=1200, b=0.5		Re=600, b=0.7	
n	L_R/r	σ	L_R/r	σ	L_R/r	σ
3	-	-	14.18	0.01615	8.942	0.1672
4	17.06	-0.001286	12.37	0.02850	8.980	0.2008
5	17.64	0.009418	12.32	0.02840	8.965	0.1928
6	17.53	0.008815	12.27	0.02834	8.960	0.1931
7	17.51	0.008554	12.28	0.02837	8.967	0.1931
8	17.52	0.008580	12.27	0.02838	8.967	0.1931
9	17.51	0.008569	12.28	0.02838	8.967	0.1931

TABLE 3.1: Convergence of the normalised initial recirculation length, L_R/r, and maximum growth rate, σ, across three blockage values with increasing polynomial order.

through and immediately downstream of the blockage. The resolution was decreased downstream to the outlet boundary. As discussed in section 3.1, each macro-element is further subdivided into $n \times n$ internal nodes, distributed according to the integration points. Functions are then represented internally by $(n-1)\times(n-1)$ tensor-product Lagrangian polynomials. An advantage of the approach is the ability to set the polynomial order at run-time, allowing resolution studies to be performed more easily.

The final internal grid resolution used for most simulations was $n = 6$, or 36 nodes per element, with no marked differences observed between predictions from simulations at this resolution and those for $n = 5$. For higher blockages and Reynolds numbers, elements of order $n = 7$, comprising 49 nodes per element, were employed to properly resolve the more strongly-varying regions of the flow field. For the highest Reynolds number tested at each blockage ratio, a grid resolution analysis was conducted, whereby

the simulation was rerun at the next three higher values of n. Comparisons were then made based on both the length of the initial recirculation zone and on vorticity profiles at points downstream of the blockage. Over the blockage range chosen, this increase in nodal concentration produced differences considerably less than 1% in the recirculation length, and in the maximum difference in the vorticity profiles over the width of the channel. Small divergences from the converged vorticity profiles for these high Reynolds number flows only became apparent at polynomial order of $n = 5$, which generally resulted, as stated before, from inadequate resolution in areas of high spatial flow gradients.

Further to this grid resolution check for the flow field, the convergence of the growth rate with increasing interpolant order was tested from the stability analysis for $b = 0.3$ and $Re = 2400$, $b = 0.5$ and $Re = 1200$ and $b = 0.7$ and $Re = 600$. Table 3.1 shows the convergence of both the growth rate for the critical wavelength from the linear stability analysis, and the length of the initial recirculation zone, L_R.

The independence of the flow predictions to the domain inlet and outlet lengths (i.e., the computational channel length upstream and downstream of the blockage) was also established. Considering that the flow begins to undergo its constriction upstream of the blockage, unlike the situation for the backward-facing step, care had to be taken to provide a sufficiently long inlet length; for at least a small portion of the solved flow field immediately after the computational inlet, the velocity profile should retain its symmetrical parabolic shape, before deforming to pass through the blockage. For the mesh constructed for $b = 0.5$, simulations were performed for $Re = 2000$ with inlet lengths varying between $2D$ and $10D$. The velocity profile only began to visibly skew at a little over one channel width upstream of the blockage. Using the different inlet lengths, no differences were observed in any of the flow fields employing an inlet length of greater than $3D$. For the remainder of the study, a conservative inlet length of $6D$ was used for all blockages. The same technique was employed to determine the standard outlet length of $50D$. As discussed later in the results, at higher Reynolds numbers, the various features of the flow extend further downstream. The outlet length of $50D$ was sufficient in the all but a few of the cases tested for the flow to re-establish its fully-developed form. Hence, with the midpoint of the constriction located at $x = 0$ and the walls at $y = 0$ and $y = 1$, the inlet was located at $x = -6$ and the outlet at $x = 50$, which

is also consistent with the values used in other recent numerical studies on a similar geometry featuring a constriction (Sherwin & Blackburn 2005). For blockages of $b > 0.6$, at the very highest Reynolds number, what resembled a convective instability was observed near the outflow boundary; this apparent non-physical instability disappeared if the outlet length was increased. However, importantly, no differences were observed in the flow field immediately downstream of the blockage between the flow fields obtained from using grids of longer outlet length.

3.2.2 Axisymmetric problem definition: steady inlet flow

While the two-dimensional channel constitutes a more classical fluid dynamics problem with its similarities to backward-facing step flow, in chapter 5, we take a step closer to the physiological reality of arterial stenoses. We take a straight tube with an axisymmetric contraction. The aim of investigating such a geometry is to explore the effect on flow behaviour of a variation of the blockage ratio of the stenotic geometry. In effect, such a variation tracks the development of an arterial stenosis from its genesis to its more pathological states. To make the problem more tractable and at the same time more applicable as a useful base case, the blockage geometry is reduced to be defined by a single parameter. This provides us with a well-defined parameter space. As well as being a simpler problem to analyse, the geometry allows comparisons to be drawn with previous work on flows past cylinders.

In this section, a more precise definition of the problem under consideration is given, followed by a description of the numerical methods employed. This geometry was also investigated experimentally. A discussion of the experimental methods used in examining the flow is given in section 3.3.

The geometry under investigation is shown in figure 3.3. It consists of a long straight tube with an axisymmetric blockage described by a single parameter, the blockage ratio, defined as

$$b = 1 - \left(\frac{d}{D}\right)^2, \tag{3.22}$$

where D is the diameter of the tube and d is the diameter at the centre of the blockage. Figure 3.3 also shows a radius of the blockage, dependent on b, which can be defined

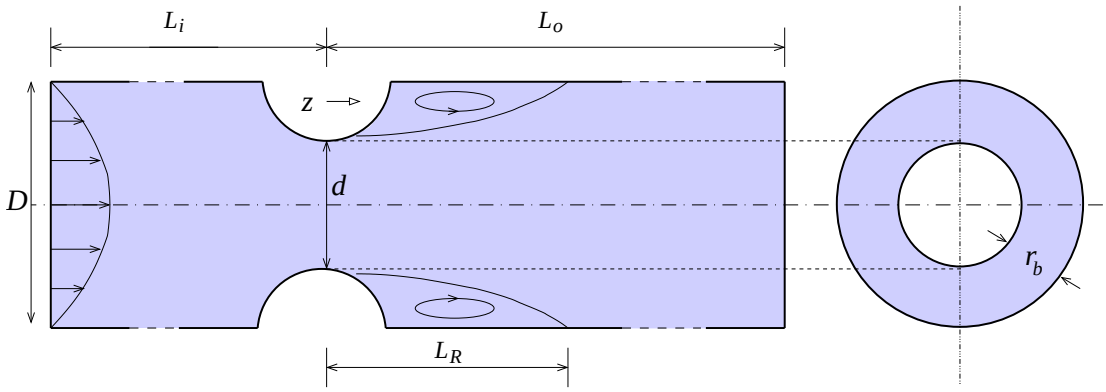

FIGURE 3.3: Schematic of the axisymmetric stenotic geometry

as $r_b = (D-d)/2 = \frac{D}{2}\left(1-\sqrt{1-b}\right)$. The Reynolds number is defined as,

$$Re = \frac{\overline{U}D}{\nu}, \tag{3.23}$$

where $\overline{U}$ is the sectionally-averaged fluid velocity, D the tube diameter and ν the kinematic viscosity. We examine flows ranging from Reynolds numbers of 50 to 2500 with blockage ratios from 0.2 to 0.95.

3.2.2.1 Boundary conditions

On the blockage surface and the cylinder walls, no-slip conditions were imposed. At the inlet boundary, an equilibrium Hagen-Poiseuille profile was prescribed. The velocity is given by

$$u(r) = -\frac{dp}{dz}\frac{1}{4\mu}\left(\frac{D^2}{4} - r^2\right) \tag{3.24}$$

where $\frac{dp}{dz}$ represents the pressure gradient in the tube, with the centreline of the tube at $r = 0$ and the tube walls at $r = D/2$, (White 1999). At $r = 0$, we obtain the maximum velocity

$$u_{max} = -\frac{dp}{dz}\frac{D^2}{16\mu}. \tag{3.25}$$

The flow rate in the tube is given as $Q = \int_0^{D/2} u(r)dA$, where A is the cross-sectional area of the tube. Hence,

$$Q = \int_0^{D/2} u_{max}\left(1 - \frac{4r^2}{D^2}\right)2\pi r dr = u_{max}\pi D^2/8. \tag{3.26}$$

Therefore, the average velocity, defined as $\overline{U} = 4Q/\pi D^2$ is one half of the maximum velocity, giving the profile implemented in the simulations as

$$u(r) = 2\overline{U}\left(1 - \frac{4r^2}{D^2}\right). \tag{3.27}$$

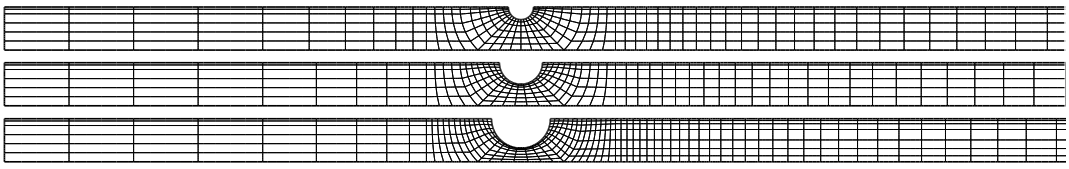

FIGURE 3.4: Test sections of three of the meshes constructed for the steady axisymmetric simulations. From top to bottom, $b = 0.50, 0.75$ and 0.90.

At the outflow boundary far downstream, the standard zero normal velocity gradient condition was imposed.

3.2.2.2 Mesh layout and resolution

Seven meshes were constructed at blockage ratios of $b = 0.20$, 0.40, 0.50, 0.60, 0.75, 0.90 and 0.95. Figure 3.4 shows the test sections of three meshes at $b = 0.50$, 0.75 and 0.90. The same macro-element resolution was retained across the blockage ratio range; however, it was found that at the higher end of the blockage ratio range, a greater resolution was required. Of course, this is not surprising given the increased velocity gradients caused by the fluid squeezing through ever smaller throats. The same basic mesh layout was used for each grid, with the macro-element distribution more highly concentrated near the cylinder walls and through and immediately downstream of the blockage. The resolution was decreased downstream to the outlet boundary.

A grid resolution study was undertaken. The final internal grid resolution used for most simulations was $n = 7$, or 49 nodes per element, with no marked differences observed between predictions from simulations at this resolution and those for $n = 6$. For higher blockages and Reynolds numbers, elements of order $n = 8$, comprising 64 nodes per element, were employed to properly resolve the more strongly-varying regions of the flow field. Convergence tests were performed on three of the meshes, at $b = 0.50$ and $Re = 2000$, $b = 0.75$ and $Re = 800$ and $b = 0.90$ and $Re = 500$, the results of which are shown in table 3.2. The table plots the convergence of the growth rate of the most unstable mode from the linear stability analysis, outlined in section 3.1.2, and of the normalised length of the steady recirculation zone, which appears in the flow immediately downstream of the blockage. The inlet length used for all meshes was $L_i = 6D$, while the outlet length L_o, varied according to the blockage ratio. At low blockage ratio, the outlet length used was $40D$, increasing to $50D$ at $b = 0.60$, $75D$ at

	Re=2000, b=0.50		Re=800, b=0.75		Re=500, b=0.90	
n	L_R/D	σ	L_R/D	σ	L_R/D	σ
5	7.413	-0.012536	18.398	0.0037702	-	-
6	7.362	-0.014418	18.378	0.0032027	41.399	0.0085549
7	7.353	-0.014795	18.376	0.0031348	41.401	0.0083672
8	7.355	-0.014779	18.375	0.0031348	41.404	0.0083672
9	7.356	-0.014783	18.377	0.0031348	41.405	0.0083752

TABLE 3.2: Convergence of the normalised initial recirculation length, L/D, and maximum growth rate, σ, across three blockage ratios with increasing polynomial order.

$b = 0.75$ and $100D$ at $b = 0.90$. These lengths were found to be more than sufficient to remove any artificial boundary effects from either the inlet or outlet.

3.2.3 Numerical pulsatile flow

Similar to the steady flow, pulsatile flow consists of a net positive flow, but with a harmonic component added on. Numerically simulating a pulsatile flow presents a number of challenges, the greatest being the implementation of a pulsatile inlet boundary condition. The Reynolds number is defined in the same manner as that for steady inlet flow, according to equation 3.17, where $\overline{U}$ is considered a temporal average of the cross-sectional area average of the fluid velocity, $\overline{u}(t)$. In equation form, $\overline{U}$, for both steady and pulsatile flow, is defined as

$$\overline{U} = \frac{1}{T}\int_0^T \overline{u}(t)\,dt = \frac{8}{D^2T}\int_0^T\int_0^{D/2} u(r,t)\,r\;dr\,dt, \tag{3.28}$$

where T is the period of the pulsation. In this manner, the steady flow becomes a limiting case of the pulsatile flow, as the amplitude of the pulsation approaches zero.

Two extra parameters need to be considered with the pulsatile flow, the pulse period and the pulse amplitude. These two parameters define the velocity waveform. In this study, a single-harmonic sinusoid added onto a steady mean flow is used.

The frequency parameter used is the period of the pulsation, T (non-dimensionalised by $D/\overline{U}$). In most previous works on pulsatile flow the Womersley number ($\alpha = R\sqrt{\frac{\omega}{\nu}}$) is taken as the principal frequency parameter. The Womersley number can characterise a large range of real, physiological arterial flow configurations. Typically, flows in larger arteries correspond to Womersley numbers between 10 and 20, while less than 10 corresponds to flow further downstream in the cardiovascular system, in

the smaller arterioles and capillaries. Therefore, the value of the Womersley number is a useful indicator as to the physiological relevance of any flow configuration one may be investigating. However, the fact that it is not independent of the Reynolds number means that its use as a frequency parameter for a fluid mechanical investigation is not ideal. In their recent work on pulsatile flows, Sherwin & Blackburn (2005) introduced a reduced velocity as a more suitable frequency parameter, which is in effect the same quantity as the non-dimensionalised pulsation period used in this study. The non-dimensionalised period, T, is related to the Womersley number by the relation $T = \pi Re/(2\alpha^2)$; or in the dimensional form $T_D = \pi DRe/2\overline{U}\alpha^2$.

The other new parameter is the pulse amplitude, A. This amplitude refers to the maximum variation of the velocity from its mean value of $\overline{U}$. Hence, an amplitude of $A = 1$ would oscillate between a maximum of $2\overline{U}$ and a minimum of 0. Accordingly, any waveform of amplitude $A > 1$ would have a minimum velocity $\overline{u}(t)$ of less than 0, in effect producing a reverse flow for a given interval of the pulse period.

3.2.3.1 Pulsatile boundary condition: Womersley's solution

The boundary conditions for the pulsatile flows are the same as those for the steady, excepting the inlet and outlet; these two are both implemented according to Womersley's analytical solution of pulsatile flow in arteries (Womersley 1955). A thorough discussion of the Womersley solution and the resulting velocity profile behavior can be found in Loudon & Tordesillas (1998), which was included in the literature review of the previous chapter (see figure 2.1). The Womersley solution represents a fully-developed and periodic solution for flow subject to a periodic pressure gradient. All pulsatile simulations were run using a single sinusoidal frequency. Although the Womersley solution can be used to calculate solutions for pressure gradients of multiple harmonics, in this work our forcing is restricted to a single sinusoidal harmonic. As discussed in chapter 2, the time-dependent complex solution to the local velocity for pulsatile flow is given by equation 9 of Womersley (1955)

$$u(r,t) = \frac{A}{\rho}\frac{T}{2\pi i}\left(1 - \frac{J_0(\alpha r i^{3/2}/R)}{J_0(\alpha i^{3/2})}\right)\mathrm{e}^{2\pi i t/T}, \tag{3.29}$$

where A is the magnitude of the pressure gradient, R is the radius of the tube, $i = \sqrt{-1}$, α is the Womersley number, $\alpha = R\sqrt{2\pi/T\nu}$, and J_0 represents a complex Bessel

function of order zero. In order to implement this equation in our boundary condition, we take the real part of this equation. This is given by equation 17 in Womersley (1955):

$$u(r,t) = \frac{M}{\rho\nu}\frac{R^2}{\alpha^2}M_0' \sin(\frac{2\pi t}{T} + \phi + \epsilon_0), \tag{3.30}$$

where M is the real part of the amplitude of the pressure gradient and ϕ constitutes a phase correction. The calculation of these two terms will be dealt with shortly. The calculation of the terms M_0' and ϵ_0 are both dependent on the Bessel functions found in equation 3.29. If we write the solutions of the two Bessel functions in terms of their modulus and phase, we have

$$J_0(\alpha r i^{3/2}/R) = M_0(r/R)\mathrm{e}^{i\theta_0(r/R)}, \tag{3.31}$$

where the modulus is given by $M_0(r/R)$ and the phase by $\theta_0(r/R)$ both of which vary with r/R. Similarly, the modulus and phase of the radially independent Bessel function of equation 3.29 can be written as M_0 and θ_0. For ease of calculation, two new terms are introduced, $\delta_0 = \theta_0 - \theta_0(r/R)$ and $h_0 = \frac{M_0(r/R)}{M_0}$, which represent the division of the two Bessel functions. M_0' and ϵ_0 are then defined as

$$M_0' = \sqrt{1 + h_0^2 - 2h_0\cos\delta_0}, \tag{3.32}$$

$$\tan\epsilon_0 = \frac{h_0\sin\delta_0}{1 - h_0\cos\delta_0}. \tag{3.33}$$

We then have all the terms needed to calculate $u(r,t)$. This solution, being linear, is then simply added on to the Hagen-Poiseuille velocity profile given earlier. The terms ϵ_0 and M_0' are independent of time and dependent on radial position. The dependence of ϵ_0 on r means that the phase of the motion in fact varies as we move from the centre of the tube to the walls. This accounts for the behaviour seen in pulsatile flows, where the development of the boundary layer over one pulse period leads to a phase lag which is more apparent the closer we are to the wall and the higher the Womersley number. Averaged over the cross-sectional area of the tube, this leads to a general phase lag in $\overline{u}(t)$, dependent on α.

In calculating the parameters for numerical simulations, we would initially use a phase correction of $\phi = 0$. Using a secant root-finding method, the phase lag of $\overline{u}(t)$ can be easily determined. The correction, ϕ, can then be set to a value such that $\overline{u}(0) = \overline{U}(1 + A)$, or that the velocity in the tube is at a maximum when $t = 0$. In a

similar fashion, an initial test with an arbitrary pulse amplitude of unity would yield an erroneous maximum velocity. The pulse amplitude could then be corrected, by making $M = A/(\overline{u}(0) - \overline{U})$. This was found to be the simplest and most easily-implemented method of calculating the pulse amplitude.

Womersley's solution, as well as the accuracy of the calculation, was verified by simulating the pulsatile flow in a straight, unblocked tube; the accuracy was confirmed in observing that the converged solution was entirely parallel over the length of the tube ($du/dz = 0$).

3.2.4 Mesh layout and validation: pulsatile flow

For pulsatile flow, it was found that a greater element concentration is required than that used in the steady inlet simulations. Whereas the steady flow consists of a fully developed time-independent flow field, the pulsatile flow in such a geometry involves a constantly developing boundary layer. At higher Womersley numbers, velocity profiles become flatter, approaching a plug flow. This results in a higher velocity gradient perpendicular to the tube walls than is found in a fully-developed Hagen-Poiseuille flow. The increased concentration was required mostly within the contraction.

New meshes were created to simulate the pulsatile flows, at blockage ratios of $b =$ 0.20, 0.40, 0.50, 0.60, 0.75 and 0.90. For the mesh constructed corresponding to a blockage ratio $b = 0.90$, a much higher spatial and temporal resolution than for the steady flow case was needed to adequately resolve the flow. Therefore, simulation of pulsatile flows at $b = 0.90$ required much larger computational times than those at lower blockage ratios. As a result of this, the parameter space at $b = 0.90$ was not explored as extensively. Rather, due to the prohibitive computational time needed, only a limited number of flow configurations were simulated at $b = 0.90$; these were mostly chosen to match and compare with configurations tested experimentally.

Figure 3.5 shows three of the meshes used. Essentially, these are the same meshes as those used for steady flow, only with a greater grid concentration. The same inlet and outlet lengths were retained. The outlet lengths chosen for the meshes were originally calculated with pulsatile flows in mind, the lengths in fact being far greater than required for steady flow. The lengths used are similar to that employed by Sherwin & Blackburn (2005), whereby a maximum length is calculated heuristically, by deter-

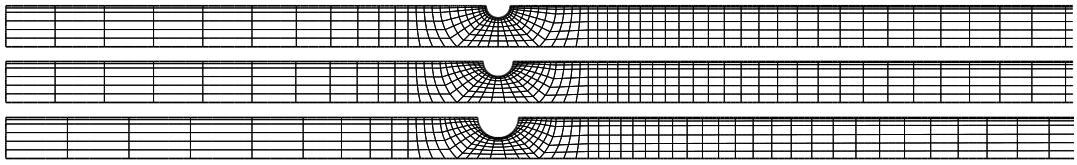

FIGURE 3.5: Test sections of three of the meshes constructed for pulsatile flow. Meshes are essentially the same as those used for steady flow, only with a greater element concentration within the blockage. From top to bottom, $b = 0.50, 0.60$ and 0.75.

	b=0.50	b=0.60	b=0.75
n	$\|\mu\|$	$\|\mu\|$	$\|\mu\|$
5	1.1726	1.3763	1.4898
6	1.1725	1.3763	1.4953
7	1.1728	1.3765	1.4942
8	1.1716	1.3761	1.4940
9	1.1708	1.3761	1.4948
10	-	1.3760	1.4955

TABLE 3.3: Convergence of the Floquet multiplier, μ, with polynomial order, n, for the azimuthal $m = 1$ mode, across three blockage ratios. All three tests were performed with $Re = 300$ and $T = 2.5$, and with an amplitude of pulsation higher than the critical pulsation amplitude A_c, as discussed in chapter 6 (i.e., at $b = 0.50$, $A = 1.25$, at $b = 0.60$, $A = 1.00$ and at $b = 0.75$, $A = 0.75$).

mining the length to which a flow might propagate, given the pulse period and flow acceleration through the stenosis.

A resolution study was conducted on the new meshes, the results being shown in table 3.3. The absolute value of the Floquet multiplier at the leading azimuthal mode in each case was chosen as the most convenient characteristic with which to measure the convergence. The three cases shown were conducted at $Re = 300$ and $T = 2.5$ and then with a pulse amplitude, A, taken from the higher end of the range of values studied. The convergence in each case is good, each multiplier at the maximum nodal concentration being within 0.2% of the multiplier calculated at $n = 6$. All the pulsatile flows simulated in this study were run using a nodal concentration of 49 (7 x 7) nodes per element, or $n = 7$.

For all the pulsatile simulations, a time step of $\triangle t = 0.00025$ was employed. The dependence of the flow on the time step was also tested. Figure 3.6 plots the variation of the Floquet multiplier for the leading instability mode at blockage ratio $b = 0.75$,

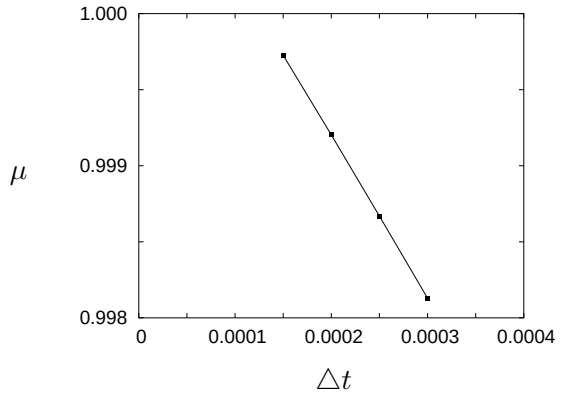

FIGURE 3.6: Dependence on time step of the Floquet multiplier, μ, of the leading perturbation mode ($m = 1$) at blockage ratio $b = 0.75$, Reynolds number $Re = 260$, pulse amplitude $A = 0.75$ and pulse period $T = 2.5$.

Reynolds number $Re = 260$, pulse amplitude $A = 0.75$ and pulse period 2.5. The flow is near the critical Reynolds number. There appears to be a linear dependence of the Floquet multiplier on the time step. If we extrapolate this plot to $\triangle t = 0$, we find a multiplier $\mu_{\triangle t=0} = 1.00130$. All the simulations for pulsatile flow in this study have been run at a minimum time step $\triangle t = 0.00025$. If we consider the error between the Floquet multiplier at $\triangle t = 0.0025$, and our extrapolated value at $\triangle t = 0$, we find a percentage error of 0.26%, which is small enough to be considered negligible.

3.3 Experimental method

In this thesis, experimental and numerical methods have been employed. This section outlines the experimental apparatus and analytical techniques used to obtain the experimental results for flows through axisymmetric stenotic geometries, an example of which has been given in figure 3.3.

3.3.1 Description of the apparatus

An experimental rig was constructed to investigate the flow for the geometry outlined in figure 3.3. A schematic of the rig design is shown in figure 3.7. The apparatus essentially operated as a closed circuit, with a pump supplying a reservoir which provides a constant pressure to the test section. The working fluid was the tap-water of Marseille, with a small amount of chlorine added. The test section consisted of a transparent perspex tube of 20 mm diameter, with inlet and outlet lengths of 2000 mm, or $100D$.

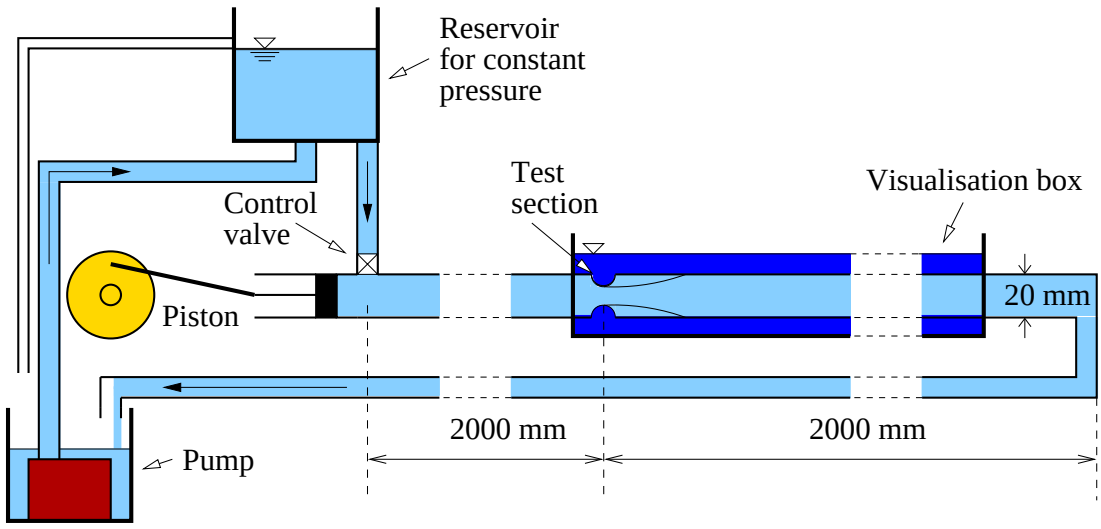

FIGURE 3.7: Schematic of the experimental rig constructed for the axisymmetric stenotic geometry of figure 3.1. The inlet and outlet lengths have been truncated.

This provided a fully-developed Hagen-Poiseuille flow at the test section. As for the meshes constructed for the numerical simulations, the long outlet length allowed the blockage to be isolated and restricted any end effects. The three removable blockage sections constructed corresponded to blockage ratios of $b = 0.50, 0.75$ and 0.90, and are shown together in figure 3.8. In the experimental rig, the stenoses were located at the downstream end of the removable blockage section; therefore, the transparent perspex tube, and hence the observable part of the flow, began immediately downstream of where the stenoses curve rejoined the tube wall, or at $z/D = r_b$. The blockage sections served as the link between the inlet and outlet lengths of tube. The axial compression of the outlet tube with the blockage section could be adjusted as needed. To remove the blockage section, the outlet tube was loosened and slipped off the blockage section, which was then worked off the inlet tube. Interference fits were used between the blockage section and the inlet and outlet tubes. Blockage sections were often warmed before being placed; considerable force also needed to be applied in removing them.

Viewing fluid through a curved surface such as the tube wall in our experiment causes significant refraction. To counter the distorted view of the internal fluid that such results from such refraction, the blockage section, outlet length and 15 diameters of the inlet length ($-15D \lesssim z/D \lesssim 100D$) were immersed in water. This was achieved by the construction of a perspex visualisation box, (shown in figure 3.7) which allowed the

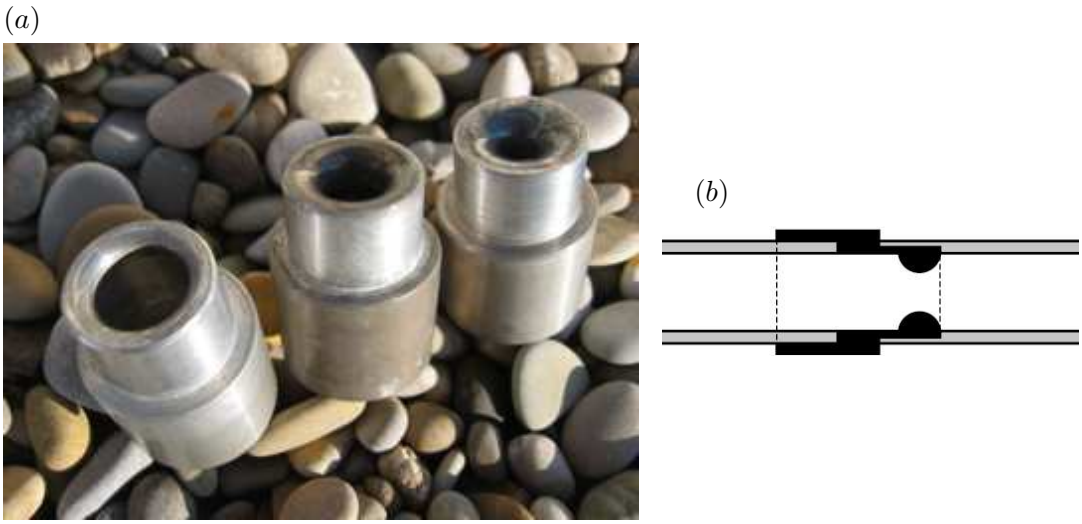

FIGURE 3.8: (a) Photo of the three removable blockage sections constructed for the experimental rig. From left to right, the blockages correspond to $b = 0.50$, 0.75 and 0.90. A small portion of the curve of the stenoses inside each section can be discerned. (b) Schematic of the removable blockage section.

experimenter to view the fluid inside the tube through a plane surface. When viewed perpendicularly, a largely undistorted view of the flow in the tube was provided.

The fluid circuit was driven by a pump, mounted inside a water receptacle on the floor, which supplied an elevated water reservoir. The concept of the elevated water reservoir is shown in the sketch of figure 3.9. The reservoir, located approximately two meters above the test section, served to provide a constant pressure to the test section. This was achieved by the placement of two walls inside the reservoir at different radii, effectively creating three chambers. The middle chamber was supplied directly by tube from the pump three meters below. This central chamber, after having filled, overflowed and filled the second chamber. The overflow of the second chamber into the third chamber led directly back down to the receptacle containing the pump. The second chamber, having a constant water level, supplied the test section. This allowed the velocity of the fluid in the tube – and therefore the Reynolds number – to be adjusted as needed via a control valve located before the entry into the inlet tube. The fluid velocity in the tube, $\overline{U}$, was measured by means of a stopwatch and a weight scale, correct to 0.01 grams. The temperature and density of the fluid were regularly measured by means of a meter which could extract a sample of the working fluid; it gave the temperature correct to 0.1 of a degree Celsius and the density to 0.001

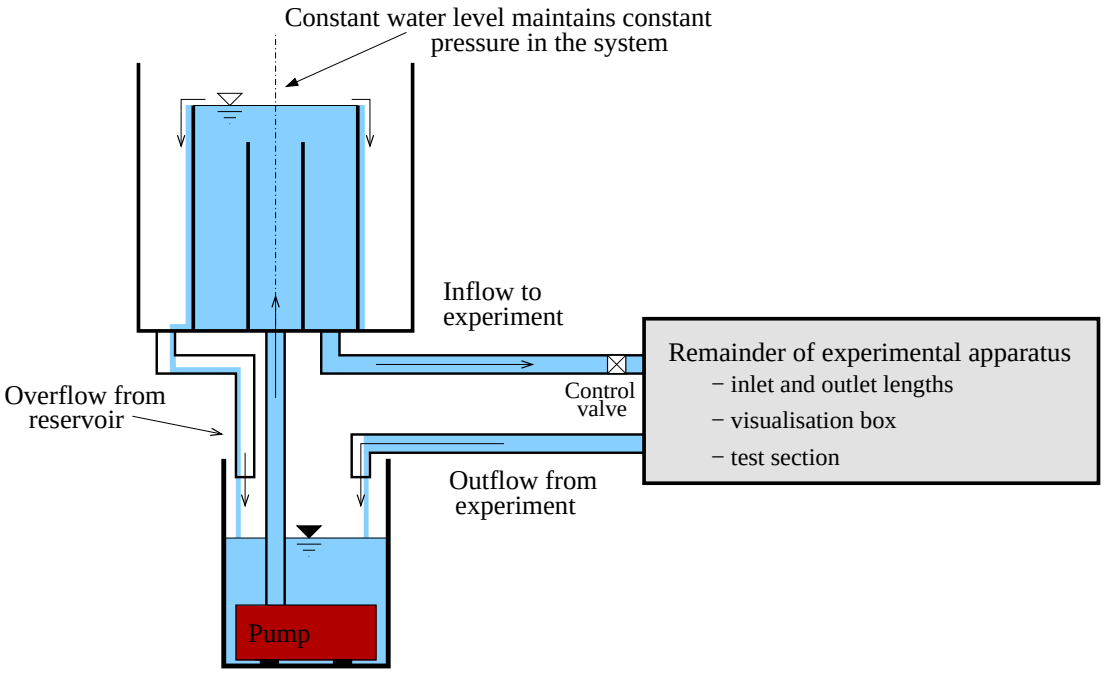

FIGURE 3.9: Sketch of the water reservoir used in the experimental reservoir. The reservoir maintained a constant water level, hence a constant supply pressure to the rig.

gm/cm^2. The outflow from the experiment was collected over one minute, weighed and then replaced in the water receptacle. For pulsatile flows, the measuring period was adjusted, if needed, to be in phase with the period of the pulsation. The velocity could then be adjusted via the control valve and then checked again to obtain the required Reynolds number.

The pressure created by the water reservoir was much greater than the pressures required in the test section to create the flows needed. This high pressure reservoir had two advantages for the experiment. Firstly, it allowed the system to be effectively flushed, by opening the control valve so the reservoir could be emptied into the system, providing a high Reynolds number flow to the test section for the duration of 10 to 15 seconds. This flushed the system of any air bubbles which may have formed, as well as move on – or at least re-agitate – debris in the system, including any settled PIV particles. The second advantage conferred by the high pressure difference between the reservoir and test section was that the action of any applied pulsation or periodic forcing would be translated downstream through the test section, and not upstream to the reservoir. This is important for the generation of periodic flows by the piston shown in figure 3.7.

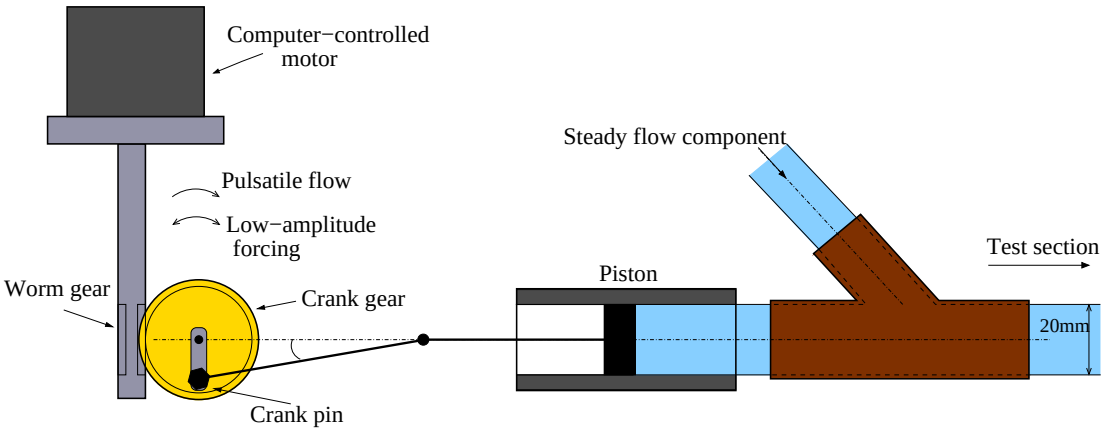

FIGURE 3.10: Schematic of the piston apparatus, added to the experimental rig in order to generate pulsatile flows of a wide range of amplitude and frequency.

The piston was added at the junction immediately downstream of the control valve, a sketch of which is shown in figure 3.10. The piston allowed the examination of flows subject to a high-frequency forcing, as discussed in section 5.3.2, and of pulsatile flow; that is, flows comprising a steady flow with a large amplitude periodic pulse added. As mentioned earlier, the pressure supplied by the water reservoir, shown in figure 3.9, was much larger than the pressure required at experimental running conditions. At running conditions, the control valve was only opened by a small amount, thus creating a large pressure drop across the control valve.

The motion of the piston was generated by a worm gear (gear ratio 70:1) and crank arrangement, translating the circular motion of the motor to a reciprocating piston motion. As the crank rotates, the movement of the crank pin away from the piston/tube centreline creates a small error in the translation of the circular motion to the linear piston motion. The design of the piston ensured this error remained negligible, with the angle of the rod to the piston/tube centreline not exceeding 8 deg with the crank pin at its maximum radial position. The motion of the worm was determined by a computer-controlled motor and could be programmed to produce a wide variety of motions. The motor could easily generate a constant angular velocity, but could also be programmed to generate more sophisticated motions, such as sinusoidally-varying angular velocities.

To generate high-amplitude, low-frequency oscillations, a constant angular velocity was supplied by the worm, thereby creating the single harmonic sinusoidal oscillation required. The frequency of the oscillation could be adjusted by directly varying the an-

gular velocity of the motor, according to the gear ratio. The amplitude of the pulsation could be adjusted by varying the radial position of the crank pin, this relating directly to the extent of the linear motion of the piston. The required stroke length, S_P, of the piston could be calculated by integrating the harmonic component of the velocity waveform and taking the amplitude of the resulting position waveform. Therefore, the stroke length was given by

$$S_P = \frac{A\overline{U}T_D}{2\pi}, \tag{3.34}$$

where T_D is the dimensional form of the pulse period; or, in terms of the non-dimensionalised period

$$S_P = \frac{ATD}{2\pi}. \tag{3.35}$$

The crank pin could then be set at the appropriate radius. Therefore, in creating a pulsatile flow, the desired period was set by the motor, followed by the stroke length of the piston. Due to its dependence on the pulsation amplitude A, the average fluid velocity $\overline{U}$ and the period of the pulsation, T_D, the stroke length was always calculated and set last.

The accuracy of the generated pulsatile flow was checked by again measuring the fluid velocity, and verifying the stroke length of the piston. Further validation was performed by taking PIV measurements of the resulting velocity profiles in an unblocked portion of the tube. The results of the PIV validation is included in chapter 6 of the thesis.

To generate low-amplitude high-frequency oscillations, a slightly different approach was taken. For such flows, the worm could not be driven fast enough, nor the small required crank pin radial position accurately enough set to generate the pulsation in the same manner as for the large-amplitude pulsatile flows. Therefore, rather than creating the pulsation with entire turns of the crank gear, the oscillation was generated instead by sinusoidally varying the angular velocity of the worm. This could be programmed relatively easily with the software controlling the motor. The resultant motion of the crank gear was a backward/forward motion, which, with the crank pin at its maximum radial position and the crank gear at the position shown in figure 3.10, created the required low-amplitude high-frequency linear motion. In this manner, the frequency and amplitude of the pulsation were set directly by the motor. The waveform produced

by the motor could be precisely controlled.

The amplitude of the pulsation is related to the amplitude of the variation of the angular displacement of the crank gear θ_s. With a pulse/perturbation amplitude A and period T_D, the amplitude θ_s, was given by

$$\theta_s = \tan^{-1}(\frac{A\overline{U}T_D}{2\pi r_c}), \tag{3.36}$$

where r_c is the radius of the crank pin position. After correcting for the gear ratio, the amplitude of the motor sine wave could then be set. Using this technique, a perturbation of a precise amplitude consisting of only a single harmonic could be accurately applied. The only source of error was the small give between the crank gear and the worm, which produced a slight error every time the worm angular velocity changed direction. However, the effect on the final perturbation waveform was not significant.

3.3.2 Diagnostic techniques

The two main diagnostic techniques employed in obtaining the experimental results of this research were coloured dye visualisations and particle image velocimetry (PIV), descriptions of which are given in this section.

3.3.2.1 Coloured dye visualisation

Coloured dye visualisation is a technique whereby a coloured second fluid is injected into the flow. The dye then becomes a part of the flow under investigation; however, the contrast in colour of the dye to the working fluid can provide information on the flow. The technique is useful in producing attractive and illuminating flow visualisations; use of the same technique as used in this thesis can be found in Leweke, Thompson & Hourigan (2004) and Meunier & Leweke (2001). While appearing at least qualitatively similar to streamlines, the dye in fact forms streaklines. A streakline can be thought of as the locus of all the fluid particles that have passed continuously through a particular point in the spatial domain. The technique cannot give velocity field data, but does give the observer, at the very least, an idea of the flow behavior. Also, depending on the flow under investigation, it can provide some quantitative data; however, it is primarily a qualitative technique.

For the visualisations presented in this thesis, the dye used is a fluoresceine solution, which is yellow-coloured dye. When illuminated by a blue laser, the dye turns a bright

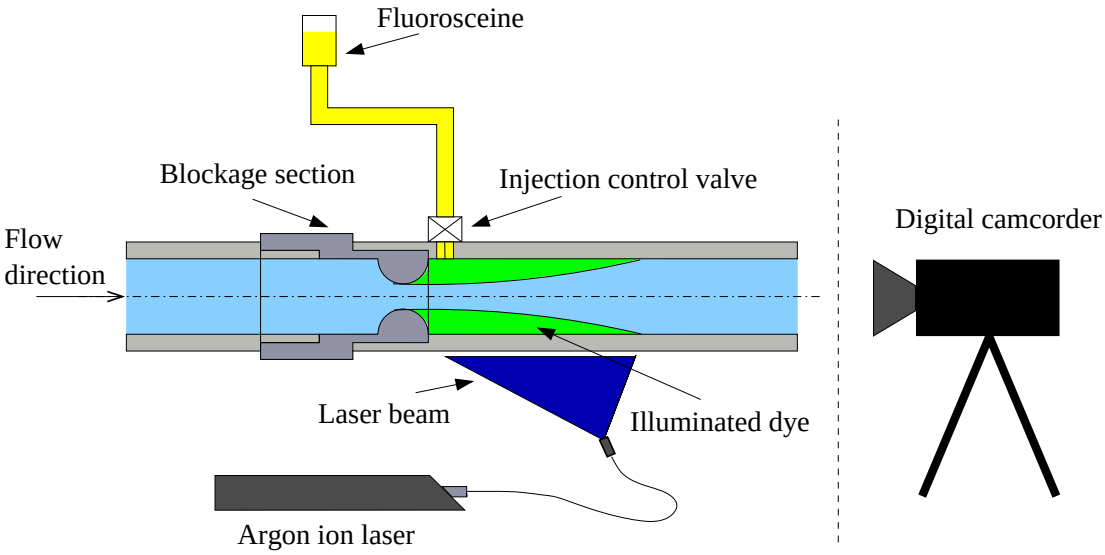

FIGURE 3.11: Sketch of the coloured dye visualisation technique, as well as of the blockage section design.

green. The laser used to highlight the dye is a continuous ion laser (Spectra Physics, model Stabilite 2017), having a total light power of 6.0W, with the power of the 488 nm ray which excites the fluoresceine at 1.5W. The laser is set beneath the test section and formed into a flat plane illuminating a single plane of the test section. With the laboratory lights dimmed, a contrast is then seen in the visualisations between the fluorescent green of the dye and the black of the uncoloured fluid.

Figure 3.11 presents a description of the experimental setup used to produce the coloured dye visualisations. A fluoresceine reservoir was set approximately one metre above the test section; this created the required pressure to inject the dye into the tube. A valve placed at the injection point provided control of the dye flow. The first injection point was attempted far upstream of the blockage, in the inlet section of the tube. However, it was found that injecting the dye upstream of the blockage was not practical. The dye would follow the behavior of the Poiseuille velocity profile, travelling quickly in the middle of the tube and slowly near the tube wall. At the blockage section, the dye would be located entirely around the centreline of the tube, passing straight through the blockage and failing to illuminate any noteworthy feature of the flow. The injection point had to be placed in the tube wall immediately downstream of the blockage. This allowed the dye to be distributed across the entire diameter of the flow region of interest. More interesting features of the flow, such as recirculation zones and

downstream vortex formations, could now be observed.

The disturbance that the injection point caused on the flow was minimal, the drilled hole being approximately 0.2 mm in diameter. At running conditions and after injection the fluoresceine flow was blocked; the hole in the tube wall was then replaced by a fluid boundary of zero net flow rate. In addition, in the immediate vicinity of the injection point, the flow was generally characterised by a low velocity recirculation zone; hence, the disturbance of the injection point on the flow could be considered negligible.

The injection of the dye was turbulent, rapid and at high velocity, significantly perturbing the flow. The flow would then be left alone until the unsteadiness caused by the injection had convected away downstream and the steady flow re-established. For analysing steady flow the technique was ideal, in that a large quantity of dye would become trapped in the recirculation zone downstream of the blockage. A high contrast was observable between the dye in the recirculation zone and the clear fluid arriving from further upstream. For stable flows, the dye could remain in the recirculation zone for extremely long time scales. For pulsatile flow, the same procedure was followed, with the pulsation of the piston being started after the steady flow had re-established. The dye trapped in the steady recirculation zone would then highlight the features of the pulsatile flow. However, due to the washing effect of pulsatile flow, after relatively short time scales the dye would be entirely convected downstream. Depending on the flow configuration under question, the dye was observable from 5 to 20 pulsation periods after the start of the piston pulsation. Results of dye visualisation for pulsatile flows therefore had to be taken a relatively short time after the commencement of the pulsation, which was not ideal, as it was possible that features of the observed flow could be artifacts of the start-up flow.

3.3.2.2 Particle image velocimetry (PIV)

The flow was quantitatively measured using particle image velocimetry (PIV), a technique whereby the displacement of small particles seeded in the fluid flow is used as an indication of the local fluid velocity. In this manner, the technique provides instantaneous velocity fields. A summary of the technique and software used is included in this section, although a more detailed description can be found in Meunier & Leweke (2003).

The flow field was seeded with tracer particles and photographed twice, at a known interval $\triangle t$. The particles were illuminated at each instant by a short-duration laser pulse. A camera was synchronised with the laser pulses to take the images as the flow field is illuminated. For the PIV results presented in this thesis, the laser pulses were provided by a pair of ND-YAG pulsed lasers (Newport, pulse energy approximately 18 mJ), while a black and white digital camera (ROPER Megaplus ES4.0, 8-bit resolution, 2000×2000 pixels) captured the images.

The major features of the image processing and PIV software are summarised here. The domain in each image was divided into interrogation windows. The particle density and window resolution was configured to produce an average of approximately 10 particles per window; further discussion of the optimum particle density can be found in Meunier & Leweke (2003). The software, by a cross-correlation algorithm, calculated the displacement of the particles between the two images and deduced the velocity field from the relation $u = v_p \triangle t$, where v_p is the velocity of the particles in the interrogation window. The algorithm used Fast Fourier Transforms (FFT) to calculate the cross-correlation functions on a window between the two images, whose maximum peak gives the average displacement of the particles in the interrogation window. By translating the windows in a second calculation run, the in-plane loss of pairs error was reduced. A further explanation of this technique is given in Westerweel (1997). An estimation of the sub-pixel displacement was achieved by applying a Gaussian fit to the peak of the cross-correlation function. The bias resulting from the use of the FFT was also reduced by increasing the cross-correlation function on the edges of the interrogation windows. More details of these techniques can be found in Raffel, Willert & Kompenhaus (1998).

The software also had several other features which improved the accuracy when high velocity gradients were present in the flow. The principal feature was the deformation of the interrogation window according to its corresponding velocity gradient (Huang, Fiedler & Wang 1993). This deformation was determined in a first calculation run, in which an estimate of the velocity field was calculated, according to which the windows were deformed. This improved the accuracy of the second run, which was also calculated at a higher spatial resolution. Further to this, the initial shape of the interrogation windows was altered to match the nature of the flow under investigation. Since the largest velocity component of the vast majority of the flow was in the axial direction,

the length of the interrogation windows was increased. The aspect ratio of the windows was set at 4, with the longer side of the window being aligned parallel to the tube walls. This technique led to an improved resolution of the radially-varying features of the flow.

For the current PIV set-up, the lasers were set in the same manner as for the coloured dye visualisations. 18 μm silver-coated hollow glass spheres were mixed with a surfactant before being added in the working fluid. Several idiosyncrasies of the experiment and the flow affected the accuracy and usefulness of the PIV method. Firstly, in pipe flow, the tracer particles tend to migrate towards the centreline of the tube. Generally, this caused a lower particle density in the near-wall vicinity, which reduced the accuracy of the method. Secondly, the curved surface of the tube caused several reflections and refractions. In the coloured-dye visualisation, this can be seen as a light blue shade, visible at the bottom of some of the visualisations presented in this thesis. Due to the stronger laser pulse used for the PIV, this reflection/refraction effect was much greater. It manifested as a bright region on the portion of the tube wall at the bottom of the PIV image. This region could be removed from the calculation of the velocity field; however, this resulted in a loss of particle information.

Aspects of the flows under investigation also limited the usefulness of the PIV method. For steady flows, averaging could be performed, whereby the results of a series of PIV results were averaged, reducing the noise error of the PIV method. Similarly, for stable and periodic pulsatile flows, the results could be phase-averaged, whereby results from the same phase over many time periods were averaged. Such averaging techniques were effective in producing reasonably accurate velocity field measurements; however, whenever the flow was unstable or not periodic, averaging became problematic and unsteady regions of the flow would simply average out to zero. In these cases, meaningful results could only be extracted from single PIV images, the accuracy of which were not reliable, especially in unsteady regions of the flow where the high spatial velocity gradients rendered the method less accurate in any case. Therefore, the majority of PIV results presented in this thesis are of stable or wholly periodic flows, these being the only flows which the method was capable of measuring with sufficient accuracy.

3.3.3 Optimisation of the apparatus

Much work was carried out in reducing the noise, vibration and sources of error in the system. There are several sources of noise in the experiment. From the surrounding environment, vibrations could be transmitted through the laboratory floor (flows on the threshold of stability could be perturbed by as little as a shift of weight from one foot of the experimenter to the other). From within the experiment there were several sources, the principal being the pump which drove the circulation through the experiment. The pump was isolated as much as possible, with padded supports being provided to the water receptacle containing it. Also, it was ensured that none of the inlet tubes to the test section were in contact with the tubing which supplied the reservoir. Therefore, the only points of contact were the tube connecting the pump with the reservoir and the water receptacle through the floor. Although the effect of this noise could be minimised, it was impossible to completely isolate. Another source of vibration was the motor driving the piston, although this was small compared to the main pump.

Imperfections within the experiment were another source. During the commissioning of the experimental rig, much effort was invested in ensuring the correct alignment of the 4 metres of straight tube upstream and downstream of the test section, including the use of a laser level. Filters and honeycomb were placed immediately downstream of the flow control valve in order to smooth the flow before its entry to the inlet section. Another source of error was in temperature differences existing within the rig.

This difficulty arose from the difference in temperature between the water inside the tube and the water around the tube, inside the visualisation box. Any temperature difference had an effect as soon as the flow reached the point at which the tube entered the visualisation box and was immersed – the blockage section began approximately 15 diameters downstream of the visualisation box entry point. Generally, the water in the tube was warmer than the water in the visualisation box, due to the pump which would slowly heat the working fluid as the experiment ran. For the steady flow at very low Reynolds numbers – when the flow had a longer resident time in contact with the tube walls – the error introduced by the temperature difference could be seen downstream of the blockage. Depending on the sign of the temperature difference, the heating or cooling of the flow through the tube walls was most pronounced on the part of the

flow that remained in contact longest with the tube walls; namely, the recirculation zone which appeared just downstream of the blockage. For steady flow at low Reynolds numbers, particularly at $b = 0.90$, a strong temperature difference could produce a loss of symmetry of the jet. Depending on the sign of the temperature difference, the jet would either "sink" or "rise". Fluid cooled by the tube walls would sink, causing a recirculation zone which was longer on the bottom side than on the top. A temperature difference of the opposite sign would produce the opposite effect. At higher Reynolds numbers, above $Re \approx 300$, the effect was not strong enough to have any observable effect, the flow moving too rapidly away for there to be any significant heat transfer. For steady flow, this effect could be managed relatively easily by placing small quantities of very hot water into the visualisation box to bring it to the temperature of the working fluid. Although requiring some delicate handling, with practice this was a method with which the experimenter could become highly proficient.

The effect of the temperature difference became more difficult to manage for pulsatile flow. The nature of the flow (isolated vortex rings forming downstream of the blockage and convecting downstream) seemed more susceptible to effects related to the temperature difference. With coloured dye visualisations, affected flows could be identified by a sinking or floating of the flow as it convected downstream. Compared with the steady flow case, the problem was difficult to manage and relatively few flows could be obtained which did not exhibit at least some temperature-related bias. To help overcome the difficulty, the visualisation box was incorporated into the experimental fluid circuit. By diverting a small portion of the reservoir pressure, a gentle flow was created in the visualisation box. This incorporation of the visualisation fluid into the working fluid reduced the problem significantly, and temperature-related biases in the downstream flows were seen less frequently and then only to a minimal extent. Nonetheless, the source of error was still present and appears in our discussion of unstable pulsatile flows in chapter 6.

3.4 Chapter summary

In this chapter, the various numerical and experimental methods used in the thesis have been presented and detailed. The spectral-element method for computing two-

dimensional and axisymmetric flow fields has been introduced, as well as its extension to linear stability analysis and the prediction of spanwise and asymmetric bifurcations.

The formulation of the geometries under investigation and the corresponding flow and boundary conditions have been described. The two-dimensional partially-blocked channel geometry and the axisymmetric stenotic geometry have been outlined. Descriptions of the steady and pulsatile flow conditions have been given, as well as their implementation as conditions on the various inlet and outlet boundaries. Studies on the independence of the simulated flow fields to grid resolution and time step have been conducted and detailed for the various flow problems investigated.

A description of the experimental apparatus constructed to model the flow through the axisymmetric stenosis geometry has been given, along with summaries of the diagnostic methods used to observe the flow and discussions on the optimisation and limitations of the apparatus.

The next chapter begins the discussion of the research results, analysing the behavior and stability of the steady flow through the partially blocked two-dimensional channel.

Chapter 4

Wake Behaviour Through a Constricted Channel

4.1 Introduction

The geometry of the constricted channel studied in this chapter is presented in figure 4.1. In examining constricted flows, we start with a much-simplified problem; in this instance, the flow in a two-dimensional channel with a semi-circular blockage on one side. The blockage is defined by a single parameter, the blockage ratio $b = r/D$, where r is the radius of the blockage and D is the channel width. The calculation of the Reynolds number, $Re = 2\overline{U}D/\nu$, is isolated from the blockage geometry, thereby affording us a well-defined parameter space.

The simulation geometry corresponding to $b = 0.5$ bears the most similarity to the geometry of that of previous work on the backward-facing step. Figure 4.2, showing streamlines and velocity profiles of the flow field for $b = 0.5$ and $Re = 1000$, gives the

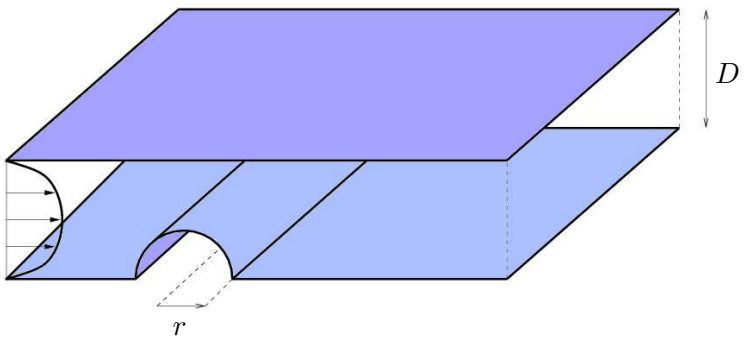

FIGURE 4.1: Schematic of the geometry under investigation.

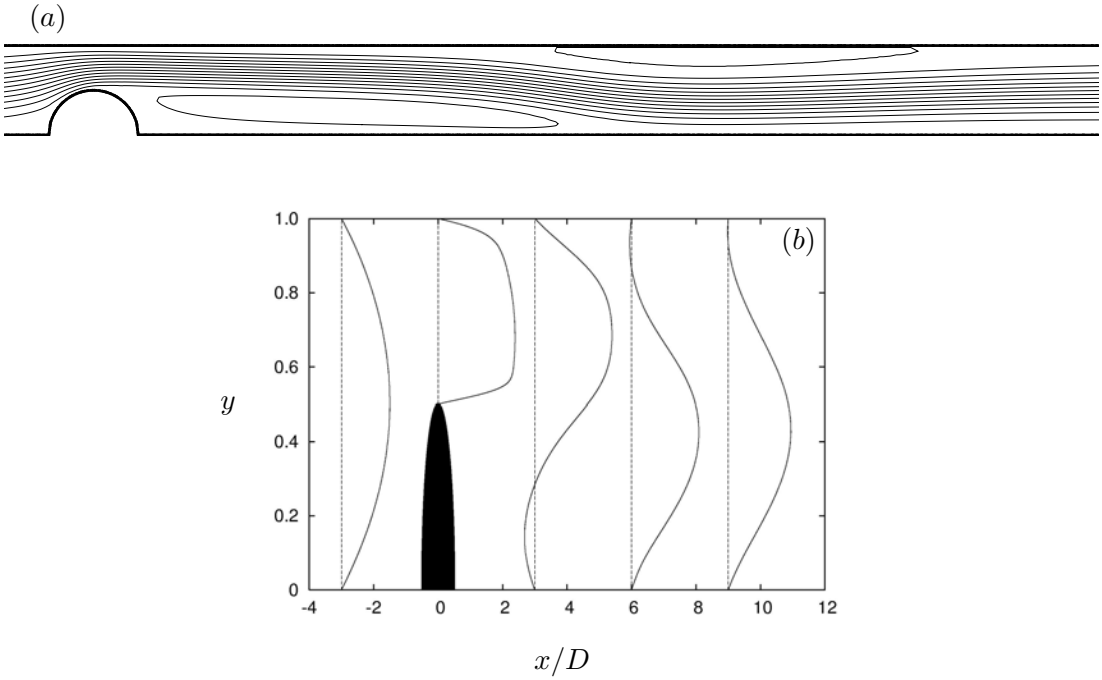

FIGURE 4.2: The flow at $b = 0.5$ and $Re = 1000$, (a) streamlines and (b) profiles of streamwise velocity, u, at various locations, including within the contraction, $x = 0$.

generic form of the flow. The initial flow recirculation zone (FRZ) is formed by the sudden expansion of the flow after the constriction and the resultant adverse pressure gradient over the back half of the blockage. A further expansion near the end of the first recirculation zone causes a second separation on the opposite wall. Flows of sufficiently high Reynolds numbers can also exhibit a third separation, with each subsequent downstream recirculation attached to alternate channel walls.

While the wake flow has many features in common with that of a backward-facing step, there exist several important differences. For example, in a backward-facing step geometry, the corner of the step fixes any flow separation to that point, regardless of the Reynolds number. In the present geometry, the separation point is not fixed by the geometry and will vary with the Reynolds number. Also, the semi-circular blockage causes a contraction of the flow upstream of the bump, in addition to the expansion and deceleration seen downstream of a backward-facing step. This links in with the absence of a fully-developed Poiseuille profile immediately upstream of the blockage, as is seen in the standard backward-facing step geometry. Instead, due to the constriction, the velocity profile at the midpoint of the blockage is markedly skewed to one side, as can be seen in figure 4.2(b).

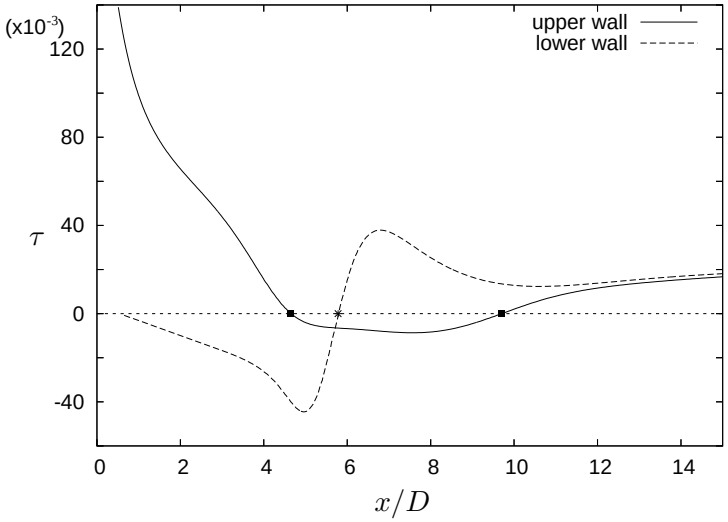

FIGURE 4.3: Distribution of (normalised) shear stress along the channel walls for $b = 0.5$ and $Re = 1000$. Points where the curves change sign are marked, showing the beginnings and ends of recirculation zones.

4.2 Flow recirculation length

One parameter characterising the flow state is the length of the first of these flow separation zones, L_R. The separation begins at a given point on the downstream side of the blockage, depending on Reynolds number; however, all flow recirculation lengths are measured from the midpoint of the blockage, at $x = 0$. The end of the recirculation zone is characterised by where the separating streamline terminates on the lower wall, where $\partial u/\partial y = 0$, or where the wall shear stress is equal to zero. Finding the precise point of reattachment is best done by tracking the wall shear stress, $\tau_{\text{wall}} = -\mu \partial u/\partial y$ (where μ is the dynamic viscosity), and finding the location where the sign changes from negative to positive. Figure 4.3 shows a representative example of the distribution of wall shear stress, normalised by the dynamic pressure according to $\tau = \tau_{\text{wall}}/\frac{1}{2}\rho\overline{U}^2 = -(2\nu/\overline{U}^2)(\partial u/\partial y)n_y$, where n_y describes the direction of the outward normal to the fluid. For the upper wall $n_y = 1$, and for the lower wall $n_y = -1$. Hence, in figure 4.3, the areas of negative τ correspond to recirculation zones, where fluid is flowing upstream in the immediate vicinity of the wall. The end of the first recirculation zone can be seen where the curve for the lower wall crosses zero, while in a similar manner the beginning and end of the recirculation zone on the upper wall are evident.

Figure 4.4(a) plots the recirculation length normalised by channel width, or L_R/D,

as a function of Reynolds number. Across the blockage range, the length of the recirculation zone seems to increase approximately linearly at lower Reynolds number. It is possible that the non-linear increase may be related to the appearance of the secondary recirculation zone on the upper wall of the channel. The boundary for this phenomenon is depicted as the dotted line on figure 4.4(a). Below this boundary, behaviour can only be described as approximately linear, but above it, the increase in recirculation length with Reynolds number does fall away.

After various attempts to collapse the data, non-dimensionalisation of the recirculation length by the blockage height, r, was found to yield the most useful result, as depicted in figure 4.4(b). For blockage ratios in the range $0.4 \leq b \leq 0.9$, the normalised recirculation lengths show a very similar Reynolds number dependence, with only a mild dependence on blockage ratio. For this blockage range, there is a fairly good collapse, with the reattachment lengths at any Reynolds number matching values for other blockage ratios to within 15% or better. Significantly reduced recirculation lengths are observed for $b < 0.3$ and the general shape of the curves is different. In particular, the variation of reattachment length with Reynolds number is much closer to linear over the Reynolds number range considered. The difference in the behaviour shown in the two regimes is probably caused by the shape of the incoming velocity profile. For small blockage ratios, the incoming velocity at the top of the blockage is much lower than the mean velocity through the channel; indeed, for $b = 0.05$ this velocity is only 28% of the mean velocity. Hence, at low blockage ratios, the effective Reynolds number is much lower than the bulk flow Reynolds number, so that only a proportionally smaller recirculation zone is formed, as the greater part of the fluid continues on relatively unperturbed by the blockage. At higher blockage ratios, the channelling of flow through the small gap between the top of the blockage and the upper wall means that the local properties of the incoming flow profile no longer control the flow behaviour.

Predictions of the reattachment length variation for the flow over a backward-facing step are included for comparison in figure 4.4(b). These are obtained from spectral-element simulations and are in agreement with accepted literature predictions using different methods (e.g. Thompson & Ferziger 1989). In addition, experimental results of Armaly *et al.* (1983) are also included. Both sets of results match well with the predictions of the reattachment length for $b = 0.5$, up to $Re \approx 400$. At higher

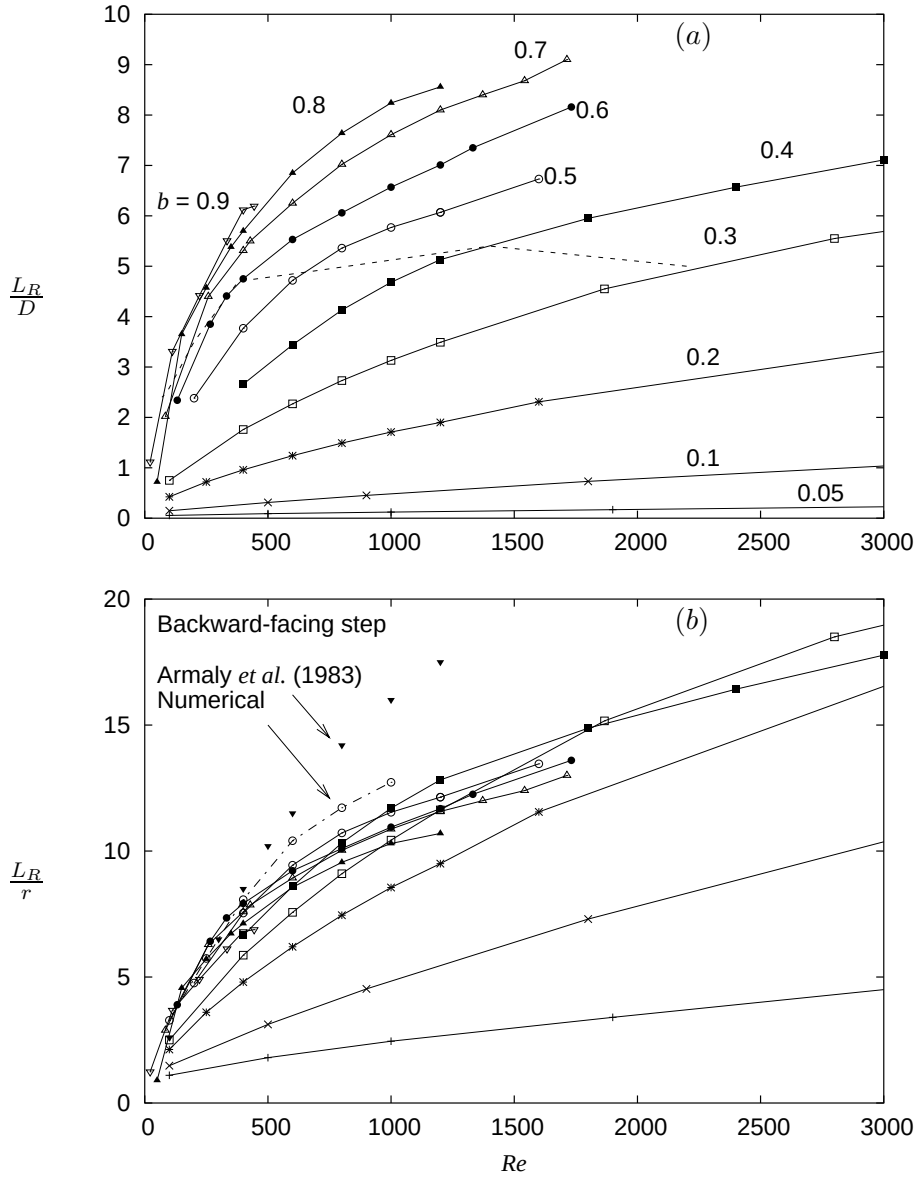

FIGURE 4.4: Plots of recirculation lengths against Reynolds number, Re, with L_R normalised by (a) channel width, D, and (b) blockage radius, r (point styles between the two graphs correspond). The dotted line in (a) shows the approximate boundary where, as Reynolds number is increased, a second recirculation zone forms on the upper wall of the channel. Also shown in (b), are separation lengths for flow over a backward-facing step obtained from spectral-element simulations and experimental measurements from Armaly *et al.* (1983).

Reynolds numbers, the predicted recirculation lengths for the current geometry increase less rapidly with Reynolds number and there is also a divergence of the experimental and numerical results for the backward-facing step alone. As mentioned in the earlier review, the divergence between experimental results and purely two-dimensional simulations has been argued to be due to a three-dimensionality formed extrinsically in the experimental flows by the presence of a jet emanating from the junctions of the side walls with the step (Williams & Baker 1997). Following on from the current focus, the more pertinent question of when the two-dimensional flow becomes intrinsically unstable to three-dimensional perturbations is addressed in section 4.4.1.

4.3 Wake behaviour

In addition to the initial recirculation zone, other wake parameters were recorded and other flow states identified. Figure 4.5 presents a parameter space map showing the boundaries for the occurrences of various phenomena in terms of blockage ratio and Reynolds number.

A second flow recirculation zone on the wall opposite the blockage was observed for $b \geq 0.3$ at sufficiently high Reynolds number. Similarly, a third recirculation zone appears on the bottom wall for $b \geq 0.6$. At $Re \gtrsim 1800$, for $b = 0.5$ and 0.6, the flow begins to shed vortices directly from the blockage, indicated on figure 4.5 by those points designated "shedding". Large vortices develop directly behind the blockage, with smaller alternating ones developing on the upper wall. Initialising these simulations from a converged steady flow solution at a lower Reynolds number, instead of from a quiescent state, shows that the onset of shedding is subcritical. Figure 4.6 plots two fields of vorticity at $b = 0.5$ and $Re = 1200$, the first showing the vortex shedding described. The second is the flow at the same Reynolds number, but this time obtained by steadily incrementing the Reynolds number from a converged solution at a lower Reynolds number. By incrementing the Reynolds number in this fashion, it was found that the flow can be held steady up to $Re \approx 2600$ for $b = 0.5$. However, it is worth noting that this is well into the transitional (turbulent) Reynolds number regime for unconstricted flow between flat plates, and well past the critical Reynolds number at which the flow is unstable to three-dimensional disturbances for flow past a

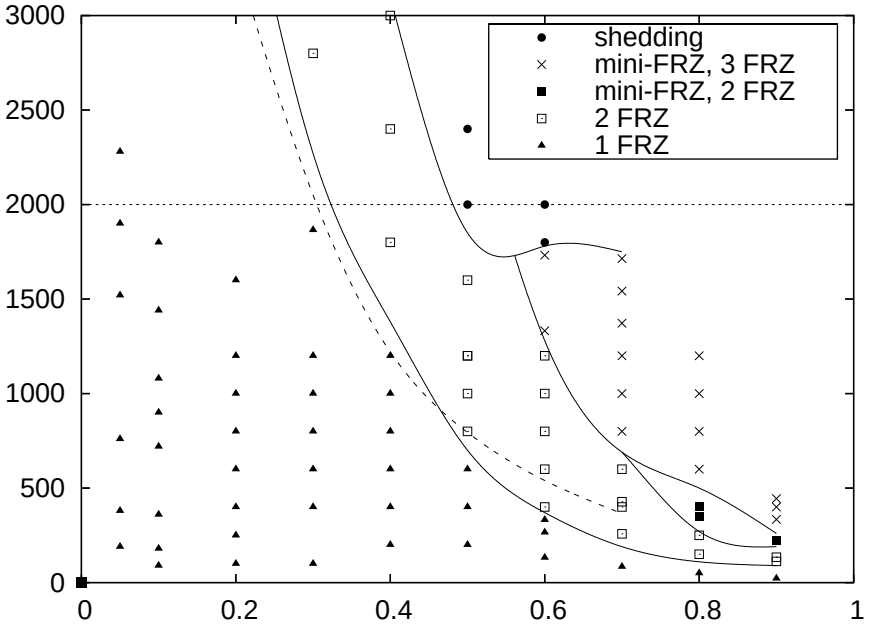

FIGURE 4.5: Parameter map showing the wake state as a function of Reynolds number and blockage ratio for stationary flow. The specific data points tested are plotted, while solid lines indicate the approximate boundaries between different flow states. The straight dashed line at $Re = 2000$ represents where we would begin to see turbulence in the unconstricted flow between two flat plates. The other dashed line indicates the critical boundary for linear three-dimensional instability, derived from the stability analysis presented in section 4.4.1. The terms 1, 2 and 3 FRZ denote the number of recirculation zones present.

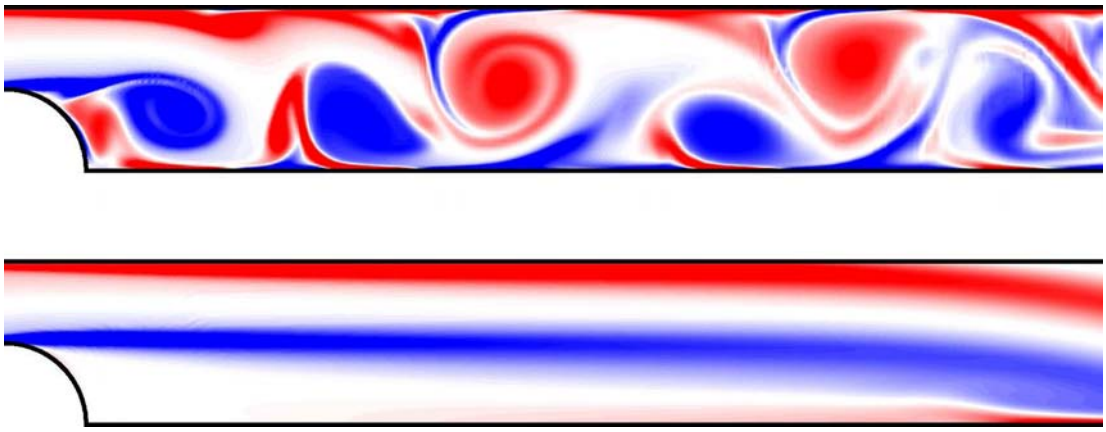

FIGURE 4.6: Vorticity plots at $b = 0.5$ and $Re = 1200$, the first depicting the shedding denoted in figure 4.5, the second showing a steady case, obtained by initializing the simulation with a converged steady solution at a lower Reynolds number.

backward-facing step. Hence, further attention has not been focused on this particular phenomenon.

For higher Reynolds number, for $b \geq 0.6$, the structure of the first recirculation zone begins to take on a different form. Occurrences of the steady structure that forms are denoted by "mini-FRZ" in figure 4.5, while examples are depicted in figure 4.7(a). The development of dimples in the initial recirculation zone can be seen in the vorticity fields, with the first field being below the boundary for the occurrence of the phenomenon and the rest being above it. At $Re = 400$ the structure is not apparent, but with increasing Reynolds number, instances of these small recirculation zones grow in strength and number and occur slightly further upstream. The behaviour of the wall shear stress of the recirculation zones changes significantly with the appearance of the vortex structure, as shown in figure 4.7(b). The sign of the wall shear stress switches several times before the termination of the main recirculation zone. In these cases, the length of the initial recirculation zone was determined by tracking the separating streamline to its termination. Figure 4.8 is a close-up of the vorticity field of the structure, at $Re = 1000$ and $b = 0.8$, with velocity vectors overlaid. In this instance, a series of three mini-recirculations and the beginnings of a fourth are apparent. A close inspection, as shown in figure 4.9, reveals further even smaller partial recirculations between those obvious in figure 4.8, nestled between the primary clockwise mini-vortices but attached to the bottom wall of the channel. In this figure, streamlines have been added to highlight the smaller recirculations present. This is somewhat reminiscent of the sequence of mini-recirculations that appear at the front of the horseshoe vortex associated with a cylinder-wall junction as the Reynolds number is increased (e.g., Thwaites 1960; Visbal 1991; Baker 1979). It should be noted that the boundary for the phenomenon shown in figure 4.5 denotes where the structure first becomes apparent, from observations of plots of the vorticity field.

Interestingly, we have not found any reference to such vortical structures in any of the literature on the flow past a backward-facing step. In that case, it may not occur until the Reynolds number is very much higher than is typically investigated. Considering that the critical Reynolds number for linear three-dimensional instability for a backward-facing step was found at $Re = 997$ by Barkley *et al.* (2002), it is likely that these structures would occur for purely two-dimensional flow only above the

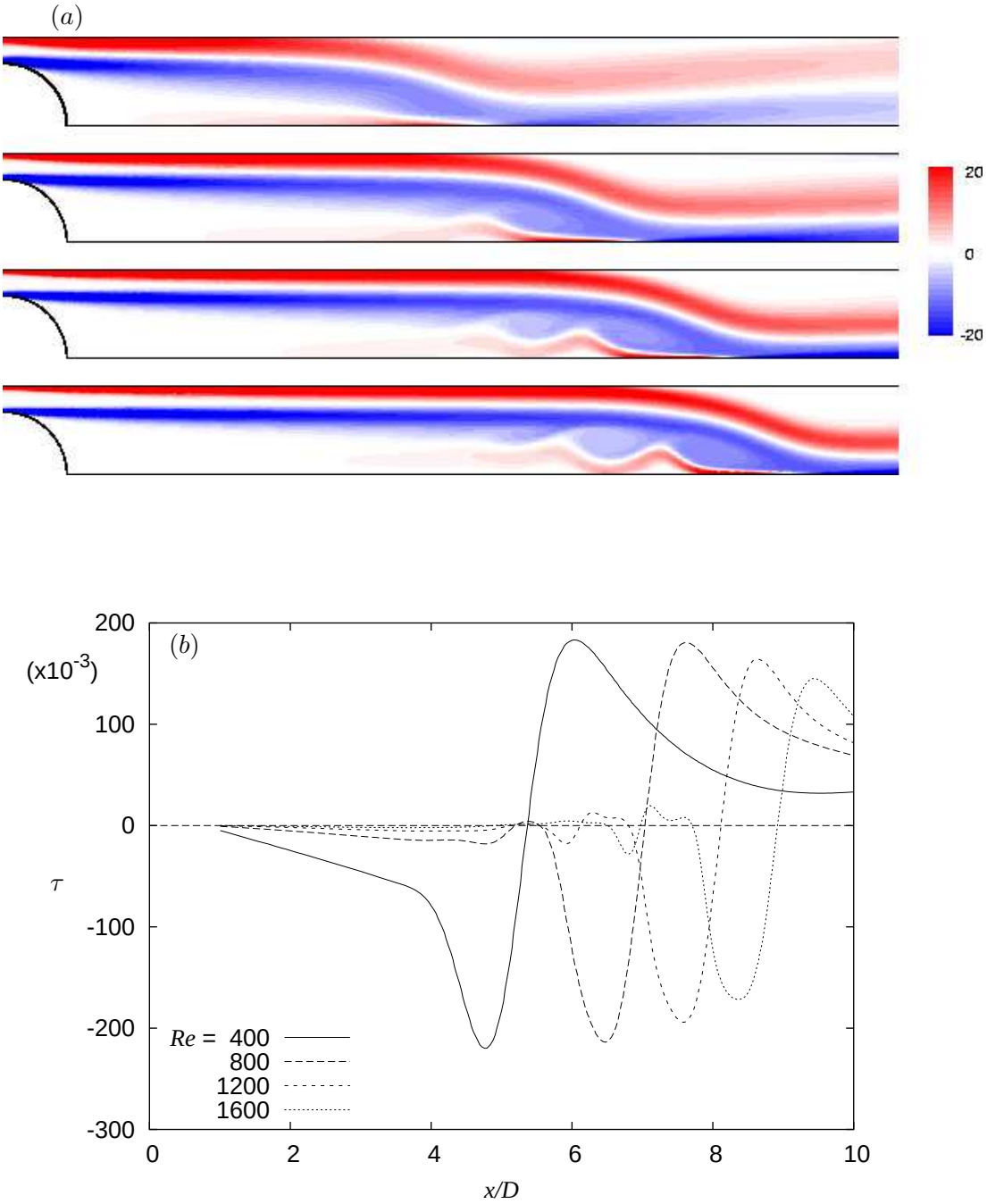

FIGURE 4.7: (a) Contours of positive and negative spanwise vorticity, depicting the variation with Reynolds number of the amplitude and location of dimpling of the initial recirculation zone, at $b = 0.7$ and $Re = 400$, 800, 1200 and 1600 (top to bottom) and (b) plots of the non-dimensionalised wall shear stress of the same flow fields.

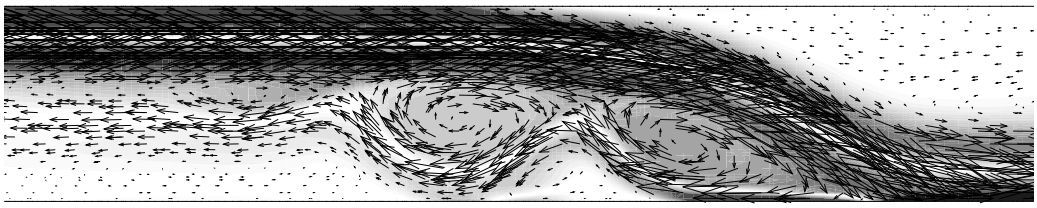

FIGURE 4.8: Close-up of the end of the initial FRZ for $b = 0.8$ and $Re = 1000$, showing the spanwise vorticity field overlaid with velocity vectors.

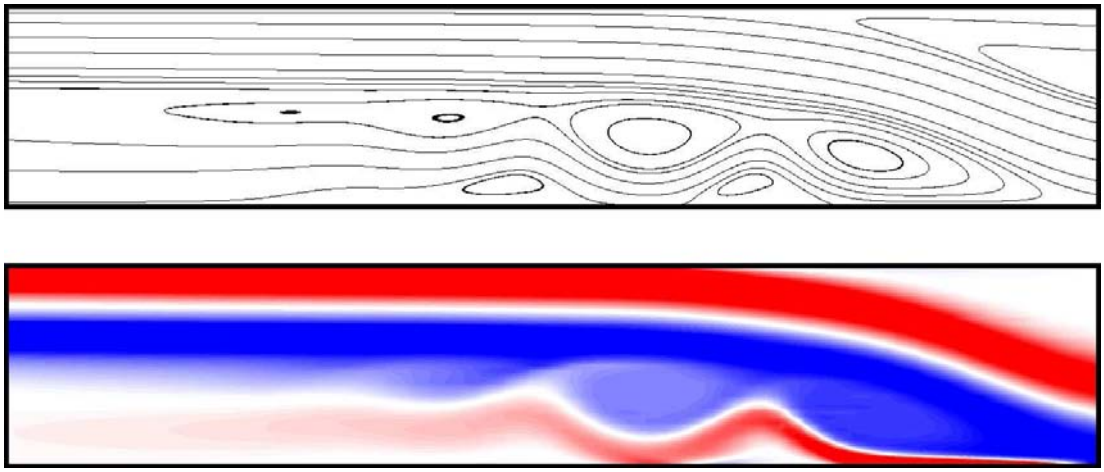

FIGURE 4.9: Streamlines and vorticity of the initial FRZ for $b = 0.7$ and $Re = 800$.

critical Reynolds number of three-dimensional instability. This question is addressed in the following section, which deals with the stability of the two-dimensional base flow.

4.4 Three-dimensional behaviour

4.4.1 Instability growth rates

Figure 4.10 shows converged non-dimensional growth rates corresponding to the dominant linear instability mode for $b = 0.4$, 0.5 and 0.6 as a function of Reynolds numbers. We initially look at the results obtained for the geometry of $b = 0.5$, which bears the most similarity to the backward-facing step, serving here as a point of reference. From figure 4.10(b) we see that for $b = 0.5$, the primary linear spanwise instability occurs at $Re \approx 800$, for a spanwise wavelength of ~ 5.7 blockage heights. After determining the curves for several Reynolds numbers, the critical Reynolds number, Re_c, and the critical wavelength, λ_c, were found by polynomial interpolation. The flow was then

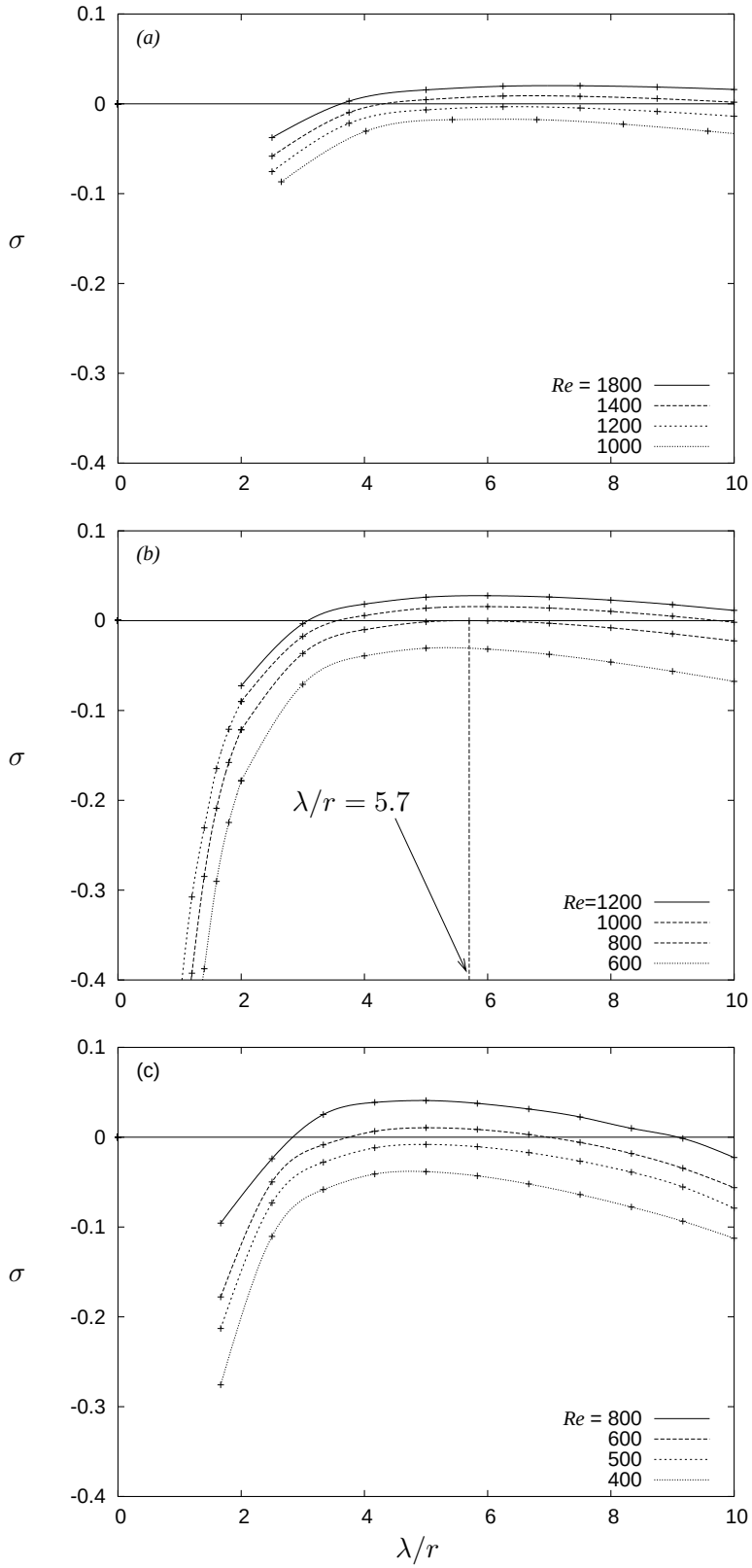

FIGURE 4.10: Non-dimensional growth rates as functions of wavelength, for blockage ratios of (a) 0.4, (b) 0.5 and (c) 0.6, at various Reynolds numbers.

simulated at this Reynolds number/wavelength combination to verify the predictions. For $b = 0.5$, the critical Reynolds number is found to be $Re_c = 794$, at a wavelength of $\lambda_c = 5.7r$.

This critical Reynolds number for the transition to three-dimensionality for the geometry of $b = 0.5$ is considerably higher than the one found by Armaly *et al.* (1983), and lower than that found by Barkley *et al.* (2002). As demonstrated by Williams & Baker (1997) and discussed in section 4.2, the reasons for the discrepancy with the experimental work of Armaly *et al.* (1983) probably lie in the inadequate channel width used in the experimental rig. Williams & Baker (1997) demonstrated that even in rigs of high spanwise dimension, wall jets emanating from where the step meets the sidewall penetrate into the mainstream flow, creating three-dimensional flow structures. This is similar to, but worse than, the difficulty in trying to produce a two-dimensional wake from a circular cylinder. In that case, aspect ratios need to be several hundred unless special end conditions are used (Miller & Williamson 1994; Norberg 1994).

The relatively small differences in critical Reynolds number and wavelength between the present case and the infinitely wide backward-facing step (Barkley *et al.* 2002) are not due to similar extrinsic effects, but are caused by differences in the flow. The critical Reynolds number and wavelength are both approximately 20% lower than the corresponding values for the step ($Re_c = 997$ and $\lambda_c = 6.9r$). Assuming that the mechanisms for the instabilities in each case are analogous (see discussion below), the discrepancy in Re_c and λ_c with the backward-facing step may be related to two differences in the flow structure and topology resulting from the altered geometry. The first is the change to the velocity profile at the separation point. Over the semi-circular blockage, the velocity profile is skewed due to the rapid constriction of the flow, with the highest velocity being closer to the bump than to the top wall. This is in contrast to the fully developed Poiseuille profile found in studies of the backward-facing step. We have not attempted to quantify this influence here. The other difference lies in the fixed point of separation present at the very edge of the backward-facing step and the mobile one in the present study. Without the sharp edge forcing the detachment of the flow, the point of separation becomes dependent on the adverse pressure gradient on the downstream half of the blockage, moving upstream with increasing Reynolds number.

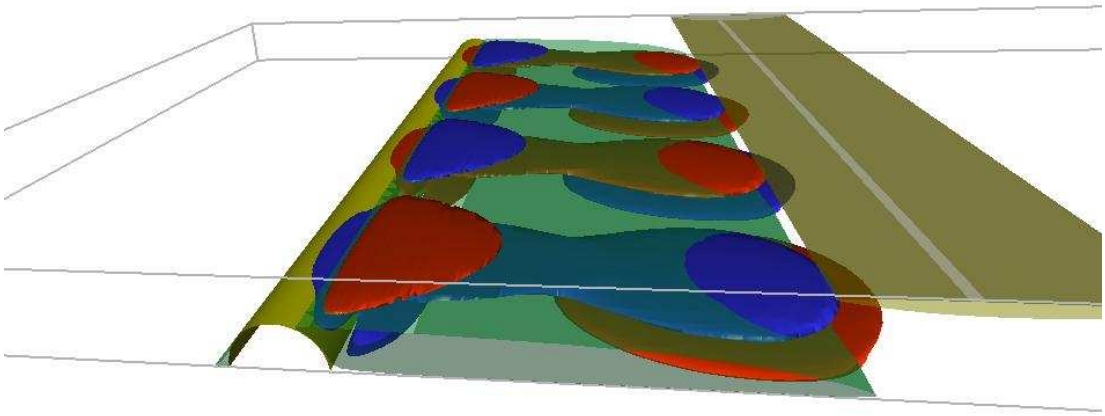

FIGURE 4.11: Two positive and negative iso-surfaces of the streamwise vorticity of the dominant mode $\lambda/r = 5.7$, for $Re = 800$ and $b = 0.5$, depicted over two spanwise wavelengths. Transparent representations of the recirculation zones of the base flow are included.

The same process of determining the critical Reynolds number and wavelength was carried out for the other blockage ratios in the range $0.3 \leq b \leq 0.7$. The critical boundary is plotted on figure 4.5. The transition to three-dimensional flow is found to occur prior to the first appearance of the mini-recirculation zones, described in section 4.3, and well before the subcritical transition to two-dimensional vortex shedding. This is discussed further in section 4.4.3.

4.4.2 Structure of the instability

The structure of the dominant mode at $Re = 800$ and $b = 0.5$, for which $\lambda/r = 5.7$, is shown in figure 4.11. It is visualised by plotting isosurfaces of the streamwise vorticity. The repeating structure of the mode consists of two layers of opposite-signed vorticity, one almost entirely located within the recirculation zone and the other extending into the mainstream flow. The mode appears to grow around the first recirculation zone. Figure 4.12 shows the spanwise vorticity field of the mode, consisting of two elongated regions of opposite-signed vorticity, whose extrema are offset at a small angle. This point will prove relevant in our discussion of instability mechanisms.

The same generic mode structure is found across the blockage range tested. The structure is qualitatively similar to that of the backward-facing step found by Barkley

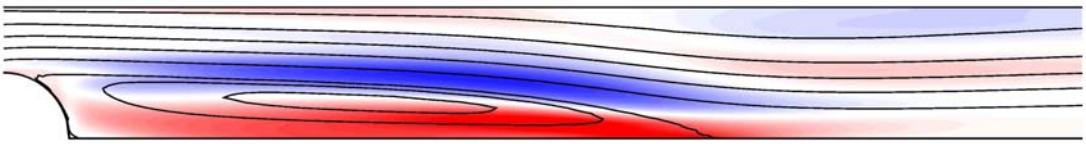

FIGURE 4.12: Positive and negative contours of the spanwise vorticity (colouring linear) of the critical perturbation mode, $\lambda/r = 5.7$, at $Re = 800$ and $b = 0.5$, overlaid with streamlines of the base flow.

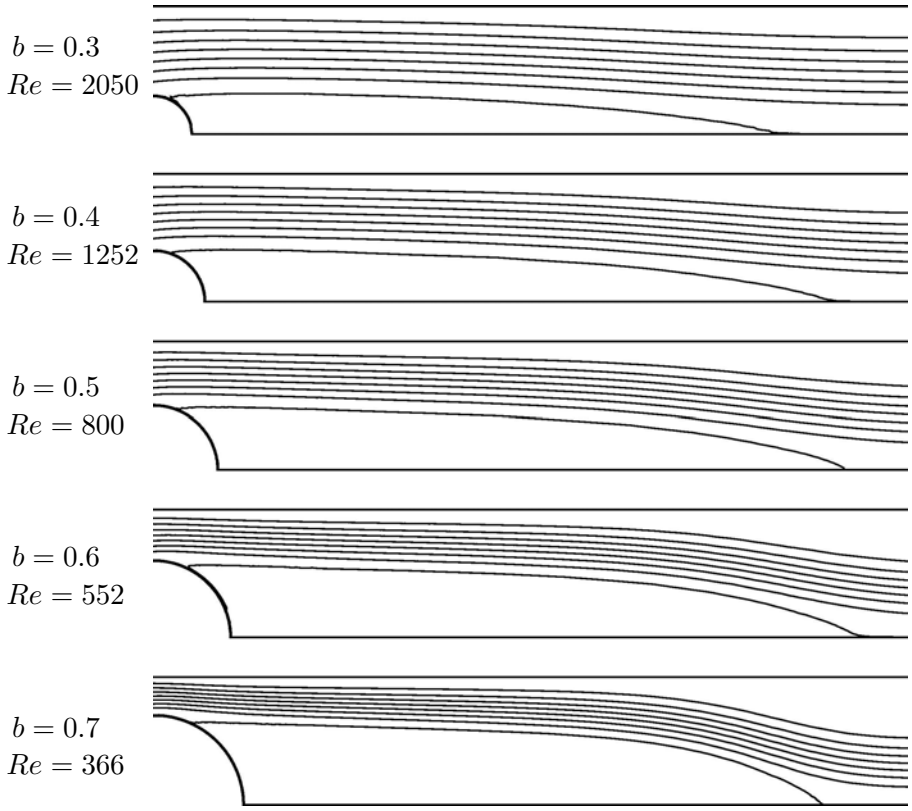

FIGURE 4.13: Streamlines of simulations performed using the critical Reynolds numbers found from linear stability analysis, $b = 0.3$ to 0.7.

et al. (2002). Figures 4.11 and 4.12 indicate that the downstream extent of the instability mode possibly scales with the length of the first recirculation zone; if this is the case, then much of the difference between the predicted critical spanwise wavelengths between the two cases can be explained by the difference in reattachment lengths at the critical Reynolds number, rather than any absolute difference between the two flows. Figure 4.13 plots streamlines of the critical flows found for blockage ratios from $b = 0.3$ to 0.7, showing a roughly similar reattachment length for each case. Figure 4.14 shows the relationship between reattachment length and critical wavelength. At the recircu-

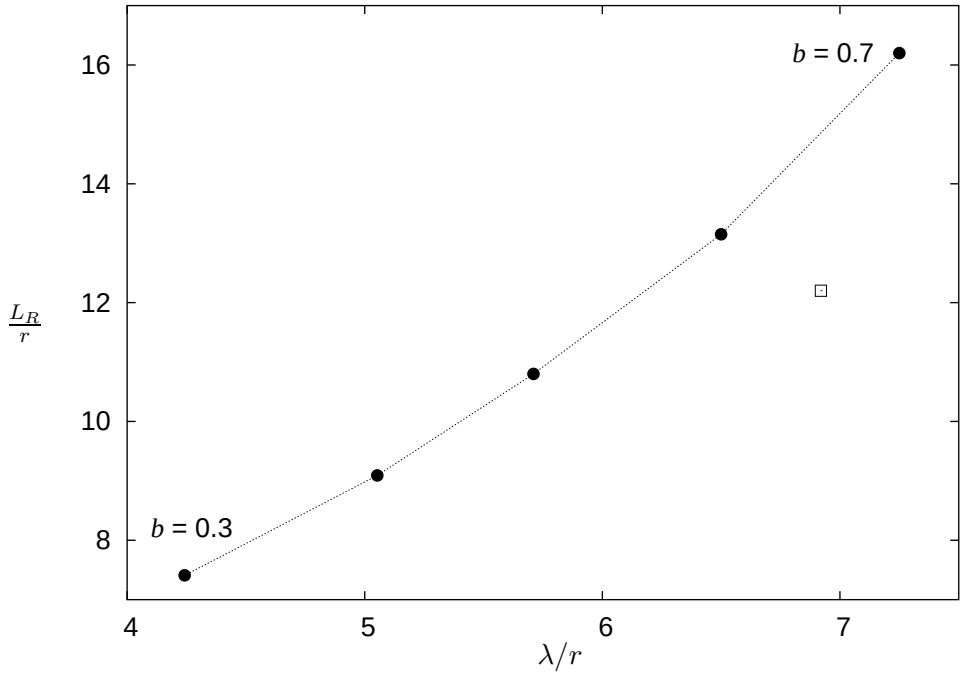

FIGURE 4.14: Plot of recirculation length at critical Reynolds number against critical wavelength. Both axes have been normalised by the blockage height. The point labelled with a square is the corresponding point for the backward-facing step taken from Barkley *et al.* (2002).

lation length corresponding to the critical Reynolds number for the backward-facing step, $L_R = 13.2$ (Barkley *et al.* 2002), the predicted critical wavelength is $\lambda/r \approx 6.5$, only slightly smaller than the $\lambda/r = 6.9$ obtained for the backward-facing step.

4.4.3 Instability mechanism - centrifugal

The strong similarity between the structure of the principal three-dimensional instability found behind the blockage and of that reported in the literature for the backward-facing step suggests we take a closer look at the previous theories on the subject of mechanisms for this instability. Ghia *et al.* (1989) postulated that the appearance of the second recirculation zone on the upper wall, by introducing a curvature to the mainstream flow, induces a Taylor-Görtler-like instability. Barkley *et al.* (2002) have attributed it again to a centrifugal mechanism, but this time located within the closed streamlines of the first recirculation zone. In recent work using adjoint stability analysis, the instability core in similar flows has been determined to be located within the recirculation zone (Marquet, Sipp, Chomaz & Jacquin 2006).

Centrifugal instability theory, as first developed by Rayleigh (1917) for axisymmetric

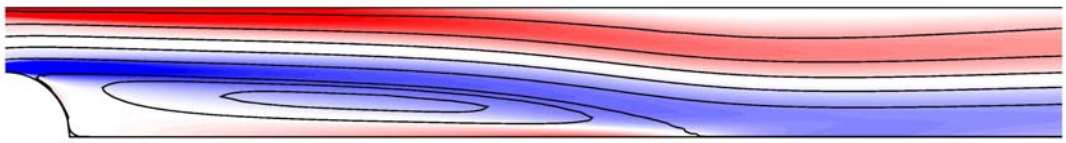

FIGURE 4.15: Streamlines and positive and negative contours of the spanwise vorticity of the base flow, with $b = 0.5$ and $Re = 800$.

inviscid flows with circular streamlines, holds that a potentially unstable condition results from the existence of a decrease in angular momentum of fluid particles as the radial distance from the centre of rotation of the flow increases, since this implies an imbalance between the radial pressure gradient and the centrifugal force acting on the fluid particles. Triggering of the instability will cause three-dimensional flow structures to form, which redistribute angular momentum between the inner and outer regions of such a vortex. The corresponding perturbations typically consist of a series of counter-rotating azimuthal vortices located in the region of decreasing circulation, and whose axial wavelength scales on the radial extent of this region. Applying this theory to irregularly curved streamlines, as in the instance found here within the initial recirculation zone, is problematic, as the flow is only locally circular, with the radius of curvature varying along any one streamline. Despite this, Bayly (1988) has successfully generalised the centrifugal instability theory, making it possible to obtain predictions for any two-dimensional flow consisting of closed streamlines.

The object of this section of the chapter is to give a comparison between the results of the linear stability analysis presented in section 4.4.1, which are not restricted to any specific instability type, and the stability of the flow to centrifugal instability calculated analytically through the method proposed by Bayly (1988). We focus initially on the case of $Re = 800$ and $b = 0.5$, the base flow of which is shown in figure 4.15.

Figure 4.16(a) plots the circulation within the recirculation zone, as a function of streamfunction, ψ. The centre of recirculation corresponds to $\psi = 0$. Centrifugal instability is predicted wherever there exists a decrease in circulation as we move away from the centre of rotation. As can be seen from figure 4.16(a), in the flow under question such a decrease exists near the edge of the recirculation zone, but the range across which it appears is extremely narrow. More quantitative predictions can be obtained by first calculating the local (i.e., as function of ψ) Floquet exponents σ_f, expressing

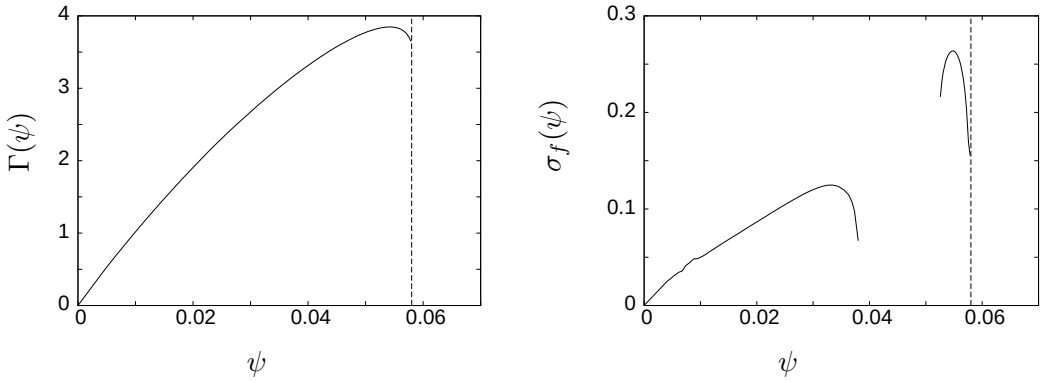

FIGURE 4.16: (a) Plot of the circulation, $\Gamma(\psi)$, within the initial recirculation zone and (b) plot of the real Floquet exponent, $\sigma_f(\psi)$, for $b = 0.5$ and $Re = 800$. Dotted lines show the boundary of the recirculation zone. Exponents calculated in the range $0.0384 < \psi < 0.0525$ are complex.

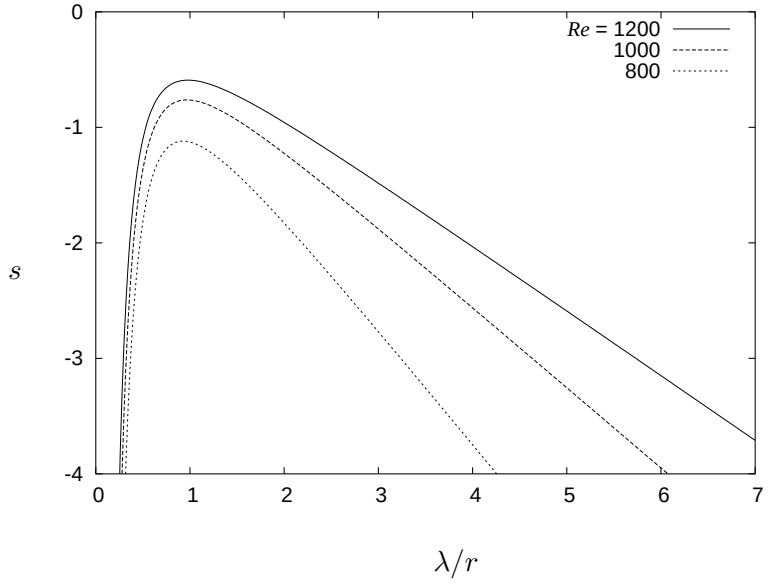

FIGURE 4.17: Total predicted growth rates of centrifugal instability, as function of normalised wavelength, for $Re = 800$, 1000 and 1200, according to the theory as presented in Bayly (1988).

the growth of perturbations (in the limit of short wavelengths) of fluid elements as they make one revolution on a closed streamline. Details on how to calculate these exponents from the base flow are found in Bayly (1988); the result is plotted in figure 4.16(b). The behaviour of $\sigma_f(\psi)$ in this graph matches closely that seen in Gallaire *et al.* (2006), in which they performed a similar analysis within the recirculation zone behind a bump on a plane wall in unbounded flow. An approximately quadratic maximum of σ_f is found at $\psi_0 \approx 0.055$, which allows the construction of centrifugal instability

modes near the corresponding streamline and the calculation of their growth rates as functions of spanwise wavelength. A second peak in $\sigma_f(\psi)$ exists closer to the centre of the recirculation zone; it occurs however, in a region of increasing outward circulation and cannot be utilised in the rest of the theory; we would not expect it to play a role in any centrifugal instability. The possibility exists that this maximum is related to an elliptical instability mechanism at play - this question is addressed in the next section of the chapter. Including a viscous damping term proportional to $-\nu(\frac{2\pi}{\lambda})^2$, the total viscous growth rate s can be expressed as

$$s(\lambda) = \sigma_f(\psi_0) - \frac{\lambda}{2\pi D}\left[-\sigma_f''(\psi_0)C(\psi_0)\right]^{\frac{1}{2}} - \frac{2A}{Re}(\frac{2\pi D}{\lambda})^2, \tag{4.1}$$

where A is a constant of O(1), and $C(\psi)$ is a complicated function of the two-dimensional base flow (for details see Bayly 1988). In equation (4.1), all quantities depending on ψ (i.e., σ_f, its second derivative σ_f'', and C) are evaluated for the most unstable streamline ψ_0.

Figure 4.17 plots the total growth rate as a function of wavelength, for $Re = 800$, 1000 and 1200, $Re = 800$ being near the critical Reynolds number determined from our earlier stability analysis. From the graph we can see that the theory predicts the flow to be stable to such an instability even up to at least $Re = 1200$. The value of the unknown coefficient A was chosen here to be 1. Other values of the same O(1) would obviously modify the predicted growth rate curves. Nevertheless, an important observation can be made concerning the least stable wavelength predicted, which has only a small dependence on the viscous correction. We see that any instability triggered in the recirculation zone by a centrifugal mechanism will be of wavelength $\lambda/r \approx 1$, significantly below the critical wavelength of $\lambda/r = 5.7$ determined from our numerical stability analysis, and shown in figure 4.10(b). Considering the narrow range of streamlines which exhibit a radially-outward decrease in circulation, it is not surprising that the wavelength predicted by the centrifugal instability theory should be of a similarly small scale. Indeed, it is evident from equation 4.1 that the growth rate has a high dependence on σ_f'', which results in a strong damping of wavelengths significantly larger than the width of the narrow "unstable" range of streamlines near the edge of the recirculation zone.

The analysis of this section seems to discount the possibility of the mechanism

of the instability shown in figure 4.11 being centrifugal in nature. While the growth rates returned by the theory are well below critical, the large difference between the wavelength predicted by the theory and of that determined from our numerical stability analysis lends the most weight to this argument.

4.4.4 Instability mechanism - elliptic

Given the strongly elongated shape of the recirculation zone in the flow under consideration, the proclivity of the flow for elliptic instability also merits investigation. This instability can occur in flows with elliptic streamlines, such as those found in a vortex exposed to an external strain field. The interaction of strain with normally neutral perturbation modes of the vortex can lead to a resonant amplification of these modes and thus to instability. The associated perturbations represent three-dimensional deformations of the vortex core, whose axial wavelengths scale on the transverse core size. A review of this mechanism is given by Kerswell (2002).

A first qualitative indication for elliptic instability is given by the structure of the instability mode, as seen in the plot of spanwise perturbation vorticity given in figure 4.12. Two regions of opposite-signed vorticity are found inside the recirculation zone, indicating a shift of its centre of rotation in a spanwise-periodic way, which is characteristic of elliptic instability.

The analysis can be made more quantitative by following the same procedure as applied by Leweke & Williamson (1998) to the three-dimensional instability of circular cylinder wakes, which was based on the theoretical work on viscous elliptic instability by Landman & Saffman (1987). For elliptic flow extending to infinity, with constant streamline eccentricity β in the range $0 < \beta < 1$, the inviscid growth rate for elliptic instability, σ_i, which is independent of axial/spanwise wavelength, can be approximated by

$$\sigma_i \approx \frac{9\varepsilon}{16}(1-\beta^m)^n, \tag{4.2}$$

where ε denotes the (constant and non-dimensional) strain rate of the flow, and where $m = 2.811$ and $n = 0.3914$ (Leweke & Williamson 1998). Despite the assumption of infinite elliptic flow with constant β made for equation 4.2, it is instructive to plot a local distribution of σ_i, using the relation (also derived from infinite flow) $\beta = 2\varepsilon/|\omega|$, where ω is the vorticity, as function of position. The result is shown in figure 4.18

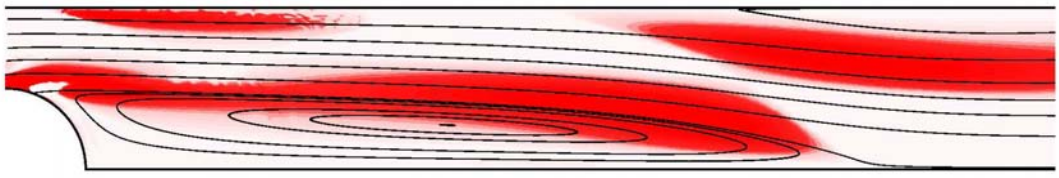

FIGURE 4.18: Contours of positive inviscid growth rate, σ_i, calculated locally from equation 4.2, along with representative streamlines. The presence of regions of positive growth rate located within the closed streamlines suggest the possibility of elliptic stability.

for the critical case with $Re = 800$ and $b = 0.5$, the base flow of which is shown in figure 4.15. The regions of strong inviscid growth rate within the mainstream flow are of no interest, as they occur upon unclosed streamlines, but a region of positive growth rate does extend into and past the centre of the recirculation zone. There is also a significant overlap between this region and the zone where the instability amplitude is strong, as observed in figure 4.12, which includes the recirculation zone and the adjacent shear layer.

To determine the total growth rate σ at the relatively low Reynolds numbers considered here, a viscous correction must be included. This effect was treated by Landman & Saffman (1987), and the result can be written as

$$\sigma = \sigma_i - \frac{2}{Re}\left(\frac{2\pi D}{\lambda}\right)^2 \frac{1 - \beta\cos^2\theta}{(1-\beta)\cos^2\theta}. \tag{4.3}$$

In the present case, we evaluate all involved quantities at the centre of recirculation, for simplicity (this choice is partly motivated by the observations made by Eloy & Le Dizes (1999) concerning elliptic instability of a vortex with non-uniform vorticity). Here, θ is the angle between the wave vector of the most unstable perturbation and the axis of rotation of the recirculation zone. It depends on the streamline eccentricity and the Reynolds number, and can in principle be obtained from figure 3 of Landman & Saffman (1987). However, in the present case, the eccentricity is always close to 1 at the centre of rotation, and without knowing beforehand the wavelength of the instability, θ cannot be determined with great accuracy. This means that unlike for the case of nearly circular base flow streamlines (i.e., low β) for which θ is always close to 60°, we are not able to predict theoretically a growth rate curve as a function of spanwise wavelength, solely based on the properties of the two-dimensional flow. We can nevertheless still perform a consistency check between the observed characteristics

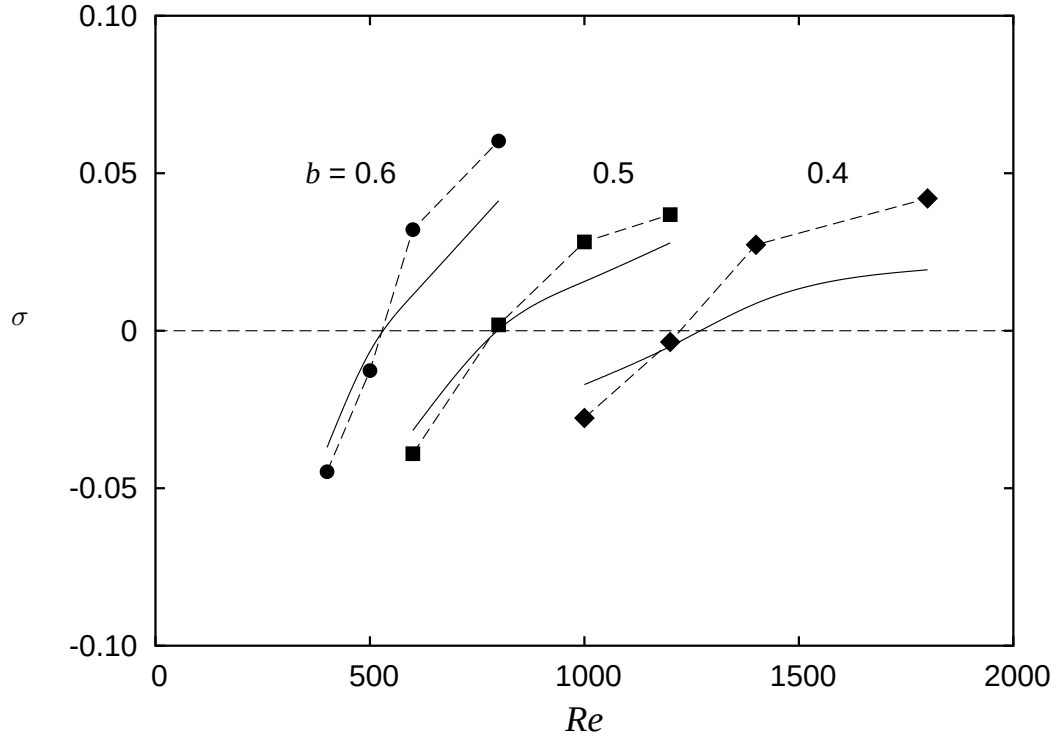

FIGURE 4.19: Comparison between the analytically calculated growth rates for elliptic instability, (symbols and dashed lines) and the maximum growth rates from the numerical stability analysis results of section 4.4.1 (lines), as function of Reynolds number.

and the theory on elliptic instability, using additional information concerning the most unstable wavelengths obtained in the stability analysis of section 4.4.1. Indeed, if the spanwise wavelength is known, the angle θ can be calculated from the following relation between spanwise and cross-sectional length scales, which can be deduced from Landman & Saffman (1987):

$$\lambda = L(\frac{2}{1-\beta})^{\frac{1}{2}} \tan\theta, \tag{4.4}$$

where L is a characteristic length scale of the base flow. For the present case, we choose it to be proportional to the minor axis of the recirculation zone. For elliptic instability, we would expect this length to be the constraining dimension on the development of the mode, at least more so than the other possible candidate, the major axis of the vortex. Once θ is known, the total growth rate of elliptic instability can be calculated using equation 4.3.

This procedure was carried out for different blockage ratios and a range of Reynolds numbers around the respective instability thresholds. Each time, the values of ε and

σ_i were calculated at the centre of the recirculation zone of the base flow, the minor axis of the latter was measured, and the most unstable wavelength obtained from stability analysis. The total growth rates resulting from these parameters and the equations above derived from elliptic instability theory are plotted in figure 4.19, where they are compared with the ones obtained from the numerical stability analysis. A proportionality factor of 1.1 between L and the minor axis of the recirculation zone was found to give the best match, and was used for all cases.

The overall agreement between the two sets of results is quite good, given the approximations and hypotheses that had to be made in order to apply elliptic instability theory to the present high-eccentricity flow. It shows that not only the observed combinations of wavelengths and growth rates of the three-dimensional instability, but also the trends and variations with Reynolds number and blockage ratio are compatible with an elliptic instability mechanism acting in this flow.

4.5 Chapter summary and discussion

An investigation of the flow through a partially blocked two-dimensional channel across a range of Reynolds numbers and blockage ratios has been presented. For blockage ratios $b \geq 0.4$, the functional dependence of the length of the initial recirculation zone on the upstream Reynolds number is insensitive to blockage ratio, if the length is normalised by blockage height. This collapse breaks down at smaller blockage ratios. For $b < 0.3$, much shorter recirculation lengths are observed, presumably because of the lower fluid velocity in the vicinity of the blockage due to the parabolic velocity profile. In addition to the standard single recirculation region at the rear of the blockage, at higher Reynolds numbers other flow behaviours were observed, including multiple downstream recirculations attached to alternating walls, vortex shedding which appeared to be convective in nature, and sets of small positive and negative vortices at the end of the main recirculation zone reminiscent of those that occur upstream of wall-body junctions. Most of these features occur at Reynolds number in excess of the critical Reynolds numbers for transition to three-dimensional flow, determined from linear stability analysis.

The stability of the flow to three-dimensional perturbations was analysed, with the

identification of a transition to three-dimensionality involving a stationary instability mode. This mode takes the form of counter-rotating cells centered around the initial recirculation zone, with the same generic structure being found between $b = 0.3$ and $b = 0.7$. The mode structure, onset Reynolds number and critical wavelength for $b = 0.5$ match well with the results taken from the literature for the flow over a backward-facing step. This is despite distinct differences in the flow profile at separation associated with the flow convergence and divergence, and the different geometry near separation. The previously proposed argument for the mechanism of the instability being centrifugal in nature was tested by means of a theoretical analysis of the flow field at the critical Reynolds number. The theory on centrifugal instabilities predicts the flow to be stable to such a mechanism and further predicts the critical wavelength, also at any other Reynolds number within our domain, to be much lower than that determined from our numerical stability analysis. Large differences between the predicted and measured critical Reynolds numbers and wavelengths provide the strongest evidence that centrifugal instability is not the mechanism at the origin of the leading three-dimensional instability mode. Any centrifugal instability would scale on the width of the band of streamlines exhibiting an outward decrease of circulation. In this case, the wavelength predicted by the absolute stability analysis is far larger than the potentially unstable streamline band.

Further analysis was carried out exploring the possibility of an elliptic instability acting in this flow. The flow under question is not ideal for such an analysis, due to the high eccentricity of the recirculation zone, hence, a straightforward theoretical prediction was not achieved; however, the observed characteristics were found to be consistent. The shape and position of the perturbation mode and an elliptical instability analysis - carried as far as the high-eccentricity flow under question would allow - were all consistent with an elliptic instability mechanism.

Chapter 5

Steady Flow Through an Axisymmetric Stenotic Geometry

5.1 Introduction

The aim of the study presented in this chapter and the next is to explore the effect on flow behaviour of a variation of the blockage ratio of a stenotic geometry. In effect, such a variation tracks the development of an arterial stenosis from its genesis to its more pathological states. To make the problem more tractable and at the same time more applicable as a useful base case, the blockage geometry is governed by only a single parameter, providing a well-defined parameter space. This chapter deals with steady inlet flow, while the next one deals with a pulsatile inlet. The study of steady inlet flow in relation to pulsatile flow is important for several reasons; firstly, the steady inlet flow is useful as a limiting case of pulsatile flow, where the amplitude of pulsation is zero. In a straight, unblocked tube, it can also be thought of as an average of the pulsatile flow. This relation is weakened by the presence of a blockage in the tube; the resulting similarity is investigated in chapter 6.

Considering that we are moving a small step closer to the simulation of realistic physiological geometries and flows, the various assumptions regarding the relation between our simulations and real blood flow need to be described. In a physiological blood flow, artery walls are compliant and respond to the fluid pressure and wall shear stresses. The walls of the tube of our model are considered to be rigid. As well as greatly simplifying our problem, the effect of compliant walls is generally considered negligible for the study of flows in larger arteries (Ku 1997; Wootton & Ku 1999). Compliant walls begin to have a more significant effect on the flow when it reaches the

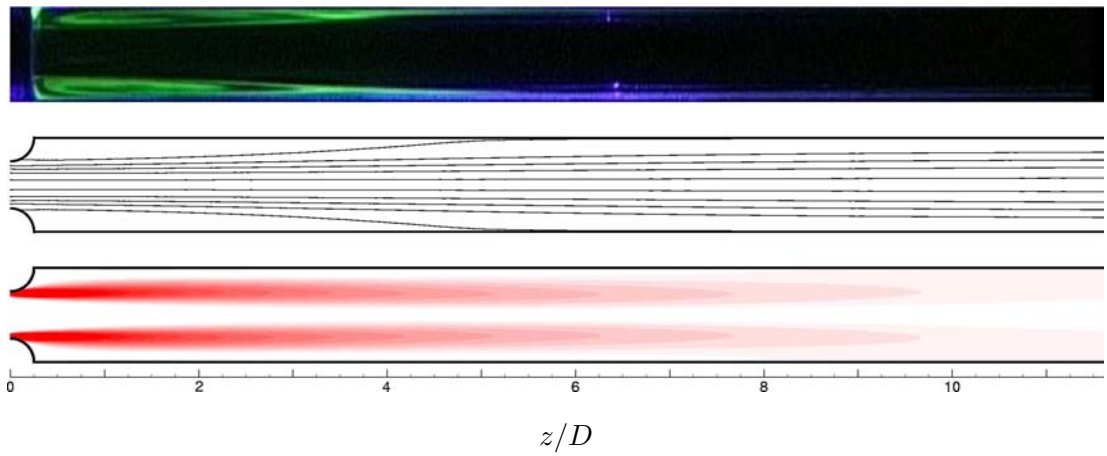

FIGURE 5.1: Comparison between the dye visualisation and numerical streamlines and vorticity, at $b = 0.75$ and $Re = 194$. Flow is from left to right.

smaller arterioles and capillaries.

Another issue relates to the non-Newtonian nature of blood. Blood is in fact a suspension of particles in a plasma. In our model, we assume the flow to be Newtonian. Similar to the assumption regarding compliant walls, for larger arteries, it is generally reasonable to assume the fluid to be Newtonian. It is only when we reach the smaller vessel diameters further down the cardiovascular system that the suspension particles begin to have a significant effect on the flow.

Flows both experimental and numerically-simulated are compared throughout this chapter. This allows observation of the relations and differences between real flows (with the effects of background noise and small asymmetries) and those simulated numerically.

5.2 Flow characteristics

Figure 5.1 depicts the generic flow structure under investigation, for $b = 0.75$ and $Re = 194$. At this Reynolds number the flow is laminar and steady. Experimentally, a recirculation zone is evident from the coloured dye trapped immediately downstream of the blockage; the rest of the dye in the mainstream flow is convected away (a reflection of the laser in the middle of the image on the bottom portion of the tube is present, and is evident in figure 5.1 as a thin, blue shade). For low Reynolds number, the dye remains in the recirculation zone long after the injection period. A comparison is made with

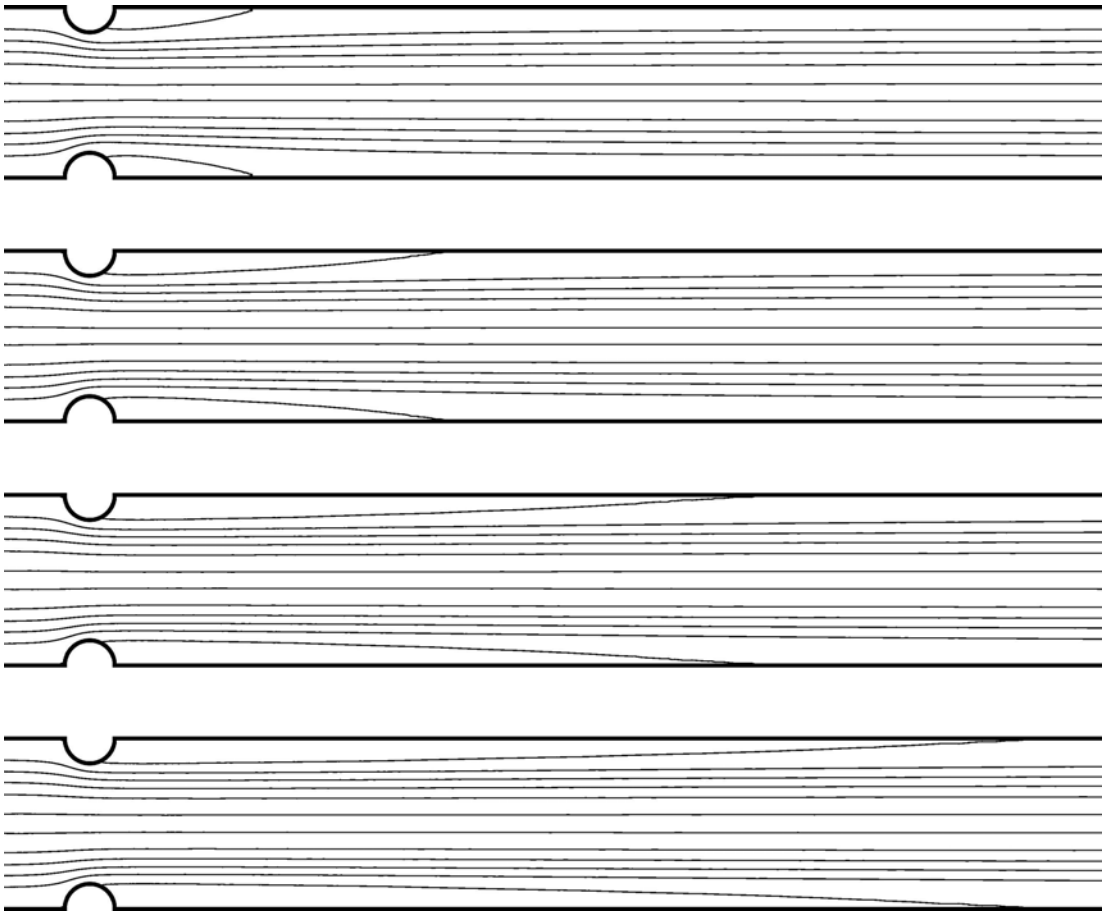

FIGURE 5.2: Streamlines at $b = 0.50$ and $Re = 200, 500, 1000$ and 1500. The terminating streamline indicates the recirculation length.

streamlines and the vorticity field taken from an equivalent numerical simulation. The recirculation zone is again apparent, this time by the separating streamline. The flow can be characterised as a confined jet emanating from the constriction, which expands downstream of the blockage. A long, thin shear layer is created by the detachment of the flow on the downstream half of the blockage. As the Reynolds number is increased, the length of the recirculation zone downstream of the blockage increases. Figure 5.2 shows streamlines for numerical simulations for a range of Reynolds numbers for $b = 0.50$. Across the blockage ratio range, the length of the recirculation zone increases linearly with Reynolds number. At its end, the recirculation zone is extremely thin, the terminating neutral streamline running nearly parallel to the wall.

Figure 5.3 compares, at the three blockage ratios tested experimentally ($b = 0.50$, 0.75, 0.90), velocity profiles taken using PIV with those taken numerically at the same

Reynolds numbers. PIV was not possible inside the contraction, $-r_b < z < r_b$, as the removable test section was not transparent; therefore only the profile of the numerical simulation is shown at $z = 0$. The agreement between the numerical and experimental results is very good; only small differences are apparent through the shear layer, where the velocity gradients are highest. Also, some differences exist close to the walls of the cylinder, where reflections of the laser caused by the curvature of the wall, as well as a lower density of particles, reduce the accuracy of the measurements. A masking was performed to remove the reflecting light from the images being treated; nonetheless, information was lost in this region. From the profiles, we see that the fully-developed Poiseuille flow upstream deforms to pass through the contraction, takes the form of a jet, and then expands, slowly re-approaching the fully-developed profile. The velocity scales on each of the three graphs are different, and are chosen to show the shapes of the profiles downstream of the contraction. The difference in scale between the three cases can be detected in the magnitude of the undeformed Poiseuille profile plotted at $z = -2D$. By comparing this profile with the profile in the blockage at $z = 0$, one obtains a sense of the greatly increased fluid velocity through the contraction; in the case of figure 5.3(c) with $b = 0.90$, the mean velocity inside the contraction is 10 times that in the unblocked tube ($\overline{U}_{(z=0)} = \overline{U}/(1-b) = 10\overline{U}$).

5.2.1 Recirculation zone lengths

At a point on the downstream surface of the blockage, the flow separates and a shear layer and recirculation zone are formed. As in chapter 4, the length of the recirculation zone, L_R, behind the blockage serves as a useful means to characterise the flow. Figure 5.4 depicts a comparison between a numerical simulation and a dye visualisation at $b = 0.90$ and $Re = 78$, as well as delineating the recirculation length, L_R. The recirculation zone is characterised by a zero wall shear stress at the point where its neutral streamline terminates at the wall, or $\tau_{(z=L_R)} = 0$. This wall shear stress behaviour along the recirculation length can be seen in figure 5.5. Here, the wall shear stress is plotted across the blockage ratio range at $Re = 600$. The wall shear stress, given by $\tau_{wall} = -\mu\partial u/\partial y$, is normalised by the dynamic pressure according to

$$\tau = \tau_{wall}/(\frac{1}{2}\rho\overline{U}^2) = -(\frac{2D}{Re\overline{U}})\frac{\partial u}{\partial y}. \tag{5.1}$$

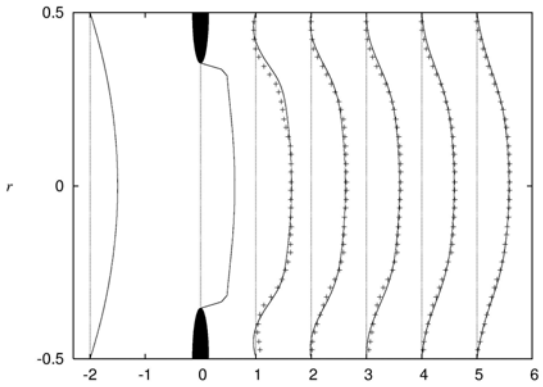

(*a*) $b = 0.50$, $Re = 791$

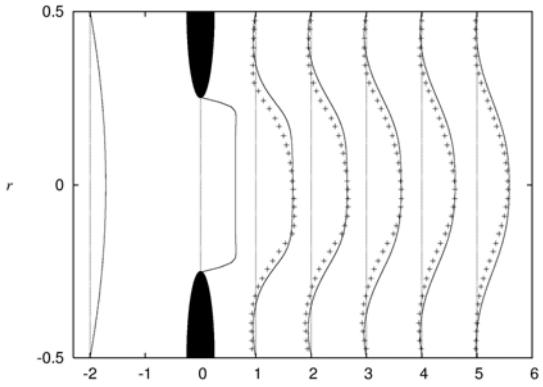

(*b*) $b = 0.75$, $Re = 306$

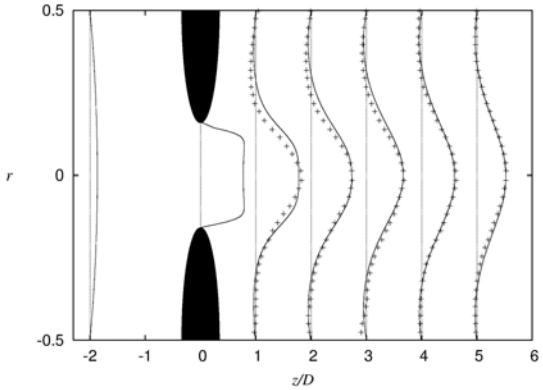

(*c*) $b = 0.90$, $Re = 104$

FIGURE 5.3: Comparison of experimental results velocity profiles (PIV) to those from numerical simulations. The scaling on the y-axis has been lengthened to better show the profiles.

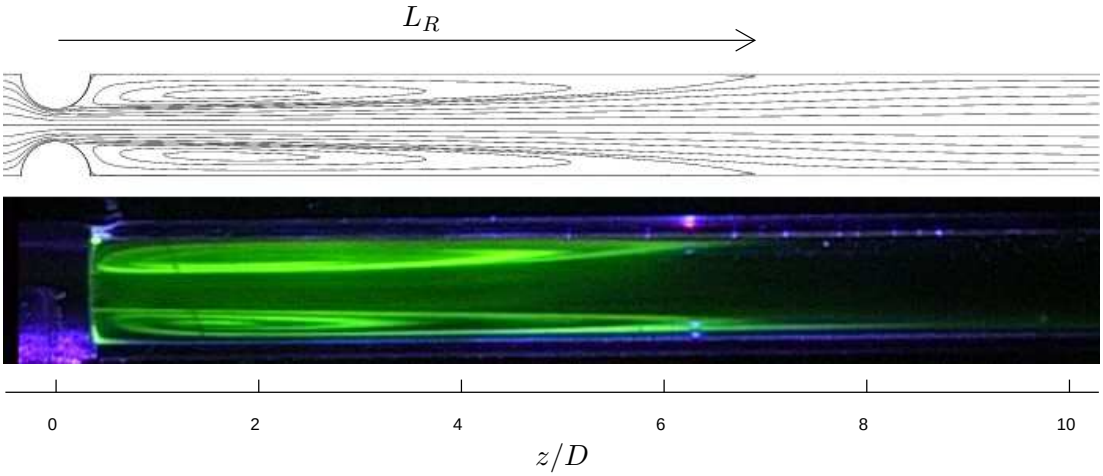

FIGURE 5.4: Comparison between numerical streamlines and dye visualisation at $b = 0.90$ and $Re = 78$. The length of the recirculation zone, L_R, is defined here.

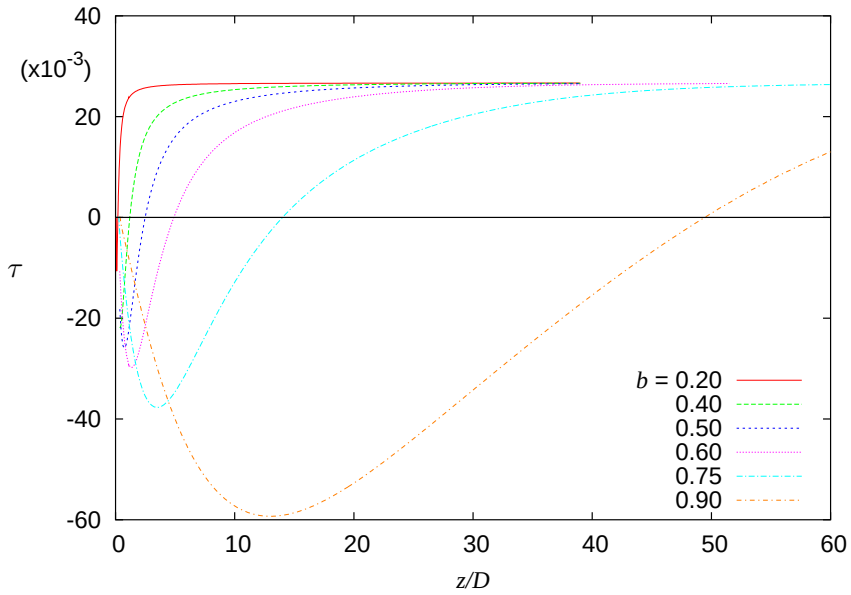

FIGURE 5.5: Distribution of dimensionless wall shear stress, τ, along the tube walls at $Re = 600$, across the blockage ratio range.

The recirculation length can be easily determined by tracking the wall shear stress and marking the z-location at which it changes sign. The increasing recirculation length, L_R, with blockage ratio is evident. At the lower extreme of the blockage ratio range, at $b = 0.20$ (a very small blockage), the end of the recirculation zone, where $\tau = 0$, is so small to be not discernible as represented on figure 5.5, whereas at $b = 0.90$, the recirculation length extends to approximately 50 diameters downstream.

In such a manner, recirculation lengths were determined across the parameter space.

Figure 5.6 shows the lengths across the blockage range tested numerically. From figures 5.6(a) and 5.6(b), we see a linear dependence of the recirculation length on Reynolds number, with the lengths at the higher end of the range increasing more rapidly. Indeed, above $b \approx 0.60$, the length increases sharply with blockage ratio when compared to the lower end of the range. This is not surprising, if we consider the increase in velocity through each of the blockage ratios. The velocity ratio at $b = 0.95$ of $\overline{U}_{(z=0)}/\overline{U} = 20$ is enormous when compared to the equivalent values of 1.25 and 1.67 for $b = 0.20$ and 0.40, respectively.

Therefore, clearly of interest is the possible existence of a relation between the different data sets for each blockage ratio, presumably in the form $L_R/D = f(b)Re$. To this end, an analogy is drawn between the present work and the wake behind a circular cylinder at low Reynolds number, before shedding occurs. Knowing that the length of the recirculation zone behind a circular cylinder varies linearly with the Reynolds number of that flow ($Re_{cyl} = U_f 2r_b/\nu$, where U_f is the freestream velocity and r_b is the radius of the blockage) (Taneda 1956), and that the fluid velocity through the contraction is analogous to the freestream velocity for the cylinder flow ($U_f = \overline{U}/(1-b)$), we can write

$$\frac{L_R}{D} = \frac{L_R}{r_b}.\frac{r_b}{D} \propto \frac{r_b}{D}.Re_{cyl}, \tag{5.2}$$

or

$$\frac{L_R}{D} = C\left(\frac{2r_b^2}{D^2\,(1-b)}.Re\right), \tag{5.3}$$

which in terms of b can be expressed as

$$\frac{L_R}{D} = C\left(\frac{1}{1-b} - \frac{1}{\sqrt{1-b}} - \frac{b}{2-2b}\right)Re, \tag{5.4}$$

where C is a constant (recall $r_b = (D-d)/2 = \frac{D}{2}\left(1-\sqrt{1-b}\right)$). In order to test the comparison, we divide the recirculation length, L_R/D, by the multiplier given in equation 5.4, which gives the scaled recirculation length, L^*, shown in figure 5.6(c). Away from the extremes of the blockage ratio, there is a good collapse of the data for the intermediate values of blockage ratio, showing that the analogy appears to hold. At $b = 0.20$, the blockage consists of a small bump on the tube wall, with $r_b = 0.0528$. At this height, the local fluid velocity is also very small, the fluid velocity decreasing quickly as we move closer to the wall. The greater part of the main fluid flow passes

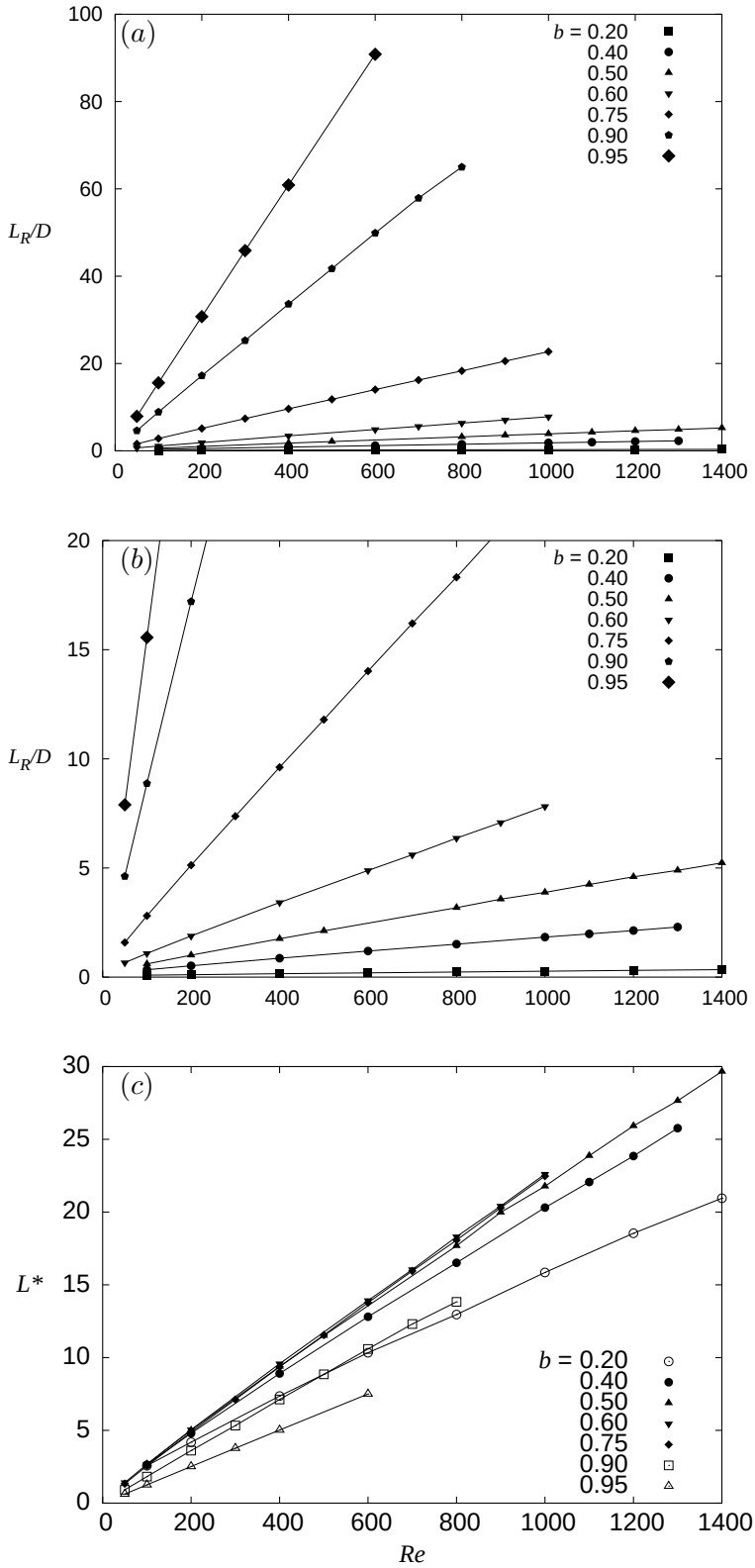

FIGURE 5.6: Recirculation zone lengths, (a) showing the complete data set, (b) zoomed in showing only lengths from $0 - 20D$ and (c) the result of the scaling described in equation 5.4.

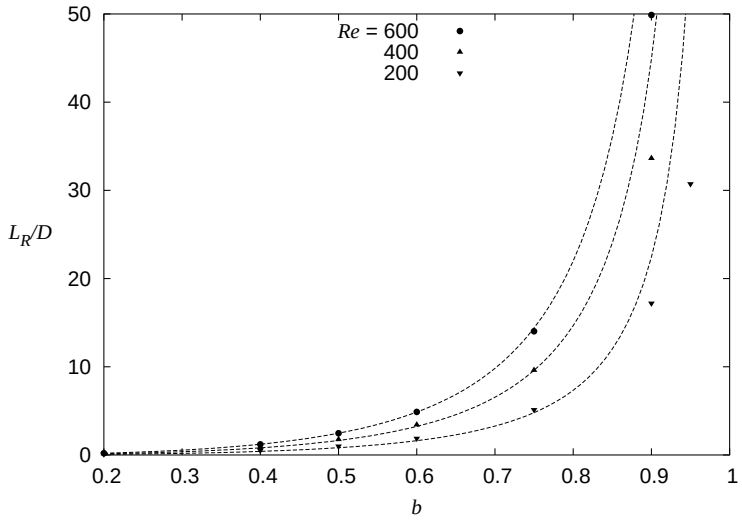

FIGURE 5.7: Variation of L_R/D with blockage ratio, at $Re = 200, 400, 600$. Dotted lines are plots of equation 5.4, with the constant C set to 0.048.

by the blockage, not perturbed to the extent of the flows through the larger blockage ratios. The difference in the flow conditions local to the blockage may account for the behaviour. At $b = 0.90$ and 0.95 there is also a divergence. These two cases are extreme, especially when we consider the contraction velocity ratio, $\overline{U}_{(z=0)}/\overline{U}$, of each case, the flow exhibiting a much stronger acceleration through the blockage in relation to the other geometries. At this end of the scale, the flow features begin to approach those of a jet entering a quiescent fluid, rather than those of a tube with a mild contraction. This can be further seen in figure 5.7, where the relation shown in equation 5.4 is compared with the measured values. The constant C was chosen to be equal to 0.048, this value giving the best match. The dotted lines, plotting equation 5.4, match well with the measured values, up to the geometry corresponding to $b = 0.75$, beyond which the analogy loses applicability.

5.2.2 Similarity

Following on from the strongly linear behaviour seen in the recirculation length variation (figure 5.6), another interesting characteristic is the presence of similarities across the Reynolds number range. At $b = 0.75$, figure 5.8 plots velocity profiles at various axial locations and a range of Reynolds numbers. By using the plotted lines in figure 5.8, and knowing the velocity field at one Reynolds number, the flow for another Reynolds number can be constructed. The profiles along the lines plotted are always identical.

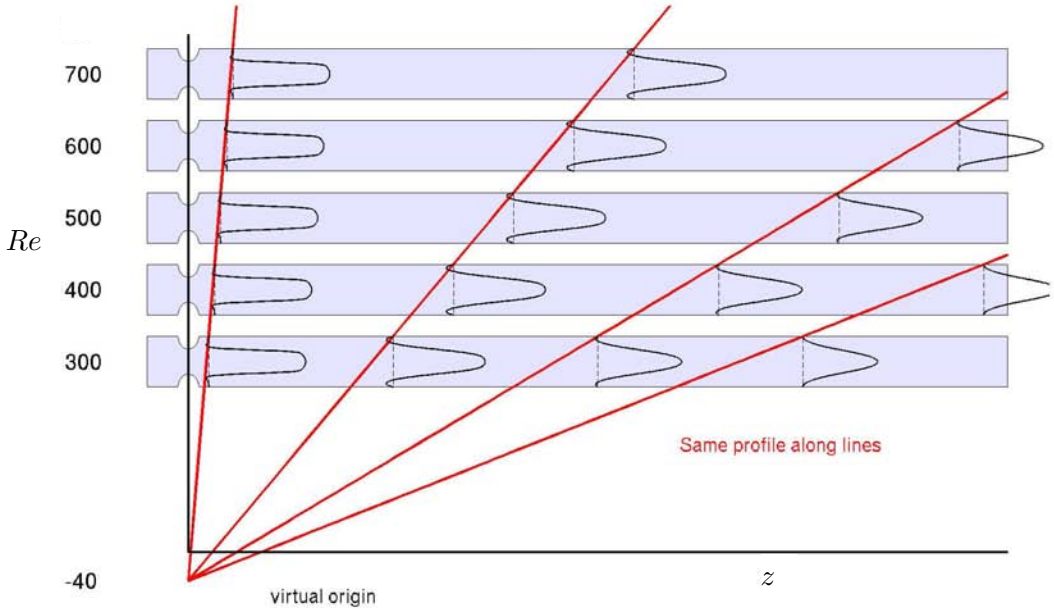

FIGURE 5.8: Graph showing similarity between profiles at different Reynolds numbers at $b = 0.75$. Across the Reynolds number range, the profiles are identical along the straight lines in the figure, which all have an origin at -40.

It is only closer to the contraction that the similarity is not as strong; however, even then the differences between the profiles are negligible. The strongly linear behaviour is in keeping with the linear behaviour seen in figures 5.6(a) and 5.6(b).

The variation of the profiles within the contractions, at $z = 0$, is shown in figure 5.9. From figure 5.9(a), we see that the profiles take an unexpected shape. Rather than u being at its maximum value in the middle of the tube, the maximum axial velocity is located at the outer edge of the contraction throat, at $r \approx 0.75(\frac{D}{2} - r_b)$, depending on Reynolds number. At high Reynolds numbers, the boundary layer formed over the blockage surface is thinner, therefore we find the local maximum of axial velocity closer to the tube wall; at low Reynolds numbers, the thicker boundary layer pushes the local maximum closer to the tube axis. Also shown on figure 5.9(a) is a single profile of absolute radial velocity, $|v|$. This v-velocity is generated by the fluid moving to the centre to squeeze through the contraction. It is likely this flow characteristic, the flow from the vicinity of the tube wall towards the centre of the tube, which accounts for the phenomenon of the near-wall velocity exceeding the centreline velocity.

In comparison to many other studies of stenotic geometries (Deplano & Siouffi 1999;

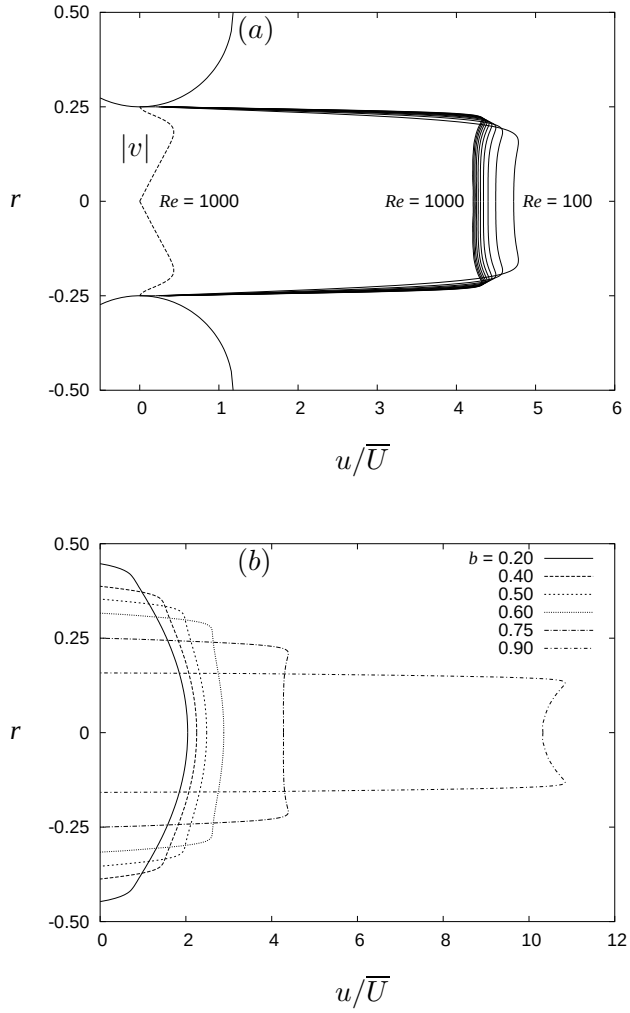

FIGURE 5.9: (a) Axial velocity profiles in the contraction of the $b = 0.75$ geometry, from $Re = 100$–1000, including a profile of absolute radial velocity, $|v|$, at $Re = 1000$, and (b) profiles in the contraction across the blockage ratio range, all at $Re = 600$.

Long *et al.* 2001; Mallinger & Drikakis 2002; Sherwin & Blackburn 2005; Stroud *et al.* 2000) the present geometry consists of a more rapid contraction of the flow. Indeed, the stenosis length is given by $2r_b = D(1 - \sqrt{1-b})$, which in the case of $b = 0.75$ corresponds to $0.5D$, as opposed to a stenosis length of $2D$ used in many other stenotic flow investigations. It is this feature of the present geometry which creates the near-wall maximum of velocity and the somewhat blunter profiles within the contraction.

The blunter velocity profiles also result in thinner shear layers emanating from the separation points than would be found in a stenotic flow of a longer stenosis length. The consequences of the thin shear layers on the stability of the flow are investigated later

in the chapter. Thus far, the analysis has dealt with the behaviour of the steady flow at low Reynolds number. In the next section, the stability of the flow as the Reynolds number is increased is investigated.

5.3 Instability

In pipe flow, it is widely assumed that the transition to turbulence commences at Reynolds numbers of approximately 2300. With the addition of a contraction, one would expect the threshold for stability to lower somewhat. Furthermore, some difference in the stability between the present problem and the more commonly chosen stenotic geometries is to be expected. This section deals firstly with a linear absolute stability analysis, followed by an investigation of how this relates to experimental flows.

5.3.1 Linear stability analysis

Figure 5.10 shows converged non-dimensional growth rates corresponding to the dominant linear instability mode for $b = 0.50$, 0.75 and 0.90, derived from the linear stability analysis technique described in chapter 3. At $b = 0.75$ and 0.90, we see that the most unstable azimuthal mode number is $m = 1$. In these cases, the flow becomes critical at $Re_c = 395$ and 770, respectively. For $b = 0.90$, the higher mode numbers fall away more rapidly than in the case of $b = 0.75$. This is a trend which continues as the blockage ratio decreases; the shapes of the stability curves change, with the higher mode numbers becoming more unstable. Indeed, at $b = 0.50$ and 0.60, the most unstable mode number is $m = 2$, the flow becoming critical at $Re_c = 2350$ and 1540, respectively. The critical Reynolds number for $b = 0.50$ of 2350 is around where we would expect to observe turbulence in a real pipe flow. However, with the analysis performed here being restricted to only absolute instabilities, we would not expect the transition in a unblocked pipe flow to manifest itself using the current techniques. The critical Reynolds number is based therefore on the flow structure resulting from the contraction.

5.3.1.1 Mode structures

Figure 5.11 depicts the structures of the unstable modes. The most unstable mode at $b = 0.50$, being of mode number $m = 2$, differs substantially from the other two cases presented, $b = 0.75$ and 0.90, those being of mode number $m = 1$. The structure of

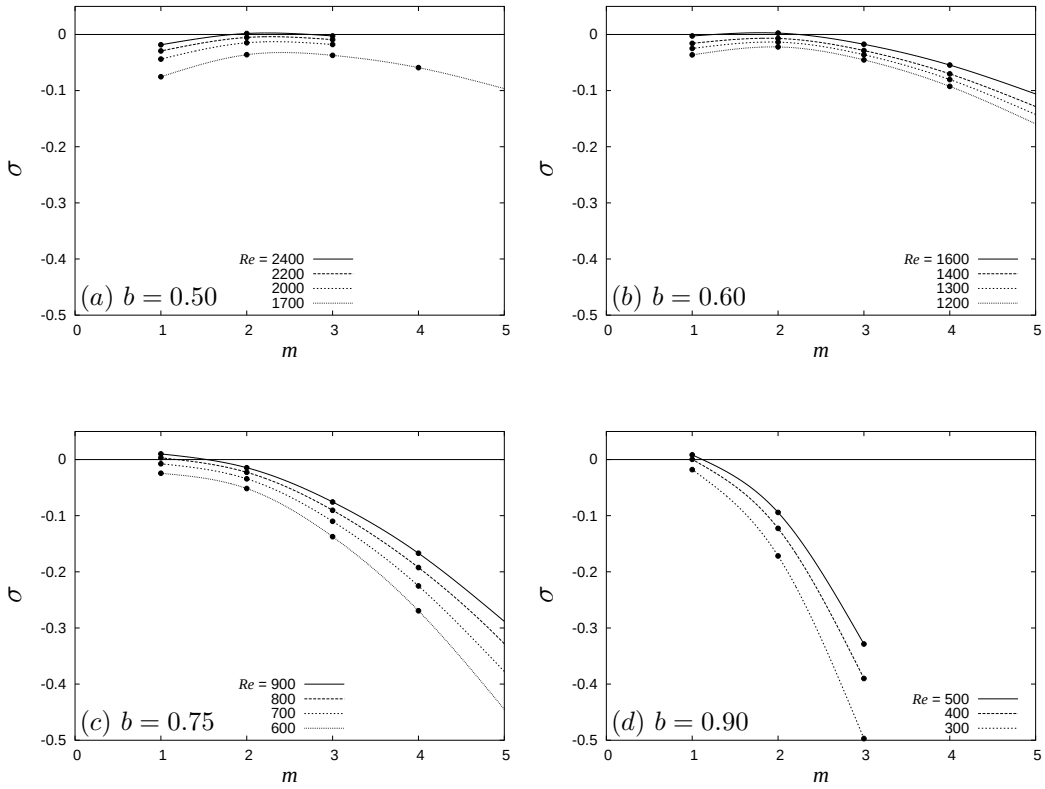

FIGURE 5.10: Plots of growth rates against azimuthal mode number, m, for absolute linear stability at $b = 0.50$, 0.60, 0.75 and 0.90. Lines have been drawn between the points to delineate the different Reynolds numbers.

the mode in figure 5.11(b), where $b = 0.75$, matches closely that reported by Sherwin & Blackburn (2005) for their geometry of identical blockage ratio. They reported a critical Reynolds number of 722, compared with the present value of 770. There is no obvious reason why the flow here should be more stable than the flow investigated by Sherwin & Blackburn (2005).

The mode at $b = 0.90$, (see figure 5.11(c)) is essentially of the same form as at $b = 0.75$. The differences with the form of the mode at $b = 0.75$ are attributable to the narrower jet and longer recirculation zone present in the mode at $b = 0.90$. Broadly speaking, the two modes are characterised by a vorticity structure reaching downstream from the inside of the contraction, symmetrical about a plane of the tube, excepting a change in sign of the vorticity. By adding the perturbation mode to the base flow, a better idea of the form of the unstable flow is obtained. A single contour of azimuthal vorticity of a linear combination of the perturbation mode and base flow is plotted in

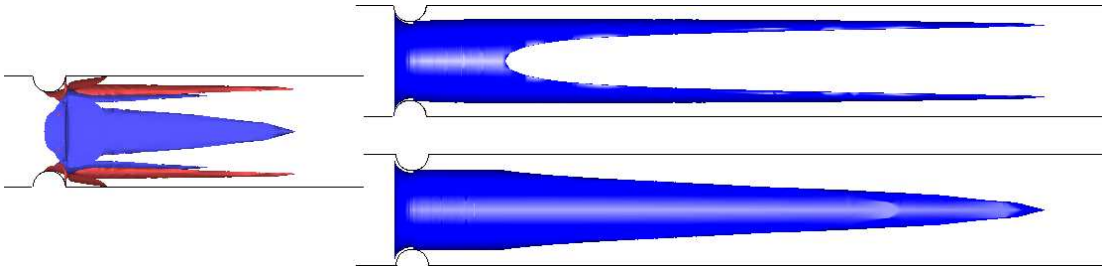

(a) $b = 0.50$

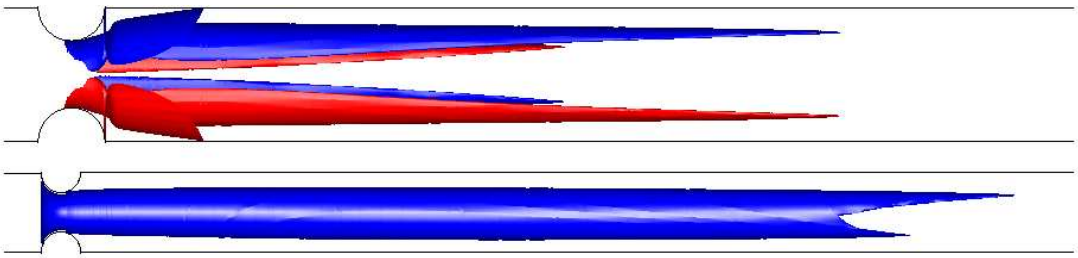

(b) $b = 0.75$

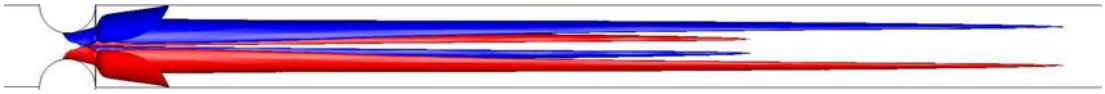

(c) $b = 0.90$

FIGURE 5.11: Plots of the most critical modes: (a) $b = 0.50$ and $Re = 2400$; at left, positive and negative isosurfaces of the streamwise vorticity of the most unstable perturbation mode ($m = 2$); at right, top and side views of an isosurface of the azimuthal vorticity for a linear combination of the base flow and the perturbation mode, (b) $b = 0.75$ and $Re = 800$; top, isosurfaces of the streamwise vorticity of the most unstable perturbation mode ($m = 1$), bottom, azimuthal vorticity of a combination of the base flow and mode and (c) $b = 0.90$ and $Re = 400$, isosurfaces of the streamwise vorticity of the most unstable perturbation mode ($m = 1$). All Reynolds numbers chosen here are slightly greater than the critical Reynolds number, Re_c, in each case.

figure 5.11(b). For a stable flow, this contour would be axisymmetrically poised about the centreline of the tube, ending at all azimuthal positions at the same axial location. From this plot of the perturbed flow we see that the instability would manifest as a loss of symmetry of the jet. The asymmetry can be seen as a tilting of the jet towards the bottom of the page, as well as in the irregular shape at the end of the plotted contour.

Whereas the mode $m = 1$ consists of a loss of symmetry of the jet downstream of the blockage, (see figure 5.11(b)) for $b = 0.50$ a different transition occurs. In this case,

the mode number of $m = 2$ results in a four-pronged configuration of the mode seen at $b = 0.75$ and 0.90. The mode is symmetrical about any plane of the tube. At the right of figure 5.11(a), the plot of the linear combination of the base flow and perturbation mode reveals a pinching of the jet emanating from the contraction; in contrast to the $m = 1$ mode, the centreline of the jet remains undeflected.

As mentioned earlier, the linear stability analysis conducted here relates to absolute instabilities. The next section of the chapter deals with the stability of the flow as observed experimentally.

5.3.2 Instability: experimental

In contrast to the numerical simulations, all the results taken under experimental conditions are inevitably subject to some level of noise, be it originating from the environment or from imperfections in the construction of the rig. Every effort was made to reduce noise and experimental error, including the isolation of the pump driving the flow through the rig and the careful alignment of the approximately 4 metres of straight pipe employed in the rig. Another important difference with the numerical investigation is the nature of the stability analysis of section 5.3.1, which only related to absolute stability. In the experiment, the presence of noise combined with the long thin shear layers which characterise the types of flow under investigation here, indicates a strong probability of convective instability playing a role in the stability of the flow.

As already shown in figure 5.6, the length of the recirculation zone increases linearly with the Reynolds numbers. Experimentally however, the behaviour reveals itself to be not as simple, nor predictable. Figure 5.12 shows dye visualisations for a range of Reynolds numbers, across the three blockage ratios tested experimentally, $b = 0.50$, 0.75 and 0.90. In the three cases, for low Reynolds number the flow is steady and matches closely with the numerical results. But as seen in the fourth image of each of the three cases of figure 5.12, at sufficiently high Reynolds numbers the flow becomes unstable. The instability seen in each case does not seem to match the types of instability predicted in section 5.3.1. Firstly, there does not appear to be any absolute loss of symmetry in the flow, which we would expect in the cases of $b = 0.75$ and 0.90. The instability seen experimentally consists of small waves developing in the shear layer, just downstream of the blockage, which propagate downstream. The instability

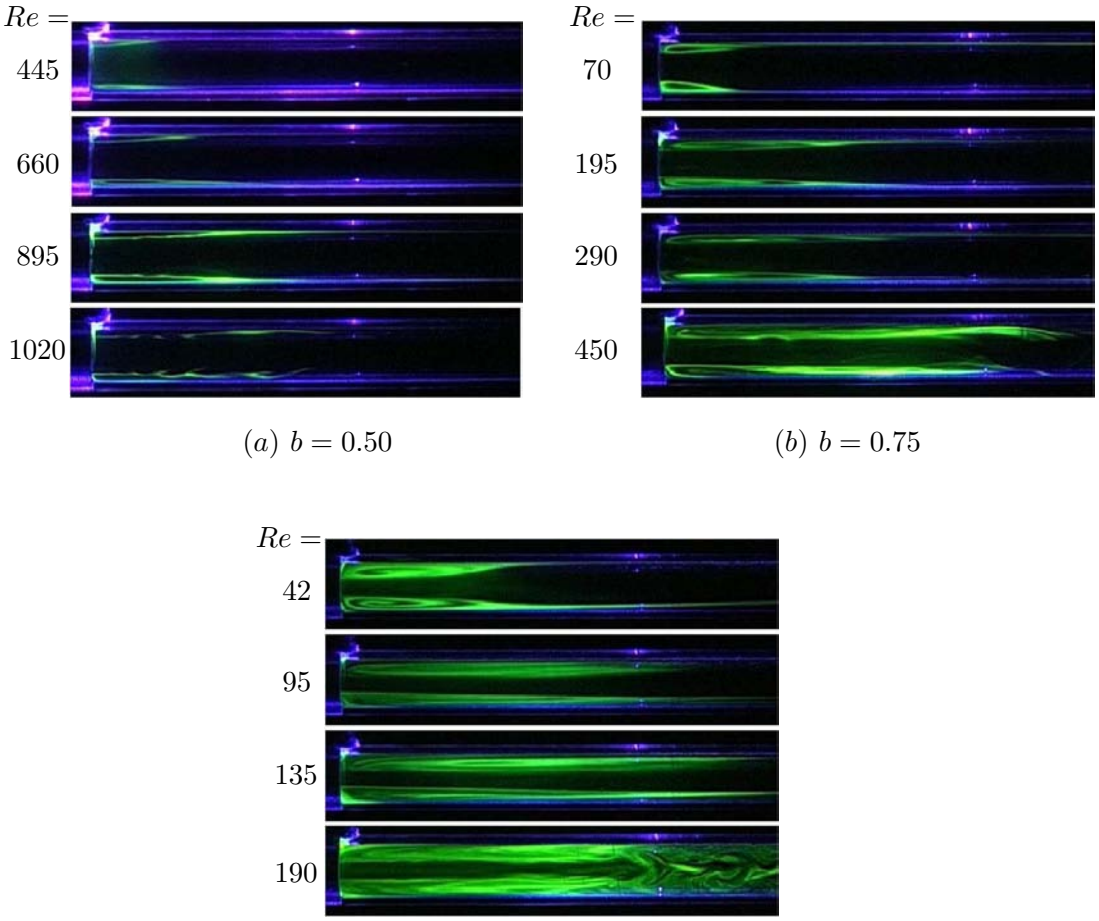

(a) $b = 0.50$ (b) $b = 0.75$

(c) $b = 0.90$

FIGURE 5.12: Dye visualisations at (a) $b = 0.50$, $Re = 445$, 660, 895, 1020 (b) $b = 0.75$, Re=70, 195, 290, 450 and (c) $b = 0.90$, $Re = 42$, 95, 135, 194. The areas immediately downstream of the non-transparent blockage section, at left, is shown.

appears to be of a Kelvin-Helmholtz type, with the long thin shear layer oscillating and responding to ambient noise in the system. The boundary for the appearance of this instability is difficult to determine precisely. For high Reynolds number, where the flow is very unstable, the waves propagating along the shear layer meet an area of general flow breakdown, usually approximately four to five diameters downstream. Such an instance is shown in the fourth image of figure 5.12(c). Here, the end of the recirculation zone is no longer apparent and the shear layer parallel with the tube walls. The two unstable cases shown in figures 5.12(a) and 5.12(b) are of Reynolds numbers closer to the critical boundary for instability. In these cases, there is no area of general unsteadiness five diameters downstream of the blockage. Rather the shear layer waves propagate the length of the separated recirculation zone, and then appear to disturb

the end of the recirculation zone. This "lifting-off" of the end of the recirculation zone is strongly reminiscent of the flapping recirculation zone observed behind a bump in an open flow. Marquillie & Ehrenstein (2003) found that the end of a recirculation zone, particularly in the case of a long thin zone, was susceptible to a lifting-off and then continuous irregular flapping.

A possible path to instability for the experimental flow begins with an excitable shear layer, which at a certain critical Reynolds number begins to oscillate gently when subject to enough noise. An example of such a flow can be seen in the third image of figure 5.12(a) at $Re = 895$, where the flow appears stable, but a small oscillation is evident on the recirculation zone. In such marginally stable cases, often the waves in the shear layer emerge a short distance downstream of the blockage and then peter out before the wave reaches the end of the recirculation zone. Therefore, the end of the recirculation zone is only subject to a negligible disturbance and remains attached to the wall. For slightly higher Reynolds numbers, such as in the fourth images of figures 5.12(a) and 5.12(b), the shear layer waves are of sufficient strength to disturb and detach the end of the recirculation zone, at which point it begins to flap. At higher Reynolds numbers, the flapping is sufficient to generate the unsteadiness seen in the fourth image of figure 5.12(c). Indeed, the shear layer waves in this particular case appear to not be strong enough to even form a clearly identifiable rolled-up vortex typical of a Kelvin-Helmholtz instability; rather the shear layer seems to gently undulate, before reaching a region of far stronger unsteadiness four to five diameters downstream. Therefore, this possible transition path for instability relies on the existence of an unstable recirculation zone end, which is set off by relatively low-level Kelvin-Helmholtz shear layer oscillations.

The boundary where we see this instability manifest itself is shown as the dotted line in figure 5.13, marked as 'convective instability (exp.)'. The boundary of the instability was chosen at the Reynolds number where a sustained unsteadiness was observed. A good example of such a case is shown in the third image of figure 5.12(a), at $Re = 895$. Below this boundary, flows could display some unsteadiness. The non-exactness of this boundary is due chiefly to the nature of the instability, which responds to latent noise in the system. Being subject to the strength of the disturbance, the response of the instability near the threshold was highly sensitive. Figure 5.13 also highlights the large

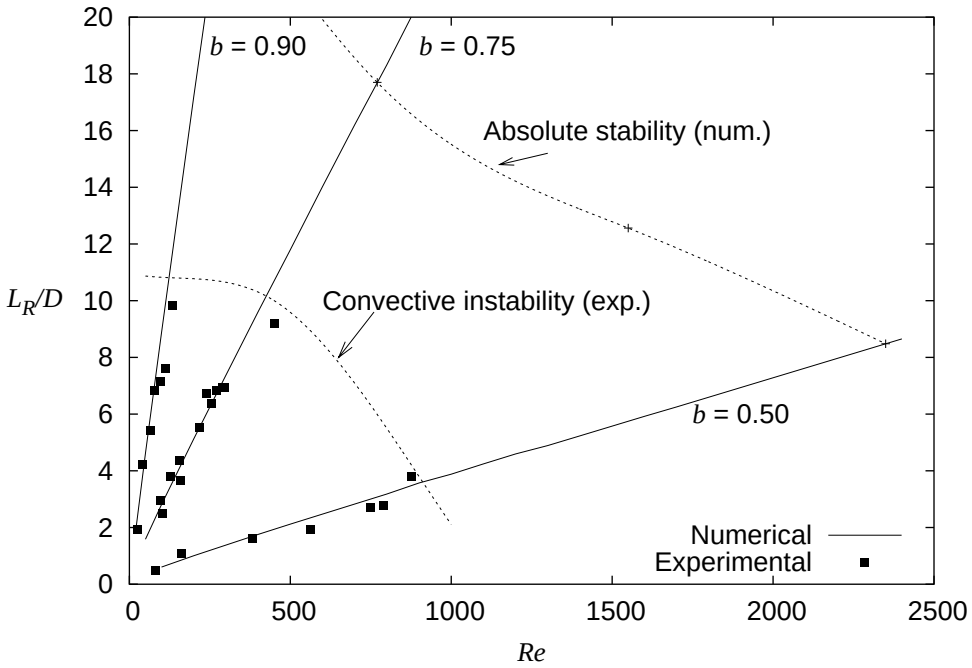

FIGURE 5.13: Description of boundaries of stability, as well as a comparison of recirculation lengths taken from experimental and numerical results. Solid black squares represent lengths taken from dye-visualisations.

difference between the boundary for convective stability and the boundary for absolute stability predicted from the numerical linear stability analysis.

Below this boundary is also plotted a comparison between the numerically determined recirculation lengths and those measured from the experiment using the dye visualisations. The results show a good agreement, up to the point where convective instability, not accounted for in the numerical simulations, sets in. Ahmed & Giddens (1983b) employed a cosine stenosis of stenosis length 2 and blockage ratio 0.75. At a Reynolds number $Re = 500$, they observed, from velocity profile measurements, a recirculation zone length of approximately $L_R = 4$, which is somewhat lower than the value for the present work. This is likely due to a difference in method. The recirculation zone, particularly for its downstream portion, is so thin as to make its detection difficult. Our method using coloured dye-visualisations, which create a high contrast between the mainstream flow and the secondary recirculation zone, allows the entire downstream extent of the separation to be observed. Predicting the recirculation zone length from velocity profiles requires a high resolution near the wall due to zone thinness; this is not always possible with experimental measurements. This would explain

the relatively large difference between the recirculation zone lengths.

The boundary for convective instability in the flow is somewhat lower than would be expected given the critical Reynolds numbers predicted in other experimental studies of steady stenotic flows. At Reynolds number $Re = 500$, Ahmed & Giddens (1983b) observed velocity oscillations of discrete frequencies, but make no mention of any turbulence. At $Re = 1000$ however, they note in addition a region of turbulence for $z/D > 4$. In relation to the present work, one would expect that the velocity oscillations of discrete frequency seen in Ahmed & Giddens (1983b) would correspond with the type of convective instability seen above the boundary plotted in figure 5.13. Indeed, what could be described as turbulence with any certainty only appeared on flows of Reynolds numbers somewhat higher than the boundary for convective instability.

What this plot highlights is that experimentally the instability seen in the shear layer plays a major role in the transition of the flow from a steady state. Hence, the instability modes shown in figure 5.11 were never visible in the experiments. It is possible that they were present, despite the unsteadiness and irregularity caused by the convective shear-layer instability, but were undetectable by the experimental methods. At the critical Reynolds numbers predicted numerically, experimental flows showed large convective growth of shear-layer modes leading to strong turbulence a short distance downstream of the blockage, such as seen in the two flows presented in figure 5.14 of the next section.

5.3.2.1 Shear-layer oscillations

Figure 5.14(a) shows an image of the unstable flow at $Re = 534$ and $b = 0.75$. In this case the shear layers emanating from the blockage appear to be parallel with the direction of the tube. The waves in the shear layer are just apparent downstream of the blockage, while the large breakdown of the flow and the recirculation zone is evident at approximately five diameters downstream. The second, larger image in the figure is a spatio-temporal diagram, constructed using the portion of the image along the straight, grey line in the first image. The same image from each frame of the film is collected and recompiled in a new image, in effect swapping the horizontal spatial dimension with time. In this way, the regular waves in the shear layer can be seen as the straight lines to the left of the diagram. As we move downstream, the spatio-temporal

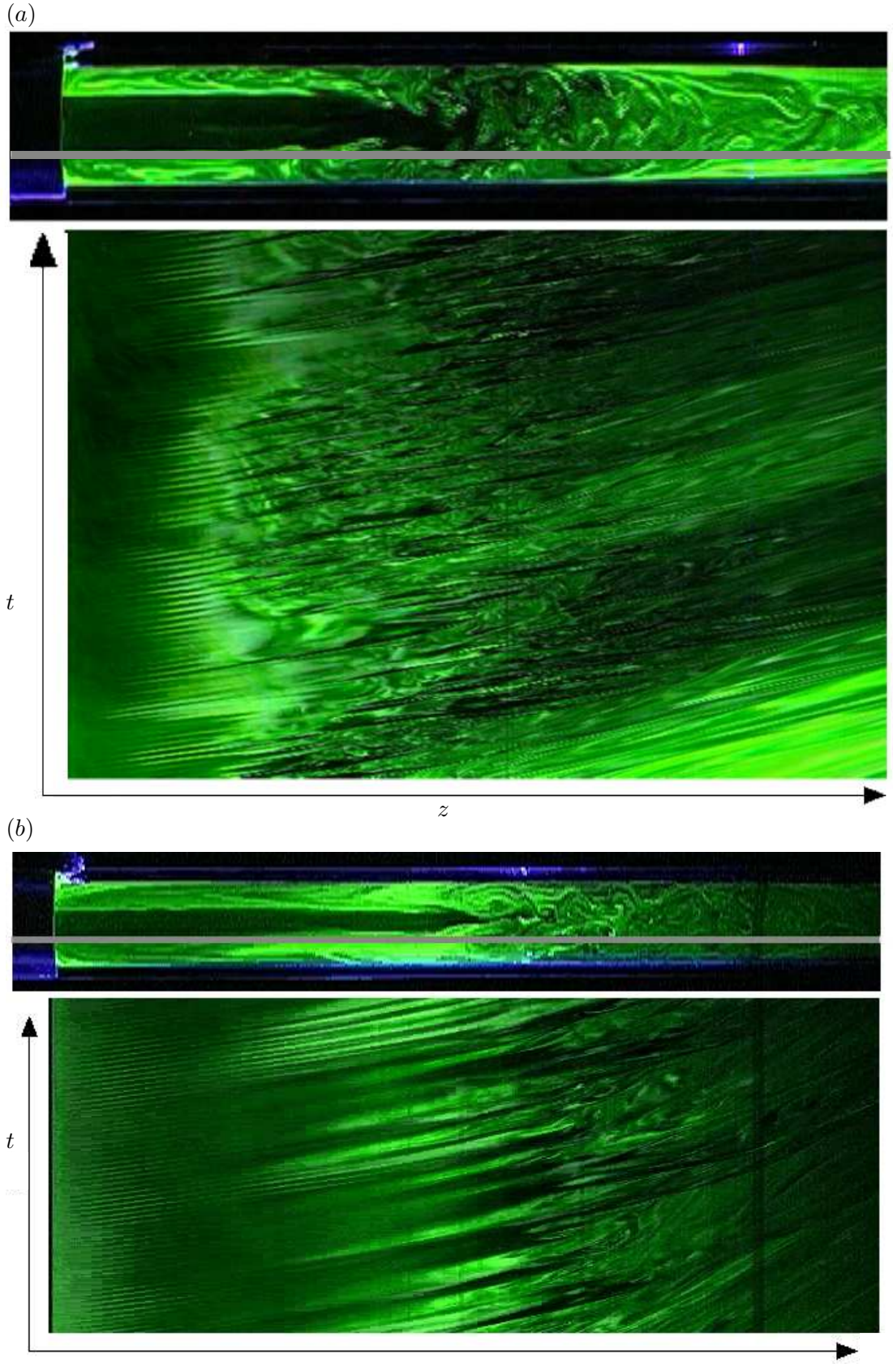

FIGURE 5.14: At top, (a) the unsteady flow at $b = 0.75$ and $Re = 534$ and bottom, (b) at $b = 0.90, Re = 194$. The spatio-temporal diagrams are constructed using the blanked out line in each case. The waves seen in the shear layer are evident as straight lines to the left of the spatio-temporal diagrams.

depiction of the flow becomes muddier, indicating the break up of the shear layer and the strong unsteadiness apparent in the unaltered image of the flow. After this section, the streaklines drawn by the dye become mixed and less meaningful. There is some evidence of the existence of an intermittency in the flow, indicated by the longer time-scale variation in the strength of the dye at the right of the spatio-temporal diagram; however, this intermittency is highly irregular and was difficult to reproduce from one experimental run to the next. The flow presented in figure 5.14(b), also highly unsteady, is at $Re = 194$ and $b = 0.90$. In this case, the shear layer waves appear at a higher frequency than that observed in the flow of figure 5.14(a). Also evident in the $b = 0.90$ case is another intermittence, particularly near $z/D \approx 3$. Some of the shear layer waves propagate the entire length of the shear layer, many quickly peter out, while several appear to combine into larger waves, which are observable right up to the beginning of the strongly unsteady area. The irregular behaviour and strength of the shear layer waves indicate that the flow is highly sensitive and also points to the possible presence of a non-uniform noise. The response of the flow to a relatively strong disturbance of a particular frequency, originating from somewhere in the rig or the environment is a possibility that needs to be addressed. To do so, the period of these shear layer waves is examined.

Using the spatio-temporal diagrams, the period of the waves can be measured and a non-dimensionalised period, T, calculated. The period was measured in seconds and then normalised according to the scaling

$$T = \frac{T_D \overline{U}}{D}, \tag{5.5}$$

where T_D refers to the measured time of the period. This same non-dimensionalised period is employed throughout the thesis and is used in describing the periodic forcing discussed later in this chapter, as well as the period of pulsation used in the investigation of pulsatile flows in the next chapter. The formulation of T is in fact the same as the reduced velocity term used in the work of Sherwin & Blackburn (2005); however, due to the application of this same non-dimensionalisation to many facets of the study, it was found to be more appropriate to think of this quantity as a non-dimensionalised period, be it of a periodic forcing, shear-layer oscillation or a large amplitude pulsatile flow.

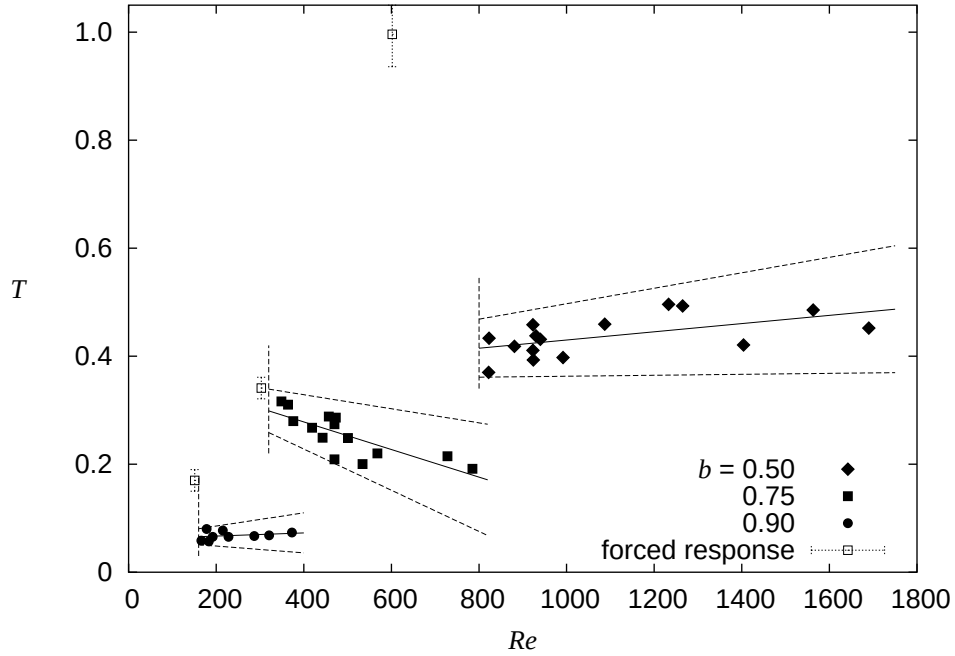

FIGURE 5.15: Measured instability periods across the blockage ratios tested experimentally. The hollow boxes indicate the forcing period, T_p, which produces the greatest response in the flow, while vertical dotted lines show the lower limit of where a period of oscillation is able to be measured – this does not necessarily match-up with the threshold of instability described in figure 5.13. Also included are 95% confidence limits for each of the three data sets.

The measurement of the period of the shear layer waves was always measured as close to the blockage as possible; this was typically 1 to 2 diameters downstream of the blockage. The initial observation was that the period of the oscillations, measured in seconds, varied strongly with Reynolds number and blockage ratio. This indicates that the oscillations are not associated with any latent frequency generated by the experimental apparatus. The result when the scaling of equation 5.5 is applied is presented in figure 5.15, which plots the non-dimensionalised periods of the shear layer oscillations, T, across the three blockage ratios tested experimentally. In cases near the threshold of instability, oscillation periods were measured from flows that did not always display sustained unsteadiness; in this way, data points were obtained at the lowest possible Reynolds numbers. Therefore, the boundaries in figures 5.13 and 5.15 do not necessarily align with each other. We see that across the three blockages tested, the non-dimensionalised period of this instability remains roughly constant, particularly in the cases corresponding to $b = 0.50$ and 0.90. However, the data set at $b = 0.75$ appears to show a small decrease in period as the Reynolds number is increased. No physical

mechanism is immediately obvious which might explain this difference; also plotted on figure 5.15 are lines of best fit for the three data sets, as well as 95% confidence intervals. The configuration of the intervals for the data set at $b = 0.75$ leaves open the possibility that the period of the instability is still roughly constant with Reynolds number at $b = 0.75$; however, the question remains open and would require further investigation.

5.3.2.2 Periodically-forced flows: experimental

In order to better understand the observed shear layer behaviour, the focus is now moved to those stable and steady flows which rest just below the threshold for convective instability, which is described on figure 5.13. To this end, the piston, as outlined in chapter 3, was employed on the experimental rig. Setting the piston motion to a very small amplitude of oscillation allows us to examine nominally stable flows just below the threshold of instability, which are subjected to a periodic excitation. The three flows considered here ($b = 0.50$ and $Re = 600$, $b = 0.75$ and $Re = 300$ and $b = 0.90$ and $Re = 150$) are chosen because experimentally they are steady and do not exhibit any apparent convective instability. All three flow configurations are not only stable, but strongly so, always returning quickly to steady state after any sort of disturbance. In this way, any response observed in the shear layer can be attributed without hesitation to the motion of the piston. The response consists of waves in the shear layer, corresponding to the frequency of the forcing, which die away further downstream. This results in no major breakdown of the flow, such as that in figure 5.14. The forcing of the piston is sinusoidal and the amplitude kept constant across the frequency range for each blockage ratio. The amplitude is chosen to be strong enough so to excite a response in the shear layer sufficiently large to be seen and measured; generally, flows at $b = 0.50$ and $Re = 600$ required an amplitude of forcing of approximately $A = 0.04$, while at $b = 0.90$ and $Re = 150$, the amplitude was approximately $A = 0.01$. An example is shown in figure 5.16, where $b = 0.75$, $Re = 290$ and the forcing is at $T = 0.3$. The forcing in this case causes a strong roll-up of the shear layer into vortices which then quickly dissipate as they move downstream. In the case presented in figure 5.16, the forcing amplitude is very high, at $A = 0.05$, which is twice the amplitude required to produce an observable response at the peak forcing period. This particular case is presented

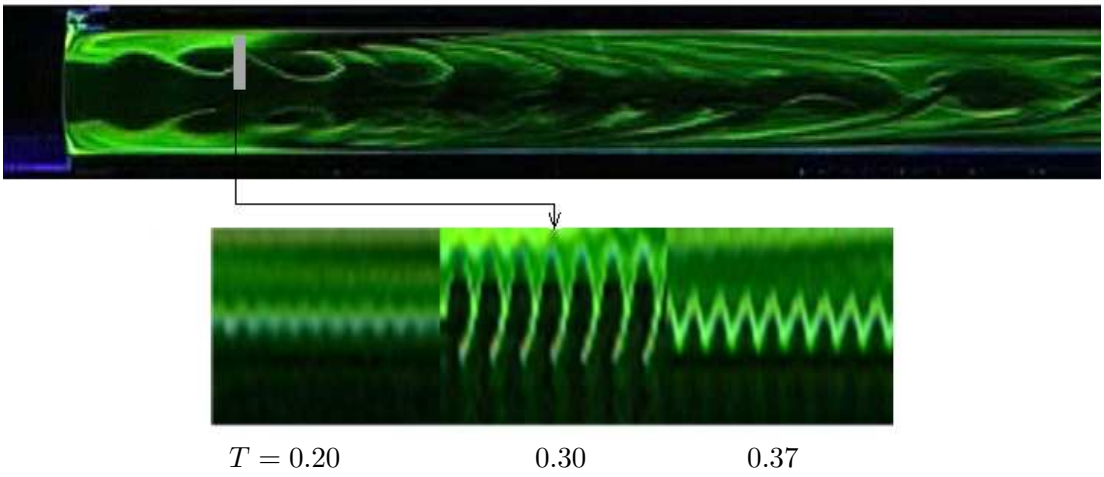

FIGURE 5.16: At top, the periodically forced flow at $b = 0.75, Re = 295$, at a frequency of $T = 0.30$. The amplitude of the forcing is at $A = 0.05$. Spatio-temporal plots of the top shear layer are shown, for $T = 0.20$, 0.30 and 0.37, left to right.

in figure 5.16 as it best highlights the difference in response which we see at different forcing frequencies. In the second part of the figure, three spatio-temporal images are shown, this time taken from the vertical grey block on the original image; a single pixel width is taken from each frame and then added together horizontally. The middle image of the trio corresponds to the flow depicted in the top image. The axial locations where the response was greatest were chosen to measure the response. In this way an approximate idea of the peak forcing frequency, T_p, could be determined. The response is very small at $T = 0.20$, while at $T = 0.30$, the forcing has caused the shear layer to roll-up; at $T = 0.37$, the response has decreased again.

After a general idea of the peak forcing frequency is obtained, a more exact peak forcing frequency can be determined. Firstly, a smaller forcing amplitude is chosen, to avoid the (non-linear) roll-up evident in figure 5.16; in this way, the stable flow configuration is retained as far as possible. Then in a single run, the forcing is begun at a period known to be less than T_p and slowly increased to a value known to be greater. In this way, the forcing inducing the greatest amplitude response in the shear layer can be determined more accurately. The three non-dimensional periods, T_p, found for each flow configuration are plotted as hollow boxes on figure 5.15.

All three values of T_p are higher than the corresponding measured periods of the self-sustaining shear layer oscillations of the higher Reynolds number flows. Only in

the case of $b = 0.75$ do the measured oscillation periods exhibit a trend towards the value of T_p; for the other two blockage ratios, T_p is significantly greater.

In summary, the forcing period at which the shear layer of flows in the stable regime respond most strongly is higher than the period of oscillation of shear layer waves seen in convectively unstable flows of higher Reynolds number. There are several possible contributing factors to this phenomenon. The parallel nature of the shear layers in the unstable regime – as opposed to the gently curved recirculation zones of the stable regime – may play a role. However, the most obvious difference between the two generic flows either side of the stability boundary is the existence in one of an area of strong unsteadiness 4 to 5 diameters downstream of the blockage, and its absence in the other. In those cases where a steady flow is forced, the excitation is evident in perturbations in the shear layer just downstream of the blockage. These perturbations or waves then die away, with the flow remaining steady and unperturbed further downstream. However, when dealing with the unforced flows of higher Reynolds number, the equivalent waves of the self-sustained instability seen in the shear layer travel the length of the recirculation, the end of which is detached and free from the wall, lost somewhere amongst the breakdown of the flow, as seen in figure 5.14. It is possible that this area of turbulence is the source of the higher frequency perturbations seen in the convectively unstable flows. A non-linear feedback from the downstream turbulence may be altering the noise profile that the flow is normally subject to in the experiment. In this scenario, the uneven excitation of the shear layer results in what would normally be the most dominant frequency being overtaken by others. Such an explanation would also account for the roughly constant period of shear-layer oscillation seen at higher Reynolds number. In the next section, an attempt is made to further explore the problem of convective instability, this time numerically.

5.3.2.3 Periodically-forced flows: numerical

The action of the piston in section 5.3.2.2 can be easily reproduced numerically. Perturbations of a wide number of frequencies and amplitudes can be applied at the inlet using equation 3.30; in all the results presented in this section, an amplitude of $A = 0.001$ is used, regardless of the Reynolds number or blockage ratio. In many simulations, this produces a disturbance in the flow which is not apparent to the naked eye. For higher

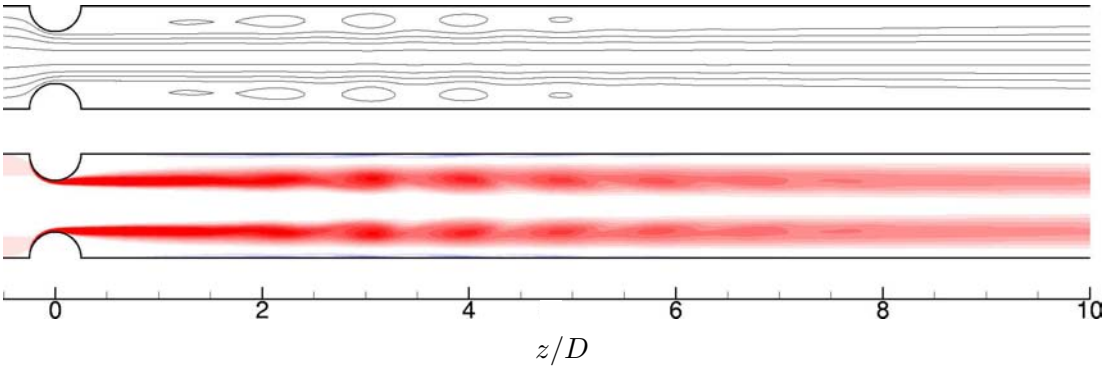

FIGURE 5.17: Streamlines and vorticity contours for the flow at $Re = 550$ and $b = 0.75$, with a perturbation of period $T = 0.35$ and amplitude $A = 0.001$.

Reynolds numbers, the excitation tends to being more obvious; figure 5.17 presents the streamlines and vorticity field at $Re = 550$ and $b = 0.75$, with a perturbation of period $T = 0.35$, which is close to T_p for this flow configuration. Here, we can see the shear layer rolling up into discrete vortices, as well as the gentle undulations in the recirculation zone, similar to what was observed in the experiments.

With the entire velocity field known, the response to the forcing can be measured more accurately. This is done by calculating the maximum (over one period of the perturbation) of the integral summation over the domain of the velocity of the perturbed flow minus the velocity field of the unperturbed base flow, of the form:

$$W = \iint (\overline{\mathbf{u}} - \overline{\mathbf{u}}_{base})^2 dr dz. \tag{5.6}$$

This expression gives a precise relative measure of the disturbance caused by the forcing, even for cases where the excited response is very small.

Figure 5.18 plots the response, W, against forcing period, T, across several Reynolds numbers and at blockage ratios of $b = 0.50$, 0.75 and 0.90. From figure 5.18(a), we see that at $Re = 600$ and $b = 0.50$ the period which excites the greatest response in the flow is $T_p = 0.92$. This compares with the value calculated from the experimental dye-visualisations of 1.00 ± 0.06. As the Reynolds number is increased, the response increases exponentially, however the behaviour of the response curve does not change significantly. It is only at higher Reynolds numbers that the curve changes and the value of T_p increases to approximately 0.98, as can be seen in the inset figure. From figure 5.18(b), at $Re = 300$ and $b = 0.75$, the peak response occurs at $T_p = 0.34$,

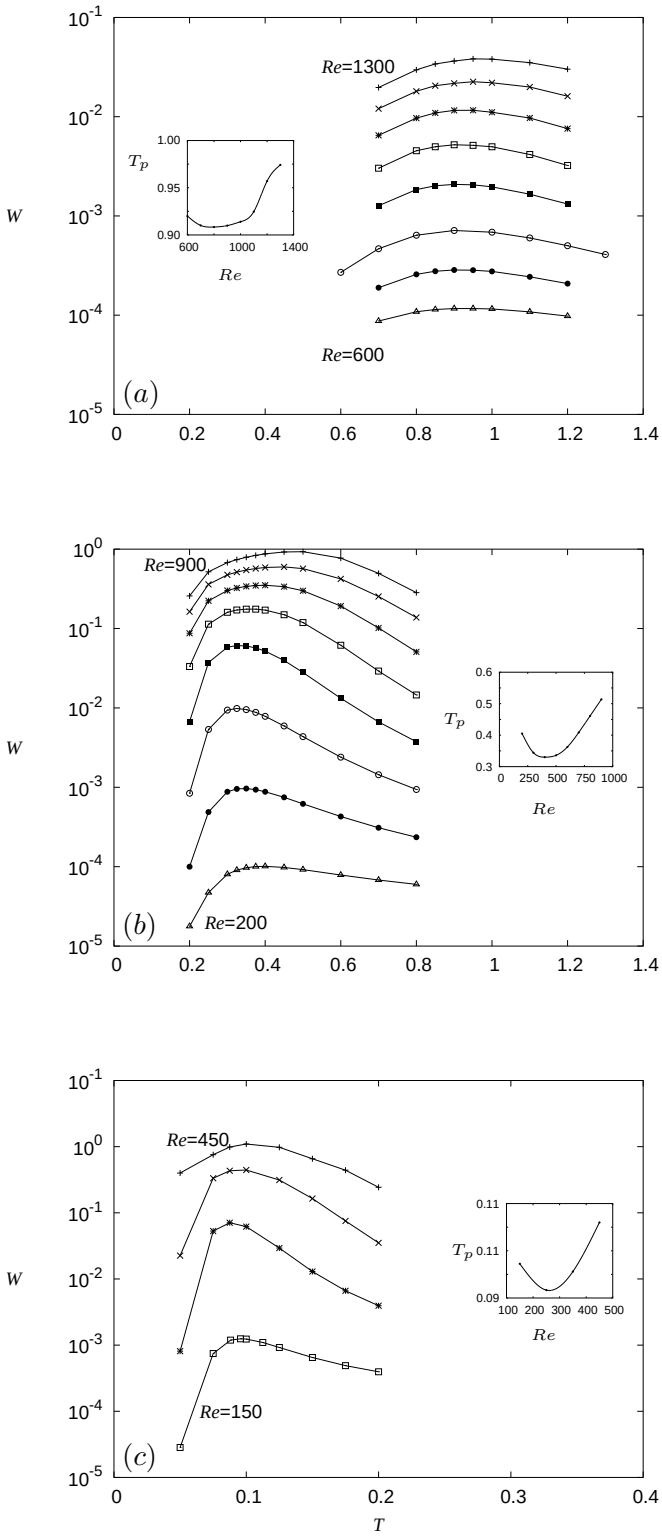

FIGURE 5.18: Plots of the domain integral, W, of the perturbed flow minus the base flow against the period of the forcing, T, calculated for numerical simulations at a range of Reynolds numbers across three blockage ratios, (a) $b = 0.50$, (b) $b = 0.75$ and (c) $b = 0.90$. Inset are plots of the variation of the period producing the greatest response, T_p, with Reynolds number.

which matches closely with the measured value shown in figure 5.15 of 0.34 ± 0.02. As we increase the Reynolds number from $Re = 200$, the period of peak response decreases slightly before increasing from $Re = 400$ onwards. In figure 5.18(c), which treats the case of $b = 0.90$, a similar behaviour of T_p is present. However, the period of peak response of $T_p = 0.097$ at $Re = 150$, does not match up as closely with the experimentally measured value of 0.17 ± 0.02.

No obvious explanation exists to explain the observed differences between the experimentally measured periods of peak response, T_p, and the numerically derived ones. A possible source of the error is the different amplitudes of forcing applied in each case. As discussed earlier, in all the numerical simulations a forcing of amplitude $0.001\overline{U}$ was employed, while in the experiments a forcing amplitude was chosen which produced an observable response in the dye visualisation. This meant that the amplitudes in the experimental cases were generally an order of magnitude greater. This is a likely source of some error, since such a great forcing, while exciting the flow at the given frequency also considerably alters the flow. In the numerical cases, the very small forcing means that the flow more closely retains its base flow characteristics.

Across the blockage ratios tested numerically, the same increase in period of peak response with Reynolds number was observed. As the Reynolds number is increased the shear layer becomes thinner, thereby changing the characteristics of any instability associated with it. However, this does not account for the small decrease in T_p with Reynolds number which is seen at the lower end of the Reynolds number range. The notion of the instability depending on the thickness of the shear layer can be further investigated by examining how the response of the flow varies with both axial location and position along the shear layer.

The variation of the response in the axial direction can be examined by considering a radial integral of the perturbation velocity, or just the inner integral of the domain integral of equation 5.6. This quantity, described as

$$W_z = \int (\overline{\mathbf{u}} - \overline{\mathbf{u}}_{base})^2 dr, \tag{5.7}$$

gives a measure of the response at discrete axial locations. Figure 5.19 plots the radial integral, W_z, of the perturbation velocity as a function of axial distance, at different forcing frequencies for three different flow configurations. The three cases – $b = 0.50$ and

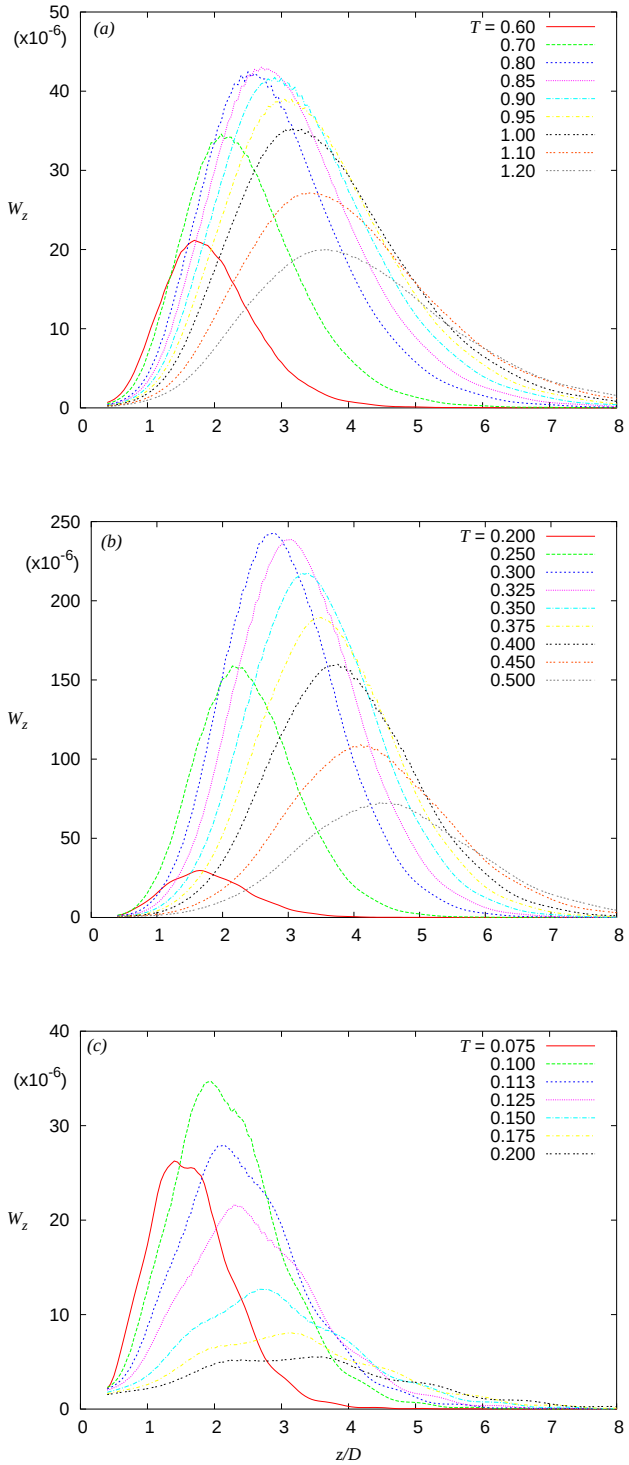

FIGURE 5.19: Plots of the radial integral, W_z, of the perturbed flow minus the base flow, as a function of axial distance, at a range of forcing frequencies, with (a) $b = 0.50$, $Re = 900$, (b) $b = 0.75$, $Re = 400$ and (c) $b = 0.90$, $Re = 150$. The curves give an indication of the axial location of the peak response for each forcing frequency.

$Re = 900$, $b = 0.75$ and $Re = 400$ and $b = 0.90$ and $Re = 150$ – are chosen as they are all located on or very close to the boundary at which convective instability is observed in the experimental flow. In each of the three cases shown, the axial location of the maximum value of the radial integral, W_z, moves downstream as the forcing frequency decreases. As we move downstream of the blockage, the thickness of the separating shear layer increases. Each forcing frequency having an optimum shear layer thickness for exciting oscillations, the axial location of the maximum value of W_z, which will be denoted as z'_{max}, varies accordingly. This is in keeping with the variation in the period of peak response, T_p, with Reynolds number, shown in figure 5.18.

With the flow configuration presented in figure 5.19(a), of $b = 0.50$ and $Re = 900$, the period producing the greatest response is $T_p = 0.91$. Interestingly, the plots of W_z corresponding to forcing periods $T = 0.80$ and 0.85 achieve greater maxima of W_z than does the curve corresponding to $T = 0.90$; this is despite the domain integral, W, of the perturbation velocity at $T = 0.90$ being greater than at $T = 0.80$ and 0.85. It is the greater downstream elongation of the curve for $T = 0.90$ which makes up for the difference in the maxima. The same behaviour is evident for $b = 0.75$ and $Re = 400$, shown in figure 5.19(b). The forcing period of $T = 0.325$ is closest to the period producing the greatest response $T = 0.33$, yet its maximum value of the radial integral of the perturbation velocity is less than that at a forcing period of $T = 0.300$.

This highlights a possible source of error between the values of T_p of figure 5.18 and the periods of peak response determined experimentally and plotted in figure 5.15. Using the experimental method described, which relies on the greatest disturbance of the shear layer observable in a dye visualisation, an experimentally determined value of T_p should in fact more closely match with the forcing period which produces the greatest perturbation at a discrete axial location. It is worth reiterating here the inexact nature of what the dye-visualisation represents in the flow. In the present problem, the dye only serves to highlight the edge of the recirculation zone; the strength of the connection between the recirculation zone boundary and a convecting disturbance in the mainstream flow is not immediately apparent.

The presence of maxima of the radial integral of disturbance, W_z, provides us with a useful characteristic of the perturbed flows. The axial locations of these maxima, z'_{max}, are plotted on figure 5.20 for the three flow configurations already shown in figure 5.19.

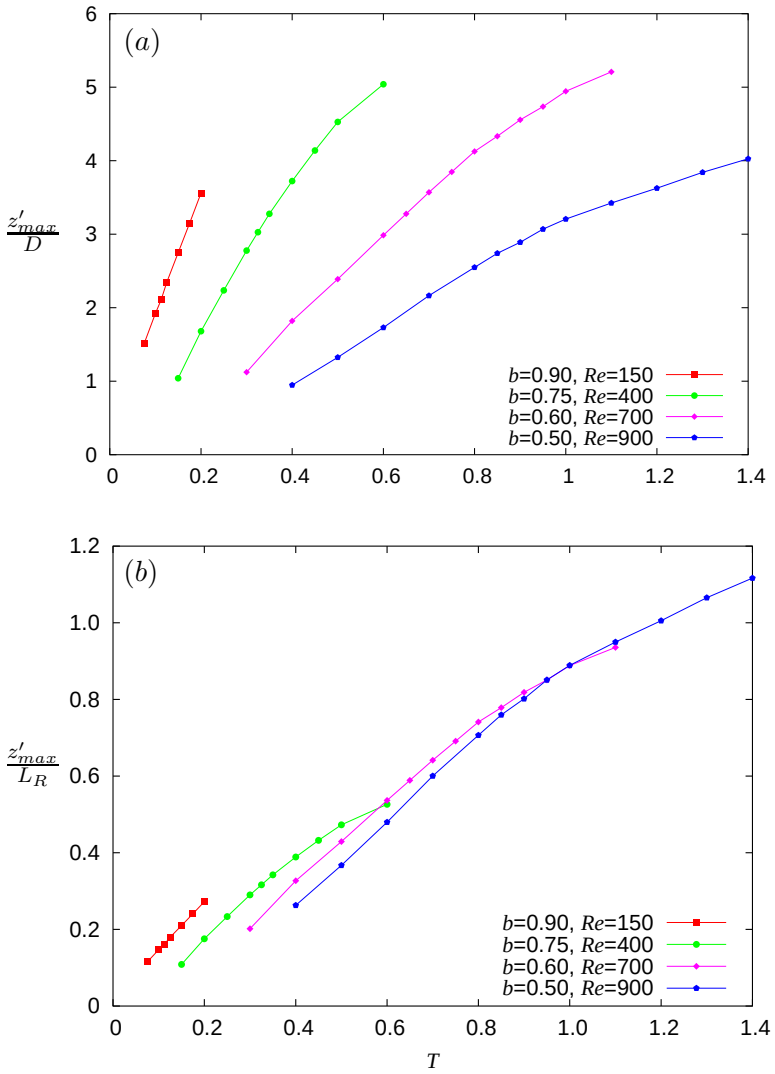

FIGURE 5.20: Variation of the axial location, z'_{max}, of the maximum value of W_z, with forcing period. The three flow configurations of figure 5.19 are represented, as well as a fourth, $b = 0.60$ at $Re = 700$. This fourth case was not tested experimentally; the Reynolds number of 700 was roughly interpolated from the boundary for convective instability shown on figure 5.13. In (a), the axial locations, z'_{max}, normalised by the tube diameter, D, are shown, while in (b) the same quantity is plotted, this time normalised by the recirculation length, L_R (for the cases presented at $b = 0.50$, 0.60, 0.75 and 0.90, the recirculation lengths are $L_R = 3.61D$, $5.57D$, $9.58D$, $12.97D$, respectively).

A fourth case, at $b = 0.60$ and $Re = 700$, is included; this configuration was not tested experimentally, the Reynolds number being interpolated from the boundary for convective instability of figure 5.13. The range of the data set for each blockage ratio is restricted by the ability to determine a maximum from the plot of W_z against z. For example, at forcing frequencies of $T < 0.2$, in the case of $b = 0.90$ and $Re = 150$, a distinct and singular maximum can no longer be determined; the excitation caused by the perturbation is low-level and not associated with the shear layer.

In figure 5.20(a), the variation of z'_{max} normalised by the tube diameter is presented. It shows that for a given forcing frequency, the axial location of the maximum value of z'_{max} will be closer to the blockage at lower blockage ratios, and further downstream for higher blockage ratios. Considering that the oscillations in the periodically-perturbed flows, as well as in the self-sustaining high Reynolds number unsteady flows, are observed along the edge of the recirculation zone, in figure 5.20(b) the axial locations of these maxima have been normalised by the corresponding length of the recirculation zone, L_R. When normalised in this fashion, there is a good collapse of the four data sets onto what is roughly a straight line. The spread of the data set after the collapse is very small, especially considering that the criterion for choosing the four flow configurations is that they be close to where the convective instability is seen in the experiment, which is itself not a sharply defined boundary. The collapse of figure 5.20(b) indicates that the relative distance along the shear layer where the radial integral of the perturbation velocity is maximal is a function of the period of forcing, with only a marginal dependence on the blockage ratio. When considered along side the differences between the four cases in shear layer thickness, the relationship is a surprising one.

Given that the method for choosing Reynolds numbers for the plot of figure 5.20(b) was not particularly stringent, figure 5.21 plots z'_{max} against the Reynolds number. It shows that there is a considerable variation in z'_{max} with Reynolds number, indicating some causal link between the four flow configurations of figure 5.20, which could account for the collapse of the data. The behaviour in figure 5.21 is consistent with the thinning shear layers seen at higher Reynolds number flows, in that the position of z'_{max} follows the location of the optimal shear layer thickness, which moves upstream as the Reynolds number increases.

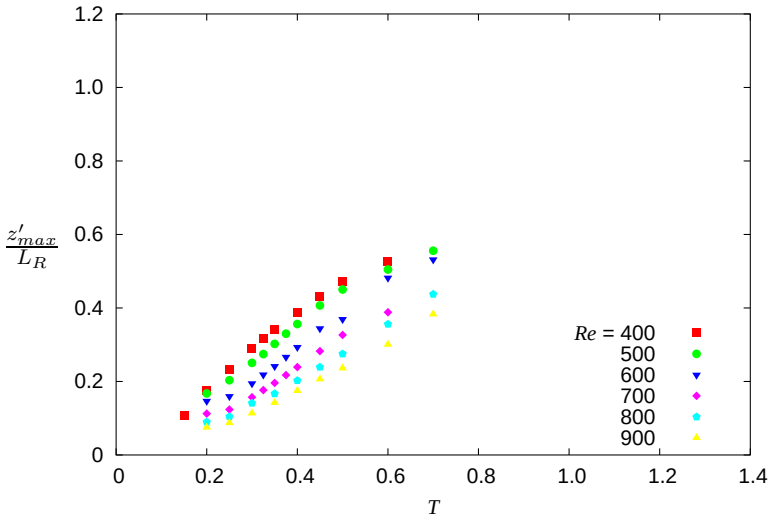

FIGURE 5.21: Variation of the axial location, z'_{max}, of the maximum value of W_z, normalised by the recirculation length, L_R, this time for a range of Reynolds numbers at a single blockage ratio $b = 0.75$. The same axes are used as in figure 5.20.

5.4 Chapter summary and discussion

A study of the steady flow through a simplified stenotic geometry of varying blockage ratio has been presented. The flow consists of a jet emanating from the contraction and then expanding downstream, creating a recirculation zone directly behind the blockage. Numerically, it was found that the length of the recirculation zone downstream of the blockage varied linearly with Reynolds number, while for a given blockage ratio, similarity was found to exist between flows of different Reynolds number. By drawing an analogy with the flow around a circular cylinder in a freestream for low Reynolds number, a good collapse of the recirculation lengths was obtained. This suggests that the reattachment length behaves similarly to the recirculation zone found in the wake of a circular cylinder at low Reynolds number.

Linear stability analysis identified unstable azimuthal modes of $m = 1$ for the blockage ratios $b = 0.75$ and 0.90, for Reynolds numbers of 770 and 395, respectively. The instability consists of a loss of symmetry, the centreline of the jet shifting off its axis. At $b = 0.50$, the most unstable mode is for $m = 2$; in this case, the instability mode takes a planar-symmetrical structure, which manifests as a thinning of the jet. Experimentally, a different instability was found to dominate. This instability consists of a convectively amplified perturbation in the shear layer, growing and causing breakdown of the flow

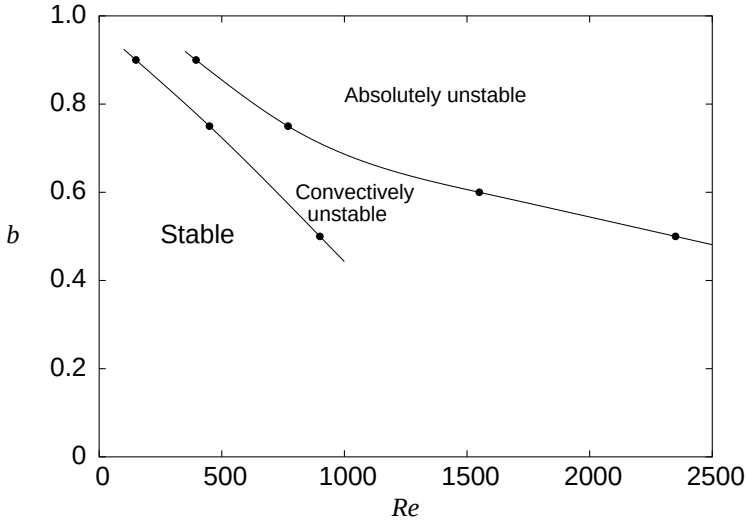

FIGURE 5.22: Map of the flow stability throughout the parameter space. The lower boundary denotes the convective instability seen experimentally, while the upper boundary is taken from linear stability analysis of the numerically derived flows.

four to five diameters downstream. A summary of the limits of absolute and convective stability investigated in this chapter are given in figure 5.22.

The period of the oscillations seen in the higher Reynolds number experimental flows downstream of the blockage was measured and, using the non-dimensionalisation $T = T_D\overline{U}/D$, shown to be roughly constant for higher Reynolds numbers. Stable flows, both numerical and experimental, when subjected to small-amplitude forcing, responded most to periods higher than those measured in the unsteady experimental flows for higher Reynolds numbers.

Several theories were suggested as to the nature of the instability and the transition to unsteadiness. The possibility was suggested that a flapping of the recirculation zone end – as observed in the flow over a bump in a freestream – may be involved in sustaining the strong unsteadiness seen downstream in high Reynolds number flows. The trigger for this behaviour may be the relatively gentle Kelvin-Helmholtz instability waves which travel down the separating shear layer and disturb the recirculation zone end. Marginally stable flows were observed which exhibited the Kelvin-Helmholtz instability, but which retained a stable recirculation zone end and did not become unsteady further downstream. A numerical investigation of the shear layer sensitivity to periodic forcing revealed a strong dependence of the axial location of greatest response to forcing, normalised by the recirculation length, on the forcing period; only a relatively

small dependence on blockage ratio was evident.

The large difference between periods measured on unsteady flows and the periods exciting the greatest response on both stable experimental flows and numerical flows is a curious phenomenon. A possible cause of this is the existence of strong downstream unsteadiness and turbulence in the self-sustaining unstable flows. The unsteadiness may generate disturbances upstream which alter the profile of the nominally white noise that the flow is usually subject to experimentally. Such a non-linear feedback between turbulent flow downstream and the unstable shear layer upstream may account for the different periods measured.

Chapter 6

Pulsatile Flow in Axisymmetric Stenotic Geometries

6.1 Introduction

This chapter extends on the work of the previous by treating the same geometry (a straight tube with an axisymmetric semi-circular blockage) but this time with a pulsatile component added to the steady inlet flow. A sketch of the velocity waveform is given in figure 6.1; further details of the pulsatile inlet flow are presented in chapter 3. The sectionally-averaged velocity oscillates sinusoidally around the temporally-averaged flow velocity $\overline{U}$, at a period T and an amplitude A. The inlet flow produces the same net mass flow; the steady flow can be thought of as either a temporal average of the pulsatile flow, or as a limiting case, where the pulsation amplitude approaches zero. The majority of numerical simulations presented here use a pulse amplitude of $A = 0.75$; it provides

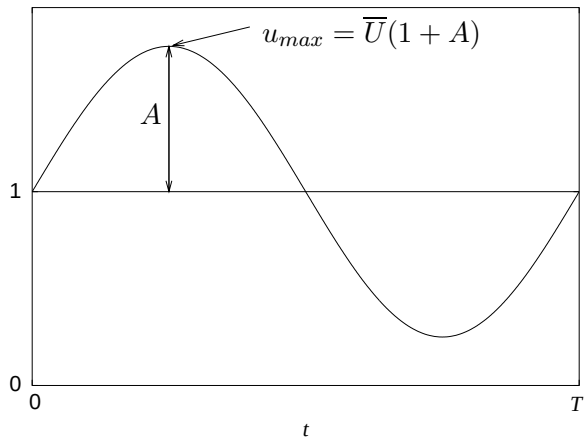

FIGURE 6.1: The inlet velocity waveform for pulsatile flow.

a useful starting point for exploring the parameter space and is a value used in recent literature, hence allowing comparisons to be made. Later sections in this chapter deal with flows of pulse amplitudes other than 0.75.

The chapter is structured in the following manner: the first section concerns the numerical simulations performed and gives a description of the blocked pulsatile flow. Floquet stability analysis of various sections of the large parameter space available are presented. The chapter closes with a presentation of the experimental results obtained. Some comparisons are drawn between numerical and experimental work.

6.2 Flow characteristics

This chapter deals initially with pulsatile flows of amplitude $A = 0.75$; this is an amplitude used in much of the literature on similar flows (Ahmed & Giddens (1984); Varghese & Frankel (2003); Sherwin & Blackburn (2005)) and provides the most reasonable approximation of a physiological realistic waveform, given that the oscillation is sinusoidal. Figure 6.2 plots contours of axial velocity up to an axial distance of $z/D = 7$ for $Re = 300$ and $T = 2.5$, across three blockage ratios $b = 0.50$, 0.60 and 0.75. The flow configuration serves here as a generic example of the types of flow under question, and the four sets of images are ordered in such a way to show the development and propagation of the flow during one period. The Womersley number in this case, of $\alpha = 13.73$ is in the range corresponding to large arteries.

At $t = 0.25T$, where the sectionally-averaged velocity is at a maximum, the flow acceleration from the velocity waveform and the blockage combined produce a plug of high axial velocity, issuing from the contraction. The acceleration is markedly stronger at $b = 0.75$, the velocity within the contraction being 4 times greater $(1/(1-b))$ than the velocity in the unblocked tube. The corresponding ratios for $b = 0.50$ and 0.60 are 2 and 2.5, respectively. This bulb of high velocity fluid continues downstream during the period of pulsation; during the same period, the bulk fluid itself moves $2.5D$ downstream.

The velocity plots of figure 6.2 and the short stenosis length of the blockage seem to indicate that the flow takes a plug-like form through the contraction. To further analyse this feature of the flow, figure 6.3 plots the velocity profiles for the same flow

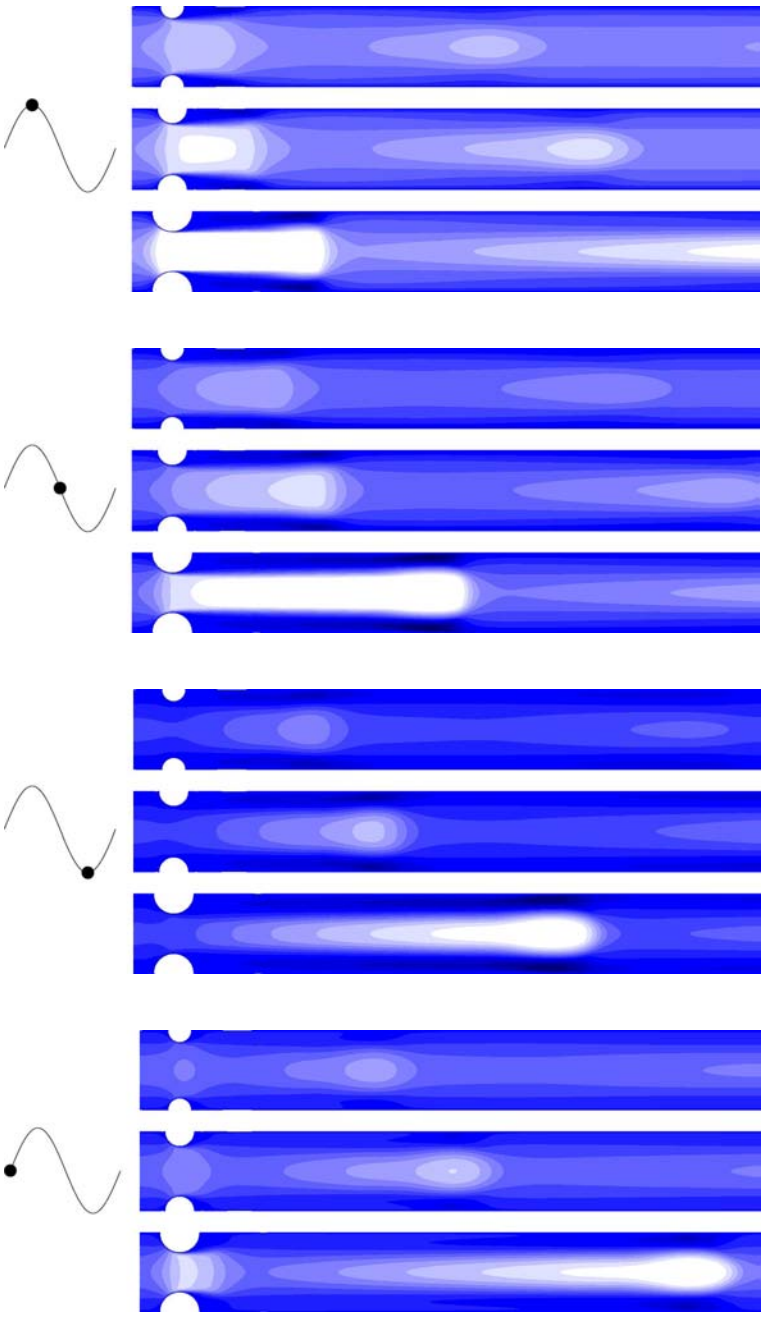

FIGURE 6.2: Contours of axial velocity of the flow through four stages of the pulse, at $T = 2.5$ ($\alpha = 13.73$), $Re = 300$, and $A = 0.75$, across three blockage ratios, $b = 0.50$, 0.60 and 0.75.

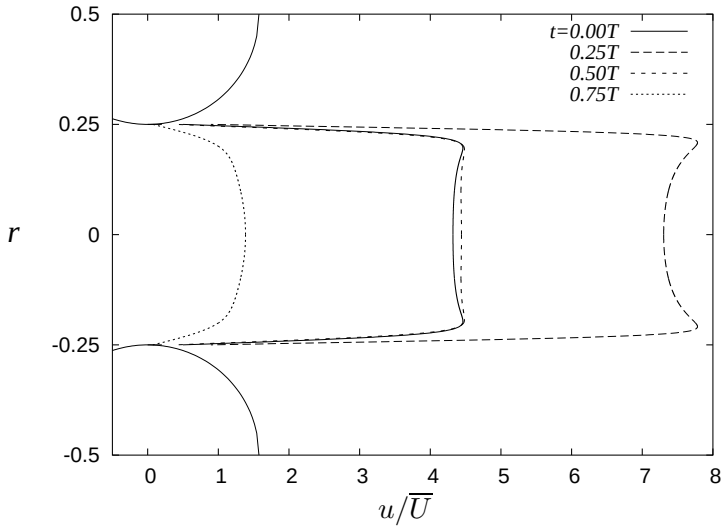

FIGURE 6.3: Axial velocity profiles in the contraction of the $b = 0.75$ geometry at four intervals during the pulse period, with $Re = 300$, $A = 0.75$ and $T = 2.5$ ($\alpha = 13.73$).

configuration and intervals in the period as in figure 6.2, however, only the case with $b = 0.75$ is considered. Here, a behaviour similar to that seen in chapter 5 is observed, where the axial velocity takes a local maximum near the inside walls of the blockage. In the pulsatile case presented, the profile corresponding to $t = T$ appears very similar to the profile observed for steady flow in chapter 5. For $t = 0.25T$, where the sectionally-averaged velocity inside the contraction reaches its maximum of $\overline{u}(t) = 7\overline{U}$, the maximum is even more pronounced. The higher axial velocity near the walls is caused by the rapid contraction of the flow, and then accentuated by the acceleration in the velocity waveform. The profiles of the two other phases presented, $t = 0.5T$ and $0.75T$, occur during the diastolic portion of the waveform and the profiles become more rounded. As in the steady flow, the existence of the local maximum of axial velocity in the throat velocity profile has implications for the flow behaviour, particularly in comparison to other studies of stenotic flows. In other studies which use a stenosis length of $2D$ for a blockage ratio of $b = 0.75$ (as opposed to a length of $0.5D$ for the present geometry at $b = 0.75$) the local maximum is either not present or not as pronounced. As seen in chapter 5, the strength and thickness of the separating shear layer can be affected by this phenomenon.

The separating shear layer can be observed in figure 6.4, which presents contours of vorticity for the same flow configuration in figure 6.2, with $Re = 300$ and $T = 2.5$,

across three blockage ratios, $b = 0.50$, 0.60 and 0.75. The strong flow acceleration through the blockage causes a flow separation to occur, with a separating shear layer emanating from the blockage walls. The shear layer rolls up, forming a vortex ring which propagates downstream and leaves a trail of vorticity in its wake. From figure 6.4, the strength and extent of convection downstream of the vortex are much greater in the case of $b = 0.75$. The axial propagation of the vortex varies strongly with the blockage ratio, the speed of the vortex convecting with a velocity closer to the heightened mean velocity inside the blockage, rather than with the mean velocity of the unblocked tube.

6.2.1 Vortex ring behaviour

The variation of the propagation of the vortex downstream warrants further investigation. Figure 6.5 plots the axial distance covered by the vortex as a function of time, for each of the blockage ratios tested. The dashed black line represents a hypothetical particle moving at the sectionally-averaged velocity in the tube, $\overline{u}(t)$. Therefore, we see that for $b = 0.20$, the vortex ring follows $\overline{u}(t)$ for the duration of its relatively short existence. It should be remembered that a ratio of $b = 0.20$ corresponds to a blockage which only extends 0.053 of a diameter into the tube, so only a relatively minor effect on the mainstream flow is to be expected. At blockage ratios of $b = 0.40$ and greater, the vortex rings travel faster than the sectionally-averaged velocity. The vortex ring velocity, excluding the effect of the sinusoidal variation of the mean velocity in the tube, seems to be constant. While the mean velocity in the tube obviously has an effect on the vortex position – evident in the periodic wobbles of the curves – the difference between the downstream velocity of the vortex ring and the mean velocity in the tube must be driven by its circulation, which would be a function of the increased velocity through the contraction and, therefore, of the blockage ratio.

We can calculate the vortex ring axial velocity immediately downstream of the blockage independently of the oscillating mean velocity in the tube, by using the two axial positions of the ring at $t - t_i = 0$ and $t - t_i = 2.5$. For the case of $b = 0.40$, the position of the vortex at $t - t_i = 2.5$ is extrapolated from the axial position at which it dissipates and is no longer observable. Doing so, we find that at $b = 0.75$, the vortex travels at a speed of approximately $3\overline{U}$; this compares with a speed of $\sim 2\overline{U}$ at $b = 0.60$ and $\sim 1.7\overline{U}$ at $b = 0.50$. Given that the downstream velocity of the

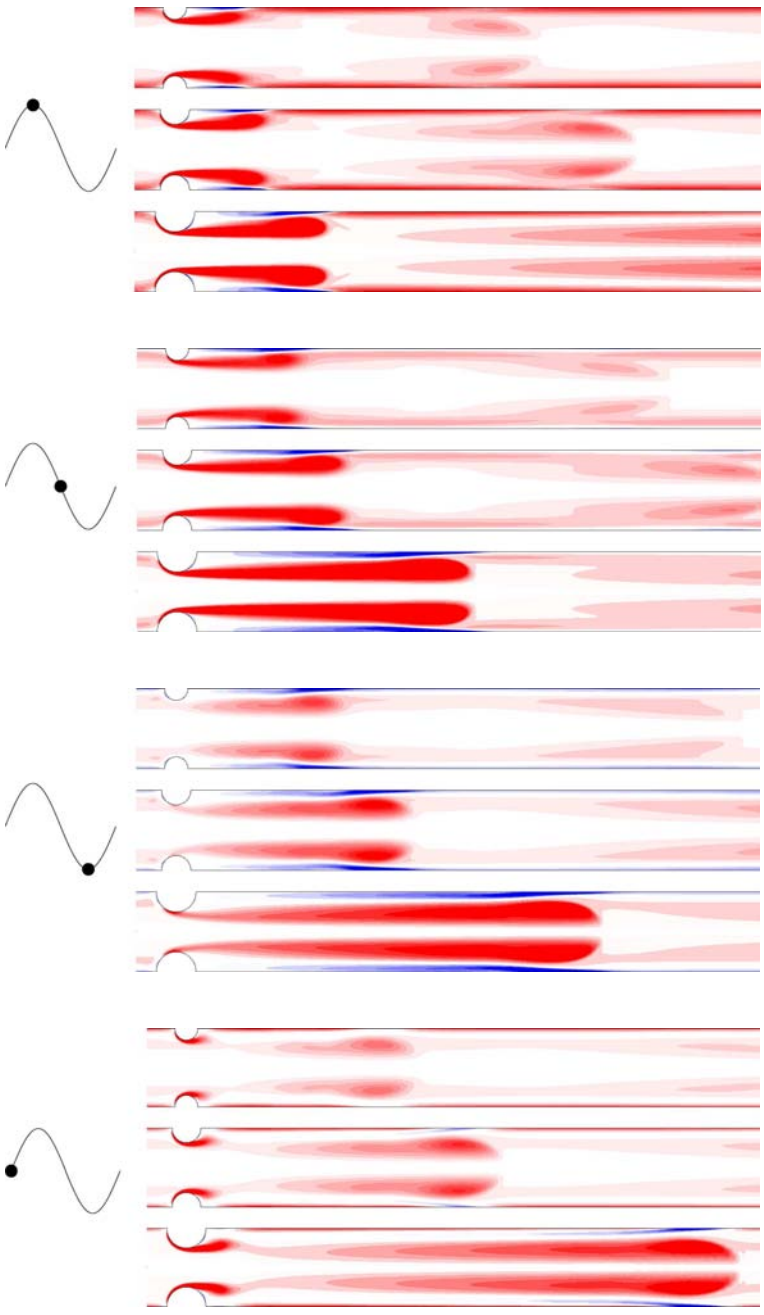

FIGURE 6.4: Negative (blue) and positive (red) contours of azimuthal vorticity of the flow through four stages of the pulse, at $T = 2.5$ ($\alpha = 13.7$), $Re = 300$, and $A = 0.75$, for three blockage ratios, $b = 0.50, 0.60$ and 0.75.

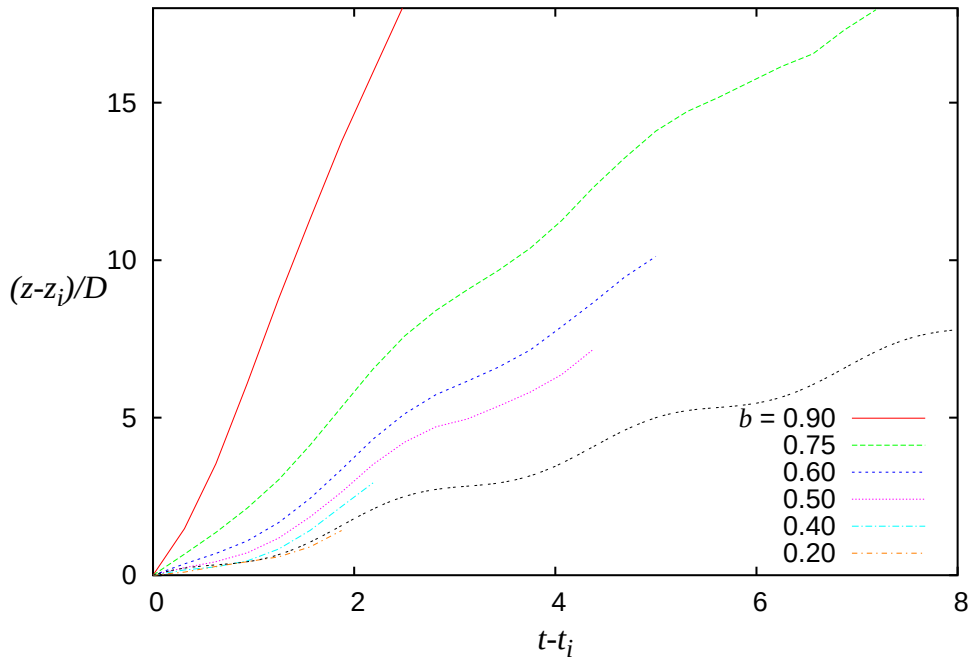

FIGURE 6.5: The position downstream of a vortex, as a function of time, for $T = 2.5$ ($\alpha = 13.73$), $Re = 300$, and $A = 0.75$, across the blockage range. The dashed black line indicates the position travelled by a particle should it convect with the sectionally-averaged axial velocity, $\overline{u}(t)$.

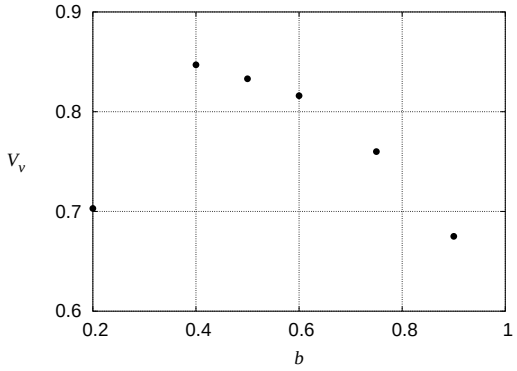

FIGURE 6.6: Values of vortex ring axial velocity, V_v, against blockage ratio, for $Re = 300$, $T = 2.5$ and $A = 0.75$.

vortex ring seems to be a function of the circulation imparted through the blockage, we normalise the vortex ring velocity by dividing by $1/(1-b)$. This quantity is the ratio of the sectionally-averaged velocity inside the contraction, and gives a measure of the circulation generated through the stenosis. This normalised value of vortex ring axial velocity, V_v, is plotted in figure 6.6 for blockage ratios of 0.40 to 0.90. A small extrapolation was required for $b = 0.40$, while a much larger extrapolation was

required for $b = 0.20$. The vortex ring velocity trend at $b = 0.20$ seems to be markedly different to that of the other blockage ratios. If we regard again figure 6.5, we see that for $b = 0.20$, the life of the vortex ring is very short and appears to travel slower than the sectionally-averaged fluid velocity. Above $b = 0.20$, we see a decrease in V_v as b increases. This variation in V_v is the same at pulse periods $T = 1.0$ and 5.0. A possible explanation for this decrease is the simple fact that a newly-generated vortex ring in the geometry $b = 0.75$ travels much further downstream during the pulse period than in lower blockage ratio geometries. In convecting downstream at a higher velocity, the vortex may be subject to a greater viscous drag from the tube wall than a vortex generated in a geometry of lower blockage ratio. Another explanation lies in the amount of circulation imparted to the vortex, as compared to the acceleration through the contraction. The axial velocity, V_v, of the vortex is due chiefly to the circulation of the vortex, which it gathers during its formation. If we examine again the vorticity contours of figure 6.4, we see that at $b = 0.75$, a large trail of vorticity is left in the wake of the vortex. This trail reduces in size at $b = 0.50$ and 0.60; the size of the trail in proportion to the strength of the vortex also appears to be smaller, particularly in the fourth panel, which corresponds to the phase interval $t = 1.0T$. The lower value of V_v for $b = 0.75$ perhaps indicates a higher proportion of the acceleration through the contraction ending up in the wake of the vortex ring, rather than as circulation within the vortex ring.

Blackburn & Sherwin (2007) made an observation regarding the behaviour of the vortex ring and the circulation generated during the pulse period, relating it to the generation of a vortex ring in an unbounded domain by the motion of piston. Gharib, Rambod & Shariff (1998) showed that a vortex ring can take up only a certain quantity of circulation during its formation before it pinches off, detaching itself from the separating shear layer feeding it. Any excess circulation generated by the piston is left in a trail of vorticity behind the vortex. Defining a formation number, $t^* = \overline{U}_p t/D$, where $\overline{U}_p$ is the mean piston velocity and D its diameter, they found that the vortex ring generally pinched off at $t^* \approx 4$, with only a small dependence on the form of the piston motion and on the Reynolds number.

We attempt here to extend the analogy, by substituting for the diameter of the piston the minimum diameter within our contraction, $D\sqrt{1-b}$, and for $\overline{U}_p$, the mean

velocity over the first half of a pulse period, which can be given by $\frac{1}{T/2}\int_0^{T/2}\overline{u}(t)dt$, or $\overline{U}(1+\frac{2A}{\pi})$. Therefore, our comparative formation number is

$$t^* = \frac{\overline{U}(1+\frac{2A}{\pi})t}{D\sqrt{1-b}}. \tag{6.1}$$

As we use the mean velocity over the first half of the pulse period, similarly, we assume the formation time, T_s, to be equal to one half of the pulse period, $T_s = T/2$. Assuming the critical formation number for which the pinch-off occurs to be 4, we can express equation 6.1 as

$$T_s = \frac{4D\sqrt{1-b}}{\overline{U}(1+\frac{2A}{\pi})}, \tag{6.2}$$

which gives us an analytical prediction of the critical pulse period for which a vortex pinch-off may occur. We can test this analysis first by varying the formation diameter, which we do by treating our formation time, T_s, as a function of blockage ratio.

Holding the amplitude constant at $A = 0.75$, figure 6.7(a) plots T_s as a function of b, predicting a critical boundary for the vortex pinching off. We see that at very high values of b, the formation time predicted to cause a pinch-off is very small; this is to be expected due to the increase in acceleration and circulation generated the greater our contraction. To test how valid the analogy is, a series of cases for $T = 4$ and blockages from $b = 0.20$ to 0.75 are selected, with formation times that span the boundary formed by equation 6.2. The locations of these five flows are represented on figure 6.7(a); corresponding plots of the vorticity fields are shown in figure 6.7(b). The phase of these plots is chosen to best highlight any pinched-off vortex.

In the work of Gharib *et al.* (1998), the test for vortex pinch-off consisted of identifying a wholly-closed vorticity contour, separated from the vorticity trailing in the vortex wake. However, this test was only possible when the formation time was considerably greater than the critical value of 4, since at formation times of just above 4, the detachment of the vortex could not be determined with certainty. The critical formation number of 4 was calculated by interpolation. In fact, the formation number represents the formation time at which a vortex ceases to consume circulation, rather than the time at which the vortex detaches. From the vorticity contour plot of figure 6.7(b) corresponding to $b = 0.75$, there appears to be a vortex ring followed by a long trail of vorticity, which would indicate some sort of pinch-off. However, at the two cases of

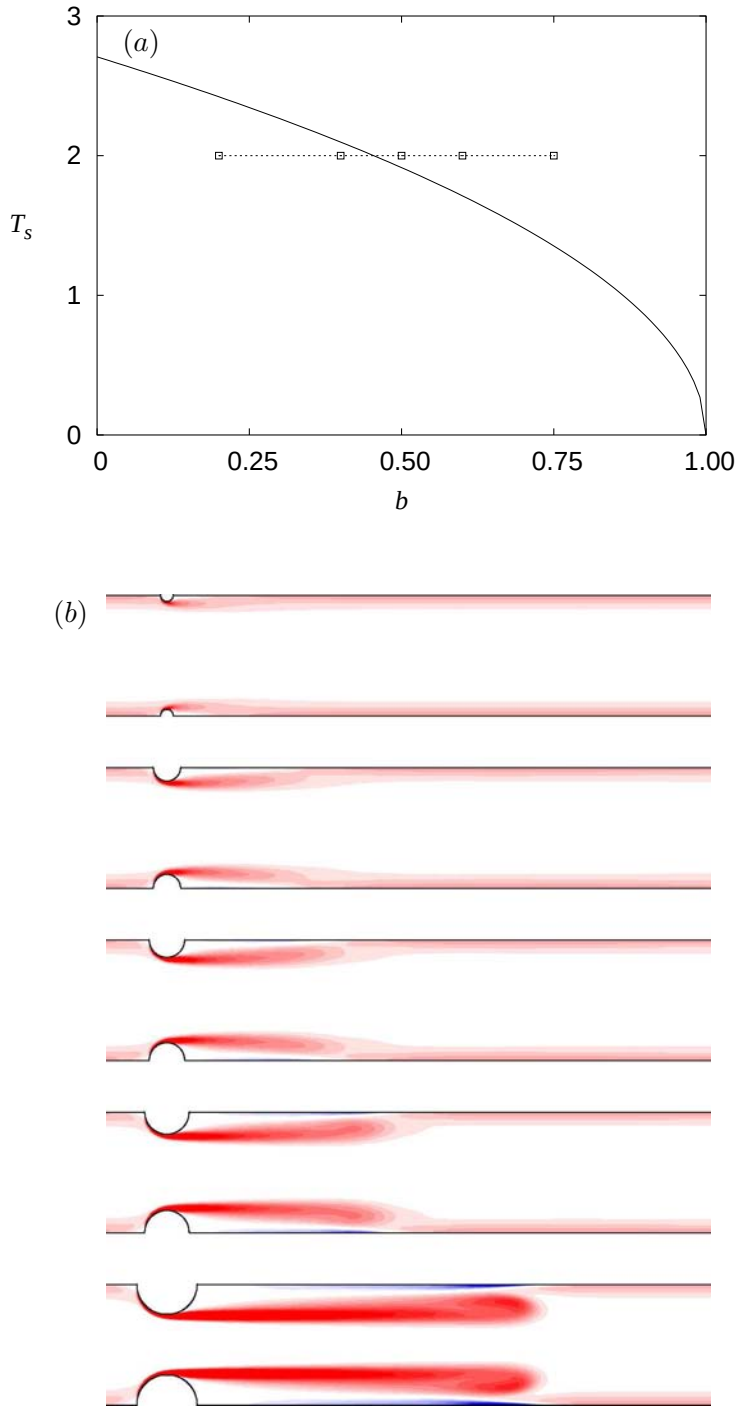

FIGURE 6.7: (a) Dotted line and points correspond to vorticity plots shown below, while the solid line refers to the theoretical boundary for pinch-off, according to equation 6.2, as a function of blockage ratio, b. (b) Contours of vorticity for flows along the dotted line plotted in (a), $T = 4$, $Re = 300$, $A = 0.75$ and b ranging from 0.20 (top) to 0.75 (bottom).

$b = 0.50$ and 0.60, no such behaviour is observed, even though the plot of figure 6.7(a) predicts that there should be.

A similar test of the analogy can be performed, this time by varying the pulse amplitude and guarding the blockage ratio constant. Figure 6.8(a) plots T_s as a function of A, with a blockage ratio of $b = 0.75$. Therefore, as the amplitude of pulsation increases, the formation velocity increases and less formation time is required to exceed the circulation needed to cause a vortex to pinch-off. Again five cases of varying amplitude A are chosen which traverse the boundary formed by equation 6.2, and are plotted in figure 6.8(b). In each case, some sort of vortex detachment is suggested by the vorticity contours.

Interestingly, a common trait to each of these five cases lies in the shape of the vortex ring. It is elongated with the axial direction of the flow, necessarily due to the presence of the tube walls. If we regard the vortex rings used in the study of Gharib *et al.* (1998), we see that in the unbounded domain, the vortex has a greater lateral expansion than in the present work; if we compare those cases of Gharib *et al.* (1998) where the formation time considerably exceeds the formation number, with the vorticity plots of figure 6.8(b), we see that in the unbounded cases, the vortex ring is approximately twice as wide as the vorticity trail behind it, while in the tubular geometry, the vortex is severely constricted and not able to develop and propagate in the same manner. This appears to be the fundamental difference between the two cases, and a meaningful quantitative comparison is not possible. Qualitatively, we can say that the same physical phenomenon is present, whereby a vortex ring, attaining a certain circulation threshold, detaches from the separating shear layer, travels downstream and leaves a trail of vorticity in its wake. This explanation is further supported by the drop in normalised vortex ring axial velocity, V_v, with increasing blockage ratio, a phenomenon which can be explained by the greater proportional quantity of circulation deposited in the vortex trail.

6.2.2 Wall shear stresses

The wall shear stress, $\tau_{wall} = -\mu \partial u / \partial r$, has been established as the primary fluid mechanical characteristic affecting biological arterial responses (Ku 1997; Wootton & Ku 1999). Teleologically, there are several reasons why this should be the case, the

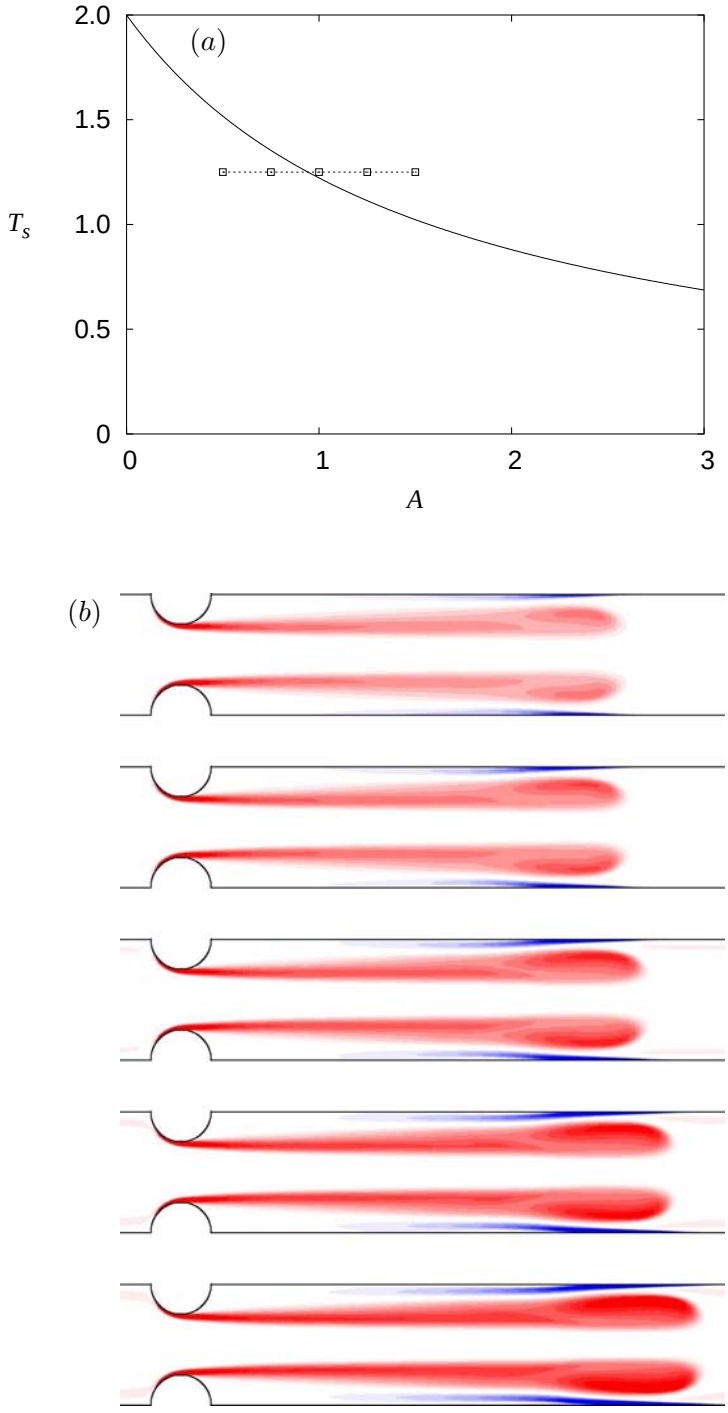

FIGURE 6.8: (a) Dotted line and points correspond to vorticity plots shown below, while the solid line refers to the theoretical boundary for pinch-off, according to equation 6.2, as a function of pulsation amplitude, A. (b) Contours of vorticity for the five flows along the dotted line plotted in (a), $T = 2.5$, $Re = 300$, $b = 0.75$ and A ranging from 0.5 (top) to 1.5 (bottom).

strongest being that the wall shear stress is the fluid mechanical characteristic that can most easily be detected by the arterial wall, manifesting itself as a force on the wall. Also, arterial stenoses generally form at positions of oscillatory and low average wall shear stress.

Figure 6.9 plots profiles of wall shear stress along the tube wall for three cases, for $b = 0.75$, $Re = 300$, $A = 0.75$, for three different pulse periods $T = 1.0$, 2.5 and 4.0 ($\alpha = 21.71$, 13.73 and 10.85). As in Chapter 5, wall shear stress is normalised as

$$\tau = \tau_{wall}/(\frac{1}{2}\rho\overline{U}^2) = -(\frac{2D}{Re\overline{U}})\frac{\partial u}{\partial y}. \tag{6.3}$$

Twenty profiles over one pulse period are shown, the intention being to delineate an envelope within which the wall shear stress oscillates. The data sets shown begin at the axial location $z = r_b$, or where the blockage ends. The first case, for $T = 1$, having a Womersley number of 21.73, models a flow configuration similar to that of a large artery close to the heart, while the second and third cases are still characteristic of large arteries, but further away from the heart. At smaller pulsation periods, the amplitude oscillation of the wall shear stress is higher than for higher pulsation periods. This is due to the greater flow acceleration of velocity waveforms of shorter period. As the three cases involve pulsations of the same pulsation amplitude, the rate of change of sectionally-averaged tube velocity is necessarily greater for shorter pulse periods, which in turn leads to increased velocity, and accordingly, increased wall stress. In the three cases, we see the wall shear stress reach a maximum just downstream of the blockage, with the maximum shifting downstream and reducing in magnitude as we increase the pulse period and decrease the Womersley number. In the case $T = 1.0$, we see a much higher maximum wall shear stress than we do for the other two cases of $T = 2.5$ and 4.0.

The wall shear stress corresponding to the steady inlet flow and the average wall shear stress of the pulsatile flow at $Re = 300$ are also plotted on figure 6.9. For $T = 1.0$, there is a considerable variation between the averaged and the steady flow wall shear stress distribution. In each of the three cases, the average wall shear stress becomes positive at approximately the same point at which the wall shear stress switches sign in the steady inlet flow; or, where the recirculation zone formed in the steady flow ends. In the three cases presented here, this switch in the sign of the wall shear

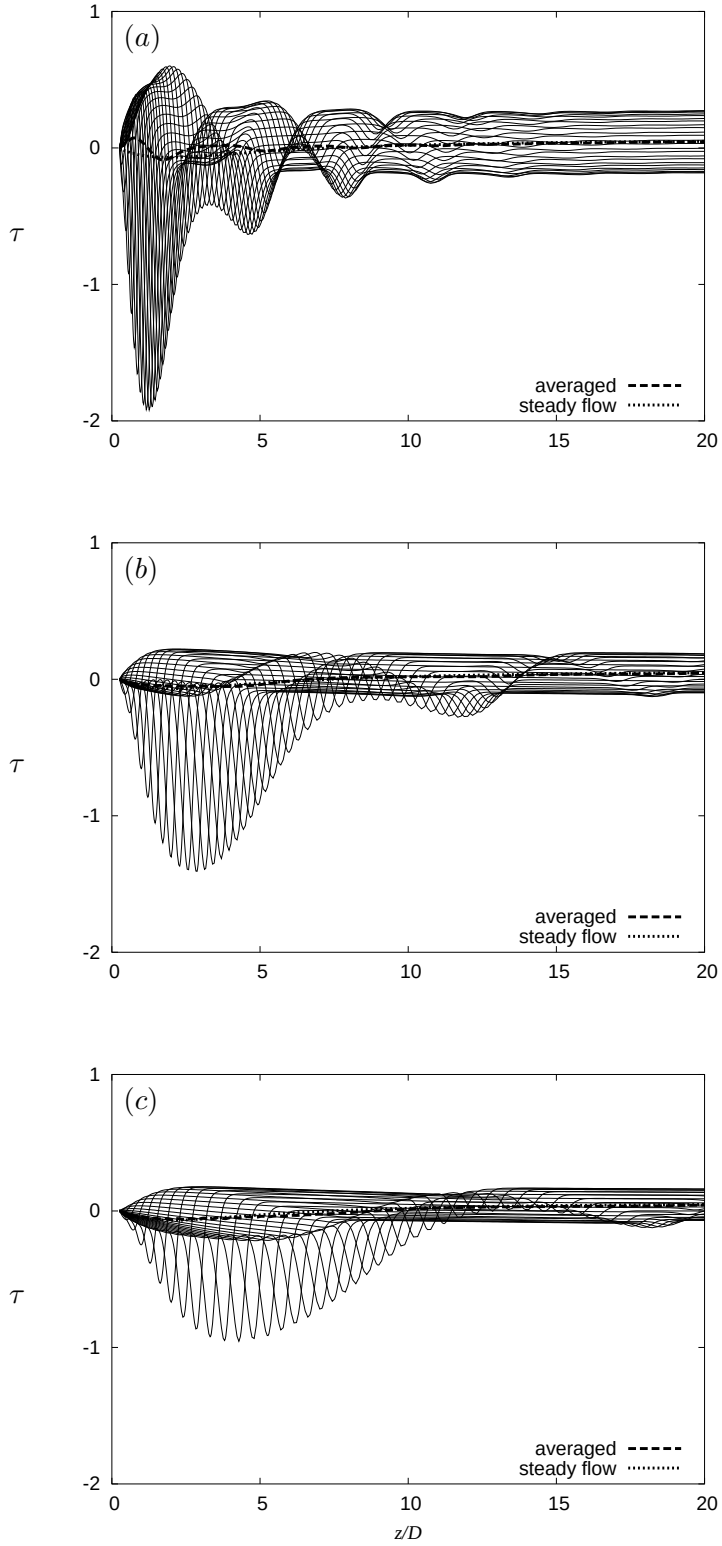

FIGURE 6.9: Variation of wall shear stress, τ, over one pulse period, for $T = 1.0$, 2.5 and 4.0, with $Re = 300$, $b = 0.75$ and $A = 0.75$. The graphs, in effect, show envelopes of shear stresses at given axial locations. The heavy dashed line indicates the wall shear stress averaged over one pulse period, while the heavy-dotted line indicates the wall shear stress distribution for steady flow at the same Reynolds number. The Womersley numbers are $\alpha = 21.71$, 13.73 and 10.85 respectively.

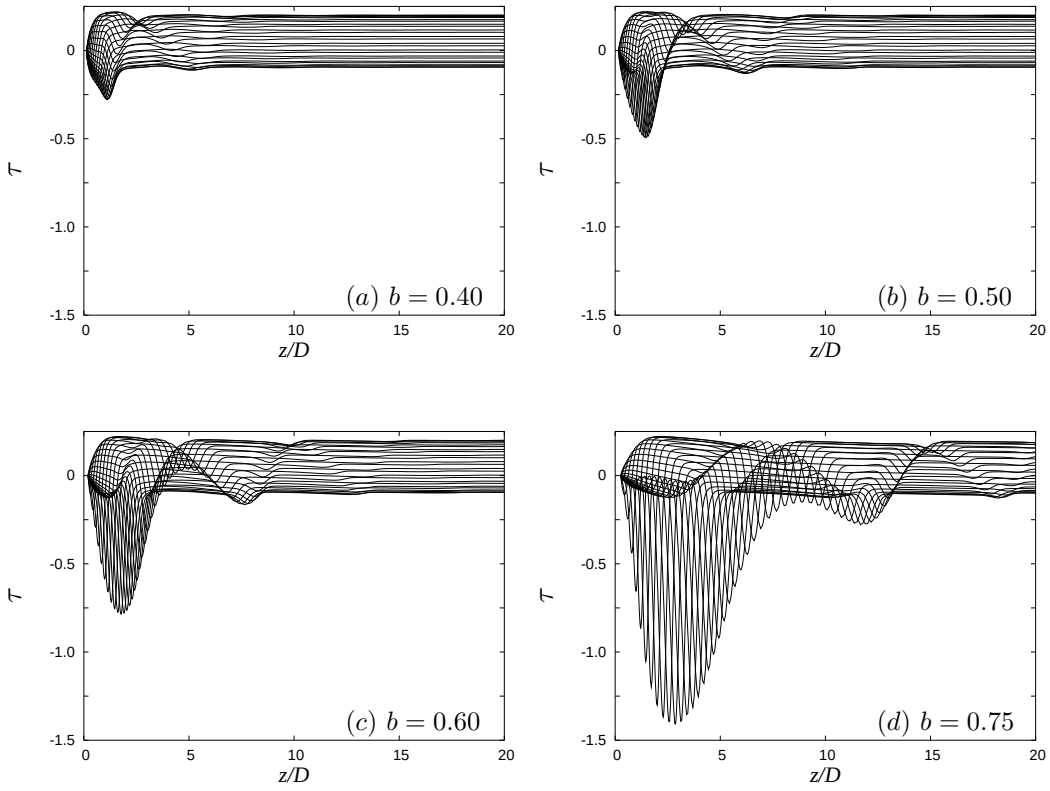

FIGURE 6.10: Variation of wall shear stress, τ, for blockage ratios of $b = 0.40$ to 0.75 over one pulse period, for $T = 2.5$, $Re = 300$ and $A = 0.75$. The graphs show envelopes of shear stresses at given axial locations. The Womersley number is $\alpha = 13.73$.

stress occurs at $z \approx 6D$, indicating an oscillatory and low average wall shear stress at this location, which are commonly thought the prime criteria for the development of stenoses. Indeed, the phenomenon of secondary stenoses, where an additional stenosis forms approximately 5 or 6 diameters downstream of the initial one could be related to such a wall shear stress distribution.

One of the aims of varying the blockage ratio in this investigation is to observe the flow throughout the growth of a blockage. Figure 6.10 tracks the wall shear stress as it varies from a blockage ratio of $b = 0.40$ to $b = 0.75$, for Reynolds number $Re = 300$ and pulsation period $T = 2.5$. In each of the four cases presented, the wall shear stress achieves a maximum local value, in absolute terms, a short distance downstream of the blockage. This maximum local wall shear stress grows sharply with blockage ratio, reaching a value for $b = 0.75$ of approximately 5 times that for $b = 0.40$. From figure 6.10(a), we see that for $b = 0.40$, the effect of the blockage on the variation of the

wall shear stress is relatively small and extends only a short distance downstream of the blockage. This is particularly the case if we consider the wall shear stress in terms of the range of values it oscillates within. At approximately 8 diameters downstream of the blockage, the wall shear stress oscillation has almost returned to its standard envelope of oscillation in an unblocked tube. It is only for $b = 0.75$ that the effect of the blockage begins to substantially penetrate downstream, with the oscillation disrupted at least up to $z = 20D$. In addition, the maximum value of local shear stress achieved during one period is shifted a short distance downstream.

6.3 Floquet stability analysis: blockage ratio effect

Floquet stability analysis was undertaken across blockage ratios $b = 0.50$ to 0.75 for a range of different pulsation periods. The goal of the analysis presented in this section is to investigate the effect of the blockage ratio on the absolute stability of pulsatile flows. In order to do this, the pulsation amplitude is maintained at $A = 0.75$ and three pulsation periods, $T = 1.0$, 2.5 and 5.0, are described in detail. Starting the stability analysis in this manner allows us to compare results with similar stability analysis results presented in Blackburn & Sherwin (2007). A summary of the results across the pulse period range is included at the end of the section.

6.3.1 Stability analysis: $T = 2.5$

The first section of the stability analysis, focusing on flows of pulsation period $T = 2.5$, begins with similar flows to those presented in figures 6.2 and 6.4. A Reynolds number flow of $Re = 300$ in such a configuration corresponds with a Womersley number of $\alpha = 13.73$, which is relevant for flows in the larger arteries.

Figure 6.11 presents results of Floquet stability analysis for flows of $T = 2.5$ across three blockage ratios, $b = 0.50$, 0.60 and 0.75. Across the three blockage ratios, the greatest magnitude Floquet multiplier corresponds to the perturbation of azimuthal mode number $m = 1$. A negative Floquet multiplier indicates a period-doubling instability, where the sign of the azimuthal vorticity of the perturbation mode changes from one period to the next. In effect, this means that the sign of the perturbation switches from one downstream vortex ring to the next. For the blockage ratios $b = 0.50$ and 0.60, the modes $m = 2$ and 3 are also period-doubling. From figure 6.11(c), only the

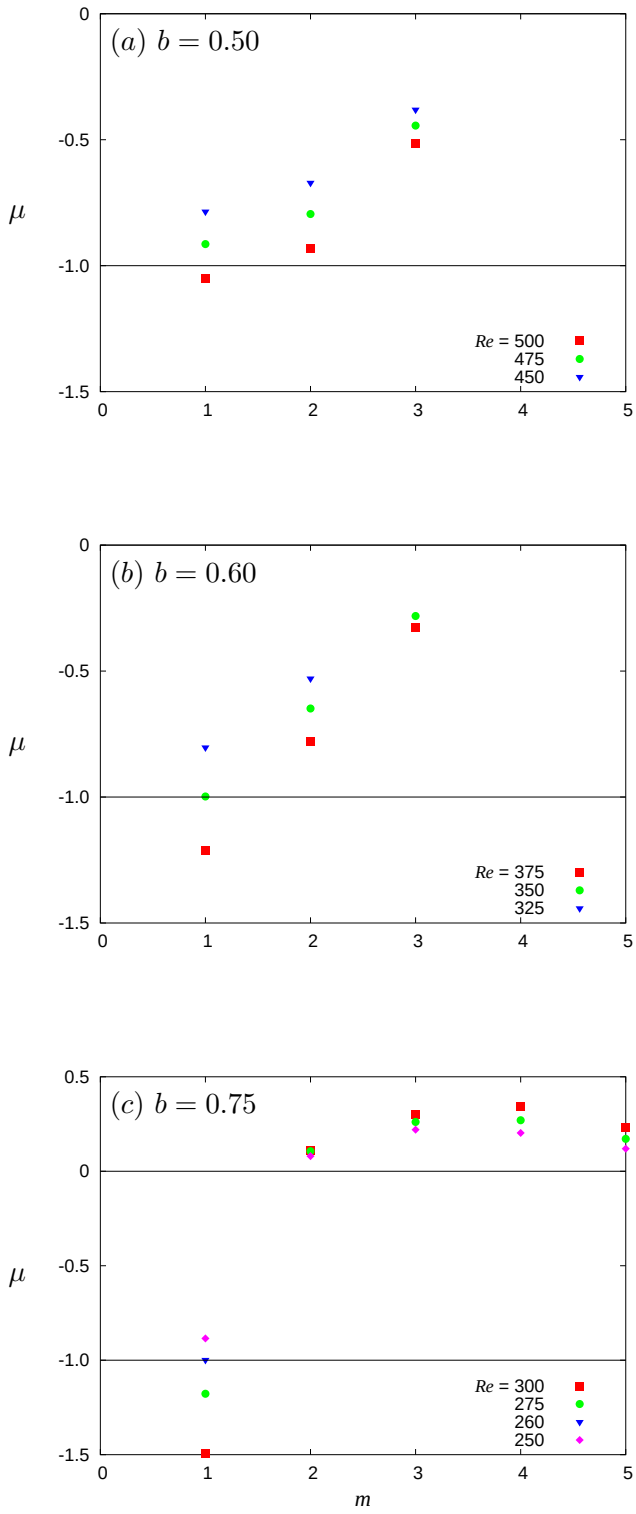

FIGURE 6.11: Floquet multipliers across blockage ratios of (a) $b = 0.50$, (b) 0.60 and (c) 0.75, for $T = 2.5$, $A = 0.75$ and various Reynolds numbers.

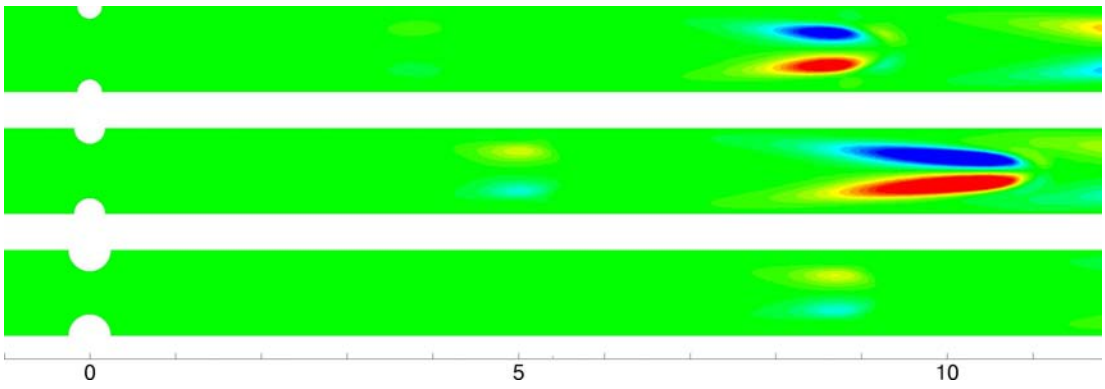

(a)

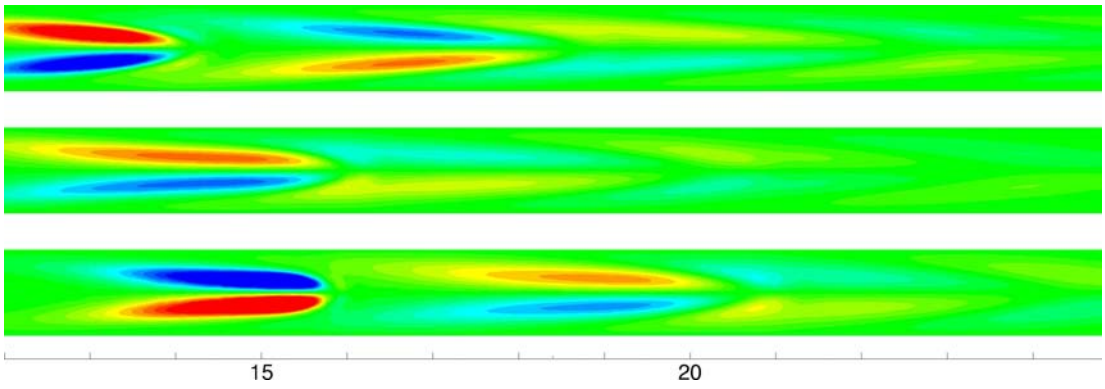

(b)

FIGURE 6.12: Contours of axial velocity (red positive, blue negative) of the leading perturbation modes ($m = 1$) near the critical Reynolds numbers, $Re = 500$, 350 and 260 for $b = 0.50$, 0.60 and 0.75, respectively. The pulsation period is $T = 2.5$, corresponding to Womersley numbers of $\alpha = 17.7$, 14.8 and 12.8, respectively.

$m = 1$ mode is period-doubling, the other modes remaining in period with the base flow.

Figure 6.12 plots contours of the axial velocity of the perturbation modes for $m = 1$ for three flows at or near the critical Reynolds number for the blockage ratios $b = 0.50$, 0.60 and 0.75. Although not presented, the maximum perturbation is centred around the vortex ring in each case. The plane shown corresponds with the azimuthal maximum of the perturbation. For the case shown for the blockage ratio $b = 0.50$, the perturbation velocity is first evident at $z/D \approx 8$. At this point, the top half of the vortex ring is subject to a negative velocity, while the bottom half is forced in the other direction. In this way, the instability consists of a tilting of the vortex ring. The direction of the

FIGURE 6.13: Two positive and negative contours of the streamwise vorticity of the perturbation mode ($m = 1$) for $b = 0.50$, $Re = 500$, $A = 0.75$ and $T = 2.5$ ($\alpha = 17.72$).

tilting alternates on each vortex, which is evident by the change in direction of the perturbation velocity on each successive vortex ring.

The axial position of the perturbation maximum changes with the blockage ratio; for $b = 0.50$, the maximum at the phase shown in figure 6.12 occurs at $z/D \approx 8.5$, for $b = 0.60$, $z/D \approx 10$ and for $b = 0.75$, $z/D \approx 15$. If we consider figure 6.5, we note that at the three blockage ratios, these axial locations are reached by the vortex ring between 5 to 6 time units after the creation of the vortex. This indicates that the difference in axial location of the maximum perturbation can be attributed to the variation with blockage ratio of the speed of the vortex as it convects downstream. For the pulse period under question, $T = 2.5$, the perturbation develops at roughly the same point during the lifetime of the vortex ring. For the case $b = 0.75$, in comparison with the very similar instability found by Sherwin & Blackburn (2005), the chief difference lies in the axial location of the maximum perturbation. For the smoother stenosis geometry of Sherwin & Blackburn (2005), for $T = 2.5$, they found the maximum perturbation to occur at $z/D \approx 20$, in comparison with $z/D \approx 15$ for the present geometry.

Figure 6.13 plots positive and negative contours of axial vorticity of the leading perturbation mode at $b = 0.50$ and a Reynolds number slightly greater than the critical, Re_c. The period-doubling nature of the mode is again evident, this time in the switching vorticity contours on each successive vortex ring. At the phase shown, the strength of the perturbation on each of the vortex shown is roughly equal, with the perturbation on the vortex reaching a maximum approximately half a period later than that shown.

The variation in Floquet multiplier in figure 6.11(c) is similar to that seen in the nearest comparable work in the literature (Sherwin & Blackburn 2005). However, for their stenotic geometry – consisting of a blockage of $b = 0.75$ but with a longer stenosis length – they found a critical Reynolds number for pulse period $T = 2.5$ of $Re_c = 389$. This is significantly greater than the corresponding critical Reynolds number for the present geometry, of $Re_c = 260$. There is also the sizable difference between the downstream location of the maximum perturbation; an explanation for this

is not immediately apparent. An analysis of the same perturbation mode at $Re = 360$ reveals an axial location of the perturbation maximum vorticity at $z/D \approx 16$; it appears that this distance is slightly further downstream than for $Re = 260$ due to the slightly greater distance travelled by the vortex ring at the higher Reynolds number. The axial location being largely independent of Reynolds number, the difference in axial location of the perturbation maximum is not due to the difference between critical Reynolds number of each case, but rather to fundamental features of the two base flows. The main difference between the two geometries is the much shorter contraction of our geometry and the effect this has on the velocity profiles emerging from the contraction. This has a direct effect on the nature of the separating shear layer which forms downstream of the blockage. There is no immediately obvious reason as to how the shear layer should directly affect the absolute stability of the flow. A clue is perhaps given by the investigation carried out in Blackburn & Sherwin (2007), in which a Floquet stability analysis was carried out on pulsatile flows that were also subjected to high-frequency low-amplitude perturbations. They found that the Floquet multiplier returned was significantly greater than the corresponding multiplier returned for an unperturbed pulsatile flow, the effect being more pronounced at higher pulse periods. The effect of the high-frequency was to excite convective shear layer oscillations, much like those observed in Chapter 5. This seems to indicate that there is some connection between the nature of the separating shear layer and the absolute stability of the flow. Hence, at $T = 2.5$, the difference between the critical Reynolds number in this study and in that of Blackburn & Sherwin (2007) would appear to be a result of the difference in contraction velocity profile in each case, and its consequences for the behaviour of the separating shear layer.

6.3.2 Stability analysis: $T = 5.0$

We now turn to results for flows of pulse period $T = 5.0$. For this pulse period, flows are characterised by longer vortex formation times and greater distance between successive vortex rings. The vortex also leaves a longer trail of vorticity in its wake than it does for shorter pulse periods.

Figure 6.14 presents the absolute Floquet multipliers for the leading perturbation mode, $m = 1$, across the three blockage ratios, $b = 0.50$, 0.60 and 0.75, with pulse period

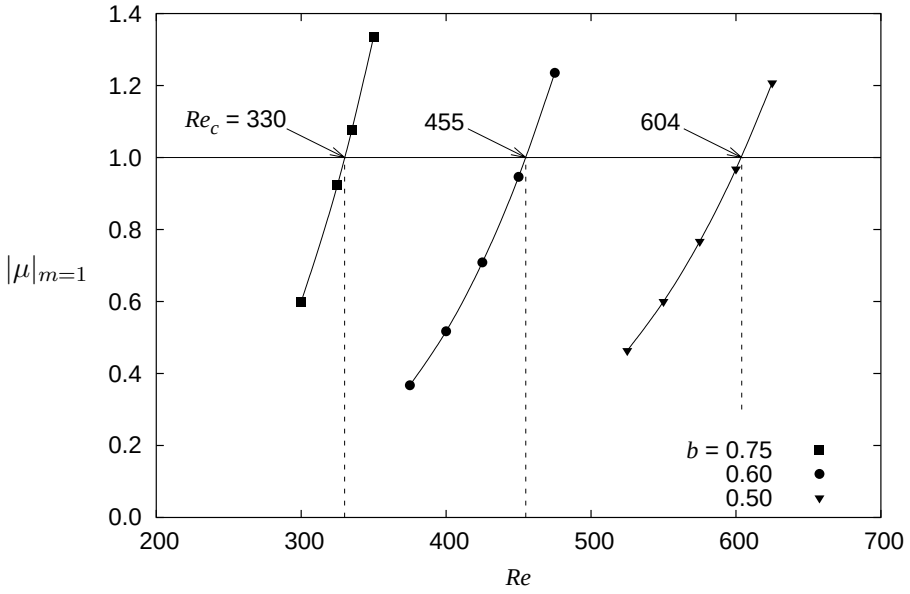

FIGURE 6.14: Absolute Floquet multipliers of the leading perturbation mode for $T = 5$ and $A = 0.75$. Across the three blockages shown, $b = 0.50$, 0.60 and 0.75, the leading mode is $m = 1$; the Womersley numbers for the critical cases are 13.8, 12.0 and 10.2, respectively.

$T = 5.0$. As is the case with $T = 2.5$, the leading mode is of azimuthal wavenumber, $m = 1$, and is period-doubling. The mode is more dominant than at $T = 2.5$, the multipliers corresponding to higher wavenumbers being significantly smaller than that of the leading $m = 1$ mode. The flows of pulse period $T = 5.0$ are significantly more stable to absolute instability than those of $T = 2.5$. For $b = 0.75$, the critical Reynolds number is $Re_c = 330$, as opposed to 260 for pulse period $T = 2.5$. Across the blockage ratio range, the critical Reynolds numbers are between 1.2 and 1.3 times greater than for $T = 2.5$.

Figure 6.15, similarly to figure 6.12, plots contours of the axial velocity of the perturbation mode, for Reynolds numbers close to critical, across blockage ratios $b =$ 0.50, 0.60 and 0.75. The structure of the modes are very similar, the chief difference being the greater spacing between successive vortex rings. The location at which the perturbation reaches its maximum is intriguing, especially in contrast to the critical flows of pulse period $T = 2.5$ in figure 6.12.

Figure 6.16 plots the axial vorticity of the perturbation mode of $b = 0.50$ and $Re = 600$. The mode bears a structure very similar to that seen in figure 6.13 for pulse period $T = 5.0$. Again, the period doubling is evident in the switching sign of the

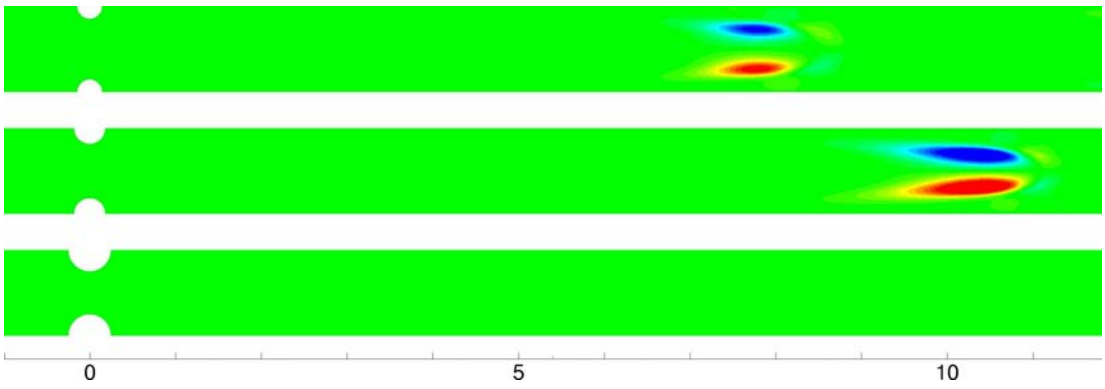

(a)

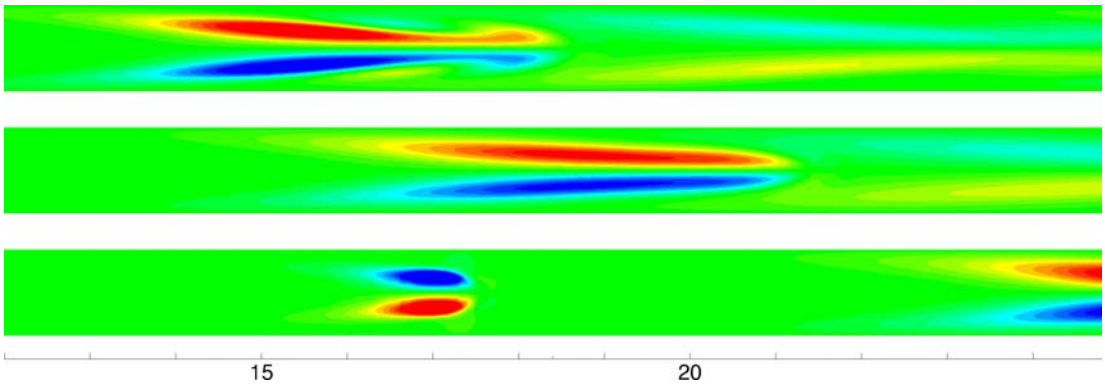

(b)

FIGURE 6.15: Contours of axial velocity (red positive, blue negative) of the leading perturbation modes ($m = 1$) near the critical Reynolds numbers, $Re = 600$, 450 and 325 for $b = 0.50$, 0.60 and 0.75, respectively. The pulsation period is $T = 5.0$, corresponding to Womersley numbers of $\alpha = 13.7$, 11.9 and 10.1, respectively.

contours from one vortex to the next.

The flow is more stable to absolute instability for pulse period $T = 5.0$ than for $T = 2.5$, exhibiting higher critical Reynolds numbers; the mode of instability in each case appears to be of the same structure and nature. Considering that the mode is ordered, consisting of a vortex-tilting of which the direction changes from one vortex ring to the next, there must be some interaction between successive rings. The fact that a vortex will tilt the opposite way to its predecessor shows that the perturbation mode relies on communication from one vortex to the next. This being the case, an increase in critical Reynolds number, Re_c, with pulse period is to be expected, since the vortex rings at greater pulse period are spaced further apart; any cooperation between vortex

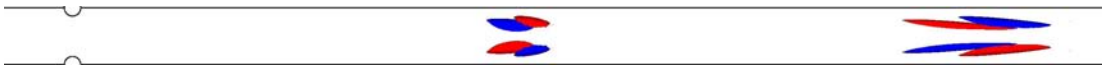

FIGURE 6.16: Two positive and negative contours of the streamwise vorticity of the perturbation mode ($m = 1$) for $b = 0.50$, $Re = 600$, $A = 0.75$ and $T = 5.0$ ($\alpha = 13.73$).

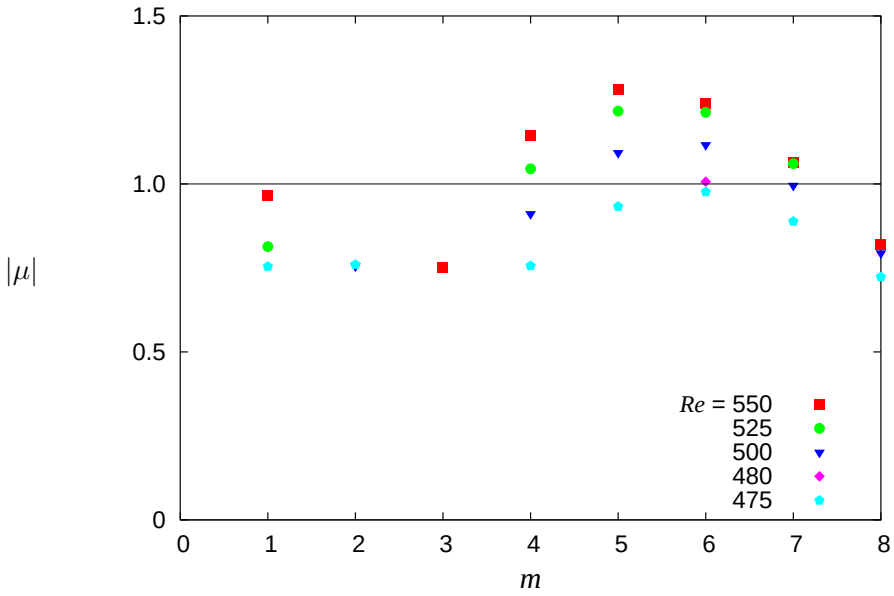

FIGURE 6.17: Absolute Floquet multipliers across a range of azimuthal wave numbers, for $b = 0.60$, $A = 0.75$ and $T = 1.0$. The leading mode is at $m = 6$, becoming critical at Reynolds number $Re_c = 479$. The mode is not period-doubling.

rings is made more difficult by the long spacing.

6.3.3 Stability analysis: $T = 1.0$

In this section, we look at the stability of flows of pulse period $T = 1.0$. These flows are characterised by much shorter vortex formation times and shorter vortex ring spacings. Following on from the conclusions drawn in the previous section regarding reliance of the $m = 1$ perturbation mode on interaction between successive vortex rings, one might expect the conditions to be more conducive for the period-doubling vortex-tilting instability at shorter pulse periods. However, bearing in mind the work of Blackburn & Sherwin (2007), who found that flows of pulse period $T \lesssim 2$ for blockage ratio $b = 0.75$ became unstable to perturbations of $m = 3$ and 4, rather than the period-doubling $m = 1$ instability, we would expect to see a different behaviour for $T = 1.0$

Figure 6.17 plots absolute Floquet multipliers, μ, for the flow of $b = 0.60$, $T = 1.0$, across a range of Reynolds numbers. Here, we see that the negative multiplier at

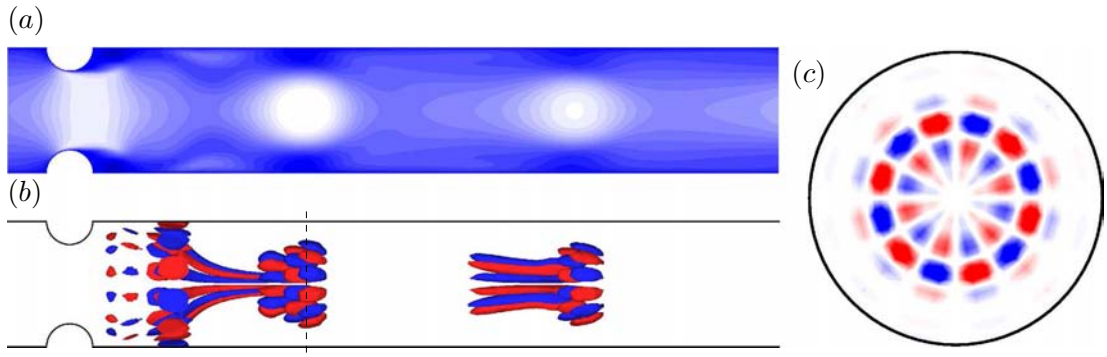

FIGURE 6.18: The base flow and the leading perturbation mode, $m = 6$, for $b = 0.60$, $Re = 480$ and $T = 1.0$ ($\alpha = 27.5$); (a) axial velocity contours of the unperturbed base flow (white positive, black negative), (b) positive and negative isosurfaces of axial vorticity of the perturbation mode and (c) positive and negative contours of axial vorticity of a cross-section of the perturbation at $z/D = 1.85$ or the dotted line on figure (b).

azimuthal wave number $m = 1$ – which corresponds to the period-doubling vortex-tilting instability discussed in sections 6.3.1 and 6.3.2 – is stable across the Reynolds number range shown. Indeed, the flow becomes critical at $Re_c = 479$, for an azimuthal wave number of $m = 6$; the multiplier is real and positive, indicating it is synchronised with the base flow. The mode is not as dominant as the period-doubling instability for pulse periods $T = 2.5$ and 5.0; relatively, the multipliers for wavenumbers $m = 5$ and $m = 7$ are only slightly more stable than the leading mode $m = 6$. This is reminiscent of the behaviour seen at small pulse periods in the work of Blackburn & Sherwin (2007), who observed a competition between the $m = 3$ and $m = 4$ modes as the pulse period was varied for $T < 2$.

Contours of the axial velocity of the base flow, along with contours of the axial vorticity of the leading perturbation mode, $m = 6$, for $b = 0.60$, $T = 1.0$ and Reynolds number $Re = 480$ – just above the critical Reynolds number, $Re_c = 479$ – are depicted in figure 6.18. The perturbation grows immediately downstream of the blockage; the vorticity appears to grow on the vortex under formation in the throat of the contraction, and interact with the next vortex downstream, where the perturbation strength is at its greatest, $z/D = 1.85$. At $z/D = 0.85$, the perturbation is at its strongest on the walls of the tube, before aligning again with the tube centreline. It is possible that this behaviour is related to the local maximum of axial velocity which is evident on figure 6.18(a) at $z/D \approx 1$, which has an unusually close proximity to the tube wall. This issue will be returned to, after discussing the stability of the flow at the other

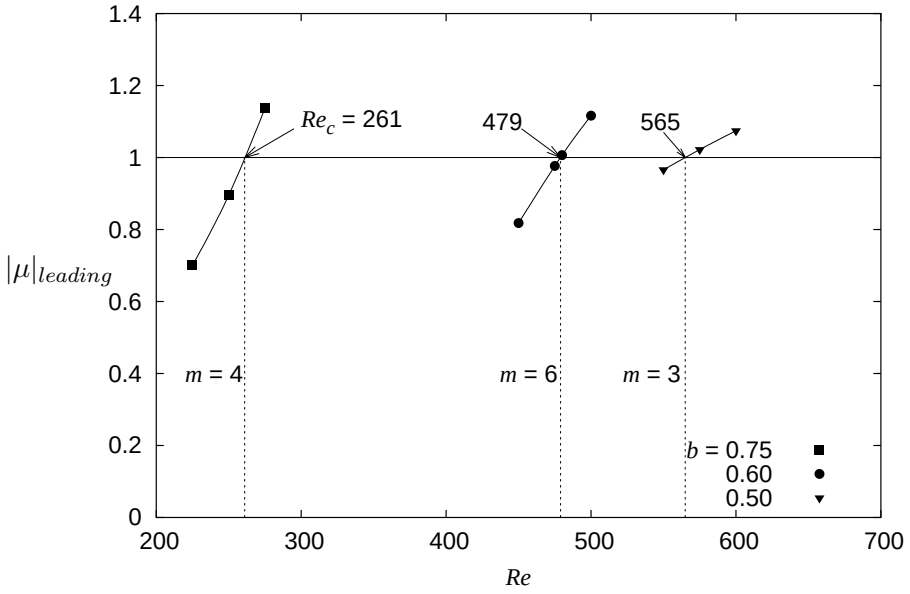

FIGURE 6.19: Absolute Floquet multipliers of the leading perturbation modes for $T = 1$ and $A = 0.75$. Across the three blockages shown, $b = 0.50$, 0.60 and 0.75, the leading mode wavenumbers are $m = 3$, 6 and 4, respectively; the Womersley numbers for the critical cases are 29.8, 27.43 and 20.2, respectively.

blockage ratios.

The perturbation mode is unusual, as it grows immediately downstream of the blockage. Most linear stability modes for pulsatile flow seen so far in the literature, and in the present work, begin their growth some distance downstream; the mode of figure 6.18 grows from the very beginning of the separating shear layer. The perturbation strength reaches a maximum at an axial location $z/D = 1.85$, which is where the cross-sectional slice of figure 6.18(c) is taken. An analysis of the more stable perturbation mode at one azimuthal mode number less than that of figure 6.18, $m = 5$, reveals a perturbation structure located further downstream of the blockage. At $m = 7$, the perturbation strength is greatest near the blockage, in a manner similar to the mode at $m = 6$.

For $T = 1.0$, a summary of the Floquet multipliers for the leading azimuthal modes for the blockage ratio range considered is presented in figure 6.19. The azimuthal wave number, m, of the leading perturbation mode is different for each of the blockage ratios tested. For the blockage range tested, the period-doubling $m = 1$ vortex-tilting instability mechanism is stable. As already observed, the leading mode for $b = 0.60$ is

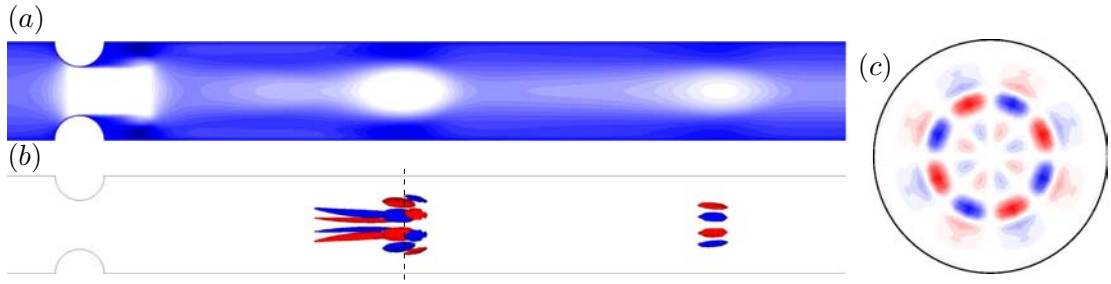

FIGURE 6.20: The base flow and plots of the leading perturbation mode, $m = 4$, at $b = 0.75$, $Re = 275$ and $T = 1.0$ ($\alpha = 20.78$); (a) axial velocity contours of the unperturbed base flow, (b) positive and negative isosurfaces of axial vorticity of the perturbation mode and (c) positive and negative contours of axial vorticity of a cross-section of the perturbation at $z/D = 3.3$ or the dotted line on figure (b).

at $m = 6$; for $b = 0.50$ the leading mode is of wavenumber $m = 3$, while for $b = 0.75$, it is $m = 4$. The critical Reynolds number for instability for the geometry of $b = 0.75$ is almost identical to that for pulse period $T = 2.5$. However, this is purely coincidental, since the leading instability mode for the flow of pulse period $T = 1.0$ corresponds to a different azimuthal wave number of $m = 3$. For blockage ratios $b = 0.50$ and 0.60, the flow is more stable than for pulse period $T = 2.5$, the critical Reynolds numbers being $Re_c = 565$ and 479, respectively.

Figure 6.20 depicts contours of the axial velocity of the base flow, along with isosurfaces of the axial vorticity of the leading perturbation mode ($m = 4$), for $b = 0.75$ and $Re = 275$, just above the critical Reynolds number, $Re_c = 261$. Similar to the mode for $b = 0.60$, the perturbation forms on the base flow vortex rings, except here the mode grows further downstream, reaching a maximum at $z/D \approx 3.3$; also, the mode vorticity does not extend upstream to the blockage in the same way as in the case of the $b = 0.60$ geometry (see figure 6.18). The instability bears a strong similarity to the wavy modes observed by Blackburn & Sherwin (2007) who found a competition between mode $m = 3$ and $m = 4$ instabilities for low pulse periods and $b = 0.75$. They argued that the modes were a type of Widnall vortex-core instability, which typically manifest as short-wavelength perturbations on unconstrained vortex rings (Widnall *et al.* 1974); the main difference for the present flow is the constraining of the vortex rings in a tube.

For $b = 0.50$, the leading perturbation mode is of wavenumber $m = 3$ and is period-doubling. Figure 6.21 plots the axial velocity of the base flow, along with isosurfaces of the axial vorticity of the perturbation mode. In this case, the perturbation is less

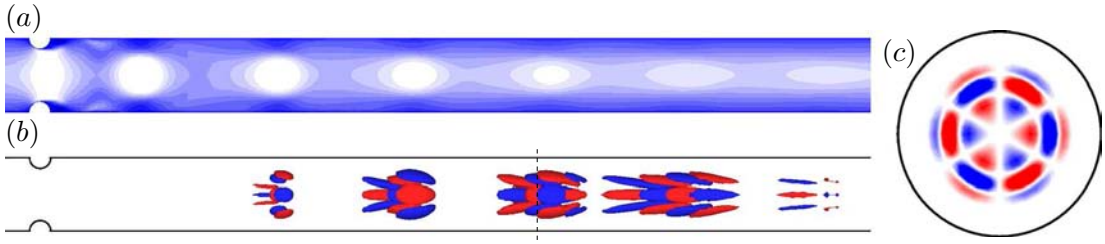

FIGURE 6.21: The base flow and plots of the period-doubling leading perturbation mode, $m = 3$, for $b = 0.50$, $Re = 575$ and $T = 1.0$ ($\alpha = 30.05$); (a) axial velocity contours of the unperturbed base flow, (b) positive and negative isosurfaces of axial vorticity of the perturbation mode and (c) positive and negative contours of axial vorticity of a cross-section of the perturbation at $z/D = 6.9$ or the dotted line on figure (b).

localised than for blockage ratios $b = 0.60$ and 0.75. The strength of the mode reaches a maximum at $z/D \approx 6.9$. The perturbation vortex structure becomes elongated as it travels downstream, dissipating as the base flow vortex ring dies away. There is no obvious reason why this mode should be period-doubling, while the modes of figures 6.18 and 6.20 are synchronous with the base flow. In figure 6.21 there does appear to be a stronger interaction between the perturbation vorticity on successive vortex rings than there is in the other two modes. Also, the mode appears to grow first around the flow in the centre of the tube, and not close to the tube walls, as is the case for the leading mode for $b = 0.60$.

In general, the change in the stability of the flow for lower pulse periods is characterised by higher wavenumber modes becoming unstable ahead of the $m = 1$ period-doubling mode seen at higher pulse periods. Also, the most unstable modes seem not to be as dominant, the leading mode varying across the blockage ratio range tested.

At four intervals over the one pulse period, figure 6.22 plots positive and negative contours of azimuthal vorticity of the base flows of the three near-marginal stability flows presented in figures 6.18, 6.20 and 6.21. This is undertaken with the intention of highlighting the characteristics of flows of $T = 1.0$ which distinguish them from flows of higher pulse period. The most obvious difference is the much reduced spacing between successive vortex rings; in addition to this, the vortex rings do not survive as far downstream as they do in flows of higher pulse period. In the $T = 1.0$ base flows, the strengths of the vortex rings at the axial locations where the period-doubling instability generally begins to grow are very weak; assuming it is the vortex ring which

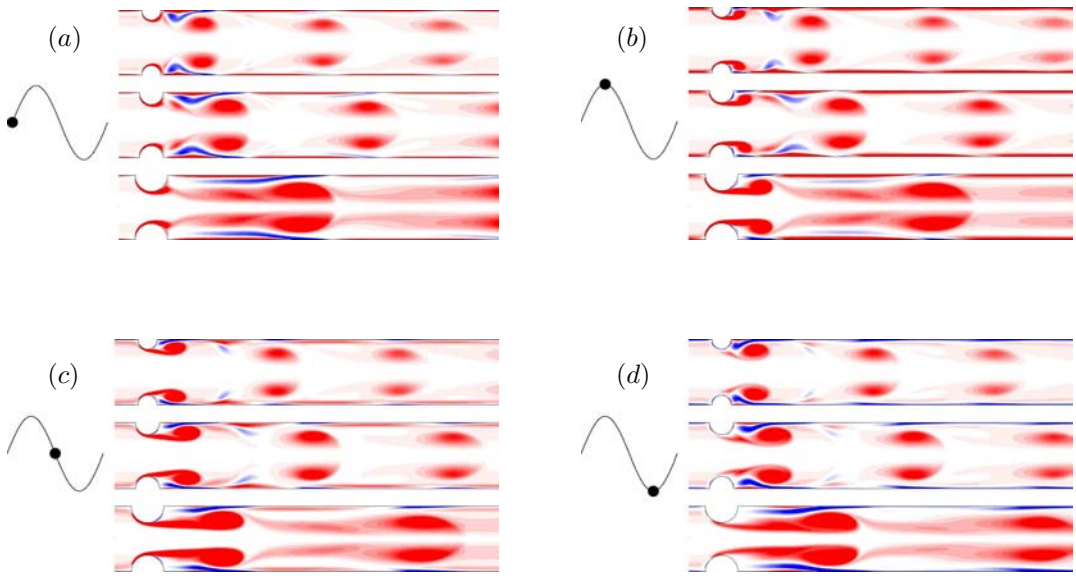

FIGURE 6.22: For blockage ratios $b = 0.50$, 0.60 and 0.75, plots of vorticity contours of the base flows for Reynolds numbers ($Re = 575$, 480 and 275, respectively) just above the critical Reynolds numbers, Re_c, plotted on figure 6.19. Plots are shown at (a) $t = 0.0T$, (b) $0.25T$, (c) $0.5T$ and (d) $0.75T$.

feeds the growth of the instability, this may explain the stability of the flow at pulse period $T = 1.0$ to the period-doubling $m = 1$ perturbation mode. Also, the reduced spacing of the vortex rings may be conducive to an interaction between vortex rings; in this way, perturbation modes dependent on such interaction may be promoted ahead of modes which are not as reliant. We observe that for pulse period $T = 5.0$, where the vortex ring spacing is much greater, the flow is significantly more stable to the higher wavenumber perturbation modes.

Another interesting phenomenon in flows of the shorter pulse period $T = 1.0$ is the behaviour of the trailing vorticity in the immediate downstream vicinity of the blockage. The appearance of a local maximum of axial velocity near the tube walls for the critical flow for $b = 0.60$ has already been noted (see figure 6.18). On the vorticity contour plots of figure 6.22, it appears as a short thread of negative vorticity which reaches into the mainstream flow, particularly in the cases with $b = 0.50$ and 0.60. For $b = 0.75$, the effect is not as apparent; however, in comparison to the vorticity plots for $T = 2.5$ on figure 6.4, the area of negative vorticity appears to be closer to the tube centreline,

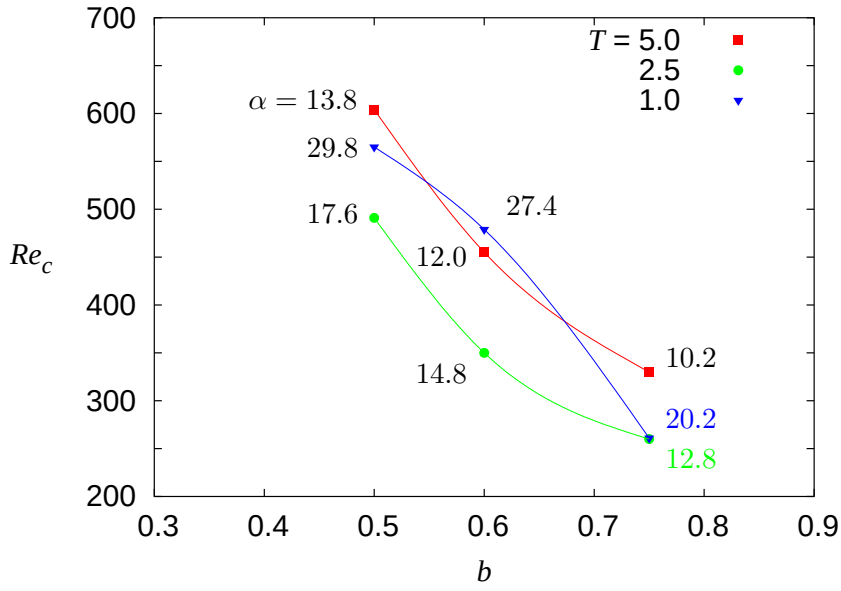

FIGURE 6.23: Critical Reynolds numbers as a function of blockage ratio for the flow configurations analysed throughout section 6.3, for pulsation amplitude constant at $A = 0.75$. The Womersley number for each case plotted in included on the graph.

with a second thread of positive vorticity between it and the tube wall. For $b = 0.50$ and 0.60, the thread of negative vorticity is drawn more obviously into the vortex wake. This vorticity behaviour in the wake of the vortex ring is markedly different from the behaviour at higher pulse period, and may be important in the promotion of the higher wavenumber perturbation modes. We also note the growth in the leading perturbation mode for $b = 0.60$, depicted in figure 6.18, which is particularly strong at $z/D \approx 0.8$ on the tube walls, close to where the maximum of axial velocity is located.

6.3.4 Stability analysis summary: $A = 0.75$

To summarise the results of the stability analysis of this section, figures 6.23 and 6.24 plot the critical Reynolds numbers determined for the various flow configurations tested. Figure 6.23 gives the variation of the critical Reynolds numbers Re_c, for three different pulse periods described earlier, $T = 1.0$, 2.5 and 5.0. The period-doubling $m = 1$ instability dominates for pulse periods $T = 2.5$ and 5.0; in figure 6.23 these two pulse periods exhibit the same curve, with the flow more stable at the longer pulse period of $T = 5.0$. For $T = 1.0$, the wavenumber of the dominant mode varies with the blockage ratio, the curve taking another more irregular form. This is indicative of the

higher wavenumber perturbation modes overtaking the period-doubling $m = 1$ mode. In figure 6.23 the critical Reynolds numbers are shown, along with their corresponding Womersley numbers, α. This is done to give an impression of where the results fall in respect to the standard Womersley numbers that we see in more physiologically realistic flows. For larger arterial vessels, flows can exhibit Womersley numbers varying from $4 \leq \alpha \leq 25$.

Figure 6.24 plots the critical numbers of various modes for three blockage ratios, $b = 0.50$, 0.60 and 0.75, across a range of pulse periods. In addition to the modes discussed in detail earlier, we find a number of other modes become dominant for other pulse periods. For $b = 0.50$ and 0.60, a subcritical mode of wavenumber $m = 2$ is dominant for the pulse period ranges $1.4 \lesssim T \lesssim 2.2$ and $1.1 \lesssim T \lesssim 1.6$, respectively. For the three blockage ratios tested, the $m = 1$ period-doubling instability mode dominates for higher pulse periods. In each case, the instability has an optimum period, at which the critical Reynolds number is at its lowest. This optimum pulse period increases slightly for lower blockage ratios. In comparison to the previous work of Blackburn & Sherwin (2007), the optimum pulse periods for both the $m = 1$ and the $m = 3$ and 4 wavy modes are much lower. In particular, for the $m = 4$ mode the optimum pulse period is $T \approx 0.4$, compared to $T = 0.875$ for the similar flow in Blackburn & Sherwin (2007). Also, the critical Reynolds number for the optimum pulse period is relatively much lower, as compared to the same value for the $m = 1$ period-doubling instability. The next section deals with the variation of the flow stability with pulse amplitude.

6.3.5 Effect of amplitude on absolute stability

In this section, the Floquet analysis is extended to investigate the effect of a change in pulsation amplitude on the absolute stability of the flow. The intention is to determine the importance of this parameter on the stability of the flow, and to also complement results of the experimental rig, which was similarly able to produce pulsatile flows of different amplitudes.

If we consider again the vorticity field plots of figure 6.8(b), which included flows for $b = 0.75$, $Re = 300$, $T = 2.5$ and amplitudes ranging from $A = 0.5$ to 1.5, we see that a change in amplitude tends not to change the fundamental behaviour of the flow, but rather increase the strength of the vortex ring. For higher pulsation amplitude, there

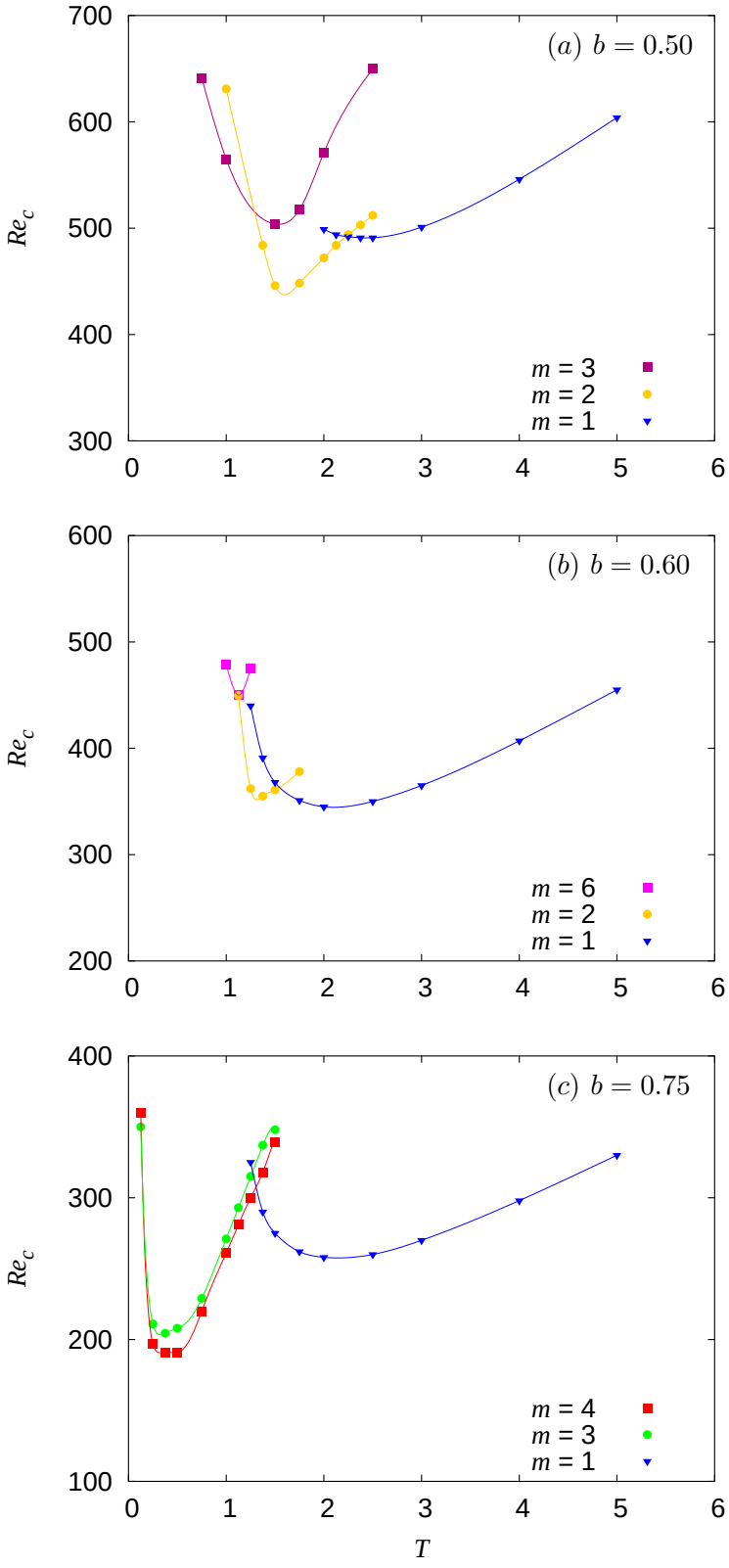

FIGURE 6.24: Critical Reynolds numbers for various modes for constant pulse amplitude $A = 0.75$ and three blockage ratios $b = 0.50$, 0.60 and 0.75, across the pulse period range.

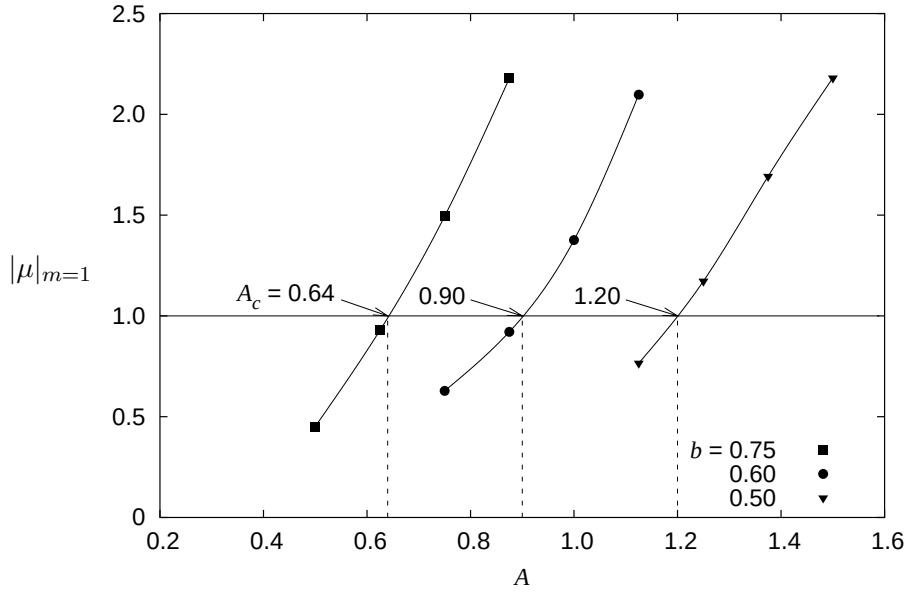

FIGURE 6.25: As a function of pulse amplitude, A, absolute Floquet multipliers of the leading perturbation mode for $T = 2.5$ and $Re = 300$. Across the three blockages shown, $b = 0.50$, 0.60 and 0.75, the leading mode is $m = 1$; the Womersley number is $\alpha = 13.73$.

is more energy in the flow, and the downstream convection of the vortex ring is slightly greater. In addition, at pulse amplitudes of $A > 1$, the sectionally-averaged velocity in the tube is negative for a portion of the diastolic phase of the velocity waveform. For the analysis of this section, the Reynolds number is kept constant at $Re = 300$, while the amplitude is varied. Flows of pulse periods $T = 1.0$ and 2.5 are considered.

For a constant Reynolds number, $Re = 300$, figure 6.25 presents the absolute Floquet multipliers for the leading perturbation mode, $m = 1$, across the three blockage ratios, $b = 0.50$, 0.60 and 0.75, with pulse period $T = 2.5$, as a function of pulse amplitude, A. For this flow configuration, all the leading perturbation modes are of azimuthal wavenumber, $m = 1$. The leading perturbation mode for each blockage ratio is period-doubling, and of the same form as the modes seen in section 6.3.1. As seen in that section, for the geometry $b = 0.75$, with pulse amplitude of $A = 0.75$, the flow becomes critical at $Re = 260$; therefore, for a Reynolds number of 300, we would expect the critical pulse amplitude to be less than 0.75, as it is for $A_c = 0.64$. The critical pulse amplitude at blockage ratio $b = 0.60$ is $A_c = 0.90$. For the geometries $b = 0.60$ and 0.75, and their corresponding critical pulse amplitudes, the flow configurations are only slightly different to those of the critical Reynolds number flows of section 6.3.1.

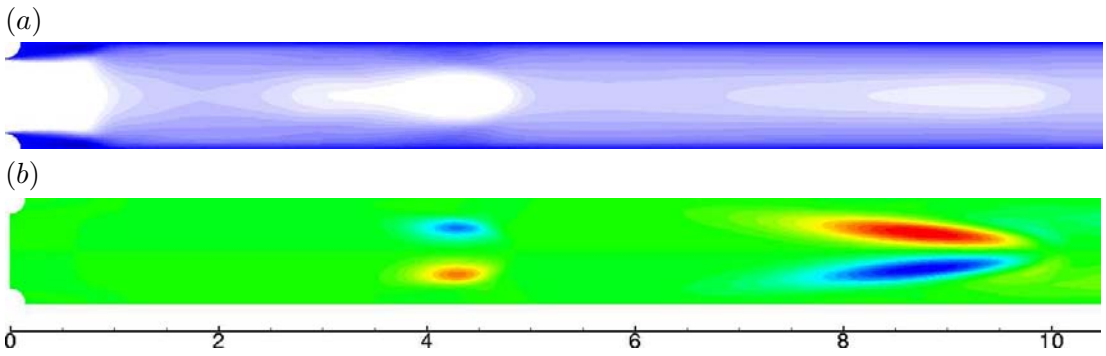

FIGURE 6.26: (a) Contours of axial velocity of the base flow for $b = 0.50$, $Re = 300$, $A = 1.25$ and $T = 2.5$ ($\alpha = 13.73$), (b) positive and negative contours of the axial velocity of the leading perturbation mode, $m = 1$. The pulse amplitude of $A = 1.25$ is slightly above the critical amplitude, $A_c = 1.20$

At $b = 0.50$, the critical pulse amplitude is $A_c = 1.20$. With a pulse amplitude being greater than one, the velocity waveform of this flow configuration consists of a section of negative velocity during diastole; because of this, for $b = 0.50$, the stability of the flow is more distinct than for the other two blockage geometries. The critical pulse amplitude, $A_c = 1.20$, for the mode $m = 1$ is only slightly ahead of the critical pulse amplitude for the mode $m = 2$, which is $A_{c(m=2)} = 1.21$. Figure 6.26 plots the axial velocities of the base flow and of the period-doubling leading perturbation mode, $m = 1$, for the flow of pulse amplitude $A = 1.25$, slightly greater than the critical pulse amplitude, A_c. In comparison to the perturbation velocities seen so far for this type of instability, this particular instance occurs very close upstream. The perturbation develops on the vortex ring at $z/D \approx 4$, as opposed to approximately 8 for the equivalent instability for $Re = 500$ and $A = 0.75$. This progression upstream of the perturbation mode with increasing pulsation amplitude is consistent with the growth of the mode being dependent on the strength of the vortex ring. For higher pulsation amplitudes, the strength of the main vortex ring is greater, allowing the growth of the mode to appear further upstream.

The decreasing stability of the mode $m = 2$ for flows of high pulse amplitude continues for flows at lower pulse period. Figure 6.27 presents Floquet multipliers across blockage ratios of $b = 0.50$, 0.60 and 0.75, for $T = 1.0$, $Re = 300$ and various pulse amplitudes. For blockage ratio $b = 0.75$, in figure 6.27(c), the behaviour is similar to that observed for pulse period $T = 1.0$ for the flow of constant amplitude

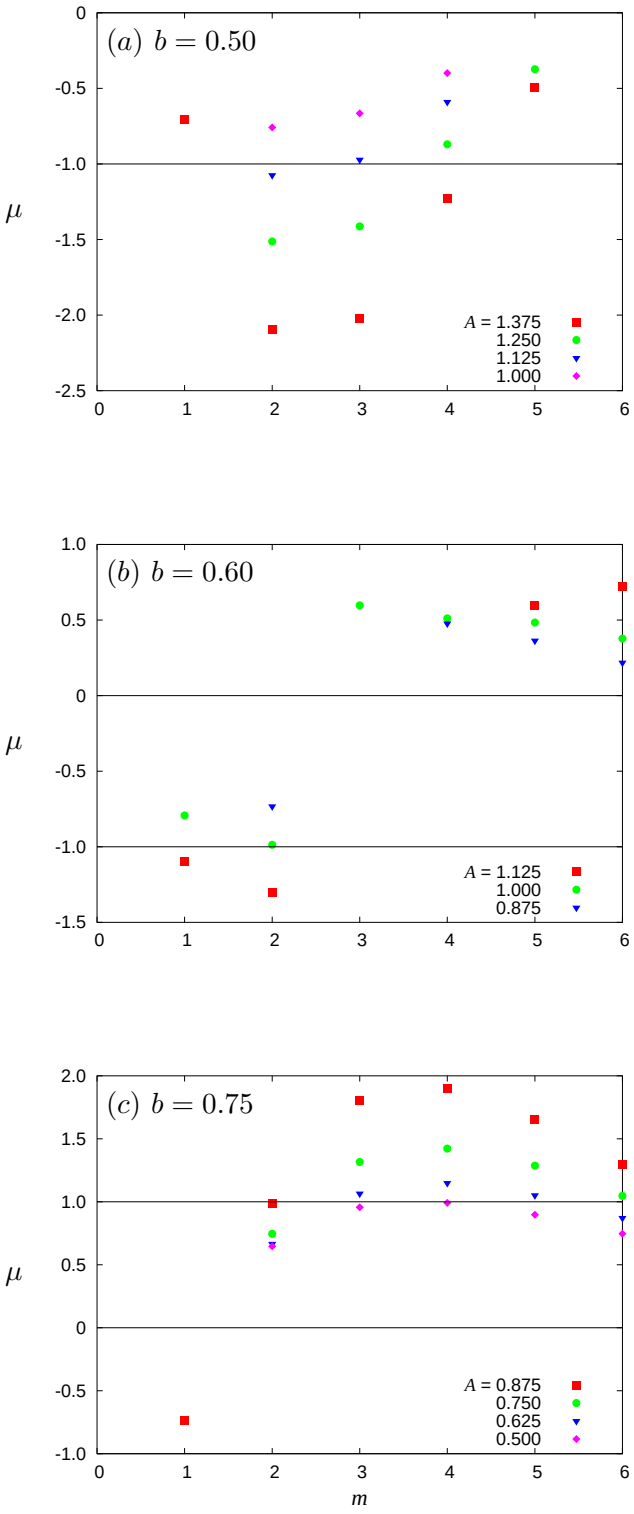

FIGURE 6.27: Floquet multipliers across different pulse amplitudes and blockage ratios of (a) $b = 0.5$, (b) 0.6 and (c) 0.75, for $Re = 300$ and $T = 1.0$ ($\alpha = 21.71$).

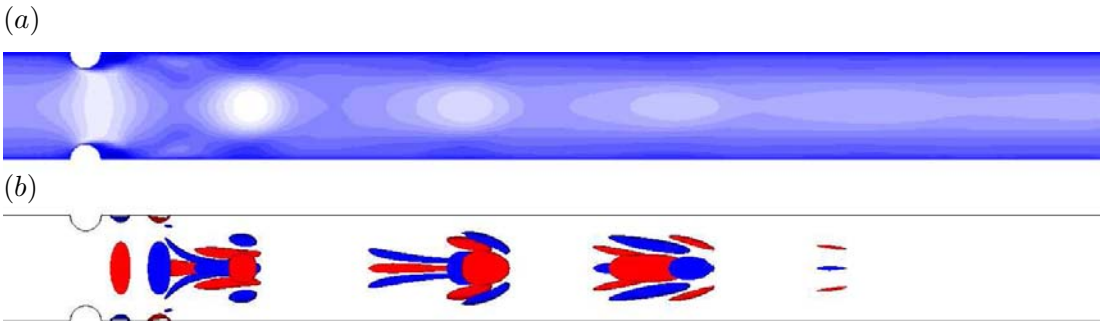

FIGURE 6.28: (a) Contours of axial velocity of the base flow and (b) positive and negative isosurfaces of the axial vorticity of the period-doubling leading perturbation mode, $m = 2$ for $Re = 300$, $b = 0.50$, $A = 1.125$ and $T = 1.0$ ($\alpha = 21.71$). The pulse amplitude is near the critical, $A_c = 1.10$.

$A = 0.75$, with the most unstable modes being of wavenumber $m = 4$. Again, in this instance, the flow configurations are very similar to those analysed in section 6.3.3; the critical amplitude for this configuration with $b = 0.75$ is $A_c = 0.51$. Inspection of the perturbation modes reveals a mode very similar to that of figure 6.20, only with a stronger interaction between successive vortex rings.

For blockage ratios of $b = 0.50$ and 0.60, the leading perturbation mode is of wavenumber $m = 2$. Figure 6.28 plots the axial velocity of the base flow with the axial vorticity of the perturbation mode, for $b = 0.50$ and pulse amplitude $A = 1.125$, just above the critical amplitude. The mode grows immediately downstream of the blockage and on the tube walls, before converging back onto the tube centreline. In this way, although the wavenumber here is $m = 2$ and the perturbation period-doubling, the mode is quantitatively similar to the mode plotted on figure 6.18, which was for a $m = 6$ perturbation with $Re = 480$, $A = 0.75$ and $b = 0.60$. Not only do the two modes appear to grow through the same areas, but the base flow in figure 6.28(a) also exhibits the local maximum of axial velocity at $z/D \approx 1$.

Figure 6.29 plots a cross-section at $z/D = 3.7$ of a linear combination of the base flow and perturbation mode for the flow shown in figure 6.28. In figure 6.29(b), we see the axial velocity take a similar form to the wavy mode shapes seen earlier, only this time for a wavenumber, $m = 2$. In figure 6.29(a), we can see the deformation that the perturbation makes on the base flow. On the plane shown, the axial velocity forms two local maxima radially offset on opposite sides of the tube centreline. Consistent with an $m = 2$ instability, the perturbation appears to squeeze the flow along a plane of sym-

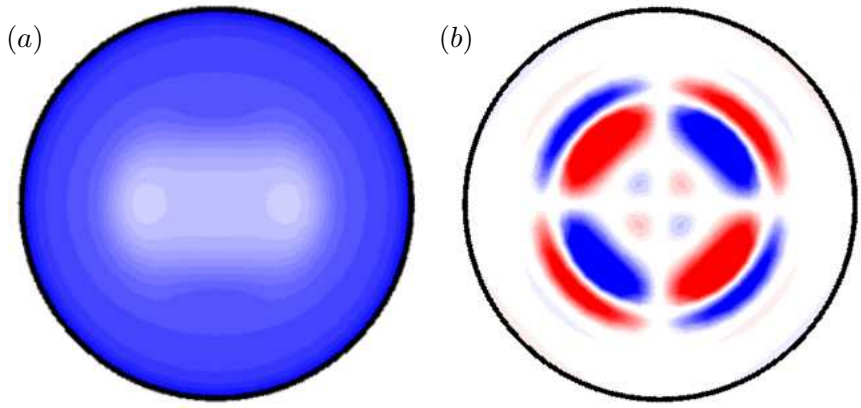

FIGURE 6.29: Cross-sections of a linear combination of the base flow and the period-doubling leading perturbation mode, $m = 2$, for $b = 0.50$, $Re = 300$, $A = 1.125$ and $T = 1.0$ ($\alpha = 21.71$), (a) contours of axial velocity and (b) contours of axial vorticity. The sections are taken at $z/D = 3.7$, which corresponds to where the perturbation mode is at its greatest strength.

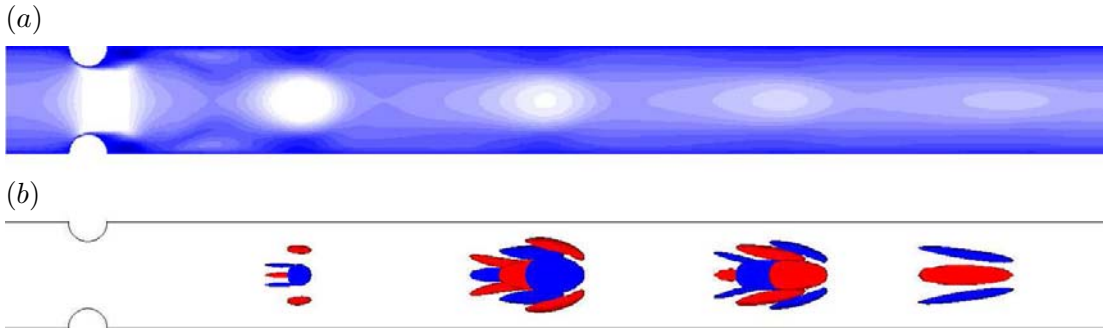

FIGURE 6.30: (a) Contours of axial velocity of the base flow and (b) positive and negative isosurfaces of the axial vorticity of the period-doubling leading perturbation mode, $m = 2$ at $Re = 300$, $A = 1.0$, $b = 0.60$ and $T = 1.0$ ($\alpha = 21.71$). The pulse amplitude is near the critical pulse amplitude, $A_c = 1.01$.

metry. The mode is period-doubling; hence the same slice of figure 6.29(a) taken one period later is identical, except rotated one quarter, or azimuthally by $\theta = \pi/2$. Therefore, the perturbation pinches each successive vortex ring azimuthally perpendicular to the previous.

Figure 6.30 plots the same parameters as figure 6.28, but this time for $b = 0.60$ and $A = 1.0$; the pulse amplitude of $A = 1.0$ is marginally smaller than the critical pulse amplitude, $A_c = 1.01$. The two modes share the same wavenumber and are both period-doubling. Furthermore, we see again a local maximum in the axial velocity of the base flow near the wall at $z/D \approx 1$; but this time the mode shows no growth in the immediate vicinity of the blockage. The mode grows on the vortex ring, reaching a

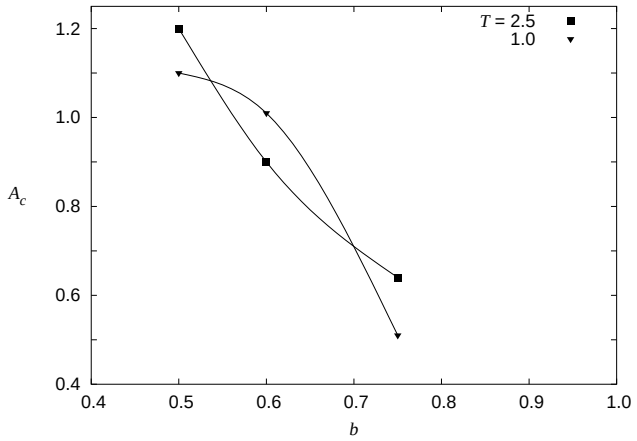

FIGURE 6.31: Critical pulse amplitudes, A_c, for the flow configurations analysed throughout section 6.3.5, for Reynolds number constant at $Re = 300$, and pulse periods of $T = 1.0$ and 2.5 ($\alpha = 21.71$ and 13.73, respectively).

maximum at $z/D \approx 4.3$.

Figure 6.31 plots a summary of the Floquet stability analysis of section 6.3.5. The variation with blockage ratio of the critical pulse amplitude is similar to the variation of the critical Reynolds number of figure 6.23 in section 6.3. For flows of pulse period $T = 2.5$, this is expected, as a similar stability behaviour is observed across the data sets, with period-doubling perturbation modes of wavenumber $m = 1$ being dominant. In contrast to figure 6.23, the stability thresholds for the different pulse periods are similar, rather than the flows of pulse period $T = 1.0$ being more stable than those of $T = 2.5$.

The question of if and how these stability behaviours manifest in real experimental flows is addressed in the following section.

6.4 Experimental results

6.4.1 Experimental validation

To create experimental pulsatile flow, the piston, as described in chapter 3, was employed. Whereas in chapter 5 the piston was used to produce steady flows subject to high-frequency, low-amplitude forcing, here, it is used to produce low-frequency, high-amplitude pulsation of magnitudes commensurate with the pulsation present in large arteries of the cardiovascular system.

Creating pulsatile flows experimentally introduces many challenges. So far in this

chapter, only numerically simulated pulsatile flows have been investigated – the experimental flow will entail many differences, the principal one being the presence of noise, of which there are several sources. From the surrounding environment, vibrations can be transmitted through the laboratory floor (flows on the threshold of stability could be perturbed by as little as a shift of weight from one foot of the experimenter to the other). From within the experiment there are several sources, the principal being the pump which drives the circulation through the experiment. The pump is isolated as much as possible, however, some connection between it and the system is inevitable. Another source of vibration comes from the motor driving the piston, although this is small compared to the main pump. Imperfections within the experiment are another source. During the commissioning of the experimental rig, much effort was invested in ensuring the alignment of the 4 metres of straight tube upstream and downstream of the test section. Another source of error stems from temperature differences existing within the rig. These sources of perturbation, noise and error are important for our discussion in this chapter; the methods used in minimising them have been described in more detail in chapter 3.

For an unblocked tube – or a section upstream of the blockage – figure 6.32(a) plots a comparison over one pulse period between the analytical Womersley solution for the velocity, $u(r,t)$, and values measured using particle image velocimetry (PIV), for $Re = 190$, $A = 0.75$ and $T = 1.75$. The values are phase-averaged over ten pulsation periods. The agreement is good, excepting some values closer to the tube walls. PIV analysis was hampered by difficulties associated with the curvature of the tube: reflections of the laser led to a loss of information near the bottom and top edges of the flow field under investigation. Also, the particle density of the fluid near the walls was found to be not as great in the mainstream flow.

Figure 6.32(b) plots the same measurements as in 6.32(a), but averaged over the cross-sectional area of the tube, thus giving the sectionally-averaged velocity, $\overline{u}(t)$. Considering the errors in figure 6.32(a), the agreement of figure 6.32(b) is good, indicating the period and amplitude of the created pulsation are reasonably accurate.

A comparison of the numerically-simulated with the PIV-measured velocity fields is shown in figure 6.33, for $b = 0.50$, $Re = 315$, $A = 0.75$ and $T = 3.92$. The PIV measurements are averaged over ten pulse periods. The phase is determined by integrating

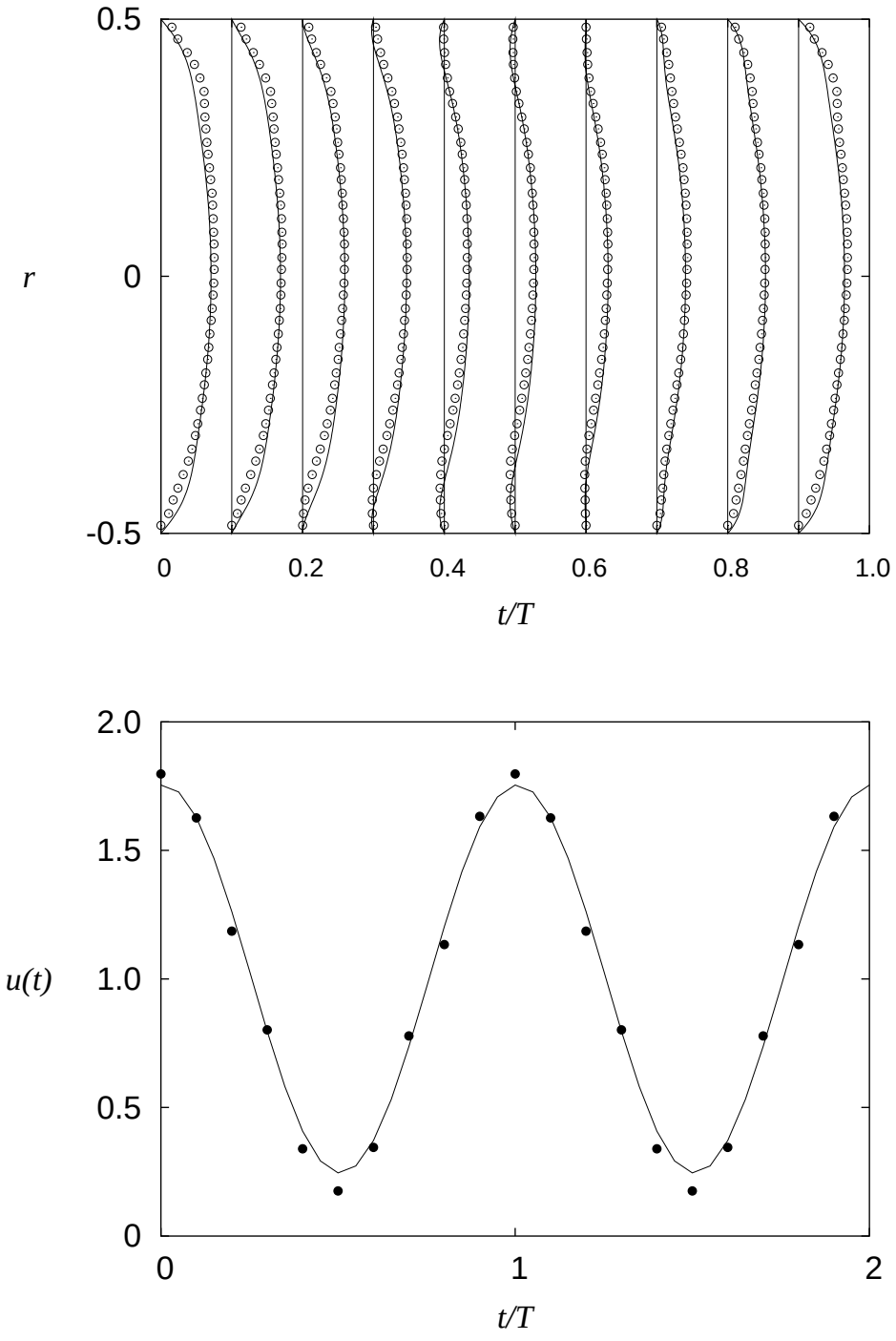

FIGURE 6.32: (a) Comparison of velocity profiles over one pulse period between PIV data (circles) and numerical data (lines) in an unblocked channel, (b) sectionally-averaged velocity, $\overline{u}(t)$, over two pulse periods, for $Re = 190$, $A = 0.75$ and $T = 1.75$ ($\alpha = 13.06$). PIV data is phase-averaged over ten pulsation cycles.

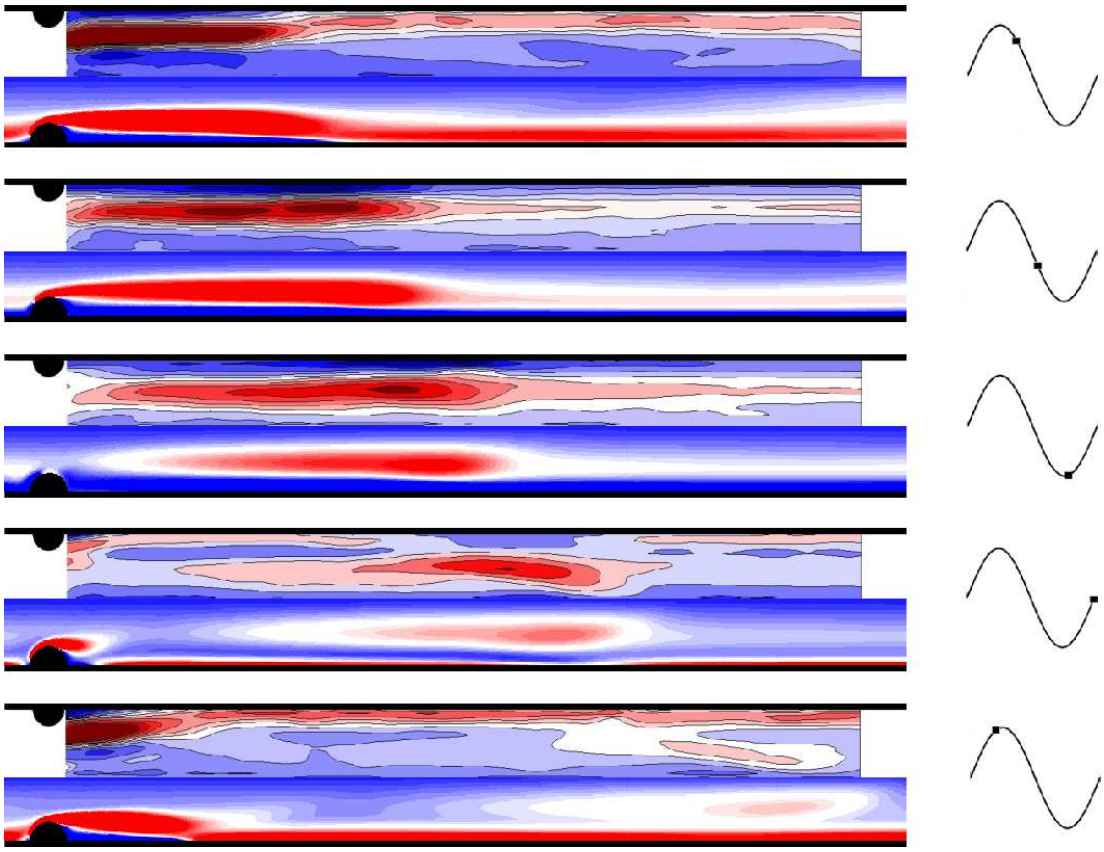

FIGURE 6.33: Contours of azimuthal vorticity of a comparison of PIV (top halves) with numerical simulations (bottom halves), over one period, for $b = 0.50$, $Re = 315$, $A = 0.75$ and $T = 3.92$ ($\alpha = 11.23$). Experimental flow fields are phase-averaged over ten pulsation periods

$u(r,t)$ at an axial location to obtain $\overline{u}(t)$, from which the position along the velocity waveform can be determined.

For this flow configuration, Floquet stability analysis predicts the flow to be stable, $Re = 315$ being approximately half the critical Reynolds number expected (figure 6.24(a)). From the experimental measurements, we see that the flow is stable; the formation of the vortex ring can be discerned, as well as its progression downstream. The vortex can be detected until the end of the field of vision at $z/D = 6.0$. The vorticity matches up well between the two data sets.

6.4.2 Stability of the experimental flow

As the Reynolds number or blockage ratio is increased, the flow becomes more prone to instability. As we examine the experimental flows, it is useful to keep in mind the

limits of instability for the steady flow through the same geometry, as presented in chapter 5. For steady flow ($A = 0$), the limits for convective stability were found to be $Re_c \approx 900$ for $b = 0.50$, $Re_c \approx 400$ for $b = 0.75$ and $Re_c \approx 150$ for $b = 0.90$. The Reynolds numbers for both steady and pulsatile flow are calculated in the same manner, however, with a pulsatile inlet velocity, the flow is fundamentally different to the steady case. When considering the pulsatile flows, is it useful to be aware of the instantaneous Reynolds number as it relates to the steady flow. The instantaneous Reynolds number is calculated using the time-dependent cross-sectional average velocity, $\overline{u}(t)$, rather than the temporal, cross-sectional average, $\overline{U}$. Therefore, the periodic Reynolds number is given by the formulation

$$Re_p(t) = \frac{D\overline{u}(t)}{\nu}. \tag{6.4}$$

The periodic time-dependent Reynolds number varies by the same magnitude as $\overline{u}(t)$; that is, by the pulse amplitude, A. The maximum value that the periodic Reynolds number attains, at $t = 0.25T$, is determined as $\hat{Re}_p = Re_p(0.25T) = (1 + A)Re$.

Figure 6.34 plots vorticity contours from PIV measurements for $b = 0.75$, $Re = 311$, $A = 0.75$ and $T = 3.81$. As in figure 6.33, the flow is phase-averaged over ten pulse periods, and the phase determined by calculating $\overline{u}(t)$ at a particular axial location. The flow parameters are largely similar to the stable flow of figure 6.33, except for the higher blockage ratio. From figure 6.24(b), the flow configuration is very close to the threshold for the period-doubling perturbation mode. Examining figure 6.34 reveals the formation of the vortex ring downstream of the blockage, but in contrast to figure 6.33, the vorticity field of the downstream region $4 \lesssim z/D \lesssim 6$ is flat, with no vortex ring detectable.

Reconsidering the flow of figure 6.33, the periodic Reynolds number attains a maximum value $Re_p(0.25T) = (1 + A)Re = 551$, which is well below the critical Reynolds number observed for steady flow. By contrast, the flow of figure 6.34 achieves a maximum value time-dependent Reynolds number of 544, which is above the stability threshold for steady flow of $b = 0.75$, determined in chapter 5. Therefore, some shear layer instability can be reasonably expected.

Indeed, dye-visualisation of the flow reveals that the flow is unsteady from one period to the next in the downstream region. At this point, it is important to define

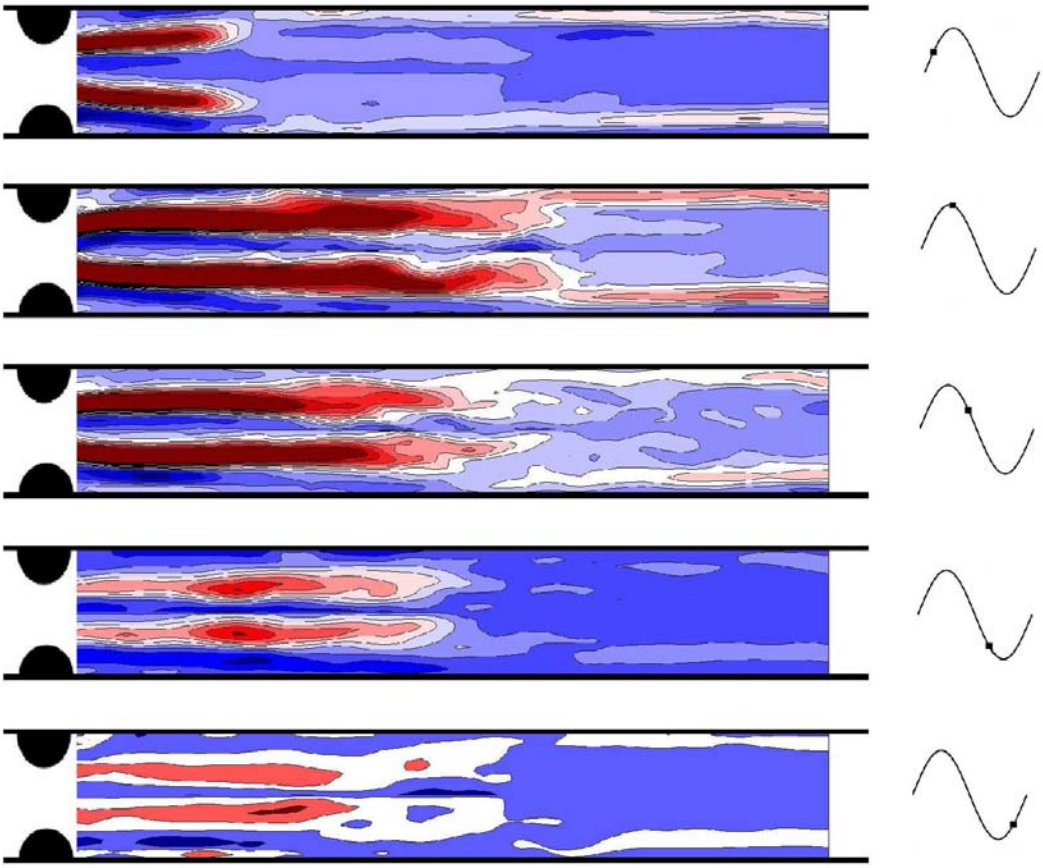

FIGURE 6.34: Contours of azimuthal vorticity from PIV measurement over one period, for $b = 0.75$, $Re = 311$, $A = 0.75$ and $T = 3.81$ ($\alpha = 11.32$). Flow fields are phase-averaged over ten pulsation periods.

exactly what is meant when a pulsatile flow is described as unstable. The base flow is by definition unsteady. However, in the context of pulsatile flow stability, steadiness is defined as periodicity; or, the exact reproduction of the same flow field from one pulsation period to the next. A pulsatile stenotic flow consisting of a large flow breakdown 4 to 5 diameters downstream of the blockage – a common form of instability for pulsatile flows – would not qualify as stable in this context. An axisymmetric flow, consisting of propagating vortex rings which gradually dissipate as they convect downstream, as in figures 6.2 and 6.4, can be considered a stable pulsatile flow.

The absence of any vorticity in the downstream region of the PIV data of figure 6.34 belies the use of phase-averages for this flow configuration. The unsteadiness in the flow is averaged out to zero across the ten PIV images used for each phase in figure 6.34.

The presence of non-periodic unsteadiness in a pulsatile flow limits the usefulness of PIV measurements. For visualising the transition of the flows under investigation, coloured dye-visualisations are more useful. However, these also have their limitations. The dye represents streak-lines of the base flow, giving at best an indication to the flow behaviour. Furthermore, the dye injected into the fluid only rests in the field of vision for a relatively short time. For steady flow, the dye can remain trapped in the steady recirculation zone for a very long time. By contrast, the "washing" nature of the pulsatile flow results in a relatively large amount of mixing downstream of the blockage, meaning a shorter residency of the dye in the field of vision. This effect is particularly strong for unstable flows. Dye-visualisations of pulsatile flows were performed by achieving a steady flow at the desired Reynolds number, injecting the dye and then allowing the flow to achieve a steady state. After the pulse was begun, the dye trapped in the recirculation zone was entrained into the flow. Typically, enough dye remained to visualise the flow for approximately ten pulse periods; less for highly unstable flows, more for very stable ones. In some cases, with high pulsation amplitudes, the mixing of the flow downstream of the blockage would be so strong as to completely color the whole region, thereby allowing a sharp distinction between the colored fluid and the clear fluid entering from upstream through the blockage. This occurred with the $b = 0.90$ blockage and a case is shown later in the chapter.

We remind the reader that the removable test blockage section of the experimental rig was constructed from steel and is not transparent. Hence, in all figures the visible part of the flow begins where the curve of the blockage surfaces rejoins wall of the unblocked tube, or at $z/D = r_b$. The field of view of all dye visualisation images begins slightly upstream of $z/D = r_b$, encompassing a small part of the non-transparent steel section.

Furthermore, the exact phase of the images taken using dye visualisation can not be determined, as the technique does not provide velocity measurements. At best, a rough guess of the phase can be made. Therefore, knowing the exact period of the flow, the phase of an image can only be determined in its relation to another. In each figure showing series of dye visualisations, the first image is given an indeterminate time t_i, which serves as a reference for later images in the figure ($t_i + T/8$, $t_i + 2T/8$, and so forth).

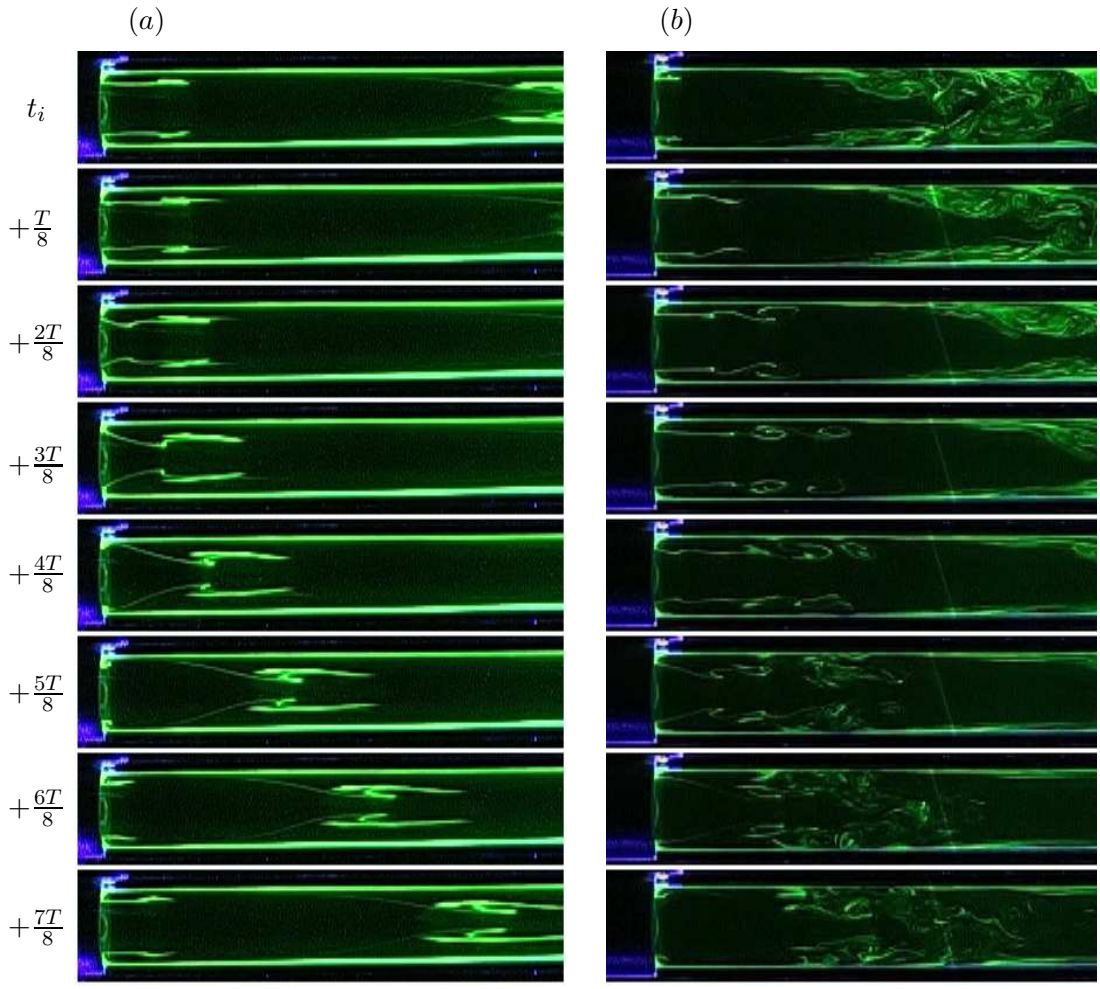

FIGURE 6.35: Coloured-dye visualisations of the flow over one pulse period, for $b = 0.5$ and (a) $Re = 328$, $A = 0.75$ and $T = 3.92$ ($\alpha = 11.46$) and (b) $Re = 686$, $A = 0.5$ and $T = 4.31$ ($\alpha = 15.81$). (The phases between the two cases are not matched)

6.4.2.1 Instability: $b = 0.50$

Figure 6.35 shows coloured dye visualisations for two flows of blockage ratio $b = 0.50$. At left, we have a flow of $Re = 328$, $A = 0.75$ and $T = 3.92$, a configuration similar to that of figure 6.33. As before, the rolling-up of the vortex ring can be seen immediately downstream of the blockage, followed by the stable progression downstream. From the earlier Floquet stability analysis, we expect this flow to be absolutely stable; experimentally, it appears to be also convectively stable, with the same vortex structure of figure 6.35(a) repeating each pulsation period.

At right, in figure 6.35(b), are dye visualisations of the flow for a Reynolds number approximately twice that of the flow of figure 6.35(a), with a slightly greater pulse

period; the pulse amplitude of $A = 0.50$ is also slightly lower. If we consider the maximum values of the periodic Reynolds number for the two flow configurations, we see that for the lower Reynolds number case $\hat{Re}_p = 574$, while for the higher Reynolds number case $\hat{Re}_p = 1029$ – the critical Reynolds number for convective instability for the steady flow of blockage ratio $b = 0.50$ is $Re_c \approx 900$. Hence, it is not surprising that we see strong unsteadiness for the higher Reynolds number case.

The instability appears to be related to convective shear layer instability. In the first image shown, a large region of mixed dye can be seen around $z/D = 4$. In the following images, this region convects rapidly downstream, indicating that the flow is in the systolic, or accelerating portion of the pulse waveform. During this same period, the shear layer emanating from the blockage can be seen developing, but not in a regular fashion. In the fourth of the series of images, at $t_i + (3T/8)$, a series of two distinct rolled-up vortices can be seen around $z/D = 2$. During the second half of the series of images, the diastole, or deceleration period, the rolled-up shear layer vortices do not convect downstream, but follow the pulse waveform, breaking down and causing a strongly mixed flow. The turbulent portion of flow then convects downstream with the mainstream pulse velocity.

The instability appears to be strongly based on the convective shear layer roll-up. Not only does the instantaneous periodic Reynolds number reach above the threshold found for steady flow, but the series of discrete shear layer vortices is consistent with a Kelvin-Helmholtz type instability.

For flows of blockage ratio $b = 0.50$, in relation to the results of the Floquet stability analysis of section 6.3, inspection of the flow for a range of Reynolds numbers with $A = 0.75$ reveals a boundary for stable vortex formation and convection downstream – as in figure 6.35(a) – for $2 \leq T \leq 3$ of $Re_c \approx 350$. This critical Reynolds number is significantly smaller than the Floquet-predicted value for $T = 2.5$, of $Re_c = 491$; the mode predicted was of the period-doubling vortex-tilting type, although no evidence of this mode was detected for the $b = 0.50$ flows. The most probable reason for the difference between the critical Reynolds numbers is, like in the steady flow, the presence of noise in the experimental flow. The type of instability observed – a convective Kelvin-Helmholtz shear layer mechanism – is dependent on some noise or disturbance in the system, and is not a mechanism detectable by our absolute linear Floquet stability

analysis. As much as the experimenter searched for period-doubling phenomena in the $b = 0.50$ flows, none was detected. However, the stability of the flows for blockage ratio $b = 0.75$ proved to be more interesting, especially in relation to the numerical Floquet stability analysis.

6.4.2.2 Instability: $b = 0.75$

Figure 6.36 presents dye visualisations over two pulse periods for blockage ratio $b = 0.75$, Reynolds number $Re = 328$, pulse amplitude $A = 0.75$ and period $T = 3.92$. For this flow configuration, the maximum of the periodic Reynolds number, $\hat{Re}_p = 574$, far exceeds the threshold for convective instability in the steady flow for this blockage ratio ($Re_c \approx 400$). The Reynolds number is slightly greater than the critical Reynolds number calculated from linear stability (see figure 6.24(c)). The flow is highly unstable; strong mixing is evident in the large regions of uniform dye distribution, such as in the first and fifth images, at $t = t_i$ and $t_i + 4T/4$. The delineation of the flow achieved by figure 6.36 stems mostly from the contrast between the well-mixed "muddy" dye-regions and the clear fluid entering from upstream of the blockage. The formation of a vortex ring from the fluid from upstream can be detected in the wide black region immediately downstream of the blockage in the first and fifth images of the figure. The radial width of this region is much larger than the internal diameter within the contraction ($D/2$), which indicates the rolling up of the vortex ring. The images which follow this indicate a strong breakdown of the vortex ring and its wake. Some evidence of Kelvin-Helmholtz type shear layer vortices can be discerned, but the dye visualisation is largely inconclusive.

Given the strong turbulence and unsteadiness in the flow of figure 6.36, a more stable flow of a slightly smaller Reynolds number is considered. Figure 6.37 presents dye visualisations over one pulse period of the flow of blockage ratio $b = 0.75$, Reynolds number $Re = 206$, pulse amplitude $A = 0.75$ and period $T = 2.43$. Floquet stability analysis on the numerical simulations predicts the flow to be absolutely stable (see figure 6.24(c)), while our maximum periodic Reynolds number is given by $\hat{Re}_p = 361$, which is on the threshold for convective instability in the steady flow. Some shear layer instability is therefore to be expected.

In the first image, we see the flow at the end of the vortex formation phase, with

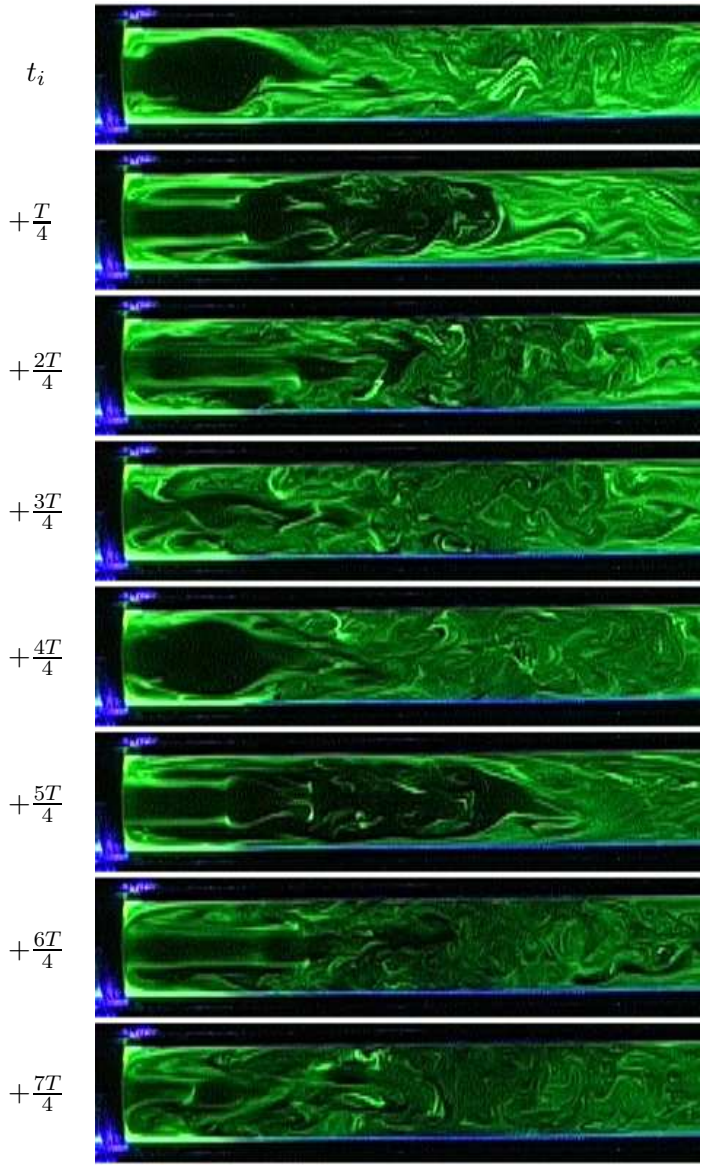

FIGURE 6.36: Coloured-dye visualisations of the flow over two pulse period, for $b = 0.75$, $Re = 328$, $A = 0.75$ and $T = 3.92$ ($\alpha = 11.46$).

a large body of clear fluid from upstream rolling up into the main vortex ring, which subsequently convects downstream. For this configuration, the flow is still unstable, but not as strongly; by contrast with the previous example, the shear layers emanating from the blockage are clearly discernible over a large portion of the pulsation. The flow breaks down at approximately 4 to 5 diameters downstream of the blockage. However, the shear layer roll-up of a Kelvin-Helmholtz type instability is not as evident as in the previous example. Indeed, any waves in the separating shear layer seem relatively

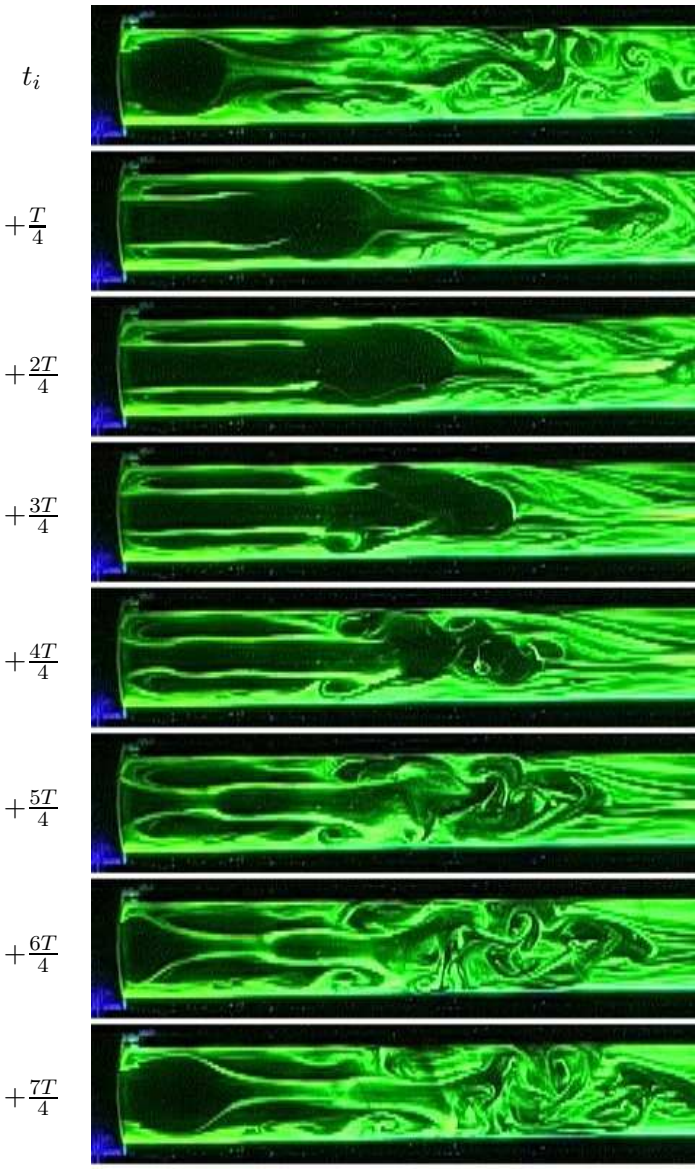

FIGURE 6.37: Coloured-dye visualisations of the flow over one pulse period, for $b = 0.75$, $Re = 206$, $A = 0.75$ and $T = 2.43$ ($\alpha = 11.54$).

gentle in comparison with the breakdown which occurs further downstream. Shear layer roll-up in the wake of the main vortex ring does not appear to be the main flow breakdown mechanism.

If we examine the downstream section of the first image in the series, a substantial region of unsteadiness exists. It may be that the stability of the vortex ring formed during the following pulse period is affected by this and that the unsteadiness is self-sustaining from one period to the next, rather than fed from shear layer vortices formed

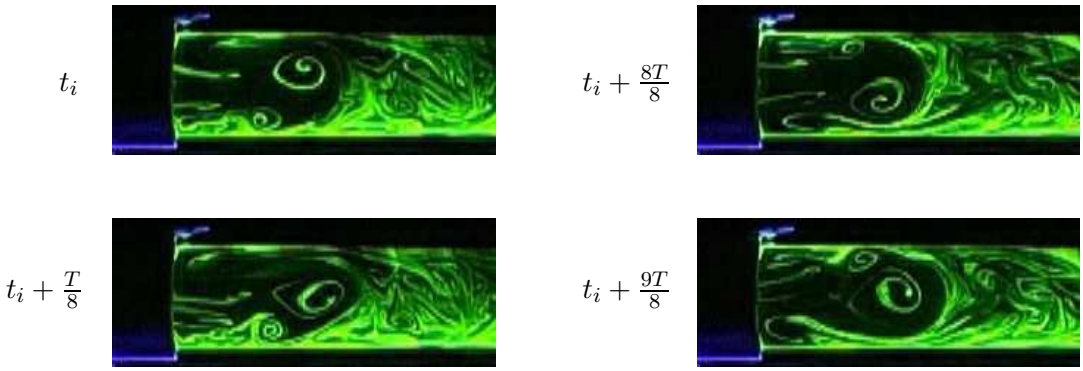

FIGURE 6.38: Coloured-dye visualisations highlighting the period-doubling instability, for $b = 0.75$, $Re = 132$, $A = 1.30$ and $T = 0.85$ ($\alpha = 15.8$). At left are shown two images at $t = t_i$ and $t = t_i + T/8$; at right the flow one period later.

slightly upstream. If this were the case, the question arises of where this unsteadiness initially comes from. This particular flow will be reconsidered shortly in the chapter.

It is in flows of blockage ratio 0.75 and pulsation amplitudes $A > 1$ that the clearest evidence of the period-doubling vortex-tilting instability reveals itself. Figure 6.38 presents several images of the flow for $Re = 132$, $A = 1.30$ and $T = 0.85$ ($\hat{Re}_p = 304$). To the left are images at $t = t_i$ and $t_i + T/8$, which show the vortex ring which forms immediately downstream of the blockage tilting heavily from top to bottom. To the right are shown the corresponding images exactly one period later. The vortex is tilting equally heavily in the opposite direction. Such configurations, with $b = 0.75$ and $A > 1$, were the only ones where period-doubling could be as clearly detected.

Special note needs to be made here of the conditions under which this particular period-doubling behaviour is observed. Firstly, Floquet stability analysis of a numerical simulation of this flow predicts it to be stable. Secondly, the position and growth of the instability is not consistent with the period-doubling vortex-tilting mode predicted throughout the earlier parts of this chapter, nor with the mode predicted in Sherwin & Blackburn (2005) for their work on a similar geometry of $b = 0.75$. Numerically, the mode growth occurs far downstream. Direct numerical simulations of the three-dimensional flow in Sherwin & Blackburn (2005) showed the instability slowly progresses upstream, with a flow breakdown settling four to five diameters downstream of the blockage. However, this "settling-in" of the unsteadiness occurred over very long time

scales. In the case of figure 6.38, the instability is apparent *directly* downstream of the blockage and appears within two periods of the pulsation beginning – there is no slow upstream progression of the instability. Therefore, the initial vortex tilting may be dependent on the pulsation initialisation or simply grows quickly. However, we observed that for the vortex-tilting instability predicted numerically in section 6.3.5 for the $b = 0.50$ and $b = 0.60$ geometries – both with critical amplitude $A > 1$ – the peak strength of the corresponding perturbation mode moved upstream (see figure 6.26(b)). This is consistent with the instability growing on the vortex ring and being dependent on its strength. At higher pulsation amplitudes, stronger circulation in the vortex rings allows the growth of the instability further upstream.

A point of some interest is the orientation of the vortex-tilting. In every observed instance of the phenomenon, the instability acts in the vertical plane. The instability must choose a direction somehow; it is more than likely that in the experiment the choice of plane is related to the direction of the gravitational force. As discussed in chapter 3, temperature differences between the fluid in the tube and the fluid in the visualisation box can have a significant effect on flows. The heating or cooling of fluid through the tube walls can lead to convection in the tube, causing strong asymmetries in the flow. This source of error is minimised as far as possible, yet it still remains, if only at a low level. Even at this scale, the direction of the error may be enough to fix the direction of the vortex-tilting instability. A similar phenomenon – where the orientation of an asymmetric instability on an axisymmetric base flow fixes at a certain angle on a given experimental rig – has been observed previously in work on the wake flows of spheres (Leweke, Provansal, Ormieres & Lebescond 1999).

Given the conditions under which we observe the period-doubling phenomenon and the nature of the numerically-predicted instability, the existence of the phenomenon here is surprising. The Floquet stability analysis for this flow predicts it to be stable and furthermore, the instability grows and operates immediately downstream of the blockage with only a short development time. A clue to the problem lies in Blackburn & Sherwin (2007), which investigates the possible interaction between convective shear layer instability and the absolute period-doubling vortex-tilting instability for a similar blockage geometry of $b = 0.75$. In effect, they performed Floquet stability analysis on a base pulsatile flow already perturbed by a low-amplitude, high-frequency forcing.

At large pulse periods, they found Floquet multipliers much greater than those found performing the stability analysis on unperturbed flows. More interestingly, the peak strengths of the perturbation modes moved far upstream. Direct numerical simulation of the perturbed flow, at $Re = 600$, $A = 0.75$ and $T = 10$, revealed a response strong enough that the period-doubling nature of the instability was no longer detectable. They did not calculate critical stability boundaries for these perturbed flows.

There are many differences to the current case. In the work of Blackburn & Sherwin (2007), a forcing was applied, rather than the noise profile of our experimental rig – the experimental flows are subject to a much wider spectrum of noise than a single-frequency forcing. Also, the case tested in that work is at a pulse period of $T = 10$, the authors finding the effect more pronounced on flows consisting of longer shear layers. Nonetheless, returning to the flow of figure 6.37 with $A = 0.75$, if we assume that generally the period-doubling instability is augmented by convective shear layer instability, that it appears further upstream and that its period-doubling nature is less apparent, it is at least consistent with the instability seen in that figure. If the instability in figure 6.37 was of the period-doubling vortex-tilting mechanism, it is possible that its exact nature would not be readily apparent.

In order to verify if we can detect any evidence of period-doubling in the flow of figure 6.37, for $b = 0.75$, $Re = 206$, $A = 0.75$ and $T = 2.43$, figure 6.39 re-plots the flow, this time at the same phase over six consecutive periods. The plot is at best inconclusive as to the presence of a period-doubling vortex-tilting mechanism at play. If there is any indication of period-doubling, it is in the flow breakdown which occurs at $4 < z/D < 6$. In the first and third images, the flow breakdown appears to have a similar upwards-tilting bias. Considering the final two images, the flow breakdowns seem to be tending in opposite directions; at $t = t_i + 4T$, the flow in this region ($z/D \approx 4$) has an upwards bias, while the same region at $t = t_i + 5T$ has a downwards bias.

These indications of period-doubling in the flow are tenuous; however, we do not expect that there should be a strong indication, given the example presented in Blackburn & Sherwin (2007). However, for our experimental flow presented in figure 6.38, with $b = 0.75$, $Re = 132$, $A = 1.30$ and $T = 0.85$, the period-doubling nature of the unstable flow is clearly evident. Blackburn & Sherwin (2007) restricted themselves to pulsatile flows of amplitude $A = 0.75$, so we cannot validate the flow against any other

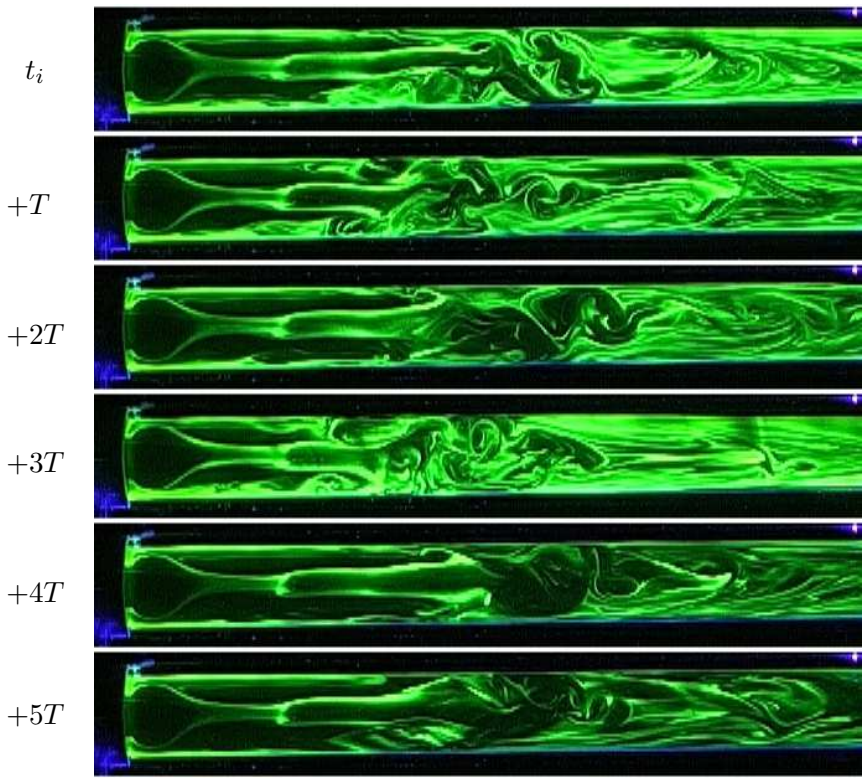

FIGURE 6.39: Coloured-dye visualisations of the flow over six pulse periods, each image at the same phase, for $b = 0.75$, $Re = 206$, $A = 0.75$ and $T = 2.43$ ($\alpha = 11.54$).

work. In relation to the flow at lower pulse amplitudes, it may be possible that in flows of pulse amplitudes $A > 1$, the period-doubling instability is generated even further upstream and acts more rapidly on the convecting vortex ring. This is consistent with the dependence of the growth of the instability on the strength of its parent vortex ring. Another aspect of flows of pulse waveform with $A > 1$ is the existence of a portion of the velocity waveform where the time-dependent sectionally-averaged velocity $\overline{u}(t)$, is less than 0; or, that during a portion of the pulsation, the flow is pulled back upstream through the blockage. This may play a role in the development of the instability being located further upstream than in flows of amplitude $A = 0.75$.

As far as comparison with previous experimental work on single-harmonic pulsatile flows in stenotic geometries of similar blockage ratio can be taken, the results presented here agree broadly with those in the literature (Ohja *et al.* 1989; Ahmed & Giddens 1984, 1983a; Ahmed 1998). The flow configurations of Ohja *et al.* (1989) and Ahmed (1998) both consist of Womersley numbers $\alpha = 7.5$, and hence consist of longer pulse periods than most of the work presented in this chapter. Nonetheless, at high enough Reynolds number, they both observed a stable jet region up to $z/D \approx 2.5$, with a transition and then breakdown of the flow at $z/D \approx 6$.

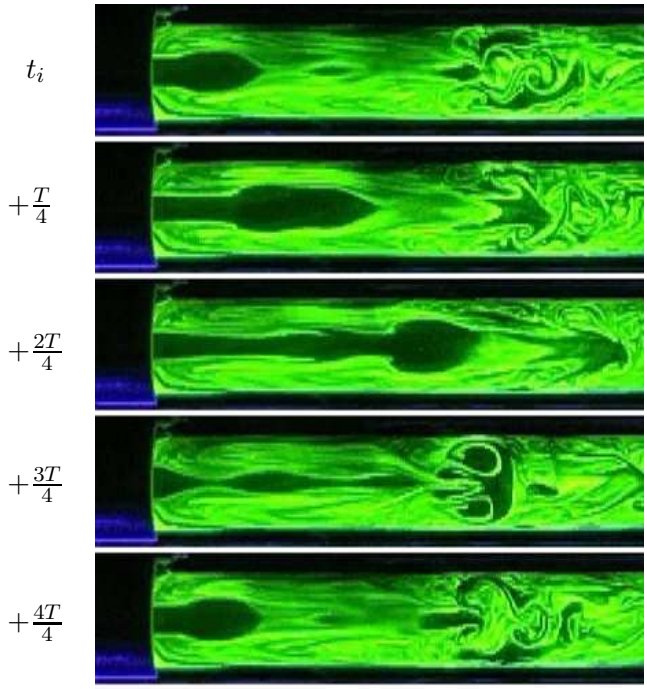

FIGURE 6.40: Dye-visualisations of the flow for $b = 0.90$, $Re = 110$, $A = 0.33$ and $T = 0.70$ ($\alpha = 15.7$). The first four images are over one pulse period, with the final image at the same phase as the first.

6.4.2.3 Instability: $b = 0.90$

For pulsatile flow, the geometry of blockage ratio $b = 0.90$ is an extreme case. In comparison to the other two blockage ratios tested experimentally, flows of $b = 0.90$ are significantly less stable.

Figure 6.40 presents the flow over one pulse period for $b = 0.90$, $Re = 110$, $A = 0.33$ and $T = 0.70$ (maximum periodic Reynolds number $\hat{Re}_p = 146$). In this example, there appears to be no convective shear layer instability immediately downstream of the blockage. Indeed, recalling the discussion in section 6.2.1 on the "pinch-off" of vortex rings after their attaining a certain amount of circulation, figure 6.40 appears to consist of a large vortex ring, followed by a second, smaller one in its wake. At approximately four diameters downstream of the blockage, the vortex breaks down, appearing to interact with the vortex ring trailing in its wake. The vortex is detectable by the large area of clear fluid arriving from upstream. At $z/D \approx 4$, where the vortex ring is destroyed, the ring entrains dye from its wake. This thread of entrained dye is obvious inside the vortex ring of the fourth image of figure 6.40. Shortly after this

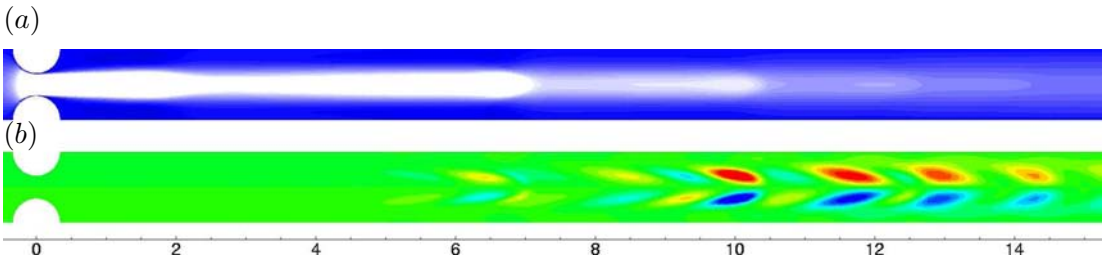

FIGURE 6.41: (a) Contours of axial velocity of the base flow and (b) of the leading perturbation mode $m = 1$, for $Re = 110$, $b = 0.90$, $A = 0.33$ and $T = 0.70$ ($\alpha = 15.7$). The mode of wavenumber $m = 1$ is not period-doubling.

moment, the vortex is destroyed, as is evident in the fifth and then first images.

Due to the large acceleration caused by the blockage, (a ten-fold increase within the blockage, in comparison to four-fold for the $b = 0.75$ blockage) pulsatile numerical simulations performed at blockage ratio $b = 0.90$ require significantly greater computational time. We have not included the $b = 0.90$ blockage geometry in the Floquet stability analysis of section 6.3. However, Floquet analysis has been performed on flow configurations matching those of the examples presented in this section, with the intention of determining the leading perturbation mode and its leading Floquet multiplier.

For the flow configuration of figure 6.40, the Floquet analysis predicts the leading perturbation mode at an azimuthal wavenumber of $m = 1$, with a stable Floquet multiplier of $\mu = 0.8619$. The axial velocity fields of the numerical base flow and the leading perturbation mode are presented in figure 6.41. For this flow configuration the leading perturbation mode is of wavenumber $m = 1$, but is not period-doubling. Instead, the vortex-tilting occurs only in the one direction. The perturbation mode grows at $z/D \approx 11$, where the vortex rings of the base flow slow and come closer together axially. Interestingly, if we regard the perturbation structure on one vortex ring, opposite direction tilting actions can be seen; however, the mode remains periodic with the base flow. This result indicates that we may well have a range of different leading perturbation modes for the $b = 0.90$ blockage.

In the experimental flow, there is no clear indication of the action of the perturbation mode of figure 6.41. Indeed, the flow seems to remain largely axisymmetric. The flow is stable until it reaches the downstream unsteadiness at $z/D \approx 4$, whereupon the main vortex ring is destroyed. However, this is not inconsistent with the mode playing

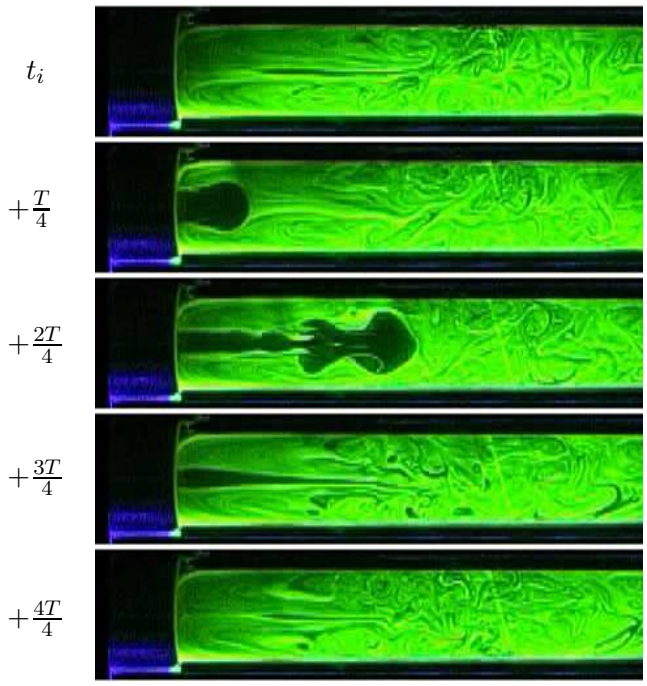

FIGURE 6.42: Dye-visualisations of the flow for $b = 0.90$, $Re = 122$, $A = 0.85$ and $T = 0.75$ ($\alpha = 15.8$). The first four images are over one pulse period, with the final image at the same phase as the first.

a role in the instability of the flow. We can imagine the non-linear growth of the perturbation mode, beginning with a loss of symmetry downstream, which alters the base flow, leading to an asymptotic flow consisting of a flow breakdown 4 to 5 diameters downstream, such as has been seen on direct numerical simulations of pulsatile stenotic flows at $b = 0.75$. The probable subcritical behavior of the various bifurcations (Sherwin & Blackburn 2005) indicates that the instability could be sustained at Reynolds numbers below Re_c; this goes some way to explaining the return of a stable Floquet multiplier of the leading perturbation mode for the obviously unstable flow presented in figure 6.40.

Figure 6.42 presents dye-visualisations for the flow of Reynolds number $Re = 122$, $A = 0.85$ and $T = 0.75$. The flow is similar to that of the previous case, except the pulse amplitude is greater. The flow is highly unsteady, the dye only serving to describe the boundary between the recently-arrived clear upstream fluid and the thoroughly mixed downstream fluid. As can be seen in the first and fifth images, the dye in the downstream region is almost uniformly mixed during the pulse period. The formation

of the vortex ring can again be seen in the second image as the fluid enters through the blockage. In the third image, the leading vortex ring is seemingly followed by smaller vortices, which are then no longer present in the fourth image. The dye structure in the third image of figure 6.42 bears a strong similarity to the visualisation of Gharib *et al.* (1998) of a vortex entering an unbounded domain (their figure 3(c)). In that example, the vortex ring is followed by a series of smaller wake vortices, similar to a Kelvin-Helmholtz instability. In the example of figure 6.40, the shear layer vortices are strong and appear to be responsible for the subsequent breakdown around $z/D = 4$.

Floquet stability analysis on the flow configuration of figure 6.42 returns a leading Floquet multiplier $\mu = 1.3118$ for a leading perturbation mode of $m = 2$. The mode is not period-doubling. Again, the direct action of the mode is not apparent on the unstable asymptotic experimental flow.

In the cases presented here for $b = 0.90$, the main vortex ring which forms each base pulse period is destroyed when it reaches $z/D \approx 4$. It is at this point where the vortex ring meets the region of strong downstream unsteadiness that the vortex breaks up, effectively adding its energy to this turbulence. Such a phenomenon is seen in the $b = 0.75$ geometry as well. The vortex ring decreases in strength as it convects downstream, until it is overwhelmed by the unsteady flow downstream. Qualitatively, there also seems to exist an interaction between the main vortex ring and the smaller vortices which are formed in its wake.

Detecting the role of any absolute instability mode in this transition is problematic, since the asymptotic state of the flow may only have limited qualitative similarity to the structure of the mode. It is possible that this is another instance where shear layer instability augments the absolute instability that would be normally seen in a noise-free numerical simulation. If this were the case, it is possible that the nature of the acting perturbation modes would not be readily detectable in the experiment. The probable subcritical nature of the bifurcations related to these linear perturbation modes is also important in comparing the instabilities seen in experimental flows with the numerically-predicted perturbation modes.

6.5 Chapter summary and discussion

This chapter has investigated various aspects of pulsatile flow through axisymmetric stenotic geometries. In particular, it has focused on the wake behaviour and stability of the flow for different blockage ratios.

Various aspects of the flow behavior have been investigated, including the velocity of the vortex ring which forms downstream of the blockage each period of a pulsatile flow. Driven by the circulation generated through the blockage, the vortex rings travels downstream, faster at higher blockage ratios than at lower ones. For a pulse period $T = 2.5$, it was found that when normalised by the velocity ratio of the stenosis throat $(1/(1-b))$, the vortex ring velocity V_v increases for lower blockage ratios, for $b \gtrsim 0.4$. This is possibly due to the higher axial velocity for higher blockage ratios of the vortex ring, inducing a stronger viscous drag via the tube walls. An analogy was attempted between the work of Gharib *et al.* (1998) and the present flow. An equivalent formation number for the stenotic pulsatile flow was formulated, however the analogy was limited by the differences in domain between the two problems. The presence of the tube walls appears to have a significant effect on the formation and shape of the vortex ring.

The variation of the wall shear stress for several flow configurations was described, with a higher maximum wall shear stress observed for cases at lower pulse periods and at higher blockage ratios. It was found that the time-averaged wall shear stress distribution for pulsatile flow matches up closely with that of the corresponding steady flow. It is only for lower pulse periods of $T \approx 1$, that the two distributions begin to diverge. For the cases considered, for pulse periods greater than 1, flows exhibit low average wall shear stresses (where the average wall shear stress changes sign) in the range $4 \lesssim z/D \lesssim 6$.

Across the three blockage ration ranges tested, Floquet stability analysis with a constant pulse amplitude $A = 0.75$ shows a period-doubling vortex-tilting perturbation mode of wavenumber $m = 1$ dominating for pulse periods $T > 1.2$ for $b = 0.75$ and $T > 2.2$ for $b = 0.50$, while for lower pulse periods, higher wavenumber modes dominate. Figure 6.43 summarises the results of the Floquet analysis for $A = 0.75$, but with respect to Womersley number - we remind the reader that larger arteries generally feature Womersley numbers in the range $10 \lesssim \alpha \lesssim 20$. Smaller arteries further down

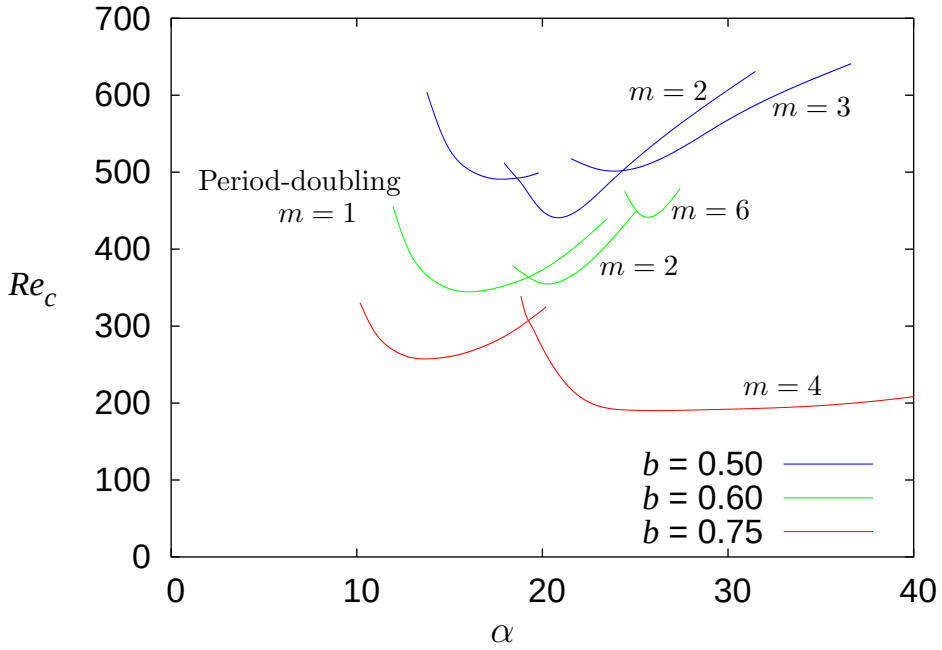

FIGURE 6.43: As a function of Womersley number α, critical Reynolds numbers of from the numerical Floquet stability analysis for $A = 0.75$. Results for three blockage ratios $b = 0.50$, 0.60 and 0.75 are shown. Flows in larger arteries are generally in the range $10 \lesssim \alpha \lesssim 20$.

the cardiovascular system feature $\alpha < 10$, although at these vessel diameters, wall distensibility and non-Newtonian features become non-negligible. The plots of figure 6.43 give an idea of the relevance of the results to more physiologically realistic flows and geometries. Although the real patient stenotic flows are likely to consist of more variable geometries and complicated multi-harmonic velocity waveforms, flows will still feature the same generic vortex ring generation. The results presented here serve as a useful base case for the study of these more physiologically realistic flows.

The initial growth of the $m = 1$ period-doubling mechanism begins far downstream of the blockage. Its axial location of maximum strength varies with the blockage ratio, but appears to be dependent on the different vortex ring velocities. The only firm evidence of any period-doubling instability in the experimental flow occurred for a blockage ratio of $b = 0.75$, but only for pulse amplitudes of $A > 1$. For these flows, vortex rings turn in opposite radial directions each pulse period. However, this particular form of tilting only occurs on the vertical plane and is generated as soon as the pulsation is begun, rather than progressing slowly upstream from a downstream location, thereby leaving the relation to the period-doubling instability seen in the

Floquet stability analysis in doubt. Instabilities for flow configurations just below the critical boundary predicted by the numerical analysis did not exhibit obvious evidence of period-doubling, but their nature is at least consistent with the action of a linear instability mode.

For the higher Womersley number (lower pulse period) range, the vortex-tilting mechanism is overtaken by higher wavenumber modes, including $m = 3$ and $m = 4$ real bifurcations for $b = 0.75$. In the cases of $b = 0.50$ and 0.60, the stability behavior followed that observed in chapter 5 for steady flow, with the $m = 2$ mode overtaking the $m = 1$ subharmonic bifurcation. For still higher Womersley numbers, a $m = 6$ real bifurcation was observed for $b = 0.60$ and a $m = 3$ subharmonic bifurcation for $b = 0.50$.

We can make comparison of these results for the $b = 0.75$ blockage with the work of Blackburn & Sherwin (2007), who investigated a similar flow, but with a smoother geometry, of stenosis length twice that of the present work. They too reported a leading period-doubling vortex-tilting perturbation mode at higher pulse period, but down to a minimum pulse period $T \approx 1.8$, whereupon the $m = 3$ and $m = 4$ "wavy" modes became dominant. This is in contrast to the present work, where the period-doubling mechanism dominates down to $T \approx 1.3$. Also, the optimum period for the period-doubling instability (i.e., the period where the critical Reynolds number for the instability is at its lowest) is for a pulse period $T = 2.15$, in contrast to $T = 3.25$ for Blackburn & Sherwin (2007). Another difference is in the critical Reynolds numbers. For a pulse period $T = 2.5$, the critical Reynolds number for the present work is $Re_c = 260$, in comparison with $Re_c = 389$ for the longer stenosis length geometry of Blackburn & Sherwin (2007). In addition, the critical Reynolds numbers at the optimum pulse periods for the $m = 4$ "wavy" mode are much lower in the present work: $Re_c = 190$ as opposed to $Re_c = 335$. The most likely explanation for these significant differences is the different blockage geometries used in each case. As has already been stated, the blockage in the present work is much shorter, meaning a more rapid contraction of the flow as it squeezes through the stenosis. This rapid contraction has implications for the velocity profiles in the throat of the blockage, as well as for the downstream separating shear layers. This difference in geometry also explains the slightly lower critical Reynolds numbers seen in the steady flow in chapter 5, in

comparison to other experimental studies (Ahmed & Giddens 1983b).

Floquet analysis was also conducted on flows of $Re = 300$, with the pulse amplitude being the variable parameter. This analysis revealed similar instability modes, with the period-doubling vortex-tilting mechanism dominating for $T = 2.5$. The chief difference seen in the perturbation modes was the further upstream position of the maximum strength of the perturbation modes for the critical flows. This is consistent with the growth of the instability mode being dependent on the strength of its parent vortex ring. For a pulse period $T = 1.0$ and blockage ratio $b = 0.75$, $m = 3$ and $m = 4$ real bifurcations once again become dominant. For $b = 0.50$ and $b = 0.60$, the period-doubling $m = 2$ mode becomes dominant, having a structure which again forms on the vortex ring, but, at least for $b = 0.50$, seems to undergo some growth in the near-wall region immediately downstream of the blockage. It was observed that for flows of small pulse period, flows can exhibit a local maximum of velocity in this same near-wall region, the effect appearing most pronounced in the case $b = 0.60$. In the vorticity field, this local axial velocity maximum manifests as a thin thread of negative vorticity which is entrained into the wake of the newly-detached vortex ring (see figure 6.22). This flow feature may play a role in the apparent boundary that exists across the blockage range between the stability behaviors at low and high pulse periods

Experimentally, a variety of coloured dye visualisations were obtained for a range of stable and unstable pulsatile flows. These dye-visualisations use a technique which has so far not been used extensively in experimental work on this subject. For the blockage ratio $b = 0.50$, convective instability seems to be the major cause of instability. A number of unstable flows were observed where the formation of discrete vortices in the separating shear layer could be discerned every pulse period; this bears the hallmarks of a Kelvin-Helmholtz type instability. Evidence could not be found of the linear instability modes predicted by the Floquet stability analysis for $b = 0.50$. Using the concept of an instantaneous Reynolds number $Re_p(t)$, it was found that the stability of the flow depended roughly on the maximum value of this periodic Reynolds number remaining below the critical Reynolds number for convective instability in the steady flow.

As already discussed, for blockage ratio $b = 0.75$, some limited evidence of the absolute linear instability modes was seen. For the $b = 0.90$ blockage ratio, flows were

generally markedly more unstable than at the lower blockage ratios tested. In the cases presented, flows were characterised by a main vortex ring travelling ahead of a series of smaller vortex roll-ups in the vorticity trailing in the wake of the ring. The action of any linear instability mode in the unsteadiness was not evident; nonetheless, the observed flow was still consistent with such an instability mechanism.

Chapter 7

Conclusions

7.1 Summary of conclusions

This chapter presents a brief summary of the conclusions of the thesis. More detailed discussion of the conclusion can be found in the results chapters themselves. The thesis has presented a number of studies on steady and pulsatile internal flows in blocked geometries, which serve as idealised models of arterial stenosis. The aim of the study has been to describe the fundamental characteristics and behaviours of stenotic flows, in order to provide useful base information for the study of flows closer to the physiological reality. The first problem reported on was the steady inlet flow through a partially-blocked asymmetric two-dimensional channel. The second part of the study focused on another geometry, a straight tube containing an axisymmetric stenosis. Steady and pulsatile flows through this geometry were investigated.

From chapter 4, the steady inlet flow through the blocked two-dimensional channel yielded a flow bearing many similarities to the flow over a backward-facing step; namely, a separated flow with a long recirculation region forming downstream of the blockage. The lengths of the recirculation zones compared well for low Reynolds numbers. At higher blockage ratios and Reynolds numbers, a vortex structure – hitherto unreported in the literature on the backward-facing step – was observed, whereby the end of the main recirculation zone developed into a series of smaller recirculations.

The stability of the blocked two-dimensional channel flow was characterised. Using linear stability analysis, the same basic perturbation mode was observed across the blockage ratio range tested, consisting of a flat-roll structure centred on the main recirculation zone; the mode was qualitatively similar to that observed by Barkley *et al.*

(2002) for a backward-facing step. The theory that the instability mechanism was centrifugal in nature was tested. Results from analytical predictions performed using the theory of Bayly (1988) showed that it was unlikely that the instability mechanism was centrifugal in nature. Further analytical predictions revealed the instability to be more consistent with elliptic instability mechanism.

In chapter 5, the steady inlet flow through an axisymmetric stenotic geometry was investigated. The geometry was chosen for its simplicity, the blockage definition having been reduced to a single parameter. The axisymmetric flow consisted of a jet, with a shear layer and a long, thin recirculation zone forming downstream of the blockage. The length of the recirculation zone was found to depend linearly on the Reynolds number. The dependence on blockage ratio was more complicated; a strong analogy was made at intermediate values of blockage ratio with the recirculation zone downstream of a cylinder in a freestream at low Reynolds number. Comparisons were made with experimental results. The recirculation zone lengths matched well, up to the point where instability was observed in the experiments. The experimental instability in the shear layer appeared to be noise-dependent convective instability, seemingly of a Kelvin-Helmholtz type.

For chapters 5 and 6, the stability of the flows has been a key focus. By establishing critical Reynolds numbers for instability for the highly idealised stenotic geometry, upper limits of stability have been established – the addition of any further geometrical complexity or asymmetry to our model will reduce the stability of the flow, lowering the critical Reynolds numbers. Linear stability analysis on the numerical simulations predicted, as expected, the flow to be less stable at higher blockage ratio, but it also found different leading modes across the blockage ratio range. Experimentally, the critical Reynolds numbers for instability were much lower, with the type of instability seen having not been predicted in our numerical stability analysis. The convective instability was investigated in more detail; the period of the oscillations observed in the unsteady flows was found to be constant when non-dimensionalised by $D/\overline{U}$, where D is the tube diameter and $\overline{U}$ the average fluid velocity. Low-amplitude high-frequency forcing of steady flows at low Reynolds number revealed the optimum forcing period (the period which excited the greatest response in the flow) to be generally higher than the period of the instability observed in the self-sustaining unsteady flows at higher

Reynolds numbers.

In relation to real physiological flows through arterial stenosis, the current work indicates that convective shear layer instability plays an important role. Early work on experimental stenotic flows (Ahmed & Giddens 1983b, 1984) aimed at identifying fundamental characteristics of stenotic flows which might be used to estimate the degree of stenosis. The period of oscillation (non-dimensionalised) observed in the self-sustaining unstable flows was approximately constant with Reynolds number, but varying with the blockage ratio. This indicates the potential for the use of spectral analysis of blood flow velocity in determining stenosis severity. Further investigation on this topic may involve a study of the variation of the instability oscillation period with the addition of further geometrical complexities.

Chapter 6 presented the investigation of pulsatile flows in the same axisymmetric stenotic geometry as in chapter 5. The behaviour of the vortex ring which forms each pulse period was analysed, with high vortex ring axial velocities observed at higher blockage ratios. When normalised by the fluid velocity ratio of the stenosis throat – itself a measure of the circulation at a given pulse period – the vortex ring velocity was found to decrease at higher blockage ratio, indicating either a lower proportion of the circulation generated in a pulse period being used in the formation of the primary vortex ring, or some resistive force on the vortex ring motion increasing with blockage ratio. The analogy of the pulsatile stenotic flow with the formation of isolated vortices generated by the motion of a piston (as described in Gharib *et al.* (1998)) was tested; only a qualitative similarity could be found. Some experimental flows at high blockage ratio ($b = 0.90$) showed Kelvin-Helmholtz shear layer roll-up in the wake of the primary vortex ring, consistent with observations made in Gharib *et al.* (1998). The variation of wall shear stress was investigated for a number of cases. It was found that for non-dimensionalised pulse periods of $T \gtrsim 2$, the time-mean of the wall shear stress matched closely with the wall shear stress distribution for the steady inlet flow.

Across the blockage ratio range tested, linear Floquet stability analysis revealed that for the greater part of the pulse period range relevant to blood flow in arteries, a vortex-tilting period-doubling perturbation of azimuthal wavenumber $m = 1$ was the leading instability mode. The peak strength of the mode appeared downstream of the blockage. At lower pulse periods, or higher Womersley numbers, a range of other instability modes

manifested. For blockage ratio $b = 0.75$, a mode of azimuthal wavenumber $m = 4$ dominated; for the blockage ratios $b = 0.50$ and 0.60, modes of wavenumber $m = 2$ led as the pulse period decreased. At very low pulse periods, at the very limit of flows relevant to real blood flows, for blockage ratio $b = 0.60$, a mode of wavenumber $m = 6$ came into play, as well as an $m = 3$ mode for $b = 0.50$. For the blockage ratio $b = 0.75$, the stability behaviour was similar to that reported in Blackburn & Sherwin (2007) for their longer, smoother stenosis, although the critical Reynolds numbers for the present work were significantly lower. This was likely due to the shorter stenosis length of the current geometry, which resulted in blunter velocity profiles in the stenosis throat. The variation of the flow stability with the pulse amplitude, A, at a constant Reynolds number of 300, was also explored. The critical pulse amplitudes at this Reynolds number were generally greater than $A = 0.75$. The period-doubling instability already mentioned was also dominant in most cases; however, in contrast to the flows of pulse amplitude $A = 0.75$, the strength of the mode moved further upstream. This is consistent with the growth of the instability being dependent on the strength of the parent vortex ring, which is greater at higher pulse amplitude.

The experimental flows were always more unstable than predicted by the linear Floquet stability analysis. Only tenuous evidence was found in the experimental flows for the action of the absolute instability modes mentioned in the previous paragraph. Period-doubling instability was observed in some cases, but not where it was expected. It was observed in flows of pulse amplitude $A > 1$ and relatively short pulse period; its orientation in the vertical plane may have been related to temperature-related convection in the experimental apparatus. In flow configurations for which the Floquet stability analysis predicted instability, the exact nature and cause of the observed instability was not always evident. Convective instability, in the form of Kelvin-Helmholtz vortex roll-up, appeared to be important in the unstable flows at blockage ratios of $b = 0.50$ and 0.90. For $b = 0.75$, unstable flows were observed, for which the principal cause of instability was not immediately evident as convective. As has been previously suggested in Blackburn & Sherwin (2007), an interaction is possible between the unstable shear layers formed and the absolute linear instability modes. Combined with the presence of hysteresis, it is possible, especially in the $b = 0.75$ case, that the linear instability modes are at play in the asymptotic flows observed in our experiments.

The thesis has presented a study primarily fluid mechanical in focus. It is beyond the scope of this thesis to describe exactly how the base flow characteristics considered here would exist in real physiological stenotic flows. However, it is likely that many of the general characteristics would be maintained. Flows through stenoses in large arteries will create a vortex ring each pulse period, so the presence of instability modes associated with vortex rings (such as the period-doubling vortex tilting) cannot be discounted.

It is still to be seen how the base flow behaviour of the wall shear stress distributions plotted throughout this thesis would relate to the wall shear stresses in a stenotic artery. For the pulsatile stenotic flow presented here, the low time-averaged wall shear stress observed downstream of the blockage (or analogously, the end of the recirculation zone in the steady case) may be related to the development of secondary stenoses, which can appear downstream of the initial stenosis.

Parts of the thesis have concentrated on the noise-related convective instability observed in both the steady and pulsatile flows. In the experiments, this form of instability dominates for the steady flow and most of the pulsatile flows considered. In our experiment, much effort was invested in reducing the noise, in order to isolate the various flow characteristics. In spite of these efforts, relative to the linear instability modes found numerically, the flows were highly unstable to convective shear layer instability. In an actual arterial stenosis, we would assume the noise in the system to be much greater. Geometrical complexities far beyond the geometries considered in this thesis – as well as external effects, such as from muscle movement or walking – would generate more than enough disturbance to excite an unstable shear layer in a flow through a real arterial stenosis. From the experimental results presented in the thesis, along with the known complexity of the cardiovascular system and its environment, we can conclude that convective shear layer instability is the principal mode of instability for blood flow in arterial stenosis. Along with the variation in instability behaviour with blockage ratio presented in chapter 5, the characterisation of actual arterial stenosis with the instability of the flow through it is a topic of further interest.

7.2 Possible future work

Presented here are a number of possibilities for future work on the results presented in the thesis:

- For the partially-blocked channel flow of chapter 4, one avenue of inquiry might be an experimental model of the flow, to observe how the results compare with the numerical predictions. A point of interest would be the possible action of any shear layer instability. The investigation of the pulsatile inlet flow in such a geometry is another possibility.

- For the steady flow in the axisymmetric stenotic geometry of chapter 5, the open questions relate to the behaviour of the convective instability observed in the experiment. One possibility is to conduct an analytical investigation of the shear layer, using either the Rayleigh or Orr-Summerfeld equations. In a similar vein, the application of eigenvalue analysis techniques, which analyse the transient growth resulting from initial disturbances, such as in Hoepffner *et al.* (2005), could provide useful information on the mechanism behind the convective instability. The possibility of relating the frequency of unstable stenotic flows to the degree of stenosis could also be investigated further.

- The primary question still left open from the work in chapter 6 is exactly how the linear instability modes determined numerically manifest in the experimental flow. The possible interaction between shear-layer convective instability and absolute instability is a subject which can investigated further.

There are a large range of further studies that could be undertaken, which build on the conclusions made in previous chapters. Most of these consist of adding some sort of complexity which takes the geometry or the flow closer to the physiological reality.

For example, a different velocity waveform could be introduced, consisting of multiple harmonics. The effect on the stability of the flow and of the wall shear stress distribution would be of most interest, along with comparisons to the cases reported here for a single-harmonic waveform. The effect of a large number of geometric complexities could be investigated, an example being the added stenosis eccentricity in the study of Varghese *et al.* (2007b). Another possibility is the study of the flow through a

stenosis with an arterial junction at a given distance, as often occurs in atherosclerosis of the carotid artery bifurcation or abdominal aorta. With the work presented in this thesis acting as a base case, the best approach for such a study would to be introduce, as far as possible, a single complexity at a time, allowing the isolation of its effect on the flow.

Bibliography

Adams, E. W. & Johnston, J. P. 1988 Effects of the separating shear-layer on the reattachment flow structure Part 2: Reattachment length and wall shear-stress. *Exps. Fluids* **6**, 493–499.

Ahmed, S. A. 1998 An experimental investigation of pulsatile flow through a smooth constriction. *Exp. Therm. Fluid Sci.* **17**, 309–318.

Ahmed, S. A. & Giddens, D. P. 1983a Flow disturbance measurements through a constricted tube at moderate Reynolds numbers. *J. Biomechanics* **16**, 955–963.

Ahmed, S. A. & Giddens, D. P. 1983b Velocity measurements in steady flow through axisymmetric stenoses at moderate Reynolds numbers. *J. Biomechanics* **16**, 505–516.

Ahmed, S. A. & Giddens, D. P. 1984 Pulsatile poststenotic flow studies with laser doppler anemometry. *J. Biomechanics* **17**, 695–705.

Anayiotos, A. S., Jones, S. A., Giddens, D. P., Glagov, S. & Zarins, C. K. 1994 Shear stress at a compliant model of the human carotid bifurcation. *J. Biomech. Eng.* **116**, 98–106.

Armaly, B. F., Durst, F., Pereira, J. C. F. & Schoenung, B. 1983 Experimental and theoretical investigation of backward-facing step flow. *J. Fluid Mech.* **127**, 473–496.

Baker, C. J. 1979 The laminar horseshoe vortex. *J. Fluid Mech.* **95**, 347–367.

Barkley, D., Gomes, M. G. M. & Henderson, R. D. 2002 Three-dimensional instability in flow over a backward-facing step. *J. Fluid Mech.* **473**, 167–190.

Barkley, D. & Henderson, R. D. 1996 Three-dimensional Floquet stability analysis of the wake of a circular cylinder. *J. Fluid Mech.* **322**, 215–241.

Bayly, B. J. 1988 Three-dimensional centrifugal-type instabilities in inviscid two-dimensional flows. *Phys. Fluids* **31**, 56–64.

Berger, S. A. & Jou, L.-D. 2000 Flows in stenotic vessels. *Annu. Rev. Fluid Mech.* **32**, 347–382.

Blackburn, H. M. & Sherwin, S. J. 2007 Instability modes and transition of pulsatile stenotic flow: pulse-period dependence. *J. Fluid Mech.* **573**, 57–88.

Canuto, C., Hussaini, M., Quarteroni, A. & Zang, T. 1990 *Spectral Methods in Fluid Dynamics*, 2nd edn. Springer Verlag (Berlin and New York).

Caro, C. G. 1978 *The Mechanics of the Circulation*. Oxford Medical.

Caro, C. G., Fitzgerald, J. M. & Schroter, R. C. 1971 Atheroma and arterial wall shear observations. correlation and proposal of a shear dependent mass transfer mechanism for atherogenesis. *Proc. R. Soc. London Ser. B.* **177**, 109–159.

Cassanova, R. A. & Giddens, D. P. 1978 Disorder distal to modified stenoses in steady and pulsatile flow. *J. Biomechanics* **11**, 441–453.

Cavalcanti, S. 1995 Hemodynamics of an artery with mild stenosis. *J. Biomechanics* **28**, 387–399.

Cheng, T., Deville, D., Dheur, L. & Vanderschuren, L. 1992 Finite element simulation of pulsatile flow through arterial stenosis. *J. Biomechanics* **25**, 1141–1152.

Chesler, N. C. & Enyinna, O. C. 2003 Particle deposition in arteries *Ex Vivo*: effects of pressure, flow and waveform. *J. Biomech. Eng.* **125**, 389–394.

Clark, C. 1976a The fluid mechanics of aortic stenosis – i. theory and steady flow experiments. *J. Biomech.* **9**, 521–528.

Clark, C. 1976b The fluid mechanics of aortic stenosis – ii. unsteady flow experiments. *J. Biomech.* **9**, 567–573.

Davies, P. F., Remuzzi, A., Gordon, E. J., Dewey, C. F. & Gimbrone, M. A. 1986 Turbulent fluid shear stress induces vascular endothelial cell turnover *in vitro*. *Proc. Nat. Acad. Sci. USA* **83**, 2114–2117.

Delfino, A., Moore, J. E., Stergiopulos, N., Vaclavik, V., Genton, C. Y. & Meister, J. J. 1998 Wall stresses in the carotid bifurcation: Effects of wall non-homogeneity and correlation with intimal thickness. *J. Vasc. Invest.* **4**, 61–71.

Deplano, V. & Siouffi, M. 1999 Experimental and numerical study of pulsatile flows through stenosis: Wall shear stress analysis. *J. Biomechanics* **32**, 1081–1090.

Dewey, C. F., Bussolari, S. R., Gimbrone, M. A. & Davies, P. F. 1981 The dynamic response of vascular endothelial cells to fluid shear stress. *J. Biomech. Eng.* **103**, 177–185.

Drazin, P. G. & Reid, W. H. 1981 *Hydrodynamic Stability*. Cambridge University Press.

Eloy, C. & Le Dizes 1999 Three-dimensional instability of Burgers and Lamb-Oseen vortices in a strain field. *J. Fluid Mech.* **378**, 145–166.

Frangos, J. A., Eskin, S. G., McIntire, L. V. & Ives, C. L. 1985 Flow effects on prostacyclin production by cultured human endothelial cells. *Science* **227**, 1477–1479.

Friedman, M. H., Hutchins, G. M., Bargeron, C. B., Deters, O. J. & Mark, F. F. 1981 Correlation between intimal thickness and fluid shear in human arteries. *Atherosclerosis* **39**, 425–436.

Fry, D. L. 1968 Acute vascular endothelial changes associated with increased blood flow rate. *Circulation Research* **22**, 165–197.

Gallaire, F., Marquillie, M. & Ehrenstein, U. 2006 Three-dimensional transverse instabilities in detached boundary layers. *J. Fluid Mech.* **571**, 221–233.

Gartling, D. K. 1990 A test problem for outflow boundary conditions – flow over a backward-facing step. *Int. J. Numer. Meth. Fluids* **11**, 953–967.

Gharib, M., Rambod, E. & Shariff, K. 1998 A universal time scale for vortex ring formation. *J. Fluid Mech.* **360**, 121–140.

Ghia, K. N., Osswald, G. A. & Ghia, U. 1989 Analysis of incompressible massively separated viscous flows using unsteady Navier-Stokes equations. *Int. J. Numer. Meth. Fluids* **9**, 1025–1050.

Giddens, D. P., Zarins, C. K. & Glagov, S. 1990 Response of arteries to near-wall fluid dynamic behavior. *Appl. Mech. Rev.* **43**, 98–102.

Giddens, D. P., Zarins, C. K. & Glagov, S. 1993 The role of fluid mechanics in the localisation and detection of atherosclerosis. *J. Biomech. Eng.* **115**, 588–594.

Glagov, S., Zarins, C., Giddens, D. P. & Ku, D. N. 1988 Hemodynamics and atherosclerosis: Insights and perspectives gained from studies of human arteries. *Arch. Pathol. Lab. Med.* **112**, 1018–1031.

Griffith, M. D., Thompson, M. C., Leweke, T., Hourigan, K. & Anderson, W. P. 2007 Wake behaviour and instability of flow through a partially blocked channel. *J. Fluid Mech.* **582**, 319–340.

He, X. & Ku, D. N. 1996 Pulsatile flow in the human left coronary artery bifurcation: Average conditions. *J. Biomech. Eng.* **118**, 74–82.

Helmlinger, G., Geiger, R. V., Schreck, S. & Nerem, R. M. 1991 Effects of pulsatile flow on cultured vascular endothelial cell morphology. *J. Biomech. Eng.* **113**, 123–131.

Helps, E. P. W. & McDonald, D. A. 1953 Systolic backflow in the dog femoral artery. *J. Physiol.* **122**, 74–82.

Hillsley, M. V. & Tarbell, J. M. 2002 Oscillatory shear alters endothelial hydraulic conductivity and nitric oxide levels. *Biochem. Biophys. Research Comm.* **293**, 1466–1471.

Hodgson, L. & Tarbell, J. M. 2002 Solute transport to the endothelial intercellular cleft: the effect of wall shear stress. *Annals. of Biomed. Eng.* **30**, 936–945.

Hoepffner, J., Brandt, L. & Henningson, D. S. 2005 Transient growth on boundary layer streaks. *J. Fluid Mech.* **537**, 91–100.

Huang, H. T., Fiedler, H. E. & Wang, J. J. 1993 Limitation and improvement of piv part ii: Particle image distortion, a novel technique. *Exp. Fluids* **15**, 263–273.

Jo, H., Dull, R. O., Hollisand, T. M. & Tarbell, J. M. 1991 Endothelial albumin permeability is shear dependent, time dependent, and reversible. *Am. J. Physiol. Heart Circ. Physiol.* **260**, 1992–1996.

Kaiktsis, L., Karniadakis, G. E. & Orszag, S. A. 1991 Onset of three-dimensionality, equilibria, and early transition in flow over a backward-facing step. *J. Fluid Mech.* **231**, 501–528.

Kaiktsis, L., Karniadakis, G. E. & Orszag, S. A. 1996 Unsteadiness and convective instabilities in two-dimensional flow over a backward-facing step. *J. Fluid Mech.* **321**, 157–187.

Karniadakis, G. E., Israeli, M. & Orszag, S. A. 1991 High-order splitting methods of the incompressible Navier-Stokes equations. *J. Comput. Phys.* **97**, 414–443.

Kerswell, R. R. 2002 Elliptical instability. *Annu. Rev. Fluid Mech.* **34**, 83–113.

Khalifa, A. M. A. & Giddens, D. P. 1978 Analysis of disorder in pulsatile flows with application to poststenotic blood velocity measurement in dogs. *J. Biomechanics* **11**, 129–141.

Khalifa, A. M. A. & Giddens, D. P. 1981 Characterization and evolution of post-stenotic disturbances. *J. Biomechanics* **14**, 279–296.

Ku, D. N. 1997 Blood flow in arteries. *Annu. Rev. Fluid Mech.* **29**, 399–434.

Ku, D. N. & Giddens, D. P. 1987 Laser doppler measurements of pulsatile flow in a model carotid bifurcation. *J. Biomech. Eng.* **20**, 407–621.

Ku, D. N., Giddens, D. P., Zarins, C. K. & Glagov, S. 1985 Pulsatile flow and atherosclerosis in the human carotid bifurcation. positive correlation between plaque location and low and oscillating shear stress. *Arteriosclerosis* **5**, 293–302.

Landman, M. J. & Saffman, P. G. 1987 The three-dimensional instability of strained vortices in a viscous fluid. *Phys. Fluids* **30**, 2339–2342.

Levesque, M. J., Nerem, R. M. & Sprague, E. A. 1989 The influence of shear stress on cultured vascular endothelial cells: the stress response of an anchorage-dependent mammalial cell. *Biotech. Progress* **5**, 1–8.

Leweke, T., Provansal, M., Ormieres, D. & Lebescond, R. 1999 Vortex dynamics in the wake of a sphere. *Phys. Fluids* **11**, S12.

Leweke, T., Thompson, M. C. & Hourigan, K. 2004 Vortex dynamics associated with the impact of a sphere with a wall. *Phys. Fluids* **16**, L74.

Leweke, T. & Williamson, C. H. K. 1998 Three-dimensional instabilities in wake transition. *European Journal of Mechanics B/Fluids* **17**, 571–586.

Lieber, B. B. & Giddens, D. P. 1990 Post-stenotic core flow behaviour in pulsatile flow and its effects in wall shear stress. *J. Biomech.* **23**, 597–605.

Liu, H. & Yamaguchi, T. 2001 Waveform dependence of pulsatile flow in a stenosed channel. *J. Biomech. Eng.* **123**, 88–96.

Long, Q., Xu, X. Y., Ramnarine, K. V. & Hoskins, P. 2001 Numerical investigation of physiologically realistic pulsatile flow through arterial stenosis. *J. Biomechanics* **34**, 1229–1242.

Loudon, C. & Tordesillas, A. 1998 The use of the dimensionless Womersley number to characterize the unsteady nature of internal flows. *J. Theor. Biol.* **191**, 63–78.

Mallinger, F. & Drikakis, D. 2002 Instability in three-dimensional, unsteady, stenotic flows. *Int. J. Heat Fluid Flow* **23**, 657–663.

Marquet, O., Sipp, D., Chomaz, J.-M. & Jacquin, L. 2006 Linear dynamics of a separated flow over a rounded backward facing step: Global modes and optimal perturbations. In *The 6th Euromech Fluid Mechanics Conference, KTH Mechanics, Stockholm, Sweden, June 26-30, 2006*.

Marquillie, M. & Ehrenstein, U. 2003 On the onset of nonlinear oscillations in a separating boundary-layer flow. *J. Fluid Mech.* **490**, 169–188.

McDonald, D. A. 1952 The velocity of blood flow in the rabbit aorta studied with high-speed cinematography. *J. Physiol.* **118**, 328–339.

McDonald, D. A. 1955 The relation of pulsatile pressure to flow in arteries. *J. Physiol.* **127**, 533–552.

McDonald, D. A. 1974 *Blood Flow in Arteries*. Williams and Wilkins.

Meunier, P. & Leweke, T. 2001 Three-dimensional instability during vortex merging. *Phys. Fluids* **13**, 2747.

Meunier, P. & Leweke, T. 2003 Analysis and treatment of errors due to high velocity gradients in particle image velocimetry. *Exp. Fluids* **35**, 408–421.

Miller, G. D. & Williamson, C. H. K. 1994 Control of three-dimensional phase dynamics in a cylinder wake. *Exp. Fluids* **18**, 26.

Mittal, R., Simmons, S. P. & Najjar, F. 2003 Numerical study of pulsatile flow in a constricted channel. *J. Fluid Mech.* **485**, 337–378.

Moore, J. E., Xu, C., Glagov, S., Zarins, C. K. & Giddens, D. P. 1994 Fluid wall shear stress measurements in a model of the human abdominal aorta: Oscillatory behaviour and relationship to atherosclerosis. *Atherosclerosis* **110**, 225–240.

Nazemi, M., Kleinstreuer, C. & Archie, J. P. 1990 Pulsatile two-dimensional flow and plaque formation in a carotid artery bifurcation. *J. Biomechanics* **23**, 1031–1037.

Nie, J. H. & Armaly, B. F. 2002 Three-dimensional convective flow adjacent to backward-facing step – effects of step height. *Int. J. Heat Mass Transf.* **45**, 2431–2438.

Norberg, C. 1994 An experimental investigation of the flow around a circular cylinder: influence of aspect ratio. *J. Fluid Mech.* **258**, 287.

Ohja, M., Cobbold, R. S. C., Johnston, K. W. & Hummel, R. L. 1989 Pulsatile flow through constricted tubes: an experimental investigation using photochromic tracer methods. *J. Fluid Mech.* **203**, 173–197.

Patel, L. & van den Berg, J. 1969 An electrical analogue of the entire human circulatory system. *Med. Electron. Biol. Eng.* **2**, 161–166.

Perktold, K. & Rappitsch, G. 1995 Computer simulation of local blood flow and vessel mechanics in a compliant carotid artery bifurcation model. *J. Biomech.* **28**, 845–856.

Pitt, R. E., Sherwin, S. J. & Theofilis, V. 2005 BiGlobal stability analysis of steady flow in constricted channel geometries. *Int. J. Numer. Meth. Fluids* **47**, 1229–1235.

Raffel, C., Willert, E. & Kompenhaus, J. 1998 *Particle Image Velocimetry: a Practical Guide*. Springer, Berlin.

Rayleigh 1917 On the dynamics of revolving fluids. *Proc. R. Soc. Lond. Ser. A.* **93**, 148–154.

Reese, J. M. & Thompson, D. S. 1998 Shear stress in arterial stenoses: a momentum integral model. *J. Biomechanics* **31**, 1051–1057.

Rosenfeld, M. & Einav, S. 1995 The effect of constriction size on the pulsatile flow in a channel. *J. Fluids Eng.* **117**, 571–576.

Sahin, M. & Owens, R. G. 2004 A numerical investigation of wall effects up to high blockage ratios on two-dimensional flow past a confined circular cylinder. *Phys. Fluids* **16** (5), 1305–1320.

Salam, T. A., Lumsden, A. B., Suggs, W. D. & Ku, D. 1996 Low shear stress promotes intimal hyperplasia thickening. *J. Vasc. Invest.* **2**, 12–22.

Sheard, G. S., Thompson, M. C. & Hourigan, K. 2003 From spheres to circular cylinders: Classification of bluff ring transitions and structure of bluff ring wake. *J. Fluid Mech.* **492**, 147–180.

Sherwin, S. J. & Blackburn, H. M. 2005 Three-dimensional instabilities of steady and pulsatile axisymmetric stenotic flows. *J. Fluid Mech.* **533**, 297–327.

Sills, H. W., Chang, Y. S., Artman, J. R., Frangos, J. A., Hollis, T. M. & Tarbell, J. M. 1995 Shear stress increases hydraulic conductivity of cultured endothelial monolayers. *Am. J. Physiol. Heart Circ. Physiol.* **268**, 535–543.

Sobey, I. J. 1985 Observation of waves during oscillatory channel flow. *J. Fluid Mech.* **151**, 395–426.

Sobey, I. J. & Drazin, P. G. 1986 Bifurcations of two-dimensional channel flow. *J. Fluid Mech.* **171**, 263–287.

Stary, H. C., Chandler, A. B., Glagov, S., Guyton, J. R., Insull, W., Rosenfeld, M. E., Schaffer, S. A., Schwartz, C. J., Wagner, W. D. & Wissler, R. W. 1994 A definition of initial, fatty streak, and intermediate lesions of atherosclerosis. a report from the committee on vascular lesions of the council on arteriosclerosis, american heart association. *Circulation* **89**, 2462–2478.

Stoker, M. 1973 Role of diffusion boundary layer in contact inhibition of growth. *Nature* **246**, 200–203.

Strony, J., Beaudoin, A., Brands, D. & Adelman, B. 1993 Analysis of shear stress and hemodynamic factors in a model of coronary artery stenosis and thrombosis. *Am. J. Physiol.* **265**, H1787–H1796.

Stroud, J. S., Berger, S. A. & Saloner, D. 2000 Influence of stenosis morphology in flow through severely stenotic vessels: Implications for plaque rupture. *J. Biomechanics* **33**, 443–455.

Stroud, J. S., Berger, S. A. & Saloner, D. 2002 Numerical analysis of flow through a severely stenotic carotid artery bifurcation. *J. Biomech. Eng.* **124**, 9–19.

Sucosky, P., Osorio, D. F., Brown, J. B. & Neitzel, G. P. 2004 Fluid mechanics of a spinner flask bioreactor. *Biotech. & Bioeng.* **85**, 34–46.

Taneda, S. 1956 Experimental investigation of the wakes behind cylinders and plates at low Reynolds numbers. *Journal of the Physical Society of Japan* **11**, 302–307.

Tarbell, J. M. 2003 Mass transport in arteries and the localization of atherosclerosis. *Annu. Rev. Biomed. Eng.* **5**, 79–118.

Taylor, C. A. & Draney, M. T. 2004 Experimental and computational methods in cardiovascular fluid mechanics. *Annu. Rev. Fluid Mech.* **36**, 197–231.

Taylor, C. A., Hughes, T. J. R. & Zarins, C. K. 1998 Finite element modeling of three-dimensional pulsatile flow in the abdominal aorta: Relevance to atherosclerosis. *Ann. Biomed. Eng.* **26**, 1–14.

Thangam, S. & Knight, D. D. 1989 Effect of stepheight on the separated flow past a backward facing step. *Phys. Fluids A* **1** (3), 604–606.

Thompson, M. C. & Ferziger, J. H. 1989 An adaptive multigrid method for the incompressible Navier-Stokes equations. *J. Comput. Phys.* **82**, 94–121.

Thompson, M. C., Hourigan, K. & Sheridan, J. 1996 Three-dimensional instabilities in the wake of a circular cylinder. *Exp. Therm. Fluid Sci.* **12**, 190–196.

Thompson, M. C., Leweke, T. & Provansal, M. 2001a Kinematics and dynamics of sphere wake transition. *J. Fluids Struct.* **15**, 575–585.

Thompson, M. C., Leweke, T. & Williamson, C. H. K. 2001b The physical mechanism of transition in bluff body wakes. *J. Fluids Struct.* **15**, 607–616.

Thwaites, B. 1960 *Incompressible Aerodynamics*. Oxford University Press.

Tobin, R. J. & Chang, I.-D. 1976 Wall pressure spectra scaling downstream of stenoses in steady tube flow. *J. Biomech.* **9**, 633–640.

Tu, C., Deville, M., Dheur, L. & Vanderschuren, L. 1992 Finite element simulation of pulsatile flow through arterial stenosis. *J. Biomech.* **25**, 1141–1152.

Tutty, O. R. 1992 Pulsatile flow in a constricted channel. *J. Biomech. Eng.* **114**, 50–54.

Tylli, N., Kaiktsis, L. & Ineichen, B. 2002 Sidewall effects in flow over a backward-facing step: Experiments and numerical simulations. *Phys. Fluids* **14**, 3835–3845.

Varghese, S. S. & Frankel, S. H. 2003 Numerical modelling of pulsatile turbulent flow in stenotic vessels. *J. Biomech. Eng.* **125**, 445–460.

Varghese, S. S., Frankel, S. H. & Fischer, P. F. 2007a Direct numerical simulation of stenotic flows. Part 1. Steady flow. *J. Fluid Mech.* **582**, 253–280.

Varghese, S. S., Frankel, S. H. & Fischer, P. F. 2007b Direct numerical simulation of stenotic flows. Part 2. Pulsatile flow. *J. Fluid Mech.* **582**, 281–318.

Visbal, M. R. 1991 On the structure of laminar juncture flows. *AIAA J.* **29**, 1273–1282.

Westerhof, N., Elzinga, G. & Sipkema, P. 1971 An artificial arterial system for pumping hearts. *J. Appl. Physiol.* **31**, 776–781.

Westerweel, J. 1997 The effect of a discrete window offset on the accuracy of the cross-correlation analysis of digital piv recordings. *Exp. Fluids* **23**, 20–28.

White, C., Haidekker, M., Bao, X. & Frangos, J. 2001 Temporal gradients in shear, but not spatial gradients, stimulate endothelial cell proliferation. *Circulation* **103**, 2508–2513.

White, F. M. 1999 *Fluid Mechanics*. McGraw-Hill International Editions.

Widnall, S. E., Bliss, D. B. & Tsai, C.-Y. 1974 The instability of short waves on a vortex ring. *J. Fluid Mech.* **66**, 35–47.

Williams, P. T. & Baker, A. J. 1997 Numerical simulations of laminar flow over a 3d backward-facing step. *Int. J. Numer. Meth. Fluids* **24**, 1159–1183.

Womersley, J. R. 1955 Method for the calculation of velocity, rate of flow and viscous drag in arteries when their pressure gradient is known. *J. Physiol.* **127**, 553–563.

Wootton, D. M. & Ku, D. N. 1999 Fluid mechanics of vascular systems, diseases, and thrombosis. *Annu. Rev. Biomed. Eng.* **1**, 299–329.